

Electronic Spectroscopy of Open-Chain and  
Aromatic Hydrocarbon Cations  
in Neon Matrices

---

Inauguraldissertation

zur

Erlangung der Würde eines Doktors der Philosophie

vorgelegt der

Philosophisch-Naturwissenschaftlichen Fakultät

der Universität Basel

von

ÁDÁM NAGY

aus Miskolc (Ungarn)

Basel, 2012

Genehmigt von der *Philosophisch-Naturwissenschaftlichen Fakultät* der  
*Universität Basel* auf Antrag der Herren

Prof. Dr. John P. Maier  
*Dissertationsführer*

Prof. Dr. Markus Meuwly  
*Korreferent*

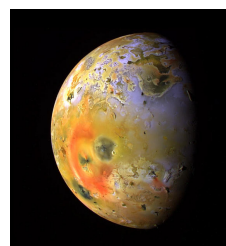
Basel, den 26. Juni 2012

Prof. Dr. Martin Spiess  
*Dekan*

Electronic Spectroscopy of Open-Chain and  
Aromatic Hydrocarbon Cations  
in Neon Matrices

---

Inauguraldissertation



ÁDÁM NAGY

Basel, 2012



*“There was always a minority afraid of something,  
and a great majority afraid of the dark, afraid of the future  
afraid of the past, afraid of the present, afraid of  
themselves and shadows of themselves.”*

Ray Bradbury (1920–2012), *The Martian Chronicles*

*Dedicated to my mother*



## ACKNOWLEDGMENTS

---

This thesis effort presents results of the work carried out by me at the *Department of Chemistry* of the *University of Basel* between January 2007 and March 2012. I wish to express my sincerest thanks to all the people who helped accomplish it:

- Prof. John Maier for initiating and supervising my work in his research group. The excellent instrumentation provided, his advices and continuous support are all highly acknowledged.
- Prof. Markus Meuwly for courteously agreeing to act as the co-referee of this dissertation and for his general interest in my research progress, as well as Prof. Thomas Pfohl for taking the responsibility of chairing my defense.
- Dr. Iryna Garkusha for sharing with me complete trust at work for so many years, and giving me all possible backing at it while tolerating my temperament. Дуже дякую! Prof. Jan Fulara is thanked also here for his noticeable suggestions as well as extensive manual help with experiments, calculations and publishing.
- Many group and department members, former and present, for creating a nice atmosphere to work and, from time to time, regenerate in. Besides the countless discussions we had on both science and life, remembered for sure will be the Engadine, our bowling sessions, the annual piggy eatings and the Silver Star rides. ☺ I am particularly grateful to Dr. Corey Rice for endless explanations, ever useful hints and tireless proofreading of this and other writings of mine; Dr. Ivan Shnitko (†) for teaching me crucial basics of matrix isolation and for the good times we had; PD Dr. Marek Tulej, Dr. Evan Jochowitz and Dr. Alexey Denisov for giving me inspiring influences on spectroscopy and support; and Dr. Anton Batalov and several other, to me unknown ex-members of the matrix crew for defining a solid, easy-to-build-on backbone to the 'old' apparatus. Thanks a lot to all of you!
- The technical staff—including the mechanical workshop (Dieter Wild, Grischa Martin, Franz Haefeli, Yannick Schmidli and Volkan Demir) for machining essential lab elements; George Holderied for constructing complex, sophisticated electronic equipments; Jacques Lecoultre for synthesizing exotic substances and trying to keep a chemist's order in the physicists' chaos; Urs Buser for software; Ruth Pfatzenberger for her graphical help with

the group website; Dr. Anatoly Johnson for program modifications; Jean-Pierre Ramseyer for sample pellets and building maintenance; and the secretary office (Esther Stalder, Daniela Tischhauser and Maya Greuter) for guiding me through administrative matters. Merci vielmools an Alle!

- Although the magnetron project did not quite come through, I appreciate all the efforts of Dr. Wilko Westhäuser and Prof. Gerd Ganteför at the *University of Konstanz* in that direction.
- Prof. John Stanton at the *University of Texas* for a computational collaboration.
- The *University of Basel*, the *City of Basel* and the *Swiss National Science Foundation* for the ‘sponsorship’ of my studies and research.
- Gyöngyi Endrész, Pál Veres and Iván Vass from the *Földes Ferenc High School* for being the greatest of teachers and launching me on the track with their outstanding passion for chemistry and mathematics. Prof. Attila Császár at the *Eötvös Loránd University* is acknowledged for his subsequent guidance and understanding.
- My friends around the Globe for being patient with me and keeping my head above water—I have learnt something from each and every one of you. To name just a few in alphabetical order: Antónia, Corey, Csabber, Csabi, Csongor, Dage, Dóri, Gábor, Gyuri, Ira, Ivan, Levi, Łukasz, Orsi, Pavel, Robi, Szeba, Yavor and Zoli, as well as many of their close friends and other halves.
- My heartiest thanks go to my family—in particular my mom, sis, grannies, dad and aunt—for everlasting moral support and encouragement. Hálás köszönet Mindannyiótoknak!
- Finally, I am immeasurably obliged to Larissa for all the strength and loving care she has been giving. Her entire family is also truly thanked.

Basel  
December 31, 2012

Ádám Nagy



## ABSTRACT

---

Considerable scientific interest has been devoted to the so-called *diffuse interstellar bands* (DIBs)—hundreds of absorption features of different strength and width, located in the visible and near infrared, and arising from the interstellar medium, whose origin remains mysterious. It is presumed that these bands are associated with electronic transitions of families of gaseous, carbon-containing molecules rather than dust grains or ices. This hypothesis has solid observational foundations and may give rise even to origins-of-life speculations. However, an unambiguous assignment of a DIB to a certain species can be made *only* upon measurement of its spectrum in the laboratory and a careful comparison with those detected along sight lines toward a variety of stars.

Advances in experimental techniques over the last two to three decades have enabled the recording of electronic spectra for a number of such clusters in the gas phase. These employ discharge/ablation ion sources, supersonic expansions and sensible, laser-based detection schemes. The main problem is, however, to *locate* the region of absorption first, because even state-of-the-art computational approaches fail to predict reliable excitation energies.

*Matrix isolation* is a suitable method to do this. With it, transient species can be embedded into rare-gas matrices at low temperatures and investigated comfortably by (a set of) spectroscopic means such as direct absorption, fluorescence emission or infrared spectroscopy.

In the course of this work, a matrix setup that draws on another important experimental tool, *mass selection*, has been re-built and further developed. Ions are produced in appropriate sources and trapped selectively in detectable amounts in solid neon at 6 K. Scanning over broad spectral ranges with the help of a dispersion spectrograph provides then the basis for high-resolution surveys in the gas phase.

With this apparatus, a number of reactive species, charged and neutral, have been investigated of relevance for astrophysics, as well as from fundamental chemistry aspects in view of the role they may play in combustion environments,

flames or early Earth-like planetary atmospheres. These include unsaturated carbon chains and polycyclic aromatic hydrocarbon derivatives. Specifically, linear  $\text{HC}_{2n+1}\text{H}^+$ , classical Hückel arenes such as benzylium, tropylium, benzotropylium, naphthylmethylium and indene-related structures, planar  $\text{C}_6\text{H}_4^+$  isomers, as well as some more exotic species were studied and are discussed herein. In most cases their vibrationally resolved electronic spectra were obtained for the first time and various chemical processes detected. Simple models such as the particle-in-a-box and the Hückel molecular orbital method, as well as (time-dependent) density functional calculations were used to describe these and provide an assignment for the observed spectroscopic features.

The effectiveness of the approach was also illustrated on the example of  $\text{H}_2\text{CCC}$ , the first molecule in the nearly a century long history of DIB research for which convincing correlation with astronomical data could be shown. The negligible intermolecular interaction in the condensed phase allowed for excellent prediction of gas-phase line positions.

## ZUSAMMENFASSUNG

---

Von grossem wissenschaftlichen Interesse ist das Erforschen der sogenannten *diffusen interstellaren Banden* (DIB)—hunderte von sichtbaren und nah-infraroten Absorptionslinien unterschiedlicher Intensität und Breite, die aus dem interstellaren Medium hervorgehen und deren Ursprung rätselhaft bleibt. Es ist wahrscheinlicher, dass diese Banden von elektronischen Übergängen gasförmiger, kohlenstoffhaltiger Moleküle stammen, als von Kristallkörnern oder Eis. Diese Hypothese beruht auf stichhaltiger Forschung auf Grund von Beobachtungen und kann sogar eine Basis für Spekulationen um die Entstehung des Lebens bieten. Eine eindeutige Zuordnung einer DIB zu einer bestimmten Spezies kann jedoch *erst dann* erfolgen, nachdem das Spektrum dieser Verbindung im Labor aufgenommen und mit den beobachteten Linien (in Richtung unterschiedlicher Sterne) sorgfältig verglichen wurde.

Fortschritte auf dem Gebiet der experimentellen Methoden in den letzten zwei bis drei Jahrzehnten ermöglichten die Aufnahmen von elektronischen Spektren für einige solcher Cluster in der Gasphase. Bei diesen Verfahren bedient man sich Entladungs-/Ablations-Ionen Quellen, Überschallexpansionen und empfindlicher, Laser-basierter Erfassungsmodelle. Das Hauptproblem besteht jedoch in der *Lokalisierung* der Absorptionsregionen, da es sogar unter Verwendung modernster rechnergestützter Ansätze nicht möglich ist die Anregungsenergien zuverlässig vorherzusagen.

Eine dafür geeignete Technik stellt die *Matrix Isolation* dar. Dabei lassen sich reaktive Verbindungen bei tiefen Temperaturen in eine Matrix aus Edelgasen einbetten und können so mittels spektroskopischer Methoden, wie z.B. der direkten Absorption, Fluoreszenzemission oder Infrarotspektroskopie, gemächlich untersucht werden.

Im Verlauf dieser Arbeit wurde eine Apparatur neu gebaut und weiterentwickelt, die ein zusätzliches, wichtiges experimentelles Werkzeug besitzt, die *Massenselektion*. In einer entsprechenden Quelle werden Ionen erzeugt und, nach Selektion, in detektierbarer Menge in festem Neon bei 6 K eingefangen. Das anschliessende Abtasten breiter spektraler Bereiche mit einem Dispersions-

spektrographen schafft die Grundlage für hochaufgelöste Aufnahmen in der Gasphase.

Mithilfe dieser Apparatur wurde eine Vielzahl von reaktiven Verbindungen untersucht, die nicht nur für die Astrophysik von Relevanz sind, sondern auch für grundlegende, chemische Aspekte im Hinblick auf die Bedeutung, die sie bei Verbrennungen, Flammen oder der Atmosphären auf frühen erdähnlichen Planeten spielen können. Diese Verbindungen schliessen ungesättigte Kohlenstoffketten und polyzyklische aromatische Kohlenwasserstoff-Derivate ein. Insbesondere, lineare  $\text{HC}_{2n+1}\text{H}^+$ , klassische Hückel Arene (z.B. Benzylum, Tropylium, Benzotropylium, Naphthylmethylum und Inden-Derivate), planare  $\text{C}_6\text{H}_4^+$  Isomere als auch exotischere kationische Spezies wurden im Rahmen der vorliegenden Arbeit untersucht und diskutiert. In den meisten Fällen wurde das für die Schwingungen aufgelöste elektronische Spektrum zum ersten Mal aufgenommen, wobei zusätzlich chemische Prozesse beobachten werden konnten. Einfache Modelle wie das Teilchen im Kasten und die Hückel-Molekülorbital-Methode, sowohl (zeitabhängige) Dichtefunktionaltheorie-Rechnungen wurden benutzt dies zu beschreiben und liefern eine Zuordnung für die erhaltenen spektroskopischen Eigenschaften.

Die Leistungsfähigkeit dieser Methode konnte auch am Beispiel von  $\text{H}_2\text{CCC}$  aufgezeigt werden. Es ist das erste Molekül in der langjährigen Geschichte der Erforschung von DIB, für welches überzeugende Übereinstimmungen mit den astronomischen Daten aufgezeigt werden konnten. Durch die vernachlässigbare Wechselwirkung in der kondensierten Phase wurden zuverlässige Vorhersagen über die Position der Gasphasenlinien gemacht.

# CONTENTS

---

ACKNOWLEDGMENTS	vii
ABSTRACT	ix
ZUSAMMENFASSUNG	xi
LIST OF FIGURES	xvii
LIST OF TABLES	xxi
ACRONYMS & ABBREVIATIONS	xxiii
PHYSICAL CONSTANTS & NON-SI UNITS	xxv
<b>I BACKGROUND</b>	<b>1</b>
<b>1 PROLOGUE</b>	<b>3</b>
1.1 SKY OBSERVATIONS & SPECTROSCOPY— A HISTORICAL SYNOPSIS	3
1.2 MATERIAL SYNTHESIS BY STARS	7
1.3 MYSTERIOUS FEATURES FROM THE INTERSTELLAR MEDIUM: THE DIFFUSE INTERSTELLAR BANDS	12
1.4 MOTIVATION AND STRUCTURE OF THE THESIS	15
Bibliography	17
<b>2 THE EXPERIMENTAL APPARATUS</b>	<b>21</b>
2.1 INTRODUCTION	21
2.2 THE SPINE OF THE SETUP—AN OVERVIEW	23
2.3 OPTICAL SCHEME WITH A MONOCHROMATOR	26
2.4 SPECTROGRAPH LAYOUT & OTHER IMPROVEMENTS	27
2.5 ION SOURCES	30
2.6 FLUORESCENCE AMENDMENT	31
2.7 INFRARED MEASUREMENTS	32
2.8 EXPERIMENTAL TRICKS & TREATS	34
2.9 THERORETICAL SUPPORT	36
Bibliography	37

<b>II</b>	<b>RESULTS</b>	<b>41</b>
<b>3</b>	<b>HIGHER-ENERGY ELECTRONIC TRANSITIONS OF</b>	
	<b>HC<sub>2n+1</sub>H<sup>+</sup> (n = 2–7) AND HC<sub>2n+1</sub>H (n = 4–7)</b>	<b>43</b>
3.1	INTRODUCTION	43
3.2	A <sup>2</sup> Π <sub>g/u</sub> ← X <sup>2</sup> Π <sub>u/g</sub> TRANSITION OF HC <sub>2n+1</sub> H <sup>+</sup> (n = 2–7)	44
3.3	VISIBLE SPECTRAL RANGE	45
3.4	UV DOMAIN	51
3.5	B <sup>3</sup> Σ <sub>u<sup>-</sup> ← X <sup>3</sup>Σ<sub>g<sup>-</sup> OF HC<sub>2n+1</sub>H (n = 4–7)</sub></sub>	53
3.6	COMPARISON OF THE ELECTRONIC TRANSITIONS OF	
	HC <sub>2n+1</sub> H <sup>+</sup> AND HC <sub>2n</sub> H <sup>+</sup> (n = 2–7)	54
3.7	OSCILLATOR STRENGTH OF THE OBSERVED	
	TRANSITIONS OF HC <sub>2n+1</sub> H <sup>+</sup> (n = 2–6)	58
3.8	CONCLUSIONS	59
	Bibliography	61
<b>4</b>	<b>ON THE C<sub>7</sub>H<sub>7</sub><sup>+</sup> BENZYLIIUM/TROPYLIUM</b>	
	<b>ION DICHOTOMY</b>	<b>65</b>
4.1	INTRODUCTION	65
4.2	VISIBLE SPECTRA	67
4.3	UV RANGE	68
4.4	COMPUTATIONAL SUPPORT	71
4.5	EARLIER EXPERIMENTAL RESULTS	74
4.6	CONCLUDING REMARKS	75
	Bibliography	81
<b>5</b>	<b>FORMATION OF AROMATICS IN DISCHARGES:</b>	
	<b>ABSORPTION AND FLUORESCENCE OF C<sub>11</sub>H<sub>9</sub><sup>+</sup></b>	<b>85</b>
5.1	DIVERSITY OF C <sub>11</sub> H <sub>9</sub> <sup>+</sup> AND C <sub>11</sub> H <sub>9</sub> <sup>•+</sup> ISOMERS	88
5.2	RESULTS AND OUTLOOK	91
	An article ( <i>J. Am. Chem. Soc.</i> <b>2011</b> , 133: 19796)	95
<b>6</b>	<b>THE INDENE-BASED CATION FAMILY C<sub>9</sub>H<sub>y</sub><sup>+</sup> (y = 7–9)</b>	<b>107</b>
6.1	INTRODUCTION	107
6.2	1-INDENYLIUM, C <sub>9</sub> H <sub>7</sub> <sup>+</sup>	108

6.3	INDENE RADICAL CATIONS, $C_9H_8^{*+}$	114
6.4	2-PROTONATED INDENE, $C_9H_9^+$	117
6.5	COMPUTATIONS	122
<b>7</b>	<b>SUMMARY &amp; OUTLOOK</b>	<b>125</b>
7.1	INVESTIGATED HYDROCARBONS	125
7.2	SPECIES FOR FUTURE CONSIDERATION & UPGRADE POSSIBILITIES	130
	Bibliography	137
<b>III</b>	<b>APPENDIX</b>	<b>141</b>
<b>A</b>	<b>SIDE PROJECTS</b>	<b>143</b>
A.1	PROTONATED BENZENE, NAPHTHALENES AND LARGER PAHS	143
A.1.1	Protonated benzene and fulvene, $C_6H_7^+$	144
A.1.2	Protonated naphthalenes, $C_{10}H_9^+$	146
A.2	NON-CARBONACEOUS COMPOUNDS	151
A.2.1	Sulfur dimers and trimers, $S_{2,3}^{-/0}$	151
A.2.2	Titanium dioxide, $TiO_2$	153
A.3	UNPUBLISHED RESULTS	156
A.3.1	Light-induced <i>cis/trans</i> isomerization of $C_6H_4^+$ species	158
A.3.2	Metal-containing clusters	160
	Bibliography	163
	An article ( <i>Astrophys. J.</i> <b>2011</b> , 728: 131)	169
	<b>CURRICULUM VITAE</b>	<b>177</b>
	PEER-REVIEWED PUBLICATIONS	179





## LIST OF FIGURES

---

Figure 1.1	Prehistoric depictions of the sky and a monument	4
Figure 1.2	Moments and scientists of spectroscopy	5
Figure 1.3	A Hertzsprung–Russell diagram	10
Figure 1.4	Cosmic abundance of lighter elements	12
Figure 1.5	The molecular nature of the Universe	13
Figure 1.6	Relative intensity of observed DIBs	14
Figure 1.7	The “Pillars of Creation”	15
Figure 2.1	Electronic spectrum of $C_4H_3Cl^+$ in the gas phase and neon	22
Figure 2.2	The mass-selective matrix isolation setup	25
Figure 2.3	Optical detection system with a monochromator	26
Figure 2.4	A photograph of the ‘new’ experimental apparatus	27
Figure 2.5	Optical detection system with a spectrograph	28
Figure 2.6	No. of deposition experiments <i>vs.</i> $m/z$ of investigated $C_xH_y$	29
Figure 2.7	Schematic drawing of two ion sources	30
Figure 2.8	Fluorescence detection scheme	31
Figure 2.9	Scheme of the infrared experiment	33
Figure 2.10	IR spectrum of $C_4H_3Cl$ and theoretical vibrational spectra	34
Figure 3.1	The $A^2\Pi_{g/u} \leftarrow X^2\Pi_{u/g}$ electronic transition of $HC_{2n+1}H^+$ ( $n = 2-7$ )	45
Figure 3.2	A visible section of the absorption spectra of $HC_{2n+1}H^+$	49
Figure 3.3	Origin wavelength of transitions of $HC_{2n+1}H^+$ and $HC_{2n+1}H$ plotted against the number of carbon atoms	51
Figure 3.4	UV range of the electronic absorption spectra of $HC_{2n+1}H^+$ ( $n = 3-7$ )	52
Figure 3.5	Bond length alternation in the odd-number carbon members of the $HC_xH^+$ polyacetylene series	55
Figure 4.1	The two most stable structural isomers of $C_7H_7^+$ and tolylium cations	66
Figure 4.2	Electronic spectrum of mass-selected $C_7H_7^+$ ions the visible region	67
Figure 4.3	Electronic spectra of $C_7H_7^+$ in the UV	69
Figure 4.4	Hückel MO diagram of tropylium and benzylium	74

Figure 4.5	A pulse radiolysis experiment of liquid BzCl compared to the UV/Vis transitions of Bz <sup>+</sup> and Bz <sup>•</sup> in neon	75
Figure 4.6	Calculated FC profile of Bz <sup>+</sup> and the experimental trace	76
Figure 4.7	Additional electronic spectra related to the Bz <sup>+</sup> /Tr <sup>+</sup> study	78
Figure 5.1	Mass spectra of 2,4-hexadiyne vapor and a butatriene/diacetylene precursor mixture	86
Figure 5.2	Expected cyclic structures for some of the stronger mass peaks	87
Figure 5.3	The (1) <sup>2</sup> B <sub>2g</sub> ← $\tilde{X}$ <sup>2</sup> A <sub>u</sub> electronic transition of naphthalene <sup>••</sup> in neon	87
Figure 5.4	Optimized ground-state structure and energy of C <sub>11</sub> H <sub>9</sub> <sup>+</sup> isomers	88
Figure 5.5	Overview plot of electronic absorption spectra of C <sub>11</sub> H <sub>9</sub> <sup>+</sup> compared to a direct absorption spectrum of BzTr <sup>+</sup>	90
Figure 5.6	Growth of PAHs in a discharge plasma from 2,4-hexadiyne	92
Figure 6.1	Graphical representation of the ‘main’ isomers of C <sub>9</sub> H <sub>y</sub> <sup>+</sup>	109
Figure 6.2	Scheme and group symmetry of some considered C <sub>9</sub> H <sub>7</sub> <sup>+</sup>	110
Figure 6.3	Electronic absorption spectra of C <sub>9</sub> H <sub>7</sub> <sup>+</sup> and C <sub>9</sub> H <sub>7</sub> <sup>•</sup>	110
Figure 6.4	Absorption spectra of C <sub>9</sub> H <sub>8</sub> <sup>••</sup> isomers	114
Figure 6.5	Electronic absorption spectra of C <sub>9</sub> H <sub>9</sub> <sup>+</sup> and C <sub>9</sub> H <sub>9</sub> <sup>•</sup>	117
Figure 6.6	The ~400–480 nm system of overlapping absorptions of C <sub>9</sub> H <sub>9</sub> <sup>+</sup> and C <sub>9</sub> H <sub>9</sub> <sup>•</sup> , and corresponding fluorescence spectra	120
Figure 6.7	Absorption spectra of C <sub>9</sub> H <sub>y</sub> <sup>+•0</sup> and comparison with calculations	123
Figure 7.1	CRD spectra of <i>l</i> -C <sub>3</sub> H <sub>2</sub> and <i>l</i> -C <sub>3</sub> D <sub>2</sub>	128
Figure 7.2	Absorption spectra of <i>l</i> -C <sub>3</sub> H <sub>2</sub> and <i>l</i> -C <sub>3</sub> D <sub>2</sub> in neon matrices	129
Figure 7.3	Top view of the xenon counter-ion source	130
Figure 7.4	Scheme of a possible magnetron-coupled layout	133
Figure 7.5	Demonstration of the temperature oscillations due to the cryostat	134
Figure A.1	Representation of C <sub>6</sub> H <sub>7</sub> <sup>+</sup> cations and their neutral counterparts	145
Figure A.2	Electronic transitions of protonated benzene and fulvene	146
Figure A.3	Electronic absorption spectra of $\alpha$ - and $\beta$ -protonated naphthalenes illustrating the observed photoinduced processes	149
Figure A.4	Photophysical process diagram of protonated naphthalenes	150
Figure A.5	Photographs characteristic for sulfur	152

- Figure A.6 Electronic transitions of  $S_n^{-/0}$  ( $n=2,3$ ) in neon 153
- Figure A.7 Images characteristic for  $TiO_2$  154
- Figure A.8 Visible part of electronic absorption spectra of titanium oxides 155
- Figure A.9 Mass spectrum of cyclooctatetraene and phenylacetylene 157
- Figure A.10 Electronic absorption spectra of  $C_8H_6^+$  157
- Figure A.11 Overview electronic absorption spectra of  $C_6H_4^+$  159
- Figure A.12 Scheme of considered  $C_6H_4^+$  isomers 159
- Figure A.13 Electronic spectra of  $C_6H_4^+$  in the 600 nm region illustrating the (light-induced) *cis/trans* isomerization processes 160
- Figure A.14 Electronic spectra recorded after the deposition of  $TiO_3^-/TiC_4^-$  161
- Figure A.15 Electronic absorption spectrum recorded after deposition of  $Al^-$  161



## LIST OF TABLES

---

Table 0.1	Energy unit conversion factors	xxv
Table 1.1	A time line of astronomical spectroscopy-related discoveries	6
Table 1.2	Harvard classification of the main sequence stars	9
Table 1.3	Molecules detected in the interstellar medium or circumstellar shells	13
Table 2.1	A selection of species with known electronic spectra in neon matrices from this laboratory	24
Table 3.1	Observed band maxima in the spectra of $\text{HC}_{2n+1}\text{H}^+$ and $\text{HC}_{2n+1}\text{H}$	46
Table 3.2	Comparison of ${}^2\Pi \leftarrow X {}^2\Pi$ transition energies of $\text{HC}_{2n}\text{H}^+$ and $\text{HC}_{2n+1}\text{H}^+$ with theoretical values	56
Table 4.1	Observed band maxima of electronic transitions of $\text{Bz}^\bullet$	70
Table 4.2	Observed band maxima of transitions of $\text{C}_7\text{H}_7^+$ cations	73
Table 4.3	Comparison of $\text{C}_6\text{H}_5\text{X}^+$ species valence isoelectronic with $\text{Bz}^+$	79
Table 6.1	Absorption band maxima of transitions of $\text{C}_9\text{H}_7^+$ and $\text{C}_9\text{H}_7^\bullet$	111
Table 6.2	Calculated ground-state totally symmetric vibrational fundamentals of $\text{C}_9\text{H}_y^+$ cations and $\text{C}_9\text{H}_y$ neutrals	113
Table 6.3	Observed absorption band maxima of transitions of $\text{C}_9\text{H}_8^{*+}$ isomers	115
Table 6.4	Absorption band maxima of transitions of $\text{C}_9\text{H}_9^+$ and $\text{C}_9\text{H}_9^\bullet$	118
Table 6.5	Fluorescence band maxima of a transition of $\text{C}_9\text{H}_9^+$ and $\text{C}_9\text{H}_9^\bullet$	121
Table 6.6	Calculated spectroscopic terms of $\text{C}_9\text{H}_y^+$ cationic and $\text{C}_9\text{H}_y$ neutral isomers compared with experimental data	124
Table 7.1	Origin wavelength of electronic transitions of classical Hückel aromatics compared with theoretical results	127
Table 7.2	Absorption band maxima and intensity of $l\text{-C}_3\text{H}_2$ and $l\text{-C}_3\text{D}_2$	129
Table 7.3	Calculated spectroscopic values of charged and neutral $\text{C}_4^{0/+/-}$ and $\text{C}_6^{0/+/-}$ isomers	131

Table A.1	Observed onsets and vibrational progressions within electronic transitions of $C_6H_7^+$ and their neutrals	147
Table A.2	Observed bands in the electronic absorption spectra of $TiO_2$	155
Table A.3	Fragmentation data of selected hydrocarbons	156

## ACRONYMS & ABBREVIATIONS

---

$0_0^0$	origin (onset; $v' = v'' = 0$ ; 'zero-zero') band of an electronic transition
1D	one-dimensional
6-311G(d,p)	Pople-type split-valence double-zeta basis set with polarization functions
X $\bullet$ +	X radical cation
<i>ab initio</i>	[Lat.] 'from the beginning' (from first principles of quantum mechanics)
bend	bending vibrational mode
CASPT2	complete active space with second-order perturbation theory
CASSCF	complete active space self-consistent field
CC2	approximate coupled-cluster singles-and-doubles method
CCD	charge-coupled device (camera)
cc-pV[D/T]Z	Dunning's correlation-consistent polarized valence-only [double/triple]-zeta (basis set)
CCSD(T)	coupled-cluster singles, doubles (and triples) method
CRDS	cavity ring-down spectroscopy
DIB	diffuse interstellar band
<i>e.g.</i>	<i>exempli gratia</i> [Lat.] ('for example')
EI	electron impact
EOM	equations of motion
<i>et al.</i>	<i>et alii</i> [Lat.] ('and others')
<i>etc.</i>	<i>et cetera</i> [Lat.] ('and so on')
FC	Franck–Condon (envelope, profile)
(FT)IR	Fourier transform infrared (spectroscopy)
FWHM	full width at half maximum
Hlg	halogen (lamp)
HMO	Hückel molecular orbital (method)
HOMO	highest occupied molecular orbital
HRD	Hertzsprung–Russell diagram
HV	high-vacuum
InSb	indium antimonide
<i>in situ</i>	[Lat.] 'in position' (in the reaction mixture)
<i>in silico</i>	[Lat.] 'performed via computer simulation'
ISM	interstellar medium
J–T	Joule–Thomson (effect)
LFP	laser flash photolysis
LIF	laser-induced fluorescence
LUMO	lowest unoccupied molecular orbital
MCP	micro-channel plate

MCT	mercury <sup>II</sup> cadmium <sup>II</sup> telluride; HgCdTe (detector)
MI	matrix isolation
MO	molecular orbital
mpHg	medium-pressure tungsten–mercury (lamp)
MS	mass spectrometry
MP2	Møller–Plesset perturbation theory of the second order
MR(D)-CI	multi-reference (double-excitation) configuration interaction
NdFeB	neodymium–iron–boron (Nd <sub>2</sub> Fe <sub>14</sub> B) magnet alloy
Nd:YAG	neodymium <sup>III</sup> -doped yttrium aluminium garnet; Nd <sup>3+</sup> :Y <sub>3</sub> Al <sub>5</sub> O <sub>12</sub>
NIR	near IR
NMR	nuclear magnetic resonance
UIR	unidentified infrared band
UV/Vis	ultraviolet/visible
PAH	polycyclic aromatic hydrocarbon
PD	photodissociation
PE	photoelectron (spectroscopy)
PES	potential energy (hyper)surface
PI	photoionization
PIB	particle-in-a-box (model)
PMT	photomultiplier tube
PR	pulse radiolysis
PT	proton transfer
QMS	quadrupole mass analyzer
REMPI	resonance enhanced multi-photon ionization
RI	resolution of identity
RT	room temperature
Si	silicon (diode)
S/N	signal-to-noise (ratio)
SOMO	singly occupied molecular orbital
stre	(bond) stretching vibrational mode
(TD) DFT	(time-dependent) density functional theory
(u)B(3)LYP	(unrestricted) Becke, (three-parameter,) Lee–Yang–Parr hybrid functional
<i>vice versa</i>	[Lat.] ‘the other way around’
<i>vs.</i>	<i>versus</i> [Lat.] (‘against’)
Xe	xenon (lamp)
ZPE	zero-point (vibrational) energy
ZPL	zero-phonon line
...	



## PHYSICAL CONSTANTS & NON-SI UNITS

---

[Å]	ångström	$1 \times 10^{-10} \text{ m}$
$a_0$	Bohr radius	$5.291\,772\,109\,2(17) \times 10^{-11} \text{ m}$
$c$	speed of light in vacuum	$2.997\,924\,58 \times 10^8 \text{ m s}^{-1}$
$e$	elementary charge	$1.602\,176\,565(35) \times 10^{-19} \text{ C}$
$\epsilon_0$	vacuum permittivity	$8.854\,187\,817 \dots \times 10^{-12} \text{ F m}^{-1}$
$h$	Planck constant	$6.626\,069\,57(29) \times 10^{-34} \text{ J s}$
$k_B$	Boltzmann constant	$1.380\,648\,8(13) \times 10^{-23} \text{ J K}^{-1}$
[ly]	light-year	$9.460\,730\,472\,580\,8 \times 10^{15} \text{ m}$
$L_\odot$	solar luminosity	ca. $3.839 \times 10^{26} \text{ W}$
[mbar]	millibar	$1 \times 10^2 \text{ Pa}$
$m_e$	electron rest mass	$9.109\,382\,15(45) \times 10^{-31} \text{ kg}$
$M_\odot$	solar mass	$(1.988\,92 \pm 0.000\,25) \times 10^{30} \text{ kg}$
$N_A$	Avogadro constant	$6.022\,141\,29(27) \times 10^{23} \text{ mol}^{-1}$
[u]	unified atomic mass unit	$1.660\,538\,921(73) \times 10^{-27} \text{ kg}$
$R_\infty$	Rydberg constant	$1.097\,373\,156\,853\,9(55) \times 10^7 \text{ m}^{-1}$
$R_\odot$	solar radius	$(6.963\,42 \pm 0.000\,65) \times 10^8 \text{ m}$
$\sigma$	Stefan–Boltzmann constant	$5.670\,373(21) \times 10^{-8} \text{ W m}^{-2} \text{ K}^{-4}$

**Table 0.1:** Energy unit conversion factors

	[J]	[kJ mol <sup>-1</sup> ]	[eV]	[cm <sup>-1</sup> ]	[E <sub>h</sub> ]
1 J	1	$6.023 \times 10^{20}$	$6.242 \times 10^{18}$	$5.035 \times 10^{22}$	$2.294 \times 10^{17}$
1 kJ mol <sup>-1</sup>	$1.660 \times 10^{-21}$	1	$1.036 \times 10^{-2}$	$8.360 \times 10^1$	$3.809 \times 10^{-4}$
1 eV	$1.602 \times 10^{-19}$	$9.641 \times 10^1$	1	$8.066 \times 10^3$	$3.675 \times 10^{-2}$
1 cm <sup>-1</sup>	$1.986 \times 10^{-23}$	$1.196 \times 10^{-2}$	$1.240 \times 10^{-4}$	1	$4.555 \times 10^{-6}$
1 E <sub>h</sub>	$4.360 \times 10^{-18}$	$2.626 \times 10^3$	$2.721 \times 10^1$	$2.195 \times 10^5$	1

---



Part I

**BACKGROUND**



*“All you really need to know for the moment is that the Universe is a lot more complicated than you might think, even if you start from a position of thinking it’s pretty damn complicated in the first place.”*  
Douglas Adams (1952–2001), *Mostly Harmless*

# 1

## PROLOGUE

---

This Universe is thought to have been formed ~13.8 billion years ago (short scale) in a single space–time expansion event commonly known as the Big Bang. [1] Our knowledge on its present, probable past and possible outcomes is a result of a long series of fundamental scientific and technological breakthroughs. [2,3] In an attempt to arouse an interest for astrochemistry in the reader, below are outlined a few of these and the consequences they have led to.

### 1.1 SKY OBSERVATIONS & SPECTROSCOPY—A HISTORICAL SYNOPSIS

*“Almost in the beginning there was curiosity.”*—This simple but profound sentence is the offbeat to Isaac Asimov’s classic, the *New Guide to Science*. [4] Indeed, mankind has long been mystified by the bright spots all over the night sky. Once evolution by natural selection resulted in sufficient growth in cranial size, [5] there came the point where *homo sapiens* got time to spend not only for basic necessities such as obtaining food and shelter, but also to satisfy natural instincts in *exploring* and making notes on the broader environment. *Science* and fine arts, respectively, have been ‘invented’ parallel (Figure 1.1). [4,6]

Early cultures associated celestial objects with deities and spirits, and related them and their movements to phenomena such as seasons, rain, drought and tides. As these circumstances were of crucial importance to survival (and religious admiration did not suffice in having a control over them), sky observations have been registered, systematized and drawn upon likely from prehistoric times already—enough to think of the most famous archaeoastronomical arrangements

such as the Bighorn Medicine Wheel, the Sun Dagger site on Fajada Butte or the Stonehenge (Figure 1.1). [7]

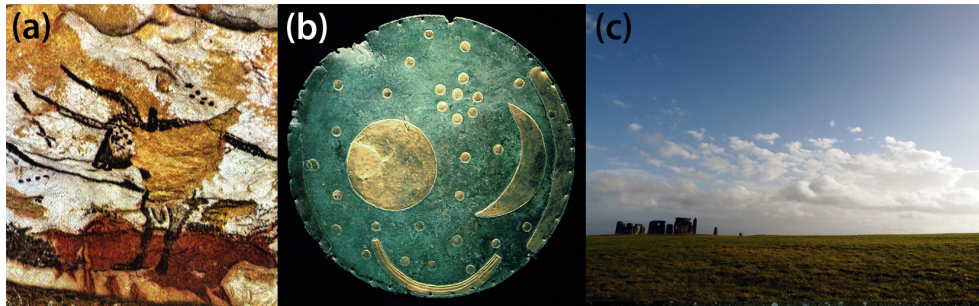


**Figure 1.1:** Two early depictions of the sky: (a) It has been suggested [8] that some of the cave paintings at Lascaux, France (ca. 17 300 BC) may incorporate prehistoric star charts in the form of dot clusters; (b) The Nebra bronze disk ( $d \sim 30$  cm) from ca. 1600 BC, the oldest known realistic representation of the Universe, was discovered by amateur metal-detector treasure hunters in 1999. (c) Stonehenge, aged some 5000 years, continues to amaze nearly a million tourists annually.

The Ancient Greeks treated *astronomy* (that is, the study of celestial objects) as a branch of mathematics and developed it to a highly sophisticated level, and also elaborated on the nature of light. However, the key points in their world view were (geometric) symmetry and perfection, and their explanations as to the characteristics of the Universe relied mainly on ‘pure’ logic and reasoning. On the other hand, their immense achievements in all fields have had lasting influence; therefore, it was not until the Renaissance that the emergence of advocates to the (empirical) scientific method enabled further advancements which initiated reconsideration of our place in the Cosmos at whole new levels. [2–4,6] On the technology front, one of the foundations for the leap forward was the development of fine glasses over the 13–15<sup>th</sup> century, which made possible the grinding and polishing of quality lenses. By the invention of the microscope in 1590 [9] and telescope in 1608, [10] the optical domain not available to the unaided human eye was stretched quickly in both ‘directions’ and the corresponding worlds became observable in details yet unknown.

From a spectroscopist's point of view, however, the year 1666 is a must to remember, when Isaac Newton carried out his landmark experiment resolving white light from the Sun through an ‘aperture’ and a prism into a continuous series of

colors on a screen, a *spectrum* (Figure 1.2). [11] However, the ‘Father of Physics’ did not manage to free his instrumentation (an early ‘spectrograph’) from the so-called chromatic aberration, which withheld him from making progress along this line. It was nearly a century and a half later that William Wollaston and Joseph Fraunhofer could carry out similar experiments with much improved apparatus, the latter thereby observing and categorizing 574 black stripes ‘missing’ from the solar spectrum. [12,13] Again some fifty years must pass by until Gustav Kirchhoff and Robert Bunsen would account for these as *atomic absorption* lines of chemical elements by investigating and analyzing spectra in the laboratory (Figure 1.2). [14] These findings were crowned by (among many others) the well-known story of helium towards the end of the 19<sup>th</sup> century. Jules Janssen and Norman Lockyer detected the second most abundant element of the Universe in the spectrum of the chromosphere of the Sun (*Ἡλιος*) more than a decade before it would be discovered on Earth by Luigi Palmieri and, even later, isolated by William Ramsey. [15]

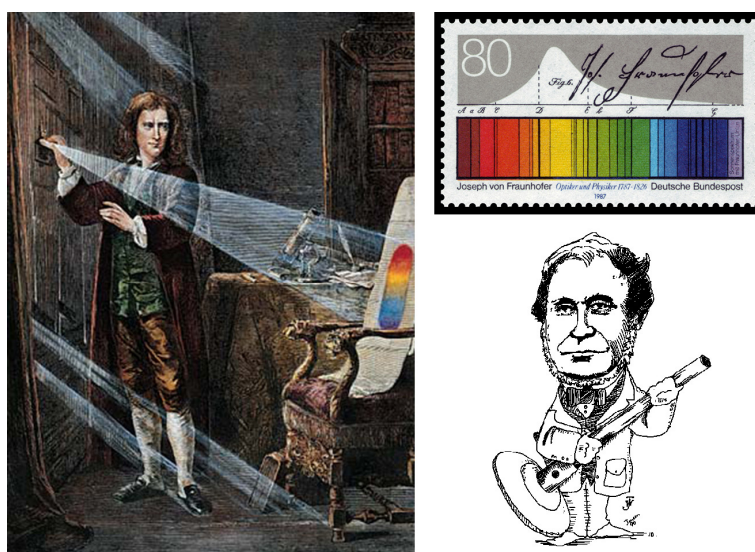


**Figure 1.2:** A few memorable moments and influential scientists of spectroscopy. *Clockwise:* Colored engraving on Newton carrying out his famous prism dispersion experiment (19<sup>th</sup> century, The Granger Collection); the Fraunhofer lines and overall brightness (curve above) as illustrated on a German postal stamp issued in 1987, on the 200<sup>th</sup> anniversary of the (first) spectroscopist's birthday; and a caricature displaying Bunsen with his well-known lab burner.

**Table 1.1:** A(n incomplete) time line of astronomical spectroscopy-related milestone discoveries. Different lists can be found in, e.g., Refs. [17–22].

Year	Scientist	Description
1608	H. Lippershey, Z. Jansen, J. Metius	Invention of the optical (refracting) telescope.
1666	I. Newton	Prism experiments with the white light from the Sun; introduction of the word 'spectrum'; first reflecting telescope. Light was thought to be composed of 'corpuscles' (particles) in nature.
1678	C. Huygens, A.-J. Fresnel	Proposal of the wave theory of light; however, the hypothesis was incomplete.
1729, 1733, 1758	C.M. Hall, G. Bass, J. Dollond	Invention and patenting of the achromatic doublet, a lens free of color distortion.
1729, 1760, 1852	P. Bouguer, J.H. Lambert, A. Beer	Publications on the 'Law of Absorption'.
1752, 1826	T. Melville, W.H.F. Talbot	First flame tests of mineral salts.
1786	D. Rittenhouse	First primitive diffraction grating using hairs.
1800, 1801	F.W. Herschel, J.W. Ritter	Discovery of the infrared and UV radiations.
1802, 1814	W.H. Wollaston, J. von Fraunhofer	Discovery and explanation of 574 lines in the solar spectrum.
1803	T. Young	The double-slit interference experiment gets carried out, which later supports one of the basic principles of quantum mechanics: the wave–particle duality. Development of the transmission grating.
1835–	C. Wheatstone, D. Alter, L. Foucault	Spectral studies of terrestrial light sources such as flames, arcs and electric sparks.
1842	C.A. Doppler	"Frequency 'shifts' for a moving observer."
1845–	G.G. Stokes	Papers published on the theory of light.
1859	G.R. Kirchoff, R.W.E. von Bunsen	Chemical analysis of compounds by producing their spectra.
1868	J. Janssen, J.N. Lockyer	Helium is discovered in the spectrum of the Sun.
1869	A.J. Ångström	Detailed study of the wavelengths of solar spectral lines; first reflection grating.
1873	J.C. Maxwell	Formulation of classical electromagnetic theory, drawing on the works of W. Gilbert, M. Faraday and many others.
1881, 1887	A.A. Michelson, E. Morley	Most famous 'failed' (interference) experiment.
1887	H.R. Herz	First experimental proof of the existence of electromagnetic (radio) waves.
1882	H.A. Rowland	Greatly improved (curved) diffraction gratings.
1885, 1888	J.J. Balmer, J.R. Rydberg	Equations to explain hydrogen's frequency spectrum.
1900	M. Planck	Explanation of the black body radiation by introducing the elemental quantum of action.
1905	A. Einstein	Explanation of the photoelectric effect with the use of the photon.
1912, 1929	V. Slipher, G. Lemiatre, E. Hubble	Galactic redshifts; expanding Universe.
1913	N. Bohr	Development of his atomic model.
1925–	W. Heisenberg, E. Schrödinger, P.A.M. Dirac, W. Pauli, M. Born, etc.	Universal explanation of the spectra of most elements and countless contributions to their better understanding.
early 1900s	P. Zeeman, H.A. Lorentz, J. Stark, W.E. Lamb, E. Rutherford, A.J.W. Sommerfeld, L. de Broglie, F.H. Hund, C.V. Raman, I.I. Rabi, G. Herzberg, R.S. Mulliken, etc.	Theoretical and experimental advances in both atomic and molecular spectroscopy.
1954, 1958	C.H. Townes, N.G. Basov, A.M. Prokhorov, A.L. Schawlow	Birth of <i>modern</i> spectroscopy with the invention of the maser and laser.



Several developments followed in the history of spectroscopy thereafter, including sophisticated experimental advances, and theories of light and matter (later all explained by quantum mechanics, QM); [16] a subjective selection of these is given in Table 1.1. It is beyond the scope of this introduction to detail these steps any further; however, the key point must be clarified: Astronomy relies on observation of spectral features (first lines, later bands) coming from ‘heavenly objects’ and a careful comparison of these with laboratory data provides information on the constitution of the Cosmos.

## 1.2 MATERIAL SYNTHESIS BY STARS

According to the prevailing cosmological model, three elements were formed in the primordial Big Bang: H, He and a little amount of Li. [1,23] One might ask then: How is it that the chemical analysis of different astronomical objects (essentially as inferred in the previous section but done nowadays at much higher sensitivities, *e.g.*, with the *Hubble Space Telescope* or the *Herschel Space Observatory*) reveals a variety of atoms such as precious metals which are also present on Earth? [24] How did carbon, the basic component of life as we know it, arise and form complex structures? [25] From where do the naturally occurring 92 elements, including the ‘heavy-weight’ *f*-block members, come from? [26] The answer to these and similar questions lies in one single word: *stars*.

To understand statements about stellar nucleosynthesis processes that lead to the completeness of the periodic table, one needs to know first something about the formation of stars. [23,27] It is widely accepted that during the birth of the Universe, as matter spread, local density anomalies caused larger clumps to collapse spontaneously, under gravitational forces. The (gravitational) potential energy thereby converted into kinetic energy and heat, which latter manifested in infrared (IR) radiation. This emission balanced the attractive forces some time and a protostar is said to have formed. However, the surrounding envelope have continued to support the core of this stellar nebula with mass, which eventually turned optically thick enough not to release in the IR anymore. This resulted in a raising temperature until nuclear processes ignited, then the developing stellar wind blew off the dust jacket and a star began to shine. [23]

A star is a black body, radiating *continuous* across the spectral regions according to Planck's law, [28]

$$B_\nu(T) = \frac{2h}{c^2} \frac{\nu^3}{\exp\{h\nu/(k_B T)\} - 1} , \quad (1.1)$$

where  $B_\nu(T)$  is the spectral radiance (the power emitted per unit surface per unit solid angle at frequency  $\nu$ ) at temperature  $T$ . However, an analysis of this electromagnetic radiation in the stellar spectra reveals absorption lines originating from atoms in the star's atmosphere, similarly to the case of the Sun (Section 1.1). It turns out that, based on the observed features, the majority of stars can be categorized in classes (Table 1.2). [29,30] In other words, to the unaided eye, there is only one type of object discernible at the night sky: white spots; however, depending on their two most important observable properties, surface temperature and luminosity  $L$ , these over a wide range of star categories (not to mention other entities).  $T$  and  $L$  are related to each other and the star's mass and radius at formation by (a formulation of) the Stefan–Boltzmann law, [31,32]

$$L = 4\pi R^2 \sigma T^4 , \quad (1.2)$$

where  $\sigma$  is the Stefan–Boltzmann constant, so that  $L/L_\odot = (R/R_\odot)^2 (T/T_\odot)^4$  and  $L/L_\odot \approx (M/M_\odot)^{3.9}$ .

It is to be repeated that the consequence of space observations of noticing the existence of stellar classes (Table 1.2) rely on a comparison of the detected spectroscopic features with laboratory data. For astronomers, of utmost importance are the so-called Balmer (Lyman, Paschen, *etc.*) [33–35] series of hydrogen, which can be explained in the framework of QM (namely, Bohr's atomic model from 1913) [36] and are described by the empirical expression

$$\nu/c = R_\infty \left( \frac{1}{n_1^2} - \frac{1}{n_2^2} \right) , \quad (1.3)$$

the Rydberg formula for H, [37] as well as the corresponding temperature-dependent level population, the Boltzmann distribution [38]

$$\frac{n_2}{n_1} = \frac{g_2}{g_1} \exp\{-\Delta E/(k_B T)\} , \quad (1.4)$$

where  $g$  denote level (orbital) degeneracies and  $\Delta E = h\nu$  is the transition energy between levels  $n_1$  and  $n_2$ .

**Table 1.2:** Harvard classification [29,30] of the main sequence (V) stars, also called dwarfs

Class	Surface $T$ [ $10^3$ K]	'Color' <sup>[a]</sup>	Mass [ $M_{\odot}$ ]	Radius [ $R_{\odot}$ ]	Luminosity <sup>[b]</sup> [ $L_{\odot}$ ]	Comment	Fraction of all dwarfs [%]
<b>O</b>	$\geq 33$	blue	$\geq 16$	$\geq 6.6$	$\geq 3 \times 10^5$	ionized He and weak H absorption	0.3 ppm
<b>B</b>	10–33	blueish white	2.1–16	1.8–6.6	$25\text{--}3 \times 10^5$	non-ionized He and stronger H	~0.1
<b>A</b>	7.5–10	white	1.4–2.1	1.4–1.8	5–25	H absorption dominates	< 1
<b>F</b>	6.0–7.5	yellowish white	1.0–1.4	1.1–1.4	1.5–5	H absorption and heavier elements	3
<b>G</b> <sup>[c]</sup>	5.2–6.0	yellow	0.8–1.0	1.0–1.1	0.6–1.5	weak H and increasing metals	8
<b>K</b>	3.7–5.2	orange	0.4–0.8	0.7–1.0	0.1–0.6	no H lines and even more heavy elements	12
<b>M</b>	$\leq 3.7$	red	$\leq 0.4$	$\leq 0.7$	$\leq 0.1$	many metals and simple molecules	76

[a] Indicated are conventional colors; apparent colors may differ. [39,40] [b] Not identical with 'brightness', which is largely influenced by the distance (to be determined by, e.g., parallax measurements, using cepheid variables, or redshifts and Hubble's law) [41] and interstellar material clouds. [c] Our Sun is a G2V-type star with a surface temperature of  $T \approx 5780$  K.

Around 1910, two scientists have independently analyzed the spectral types, and plotted  $L$  and  $T$  of all stars to produce the scatter graph named after them, the Hertzsprung–Russell diagram (HRD) (Figure 1.3). [42,43] It is the 'periodic table of astronomers'. In Table 1.2, classes of the so-called main-sequence stars (also known as dwarfs) are only indicated: They occupy the region in the HRD along the line from top left to bottom right and comprise over 90 % of all stars; thus, they may be considered as the workhorses of molecular synthesis of the Universe. However, there are other regions on a HRD to be recognized as well as some objects relevant but not even indicated (brown dwarfs, neutron stars, etc.); how do they come about? And how does the nucleosynthesis itself happen?

Once large clouds of H and He condensed into protostars as outlined before, depending on the initial cloud density and size, dwarfs of different masses ( $\sim 0.1\text{--}120$  up to perhaps  $1000 M_{\odot}$  'megastars') have been born. From this zero age on, material was formed in the cores of these stars under high temperatures and pressures in nuclear fusion processes, the most important of whose being the proton–proton chain reaction, the triple-alpha process, the CNO cycle and the alpha capture. [23] The products of these recombinations have a slightly lower mass than the combined mass of the reactants and the basis for the energy

thereby radiated away lies in the mass–energy equivalence of Einstein's famous equation,  $E = mc^2$ . [44] Because the iron group is at the broad maximum of the binding energy curve, the fusion of elements heavier than Fe dramatically absorbs energy. [45] Thus, atoms up to about  $^{56}\text{Fe}/^{62}\text{Ni}$  are only synthesized such way. Specifically, in main-sequence stars ca. 90 % of the energy comes from the first reaction series above: proton ‘burning’ into helium; the other processes join in rather at a later stage in their life cycle (see below). In the case of the Sun, this means some  $6 \times 10^{14}$  J energy released in the form of stellar winds and electromagnetic radiation, and  $\sim 6 \times 10^{11}$  kg of H converted into He *per second*. [23]

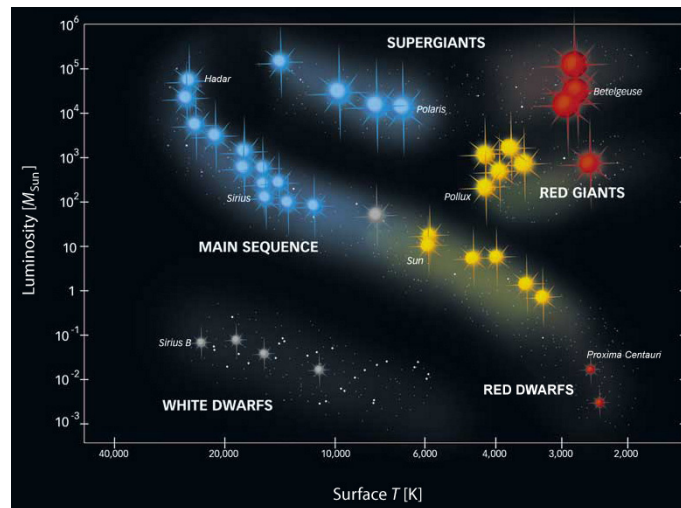


**Figure 1.3:** In a Hertzsprung–Russell diagram, [42,43] luminosity of the star is plotted against its surface temperature.

Although most stars spend some time on the main sequence (except brown dwarfs and other sub-stellar objects,  $M < 0.08 M_{\odot}$ , which never reach the sufficient  $T$  to fuse H, but may nevertheless burn  $^2\text{D}$ ) and contribute thereby to the *synthesis* of different elements, the *release* of these elements into the Cosmos results from another stage in their evolution: their death.

The life of low- and middle-mass stars ( $\sim 0.5\text{--}10 M_{\odot}$ ) ends on the main sequence (Figure 1.3) once all the H in the core has been converted into He. From that point on the core contracts, H in the upper layers gets burned, which means that there is a greater energy flux to the surface, lifting the outer layers. The star becomes a

red giant with tens to hundreds of  $R_{\odot}$ . The core turns into a degenerate electron gas and starts fusing He into carbon.

Eventually, core thermonuclear shutdown occurs but fusion continues in the shell, then the star develops a super wind by convection that blows off the over-shell of the star, leaving a hot core behind. The expelled material forms a cloud that consists of a heated gas; it is called a planetary nebula (for historical reasons) and expands until dissipated into the interstellar medium (ISM), carrying matter in the form of atomic nuclei. The core stays behind as a white dwarf composed mostly of carbon and, not having access to an energy source anymore, it will slowly cool down to form a black dwarf. [23]

Large,  $M > 20 M_{\odot}$  stars (maybe a permil of all stars) at end their life cycle fall their cores so densely (reaching  $\sim 5 \times 10^{17} \text{ kg m}^{-3}$ ), that it becomes comparable to the approximate density of the atomic nucleus and a neutron star is said to have formed. These objects are so unstable that they blow off matter from their outer regions in violent shock waves or explosions (a nova or supernova event), thereby releasing excessive amount of energy enough for the formation of elements heavier than Fe via neutron capture. With that, the circle closes and new stars may be born from newly collapsing, unstable material clouds, 'stellar nurseries'. For instance, our Sun is relatively young ( $\sim 4.6$  billion yr) and rich in heavy elements, pointing with all likelihood to be (at least) a second-generation star.

So, the thermonuclear fusion energy sources within different types of stars synthesizes all the atoms that make up life on Earth (Figure 1.4), which are ejected and inhomogeneously distributed by processes at the end of these stars' life cycle. The 'recycled' material then enriches space in the form of new stars, protoplanetary disks and other astronomical objects, and leads eventually to the development of life itself. "We're made of star stuff.", as Carl Sagan put it. [6] This scheme also means that though the vast areas of space between *perceptible* celestial bodies is often thought of as being completely empty, this is not true. Even the voids between galactic superclusters, the largest known structures of the Cosmos, contain some material, estimated to be a few  $\text{H m}^{-3}$  on average. [46] Although this is some eight orders of magnitude higher a vacuum than that experimentally achievable on Earth ( $\sim 10^{-12}$  mbar), [47] it is not by any means *absolute*.

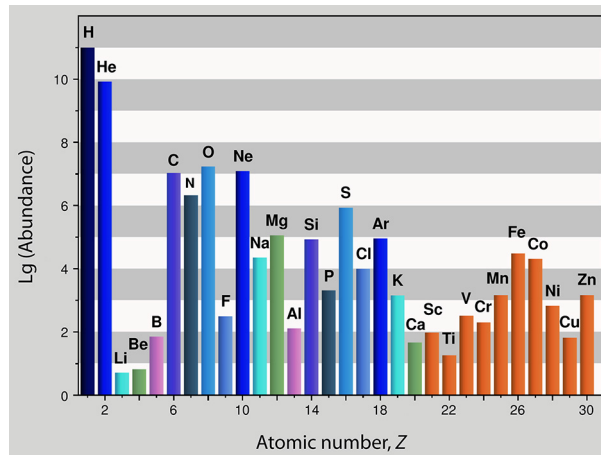


**Figure 1.4:** Cosmic abundance of lighter,  $Z \leq 30$  elements.

### 1.3 MYSTERIOUS FEATURES FROM THE INTERSTELLAR MEDIUM:

#### THE DIFFUSE INTERSTELLAR BANDS

Much denser is the ISM, which comprises gas (primarily hydrogen and helium—remnants of the the Big Bang), plasma and cosmic rays, and specks of particle grains, dust and ices. The presence of solid material (with sizes up to the micrometer range) is revealed by the ‘reddening’ of stellar spectra: Interstellar dust absorbs and scatters blue light waves more than reds (in other words: the extinction is inversely proportional to wavelength), making stars appear redder than they are. [23,27,39] (The same phenomenon is observable at sunsets, when our Sun looks red after its rays having to pass through Earth’s atmosphere ‘side-ways’.) However, the majority (~99 %) of the material in the ISM consists of gaseous, molecular species.

Since the first detection of molecules in space (CH, CH<sup>+</sup> and CN in the period 1937–1941), there has been a steady increase in the number of the observed species. Currently, ~170 molecules are confirmed to be present in the ISM or circumstellar shells, including a number of molecular anions and cations that cope with the supposedly harsh radiation conditions, all sorts of complex, organic molecules up to 13 atoms (including open-chain as well as cyclic hydrocarbons, alcohols, aldehydes, amides, carboxylic acids, cyanides, ethers and esters), and the recently detected C<sub>60</sub> and C<sub>70</sub> (Figure 1.5 and Table 1.3). [48,49] The list concerning extragalactic molecules also grows, to date it is over 50. [48]

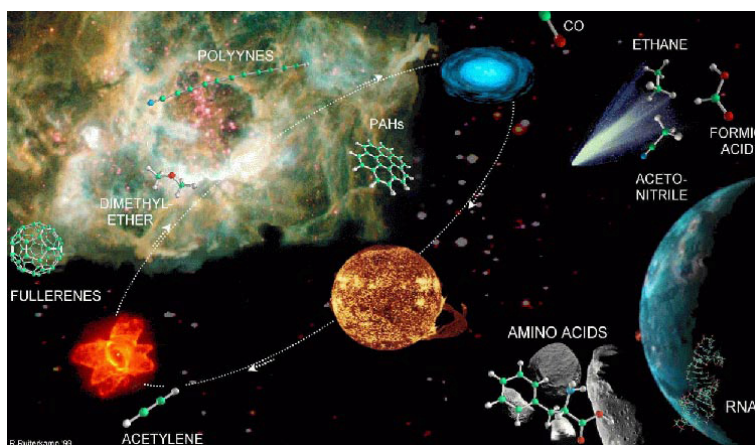


**Figure 1.5:** Artist's impression on the molecular nature of the Universe.

**Table 1.3:** Molecules detected in the interstellar medium or circumstellar shells [48]<sup>[a]</sup>

2	3	4	5	6	7	8
H <sub>2</sub>	C <sub>3</sub>	<i>c</i> -C <sub>3</sub> H	C <sub>5</sub>	C <sub>5</sub> H	C <sub>6</sub> H	CH <sub>3</sub> C <sub>3</sub> N
AlF	C <sub>2</sub> H	<i>l</i> -C <sub>3</sub> H	C <sub>4</sub> H	<i>l</i> -H <sub>2</sub> C <sub>4</sub>	CH <sub>2</sub> CHCN	HC(O)OCH <sub>3</sub>
AlCl	C <sub>2</sub> O	C <sub>3</sub> N	C <sub>4</sub> Si	C <sub>2</sub> H <sub>4</sub>	CH <sub>3</sub> C <sub>2</sub> H	CH <sub>3</sub> COOH
C <sub>2</sub>	C <sub>2</sub> S	C <sub>3</sub> O	<i>l</i> -C <sub>3</sub> H <sub>2</sub>	CH <sub>3</sub> CN	HC <sub>3</sub> N	C <sub>7</sub> H
CH	CH <sub>2</sub>	C <sub>3</sub> S	<i>c</i> -C <sub>3</sub> H <sub>2</sub>	CH <sub>3</sub> NC	CH <sub>3</sub> CHO	H <sub>2</sub> C <sub>6</sub>
CH <sup>+</sup>	HCN	C <sub>2</sub> H <sub>2</sub>	H <sub>2</sub> CCN	CH <sub>3</sub> OH	CH <sub>3</sub> NH <sub>2</sub>	CH <sub>2</sub> OHCHO
CN	HCO	NH <sub>3</sub>	CH <sub>4</sub>	CH <sub>3</sub> SH	<i>c</i> -C <sub>2</sub> H <sub>4</sub> O	<i>l</i> -HC <sub>6</sub> H
CO	HCO <sup>+</sup>	HCCN	HC <sub>3</sub> N	HC <sub>3</sub> NH <sup>+</sup>	H <sub>2</sub> CCHOH	[CH <sub>2</sub> CHCHO]
CO <sup>+</sup>	HCS <sup>+</sup>	HCNH <sup>+</sup>	HC <sub>2</sub> NC	HC <sub>2</sub> CHO	C <sub>6</sub> H <sup>-</sup>	CH <sub>2</sub> CCHCN
CP	HOC <sup>+</sup>	HNCO	HCOOH	NH <sub>2</sub> CHO		H <sub>2</sub> NCH <sub>2</sub> CN
SiC	H <sub>2</sub> O	HNCS	H <sub>2</sub> CNH	C <sub>5</sub> N		[CH <sub>2</sub> OHCHO]
HCl	H <sub>2</sub> S	HOCO <sup>+</sup>	H <sub>2</sub> C <sub>2</sub> O	<i>l</i> -HC <sub>4</sub> H		
KCl	HNC	H <sub>2</sub> CO	H <sub>2</sub> NCN	<i>l</i> -HC <sub>4</sub> N		
NH	HNO	H <sub>2</sub> CN	HNC <sub>3</sub>	<i>c</i> -H <sub>2</sub> C <sub>3</sub> O		
NO	MgCN	H <sub>2</sub> CS	SiH <sub>4</sub>	[H <sub>2</sub> CCNH]		
NS	MgNC	H <sub>3</sub> O <sup>+</sup>	H <sub>2</sub> COH <sup>+</sup>	C <sub>5</sub> N <sup>-</sup>		
NaCl	N <sub>2</sub> H <sup>+</sup>	<i>c</i> -SiC <sub>3</sub>	C <sub>4</sub> H <sup>-</sup>			
OH	N <sub>2</sub> O	CH <sub>3</sub>	HC(O)CN			
PN	NaCN	C <sub>3</sub> N <sup>-</sup>				
SO	OCS	[PH <sub>3</sub> ]				
SO <sup>+</sup>	SO <sub>2</sub>	HCNO				
SiN	<i>c</i> -SiC <sub>2</sub>	HOCN				
SiO	CO <sub>2</sub>	HSCN				
SiS	NH <sub>2</sub>	H <sub>2</sub> O <sub>2</sub>				
CS	H <sub>3</sub> <sup>+</sup>					
HF	H <sub>2</sub> D <sup>+</sup>		9	10	11	≥12
HD	HD <sub>2</sub> <sup>+</sup>					
[FeO]	SiCN		CH <sub>3</sub> C <sub>4</sub> H	CH <sub>3</sub> C <sub>5</sub> N	HC <sub>9</sub> N	<i>c</i> -C <sub>6</sub> H <sub>6</sub>
O <sub>2</sub>	AlNC		CH <sub>3</sub> CH <sub>2</sub> CN	(CH <sub>3</sub> ) <sub>2</sub> CO	CH <sub>3</sub> C <sub>6</sub> H	C <sub>2</sub> H <sub>5</sub> OCH <sub>3</sub>
CF <sup>+</sup>	SiNC		(CH <sub>3</sub> ) <sub>2</sub> O	(CH <sub>2</sub> OH) <sub>2</sub>	C <sub>2</sub> H <sub>5</sub> OCHO	<i>n</i> -C <sub>3</sub> H <sub>7</sub> CN
[SiH]	HCP		CH <sub>3</sub> CH <sub>2</sub> OH	CH <sub>3</sub> CH <sub>2</sub> CHO		HC <sub>11</sub> N
PO	CCP		HC <sub>7</sub> N	[H <sub>2</sub> NCH <sub>2</sub> COOH]		C <sub>60</sub>
AlO	AlOH		C <sub>8</sub> H			C <sub>70</sub>
OH <sup>+</sup>	H <sub>2</sub> O <sup>+</sup>		CH <sub>3</sub> C(O)NH <sub>2</sub>			
CN <sup>-</sup>	H <sub>2</sub> Cl <sup>+</sup>		C <sub>8</sub> H <sup>-</sup>			
SH <sup>+</sup>	KCN		C <sub>3</sub> H <sub>6</sub>			
SH	FeCN					
HCl <sup>+</sup>	HO <sub>2</sub>					

[a] Indicated in the header is the number of atoms. Charged species are colored; in brackets are questionable or rebutted assignments.

Again, these detections must utilize spectroscopy as no methods exist today for the *direct* sampling of the ISM—*Voyager 1*, the farthest manmade object from Earth, was launched 35 years ago but has yet traveled only less than 20 billion kilometers (ca. 17 light hours), whereas the nearest star to the Sun, Proxima Centauri, is located as much as 4.2 ly away. Most of the species above (Table 1.3) were detected by radio, micro- and mm-waves from the 1970s on, drawing on pure rotational transitions induced by permanent dipole moments. However, there are other regions of the electromagnetic spectrum which can be observed to identify new molecular species.

Among the longest-standing astronomical riddles are those associated with a group of interstellar spectroscopic features, the so-called diffuse interstellar bands (DIBs). These are broader than stellar line absorptions in the near IR (NIR) to visible domains—from ca. 400–900 nm (Figure 1.6). Such bands were first detected in 1922 by Mary Heger [50] and to date more than 600 DIBs of different strength and width have been recorded, [51–53] the latter property ranging from a fraction to tens of an Å. [54–56]

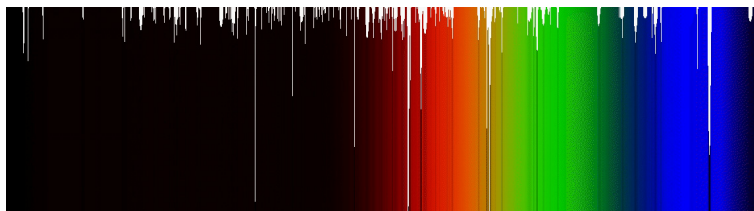


**Figure 1.6:** Relative intensity of observed DIBs. [53]

The gas in the ISM is not distributed uniformly, but rather contracted into clouds. Depending on the physical (and chemical) properties of these material accumulating regions, different types of such clouds can be distinguished such as diffuse, translucent and dark molecular ones (Figure 1.7). DIBs are associated with the diffuse ISM, characterized by a low particle density ( $\sim 1\text{--}10^2$  molecules/cm<sup>3</sup>) and temperatures ranging from a few to a hundred Kelvins. In view of these, the abundance of ‘CHON’-type organic species (Figure 1.4 and Table 1.3) and a number of other factors, several hypotheses have been put forward as to the origin of DIBs. These ‘carrier’ candidates include dust grains, porphyrins,



long and unsaturated carbon chains, polycyclic aromatic hydrocarbons (PAHs) and fullerenes, and even excited H<sub>2</sub>. [49,54–57]

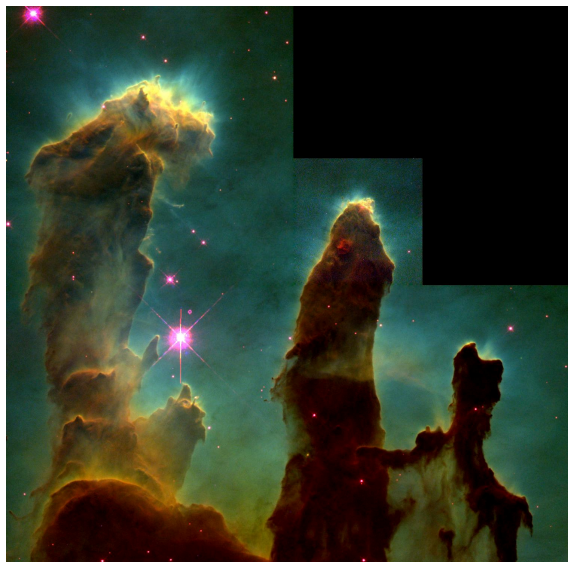


**Figure 1.7:** The “Pillars of Creation”, one of the most famous space photographs as taken by the *Hubble Space Telescope* of elephant trunks of interstellar gas and dust in the Eagle Nebula, some 7 000 ly from Earth. *Credit:* NASA, ESA, STScI, J. Hester and P. Scowen.

Most important for this study was that carbon clearly plays a dominating role in (the majority of) these proposals and, thus, several such species were investigated in these as well as many other laboratories.<sup>1</sup> However, apart from a few rather accidental matches, there had not been any solid proof as to a certain species belonging to one or more DIBs.

#### 1.4 MOTIVATION AND STRUCTURE OF THE THESIS

The aim of this work was to investigate reactive species of both open-chain and aromatic origin (with a primary focus on cations) that have been assumed to be of relevance for DIB research. *Reliable* help is to be provided for gas-phase measurements as to where to search for and what kind of absorptions, which

---

<sup>1</sup> For discussions on the characteristics of interstellar material clouds and DIBs, see also the introductory chapters of (more recent) Ph.D. theses from this research group at the University of Basel, Faculty of Science.

data, once obtained, may in turn be compared directly with astronomical spectra. The dissertation is structured as follows.

After this introductory chapter, the attention is directed to the matrix isolation technique, as well as the mass-selective experimental setup which has been rebuilt, improved and further developed as an organic part of this doctoral work ([Chapter 2](#)). The elements of this apparatus are described.

In the second, main part of the thesis some of the results are discussed. [Chapter 3](#) describes new laboratory data on the linear, odd-carbon polyacetylene cation series,  $\text{HC}_{2n+1}\text{H}^+$ , and their neutral counterparts. [Chapter 4](#) moves on from open-chain species to address prototypical representatives of ‘classical’ Hückel aromatic (planar, with  $4x + 2$  valence electrons) cations, that is,  $\text{C}_7\text{H}_7^+$  isomers. This information is then broadened by findings on larger, bicyclic arenes, namely  $\text{C}_{11}\text{H}_9^+$  ([Chapter 5](#)) and a set of indene-related compounds,  $\text{C}_9\text{H}_7^+$  ([Chapter 6](#)). In [Chapter 7](#) the outcomes are summarized and concluded, and an outlook as to some of the possible modifications and improvements to the experimental setup is provided. A selection of ideas for species that are worth considering to study in the future is also given there.

An overview of other applications of the apparatus complements the thesis by describing some key results of additional projects ([Appendix A](#)). These include the electronic spectroscopy of a selection of protonated PAHs, other exotic hydrocarbons and different non-carbonaceous compounds, and the various chemical processes thereby observed, *e.g.*, *cis/trans* photoisomerization or quantum tunneling. Furthermore, a number of spectra without detailed/final assignment are listed for future reference.

## Bibliography

- [1] M. Rees. *Universe: The definitive visual guide*. New York: DK Publishing, **2008**.
- [2] J. Gribbin. *The scientists: A history of science told through the lives of its greatest inventors*. New York: Random House, **2004**.
- [3] J. Gribbin. *Science: A history 1543–2001*. London: Penguin Books, **2003**.
- [4] I. Asimov. *Asimov's New Guide to Science*. London: Penguin Books Ltd, **1987**.
- [5] R. Dawkins. *The greatest show on Earth: The evidence for evolution*. London: Bantam Press, **2009**.
- [6] C. Sagan. *Cosmos*. New York: Ballantine Books, **1985**.
- [7] A.F. Aveni. *Stairways to the stars: Skywatching in three great ancient cultures*. USA: John Wiley & Sons, **1999**.
- [8] M. Rappenglück. *Ice Age star map discovered*. BBC News (Ed.: D. Whitehouse), **2000**;  
<http://news.bbc.co.uk/2/hi/science/nature/871930.stm>.
- [9] *Microscopes: Time line*. The official web site of the Nobel Prize;  
<http://www.nobelprize.org/educational/physics/microscopes/timeline/index.html>.
- [10] *The telescope*. The Galileo Project;  
<http://galileo.rice.edu/sci/instruments/telescope.html>.
- [11] I. Newton. *A new theory about light and colours*. Phil. Trans. R. Soc. London **1672**, 6(80): 3075–3087; *Am. J. Phys.* **1993**, 61(2): 108–112.
- [12] W.H. Wollaston. *A method of examining refractive and dispersive powers, by prismatic reflection*. Phil. Trans. R. Soc. London **1802**, 92: 365–370;  
<http://www.jstor.org/stable/107124>.
- [13] J. Fraunhofer. *Bestimmung des Brechungs- und Farbenzerstreuungs-Vermögens verschiedener Glasarten, in Bezug auf die Vervollkommnung achromatischer Fernröhre*. Gilbert's Ann. Phys. **1817**, 56: 264–313.
- [14] R. Bunsen, G. Kirchhoff. *Untersuchungen über das Sonnenspektrum und die Spektren der chemischen Elemente*. Ann. Phys. Chem. **1860**, 110: 161–189;  
<http://www.chemteam.info/Chem-History/Kirchhoff-Bunsen-1860.html>.
- [15] W. Ramsey. *Helium, a gaseous constituent of certain minerals. Part I*. *Proc. R. Soc. London* **1895**, 58(347–352): 80–89.
- [16] J. Gribbin. *In search of Schrödinger's cat: Quantum physics and reality*. New York: Bantam Books, **1984**; Hungarian edition: Akkord Kiadó, **2001**.
- [17] V. Thomsen. *A timeline of atomic spectroscopy*. *Spectroscopy* **2006**, 21(10): 32–42;  
<http://www.spectroscopyonline.com/>.
- [18] *The history of spectroscopy, A perspective*. G.R. Harrison Spectroscopy Laboratory, MIT, Cambridge; <http://web.mit.edu/spectroscopy/history/spec-history.html>.
- [19] *A brief (incomplete) history of light and spectra*. ChemTeam: A tutorial for high school chemistry; <http://www.chemteam.info/electrons/spectrum-history.html>.

- [20] N.C. Thomas. *The early history of spectroscopy*. *J. Chem. Educ.* **1991**, 68(8): 631–633; and references therein.
- [21] Y.P. Varshni, J. Talbot. *History of astronomical spectroscopy*. Laser Stars: Plasma recombination lasers in stellar atmospheres; <http://laserstars.org/spectra/>.
- [22] M. Tulej. *Spectroscopy and related aspects*. Lecture notes, University of Basel, **2008**.
- [23] A.M. Shaw. *Astrochemistry: From astronomy to astrobiology*. Chichester: John Wiley & Sons, **2007**.
- [24] J.J. Cowan, C. Sneden. *Heavy element synthesis in the oldest stars and the early Universe*. *Nature* **2006**, 440(7088): 1151–1156; and references therein.
- [25] See, e.g., A. Evans, J.Th. van Loon, C.E. Woodward, R.D. Gehrz, G.C. Clayton, L.A. Helton, M.T. Rushton, S.P.S. Eyres, J. Krautter, S. Starrfield, R.M. Wagner. *Solid-phase C<sub>60</sub> in the peculiar binary XX Oph?* *Mon. Not. R. Astron. Soc. Lett.* **2012**, 421(1): L92–L96.
- [26] See, e.g., I.U. Roederer, J.E. Lawler, J.J. Cowan, T.C. Beers, A. Frebel, I.I. Ivans, H. Schatz, J.S. Sobeck, C. Sneden. *Detection of the second r-process peak element tellurium in metal-poor stars*. *Astrophys. J. Lett.* **2012**, 747(1): L8/ 1–5; and references therein concerning some recent discoveries.
- [27] H.H. Voigt. *Abriss der Astronomie*. Mannheim: Bibliographisches Institut, **1991**.
- [28] M. Planck. *Zur Geschichte der Auffindung des physikalischen Wirkungsquantums*. *Naturwissenschaften* **1943**, 31(14–15): 153–159.
- [29] A.J. Cannon, E.C. Pickering. *Classification of 1688 southern stars by means of their spectra*. *Ann. Harvard Coll. Observatory* **1912**, 56(5): 115–164.
- [30] J.S. Allen. *The classification of stellar spectra*. UCL Astrophysics Group, London; [http://www.star.ucl.ac.uk/~pac/spectral\\_classification.html](http://www.star.ucl.ac.uk/~pac/spectral_classification.html).
- [31] J. Stefan. *Über die Beziehung zwischen der Wärmestrahlung und der Temperatur* in Sitzungsberichte der mathematisch-naturwissenschaftlichen Classe der kaiserlichen Akademie der Wissenschaften, Vol. 79, pp. 391–428, **1879**.
- [32] L. Boltzmann. *Ableitung des Stefan'schen Gesetzes, betreffend die Abhängigkeit der Wärmestrahlung von der Temperatur aus der electromagnetischen Lichttheorie*. *Ann. Phys.* **1884**, 258(6): 291–294.
- [33] J.J. Balmer. *Notiz über die Spectrallinien des Wasserstoffs*. *Ann. Phys.* **1885**, 261(5): 80–87.
- [34] T. Lyman. *The spectrum of hydrogen in the region of extremely short wave-lengths*. *Astrophys. J.* **1906**, 23(3): 181–210.
- [35] F. Paschen. *Zur Kenntnis ultraroter Linienspektren*. *Ann. Phys.* **1908**, 27: 537–570.
- [36] N. Bohr. *On the constitution of atoms and molecules*. *Philos. Mag.* **1913**, 26: 1–24; *Philos. Mag.* **1913**, 26(153): 476–502.

- [37] J.R. Rydberg. *Recherches sur la constitution des spectres d'émission des éléments chimiques*. Den Kungliga Svenska Vetenskapsakademiens Handlingar, Vol. 23, No. 11, **1889**.
- [38] D.C. Harris, M.D. Bertolucci. *Symmetry and spectroscopy: An introduction to vibrational and electronic spectroscopy*. New York: Dover Publications, **1989**.
- [39] *The Colour of Stars*. CSIRO: Australia Telescope Outreach and Education, **2004**; [http://outreach.atnf.csiro.au/education/senior/astrophysics/photometry\\_colour.html](http://outreach.atnf.csiro.au/education/senior/astrophysics/photometry_colour.html).
- [40] M.N. Charity. *What color are the stars?* Vendian Systems, **2008**.
- [41] E.P. Hubble. *A relation between distance and radial velocity among extra-galactic nebulae*. *Proc. Natl. Acad. Sci. USA* **1929**, 15(3): 168–173.
- [42] E. Hertzsprung. *Zur Bestimmung der photographischen Sterngröße*. *Astron. Nachr.* **1907**, 176(4204): 49–60.
- [43] H.N. Russell. *Relations between the spectra and other characteristics of the stars*. *Pop. Astron.* **1914**, 22: 275–294.
- [44] A. Einstein. *Ist die Trägheit eines Körpers von seinem Energieinhalt abhängig?* *Ann. Phys.* **1905**, 323(13): 639–641.
- [45] C.R. Nave. *Nuclear binding energy*. HyperPhysics, Georgia State University, Atlanta, **2012**; <http://hyperphysics.phy-astr.gsu.edu/hbase/nucene/nucbin.html>.
- [46] M. Tadokoro. *A study of the Local Group by use of the virial theorem*. *Publ. Astron. Soc. Japan* **1968**, 20(3): 230–238.
- [47] G. Gabrielse, X. Fei, L.A. Orozco, R.L. Tjoelker, J. Haas, H. Kalinowsky, T.A. Trainor, W. Kells. *Thousandfold improvement in the measured antiproton mass*. *Phys. Rev. Lett.* **1990**, 65(11): 1317–1320.
- [48] *Molecules in Space*. The Cologne Database for Molecular Spectroscopy (CDMS), Universität zu Köln, I. Physikalisches Institut, **2012**; <http://www.astro.uni-koeln.de/cdms/catalog>.
- [49] *The Molecular Universe*. Proc. IAU 280 (Toledo); Eds.: J. Cernicaro, R. Bachiller, Cambridge: Cambridge University Press, **2011**.
- [50] M.L. Heger. *Further study of the sodium lines in class B stars; The spectra of certain class B stars in the regions 5630A–6680A and 3280A–3380A; Note on the spectrum of  $\gamma$  Cassiopeiae between 5860A and 6600A*. *Lick Observatory Bulletin* **1922**, 337: 141–148.
- [51] G.H. Herbig. *The diffuse interstellar bands*. *Ann. Rev. Astron. Astrophys.* **1995**, 33: 19–73.
- [52] P. Jenniskens, F.-X. Désert. *A survey of diffuse interstellar bands (3800–8680 Å)*. *Astron. Astrophys. Suppl. Ser.* **1994**, 106: 39–78.
- [53] P. Jenniskens. *Diffuse Interstellar Band Catalog*. NASA, **2009**; <http://leonid.arc.nasa.gov/DIBcatalog.html>.

- [54] P.J. Sarre. *The diffuse interstellar bands: A major problem in astronomical spectroscopy*. *J. Mol. Spectrosc.* **2006**, 238(1): 1–10.
- [55] F. Salama. *PAHs in astronomy—A review*. *Proceedings of the IAU: Symposium No. 251 (Organic Matter in Space)* **2008**, pp. 357–366.
- [56] N.L.J. Cox. *The PAH-DIB hypothesis*. In *PAHs and the Universe*; Eds.: C. Joblin, A.G.G.M. Tielens, *EAS Publications Series* **2011**, 46: 349–354.
- [57] *The diffuse interstellar bands*. IAU Symposium No. 297 (Conference to be held in Haarlem, Netherlands); Eds: J. Cami, N. Cox, **2013**.

*“A worker may be the hammer’s master, but the hammer still prevails.  
A tool knows exactly how it is meant to be handled,  
while the user of the tool can only have an approximate idea.”*  
Milan Kundera (b. 1929), *The Book of Laughter and Forgetting*

# 2

## THE EXPERIMENTAL APPARATUS

---

### 2.1 INTRODUCTION

As briefly outlined in the previous chapter, in order to decide whether a certain species can be held responsible for DIBs, spectroscopic data need to be accumulated in the laboratory. High-resolution electronic spectra for several carbonaceous clusters have been recorded in the gas phase, employing discharge/ablation ion sources, supersonic expansions and laser-based detection schemes. [1] The main trouble lies in *locating* the region of absorption first, because even state-of-the-art computational approaches may not predict excitation energies reliably. *Matrix isolation* (MI) spectroscopy is a suitable method of choice.<sup>1</sup> [2–10]

A few decades back the standard approach for performing spectroscopy on transient species was the following. In room-temperature solvents reactive radicals and ions were observed after employing *in situ* synthesis methods such as pulse radiolysis (PR) or flash photolysis (LFP). In these, an energetic pulse is provided to the system, which induces chemistry such as bond breaking and/or formation, and the appearance/extinction of species may be monitored with ‘direct’ electronic absorption for instance. However, the main obstacle is clear: Because there is no selectivity or separability, the assignments can rely ‘only’ on kinetic (lifetime) and energetic (stability, endo-/exothermicity of reactions) information, and

---

<sup>1</sup> It is presumed that the reader is by and large familiar with spectroscopy and the underlying theoretical concepts, and perhaps even MI. (If this is not the case, exhaustive information can be found in the referred literature.) Thus, instead of discussing various circumstances such as physical/chemical properties of matrices, observable features and selection rules, or cryogenic vacuum technology, the elements of the employed setup are detailed in this chapter. Other relevant topics will be addressed at appropriate places in the text.

precursor specificity. Regardless (or exactly because of) how complete this range of tools may sound, it is not always unambiguous.

An alternative to these investigation methods is MI. Although this approach in its most restricted sense (that is, using noble gases as a ‘host’) originates some sixty years back, [2] it is not by any means outdated. In fact, (neon) matrix data over broad spectral ranges are still one of the best starting points for high-resolution, gas-phase surveys (Figure 2.1). With this method, species of interest can be embedded in low-temperature solid ‘crystals’ and the sample investigated conveniently. The low perturbation of the environment on the species of interest (‘guest’) and the modest concentration of the latter mimic the interaction-free conditions of gas-phase techniques. [2–11]

However, in order to provide reliable information on reactive species, first they have to be produced in these matrices, too. PR and LFP are again reliable ‘sources’ to do so, but the chemical reactivity and corresponding relaxation processes (diffusion and recombination reactions) remain an issue even in the case of an inert matrix. This results in a diversity of species and may hinder the assignment.

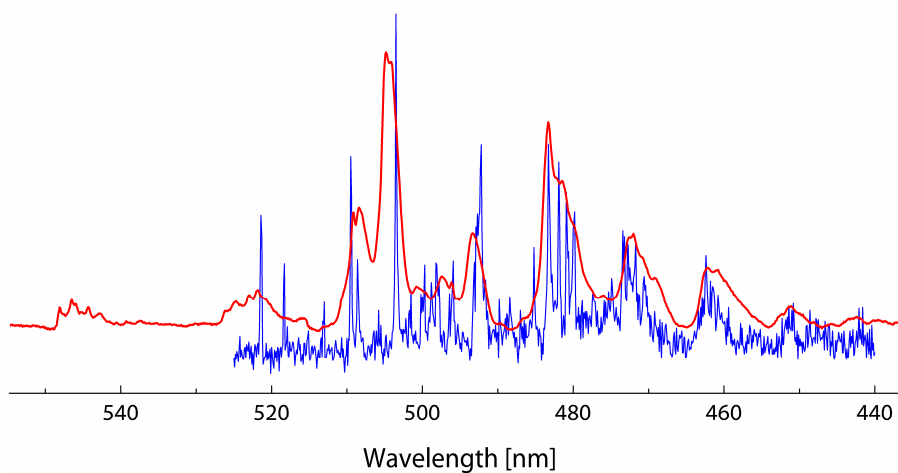


**Figure 2.1:** Low-resolution  $\tilde{A}^2A' \leftarrow \tilde{X}^2A''$  electronic spectrum of (multiple isomers of)  $C_4H_3Cl^+$  recorded in a 22-pole ion trap (blue trace; *courtesy*: Ion Trap Lab) and in a 6 K neon matrix (red; this work). The latter spectrum is shifted by  $\sim 2.4$  nm to shorter wavelengths to match the gas-phase vibrational band at 483.27 nm and indicates the similarity of the absorption patterns. [11]



Therefore, another important experimental advance shall be considered: *mass selection*. However, such an implementation of the technique has been realized successfully only in a limited number of cases. [12–21] Clearly, there are different technicalities to overcome—an appropriate ion source running for several hours to obtain reasonable amount of sample to investigate, taking care of space charge issues that is a result of compress charged species into a small volume, suppressing the fragmentation upon ions arriving at the matrix or the employ of a sensitive detection system are to name just a few. These are addressed below.

## 2.2 THE SPINE OF THE SETUP—AN OVERVIEW

The apparatus used in this work employs MI in combination with mass selection. Its continuous development has been described in detail; [22] it was used to study a wide variety of species (Table 2.1).

The setup consists of a high-vacuum (HV) chamber system (Figure 2.2). Ions are produced in appropriate sources (Section 2.5) and extracted from the formation zone with a set of electrostatic lenses. They are deflected by an electrostatic (opposite pole pairs) bender where the majority of neutrals such as the carrier gas are pumped off, then focused into a quadrupole mass filter (QMS; EXTREL) where ions of interest are selected at about unity  $m/z$  mass resolution.

The potential applied on the opposite filter electrodes ( $d = 19$  mm,  $l = 20$  cm) is

$$\Phi = B \pm \{U + V \cos(2\pi ft)\} \quad , \quad (2.1)$$

where  $B$  denotes a reference potential,  $U$  stands for a DC voltage (up to a few tens of volts) and  $V$  is the peak amplitude of a RF voltage (ca. 3–4 kV) at frequency  $f$  (1.2 or 1.7 MHz). Ions with an unstable trajectory exit the QMS at this stage and get pumped away. Calibration of the QMS is done on a regular basis with a Ne/Ar/Kr/Xe = 1:1:1:1 mixture.

The mass-selected beam is then co-deposited with high-purity (5.0) neon and, in most cases, an electron scavenger (Section 2.8) for 3–6 hours onto a rhodium-/chromium-coated sapphire substrate plate mounted on an oxygen-free, high thermal conductivity (‘OFHC’) copper plate to build a matrix sample  $\sim 150$   $\mu\text{m}$  in thickness (Figure 2.2).

**Table 2.1:** A selection of species for which electronic spectra were obtained in neon matrices in this laboratory<sup>[a]</sup>

Species <sup>Charge[b]</sup>	Reference
<b>Bare (hydro)carbon chains and rings</b>	
$C_n^+$ ( $n = 2,6-9$ ), $C_n$ ( $n = 6,8$ ), $c-C_n$ ( $n = 10,12$ )	<i>J. Chem. Phys.</i> <b>2005</b> , 123(4): 44305/1-6; <i>J. Chem. Phys.</i> <b>2004</b> , 120(16): 7520-7525; <i>J. Chem. Phys.</i> <b>1999</b> , 111(16): 7397-7401
$I-C_nH^+$ ( $n = 6,8$ )	<i>J. Phys. Chem. A</i> <b>2006</b> , 110(9): 2885-2889
$HC_nH^{0/+}$ ( $n = 4-15$ )	<i>J. Chem. Phys.</i> <b>2010</b> , 133(2): 024304/1-9; * <i>J. Phys. Chem. A</i> <b>2007</b> , 111(46): 11831-11836; <i>Chem. Phys.</i> <b>1994</b> , 189(2): 335-341
$H_2C_nH^+$ ( $n = 3,4,6,8$ ), $H_2C_8H$ , $c-C_3H_3^+$	<i>J. Phys. Chem. A</i> <b>2006</b> , 110(35): 10404-10408; <i>J. Chem. Phys.</i> <b>2001</b> , 114(23): 10355-10361
$C_{2n}^-$ ( $n = 4-7$ ); $C_{2n-1}H^-$ ( $n = 4-7$ ); $HC_{2n}H^{-/0}$ ( $n = 6-12$ )	<i>J. Chem. Phys.</i> <b>1999</b> , 110(3): 1492-1496; <i>J. Chem. Phys.</i> <b>1997</b> , 107(12): 4468-4472; <i>J. Chem. Phys.</i> <b>1997</b> , 107(1): 22-27; <i>J. Phys. Chem. A</i> <b>1997</b> , 101(29): 5292-5295 <i>J. Phys. Chem. A</i> <b>1998</b> , 102(48): 9785-9790; <i>Chem. Phys.</i> <b>1997</b> , 216(3): 401-406
<b>Substituted/terminated carbon species</b>	
$HC_6N$ , $DC_6N$	<i>J. Chem. Phys.</i> <b>2001</b> , 114(18): 7918-7922
$NC_2N^+$ , $HC_3N^+$ , $H_3C_4N^+$	<i>J. Phys. Chem.</i> <b>1985</b> , 89(15): 3190-3193
$C_{2n-1}N^{-/0}$ ( $n = 3-7$ ); $HC_{2n-1}N^-$ ( $n = 6-12$ )	<i>J. Chem. Phys.</i> <b>1999</b> , 110(3): 1492-1496
$C_2N_2^+$ , $C_2Cl_2^+$	<i>J. Chem. Phys.</i> <b>1989</b> , 90(1): 600-601
$XC_nN^+$ ( $X = Cl, Br, I$ ; $n = 1, 3$ )	<i>J. Chem. Phys.</i> <b>1989</b> , 83(2): 506-510; ○
$XC_2X^+$ ( $X = Cl, Br, I$ ); $ICl_4^+$	<i>J. Chem. Soc. Faraday Trans. 2</i> <b>1985</b> , 81(10): 1565-1586 ○ <i>Mol. Phys.</i> <b>1984</b> , 51(2): 437-444 ○ <i>Chem. Phys. Lett.</i> <b>1983</b> , 96(6): 645-648 ○
$C_nCl^{0/+}$ ( $n = 3-6$ ), $C_3Cl^-$	<i>J. Phys. Chem. A</i> <b>2005</b> , 109(25): 5553-5559; <i>J. Phys. Chem. A</i> <b>2004</b> , 108(19): 4219-4223
$C_4H_3Cl^+$	<i>Mol. Phys.</i> <b>2012</b> , 110(24): 3077-3084 *
$C_nS^{0/-}$ ( $n = 2,6$ ), $C_5S$	<i>J. Mol. Spectrosc.</i> <b>2003</b> , 222(1): 15-21; <i>J. Phys. Chem. A</i> <b>2003</b> , 107(42): 8856-8858
$C_2O^-$ , $C_4Y^-$ ( $Y = O, S$ )	<i>J. Phys. Chem. A</i> <b>1998</b> , 102(20): 3459-3461; <i>J. Phys. Chem. A</i> <b>2001</b> , 105(20): 4894-4897
$BC_n^{0/-}$ ( $n = 1,2$ ), $SiC^{0/-}$	<i>J. Phys. Chem. A</i> <b>1998</b> , 102(46): 9106-9108; <i>J. Phys. Chem. A</i> <b>1997</b> , 101(3): 275-277
$CsC_2^{0/-}$ , $C_5C_4$	<i>J. Phys. Chem. A</i> <b>2007</b> , 111(31): 7551-7554
<b>PAHs and related compounds</b>	
$C_6H_7^+$ : HBenzenes <sup>0/+</sup> /HFulvenes <sup>0/+</sup>	<i>J. Am. Chem. Soc.</i> <b>2010</b> , 132(42): 14979-14985 *
$C_7H_7^+$ : Benzylum/Tropylium	<i>Angew. Chem. Int. Ed.</i> <b>2011</b> , 50(13): 3022-3025 *
$C_{10}H_9^+$ : HNaphthalenes <sup>+</sup>	<i>J. Phys. Chem. A</i> <b>2012</b> , online; doi: 10.1021/jp310612j *
$C_{11}H_9^+$ : Benzotropylium and other isomers	<i>J. Am. Chem. Soc.</i> <b>2011</b> , 133(49): 19796-19806 *
$C_{14}H_{11}^+$ : Anthracenes <sup>+</sup> /HPhenantrenes <sup>+</sup>	<i>Astrophys. J.</i> <b>2011</b> , 728(2): 131/1-7 *
$C_{16}H_{11}^+$ , $C_{24}H_{13}^+$ : HPyrenes <sup>+</sup> , HCoronenes <sup>+</sup>	<i>J. Phys. Chem. A</i> <b>2011</b> , 115(40): 10972-10978; *
$C_{60}^{+/-}$	<i>J. Mol. Struct.</i> <b>2012</b> , 1025: 147-150 *
$C_{70}^{0/+/-}$	<i>Chem. Phys. Lett.</i> <b>1993</b> , 211(2-3): 227-234 <i>Chem. Phys. Lett.</i> <b>1993</b> , 206(1-4): 203-209
<b>Pure non-carbonaceous clusters</b>	
$S_n^{-/0}$ ( $n = 2,3$ )	<i>Chem. Phys.</i> <b>2008</b> , 346(1-3): 8-12
$B_3^{0/-}$	<i>Chem. Phys. Lett.</i> <b>2005</b> , 404(4-6): 315-317; <i>J. Chem. Phys.</i> <b>2003</b> , 119(18): 9703-9709
$Si_n^{0/-}$ ( $n = 2-4$ )	<i>J. Phys. Chem.</i> <b>1996</b> , 100(46): 18042-18047
$TiO_2$	<i>Chem. Phys.</i> <b>2008</b> , 353(1-3): 115-118

[a] Note that results obtained using the 'new' experimental apparatus (this work—see in particular Sections 2.4 and 2.6—and Ref. [22i]) are also included; they are marked by an asterisk. The studies without mass selection (circles) are shown for completeness. [b] In cases, multiple (e.g., linear and cyclic) isomers of a certain constitutional formula may be possible to detect; examples are provided throughout this work.

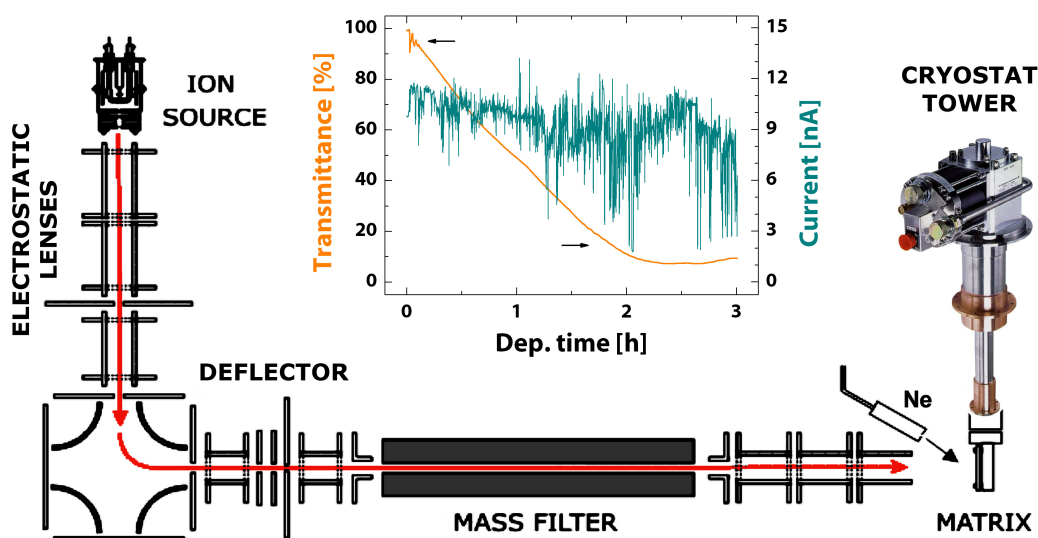


**Figure 2.2:** The mass-selective matrix isolation setup. Ions are produced in an appropriate source (Section 2.5), deflected by  $90^\circ$  and guided into a quadrupole mass filter. Charged species of a selected  $m/z$  are co-deposited with neon onto a cold substrate. In the inset are shown a current and a transmission curve.

The substrate is held at 6 K by a closed-cycle helium refrigerator. The base temperature of the cold finger is  $\sim 3$  K; a DC potential ( $\sim 8.5$  V @ 0.5 A) is applied on two resistive heater rods ( $R_{\text{tot}} = 25 \Omega$ ) to raise the temperature to the operating 6 K, a value secure from matrix cracking due to instrumental (pump and cryostat) vibrations. Polished aluminum shielding is used around the second stage of the cold head to protect the sample from black-body (IR) radiation.

The advance of the deposition is finely regulated by the neon inflow and monitored by the decay of the light intensity from a (green) light emitting diode passing through the matrix to a photomultiplier (PMT; HAMAMATSU) tube. 5–15 % clear samples are grown (Figure 2.2, inset).

The matrix is not grounded; the incoming (ion) current  $I_{\text{mtx}}$  is measured by a picoammeter. The deposited charge can be calculated from  $Q_{\text{dep}} = I_{\text{mtx}} \times t$ . A typical deposition accumulates 1–100  $\mu\text{C}$  of ions, which corresponds to  $\sim 6 \times 10^{12}$ – $6 \times 10^{14}$  of charged species. The matrix volume of  $V_{\text{mtx}} \approx 2 \times 2 \times 0.015 \text{ cm}^3$  means in the frame of the cubic closely-packed approximation (one neon atom occupying  $8 \times 10^{-23} \text{ cm}^3$ ) that  $\sim 10^{21}$  Ne builds up a matrix. The host/guest ratio is then inferred to be on the order of  $10^6$ – $10^8$ ; it is probably an overestimate by a factor of

about two because of the partial charge neutralization upon ions arriving at the matrix surface. Nevertheless, it is significantly higher than 100–10 000, usual transmission-type experiments, [3] which underlines the sensitivity of the optical detection scheme (Section 2.3).

The system is separated into four differential chambers, separate rotary-backed HV pumps being attached to each stage, which enables a drop of pressure ca. two orders of magnitude from the source ( $\sim 10^5$ – $10^6$  mbar) to the deposition chamber.

### 2.3 OPTICAL SCHEME WITH A MONOCHROMATOR

Earlier, the matrix chamber was coupled with a  $f = 0.5$  m Czerny–Turner monochromator (SPEX 1870) with a  $(64 \text{ mm})^2$ , 1200 grooves/mm dispersion grating of accuracy  $\pm 0.2$  nm. Light from a 75 W Xe or a 100 W Hlg lamp was passed through the  $\sim 200 \mu\text{m}$  entry slit of the monochromator and chopped by a light chopper, which was connected through a lock-in amplifier to an oscilloscope and a PC. Monochromatic light was then compressed in a narrow rectangular form on two quartz lenses, entered the deposition chamber on a viewport and passed through the matrix in the so-called ‘wave guide’ mode (Figure 2.3). In such a fashion, it gets internally reflected in the sample—on the coating mirror of the substrate and, due to the vacuum/neon refractive index  $n \approx 1.3$  (critical angle  $\sim 80^\circ$ , no. of reflections  $< 10$ ), on the outer surface of the neon mass. Range-specific (PMT or Si diode) signal detectors and a LABVIEW program were utilized for the recordings. [22g,22h]

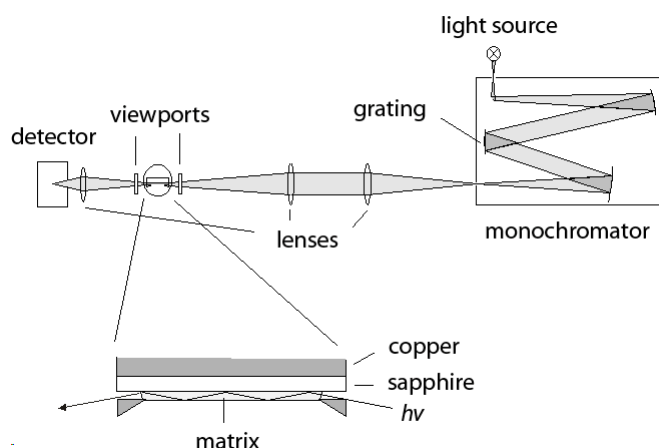


**Figure 2.3:** Optical detection system with a monochromator. Blown up is the wave guide arrangement.

## 2.4 SPECTROGRAPH LAYOUT & OTHER IMPROVEMENTS

The setup outlined above has been employed successfully for two or so decades for the characterization of radicals and ions of astrophysical interest ([Table 2.1](#)). However, because of both logistical and technical reasons, the laboratory has been moved, and the apparatus re-built and improved in several aspects in the course of this work ([Figure 2.4](#)).

First, all rubber seals in the matrix chamber were replaced with copper gaskets (ISO-K *vs.* CF flange connections) and diffusion pumps by turbomolecular ones. The gaskets do not, in contrast to the O-rings, evaporate their material into a higher vacuum, whereas the turbos are advantageous over the oil pumps—with the latter an electrical fallout could (and did) cause serious contamination to the system. These reforms secured a vacuum in the matrix chamber by more than one order of magnitude higher than before; the pressure is now below  $10^{-8}$  mbar at room temperature. A gate valve has been also inserted to ensure the smoothness of the daily source maintenance operations ([Section 2.5](#)).

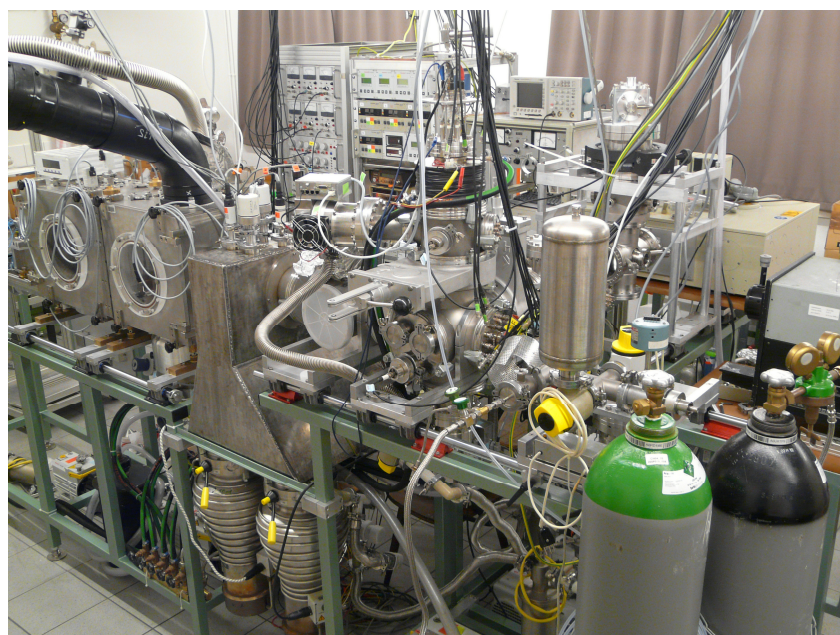


**Figure 2.4:** A photograph of the ‘new’ experimental apparatus. Note that the layout contains considerations for the implementation of a magnetron sputtering ion source ([Chapter 7](#)).

Secondly, the three-stage, closed-cycle helium cryostat has been replaced by a two-stage, Gifford–McMahon-type one (SUMITOMO RDK-408D2). This brought with the re-design of the matrix chamber, the insertion of a new temperature detector and heater rods/plates, and other upgrades. An additional chamber extension with two new ion lenses and differential pumping walls were also introduced between the deflector and QMS regions, as well as additional Pirani and Penning gauges.

However, the main improvement concerns the optical detection system. The monochromator and the PMT/Si diode detectors have been replaced by a spectrograph with a focal length of 0.3 m, a resolution  $\sim 0.1$  nm and an effective aperture  $f/4$  (ANDOR Shamrock 303). It is equipped with three gratings on a rotatable turret and two thermoelectrically cooled, range-specific (open electrode, OE, or back illuminated, BU) CCD cameras (Figure 2.5).

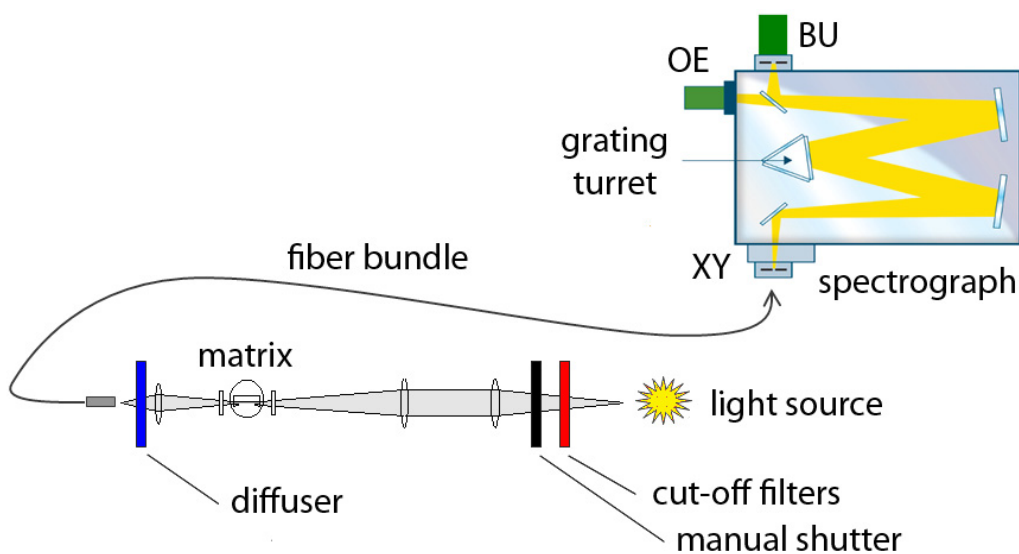


**Figure 2.5:** Optical detection system with a spectrograph.

In the present arrangement the light that probes the matrix during the recording of spectra has an intensity several orders of magnitude higher than previously, where instead of broadband radiation, monochromatic light was used. Therefore, care has to be taken to minimize photoconversion of the species during the measurement. This is achieved by means of appropriate short-wavelength cut-off filters and by minimizing the exposure time of the matrix.

Electronic absorption spectra of the species are collected in several overlapping sections covering 220–1100 nm. (The spectral width of a single section depends on the dimension of the active area of the CCD and the resolution of the 600 or 1200 gr./mm grating used.) The scans are always started from the longest wavelength and continued into the UV. The spectrum is then recorded again to test whether photoconversion of the species had taken place. The recorded spectra are calibrated using pen-ray (Ne/Ar/Kr/Xe/Hg atomic line) lamps.

With these and several other, minor improvements, numerous hydrocarbon cations were investigated (Figure 2.6) and are discussed in this dissertation.

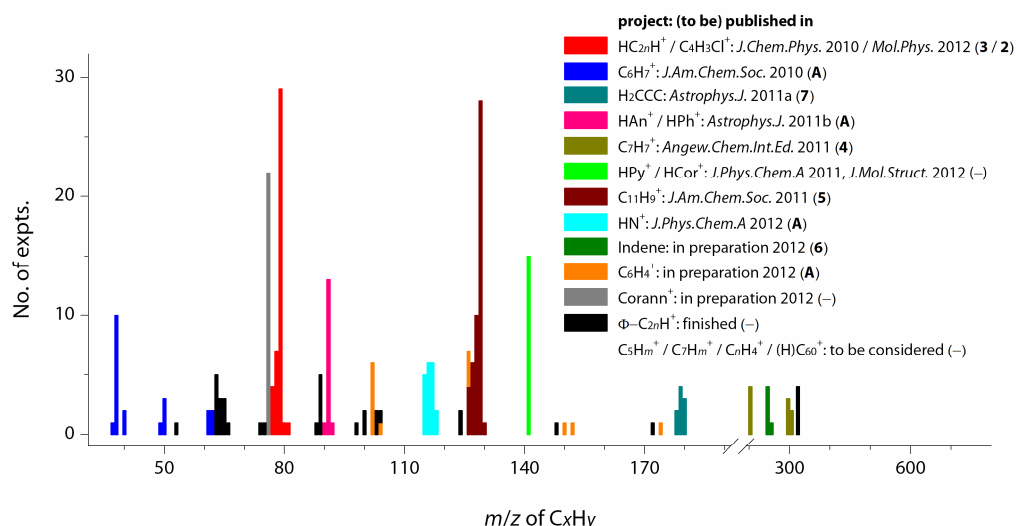


**Figure 2.6:** Number of deposition experiments carried out vs. mass/charge ratio of the hydrocarbons investigated. Chapter labels of this work in which the belonging projects are detailed are indicated in **bold**.

## 2.5 ION SOURCES

The species it is concerned with are not commercially available compounds but rather exotic ions. Different methods can be used for the ‘synthesis’ of these. There are two types of (home-built) source designs: hot-cathode discharge and cesium sputtering (Figure 2.7). The first is similar to conventional electron impact except that the electrons emitted from a hot (~2000 °C) tungsten filament are confined to a central region by a voltage of ~50 V applied on a cylindrical anode, and an electromagnetic coil. The latter causes the electrons to move spirally within the source, and the chemistry occurs in the resulting plasma in the form of ionization, fragmentation and ion–molecule reactions. The anode voltage, along with the potentials on the extractors, largely determines the (thermal and kinetic) energy the ions have access to during their formation and flight.

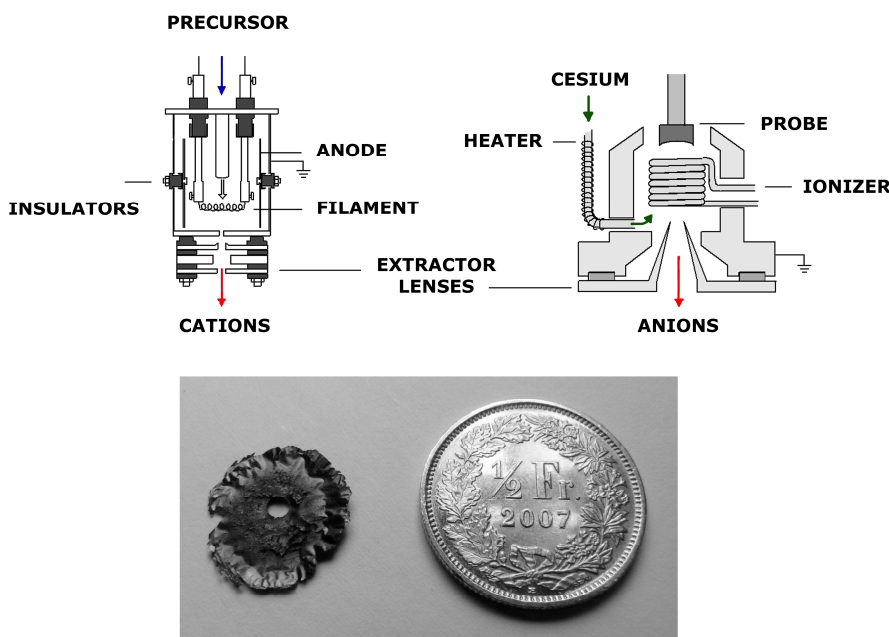


**Figure 2.7:** Schematic drawing of two ion sources—*left*: a hot-cathode discharge source; *right*: the cesium sputtering source. A carbon soot layer as accumulated on the housing of the cation source after a few hours in use is shown at the bottom.

As for the precursor selection and inlet: Gases and liquids with reasonably high vapor pressure, outgassed by freeze–pump–thaw cycles, are introduced as a 15–30 % mixture with a carrier gas (helium or argon) through a thin metal tubing. Liquids with low equilibrium pressure are inserted by flowing gas over it in a



bubbler, whereas solids are put directly in the throat of the source or into a resistively heated oven. Commercially available organics as well as in-house synthesized, highly reactive starting materials such as diacetylene are drawn on.

In the second type, cesium sputtering is utilized (Figure 2.7, right). Liquid cesium from a container is evaporated onto a coaxial tantalum wire (~1000 °C) by heating the side tube to ca. 300 °C. It gets ionized there and the heavy Cs<sup>+</sup> bombard ('sputter') the metallic/composite rod to release different, mainly negatively charged species. The limitation of this source is that the current version does not support the insertion of gaseous/liquid mixtures; furthermore, the sample must be conductive. In this work the cation source was mostly used; some examples for anions are given in Appendix A.

## 2.6 FLUORESCENCE AMENDMENT

Electronic absorption spectra of highly unsaturated hydrocarbons are relatively straightforward to assign given that these species have few constitutional isomers and the spectra may follow trends. Such an example will be shown in Chapter 3. However, if the number of atoms in the species under investigation is large enough, the assignment becomes increasingly complex. For the results presented in Chapter 5, a new experimental configuration has been established.

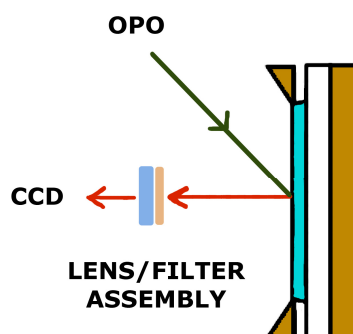


**Figure 2.8:** Fluorescence detection scheme.

Wavelength-dispersed fluorescence spectra can now be obtained by exciting the species embedded in neon at an angle of incidence  $\sim 45^\circ$  with a pulsed (20 Hz), Nd:YAG-pumped, tunable optical parametric oscillator laser (OPO; EKSPLA

NT 342/3/UVE), having a bandwidth  $\sim 3\text{--}8\text{ cm}^{-1}$  and energies  $\sim 2\text{--}30\text{ mJ}$  depending on the spectral region, which are associated with the degree of harmonic of the 1064 nm emission. The coherent beam from the laser is guided with the help of two mirrors and some irises onto the matrix. The emission data is collected perpendicular to the substrate surface (Figure 2.8)—the light is focused with a short-focus lens into the optical fiber bundle and transmitted to the same spectrograph and cameras as used for the absorption measurements.

Fluorescence spectra are recorded in 50–60 nm overlapping sections by exciting distinct absorption bands seen in the spectra obtained after depositing a given species. The signal is usually accumulated over  $\sim 1000$  laser shots per section. The fluorescence is measured starting  $\sim 2\text{ nm}$  from the excitation wavelength upward to avoid saturation of the CCDs with scattered laser light. The method can be used routinely in the UV/Vis regions; its application in the IR might provide information, too (Section A.1, Appendix A). An upgrade to this technique is suggested in Chapter 7.

## 2.7 INFRARED MEASUREMENTS

A custom-modified Fourier transform IR (FTIR) spectrometer (BRUKER IFS 66v/S) can be used to study the trapped species in the infrared region of the electromagnetic spectrum. It is based on a classical Michelson interferometer, and is equipped with appropriate sources (globar, tungsten), exchangeable beam splitters (KBr, quartz) and liquid N<sub>2</sub>-cooled detectors (MCT, InSb) for the measurement of the 600 to 12 000  $\text{cm}^{-1}$  domain with an accuracy  $\pm 0.2\text{ cm}^{-1}$ . It is internally calibrated by the 633 nm line of a HeNe laser, and evacuated by a rotary vane pump to a few mbar to suppress the H<sub>2</sub>O/CO<sub>2</sub> content of the spectra.

The matrix sample is positioned so that the signal becomes optimal on the detector by rotating the cryostat tower by an angle  $\sim 110^\circ$  to that for the UV/Vis scans. 'Light' then enters through a window into the deposition chamber where it is doubly reflected from the substrate with the help of a concave mirror located in a side arm, and exits toward the detector (Figure 2.9). The signal is optimized by fine aligning screws of mirror mounts in the spectrometer.

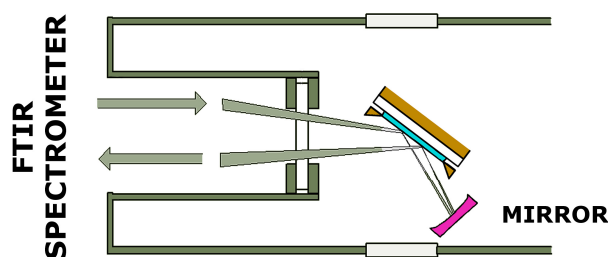


**Figure 2.9:** Scheme of the infrared experiment.

It is a complementary/confirmatory method to the optical measurements—Taken an approximate incidental and reflection angle of  $45^\circ$ , the (IR) path length can be estimated as  $4 \times \sqrt{2}$ , that is, smaller than 1 mm, which is minor to the wave guide configuration (Section 2.4). Furthermore, the electron scavenger commonly applied for the trapping of cations,  $\text{CH}_3\text{Cl}$  (Section 2.8), is a strong IR absorber; because it is inserted in several orders of magnitude higher concentration than the guest species, it prohibits concluding measurements. Nevertheless, in some cases such an approach can be useful and an example is given below.

Diacetylene is a commonly used precursor for the production of unsaturated hydrocarbons and its synthesis route [23] has been slightly modified. The initial material, 1,4-dichloro-2-butyne (DCIB), loses two HCl in a (stepwise) reduction reaction with KOH; thus, to obtain the highest  $\text{HC}_4\text{H}$  purity, fractions of the product are repeatedly taken during the low-temperature ( $[-50, -10]^\circ\text{C}$ ) vacuum distillation. It was found that  $\text{C}_4\text{H}_3\text{Cl}$  forms as a minor intermediate in this process as a result of ( $\alpha$  or  $\delta$ ) elimination of a single HCl from DCIB. A distillation fraction highly contaminated with  $\text{C}_4\text{H}_3\text{Cl}$  was used as the precursor for  $\text{C}_4\text{H}_3\text{Cl}^+$  to obtain the spectra shown in Figure 2.1. [11] It was desirable to determine the structure of the initial material in the first place. A combination of FTIR scans and quantum chemical calculations allowed for this (Figure 2.10).

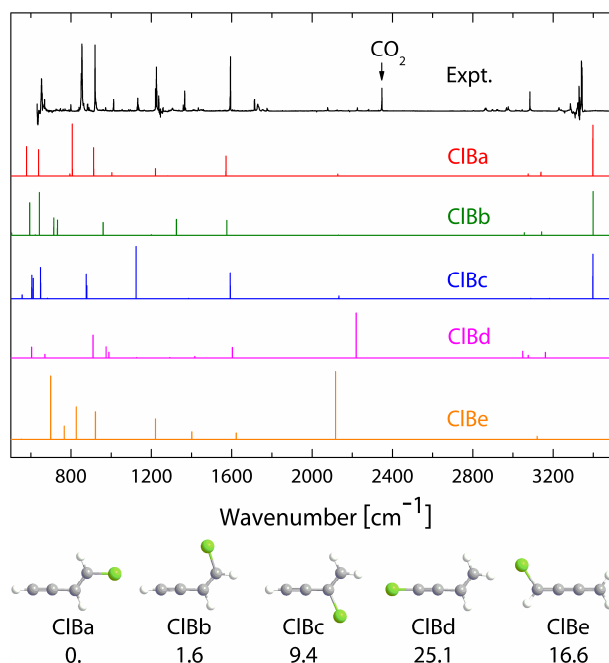


**Figure 2.10:** IR spectrum of a directly deposited diacetylene sample contaminated with  $C_4H_3Cl$  (black) and theoretical vibrational spectra obtained with DFT at the B3LYP/cc-pVTZ level of theory (colored). Bands of  $HC_4H$  were removed from the experimental trace. Beneath are depicted the  $C_4H_3Cl$  isomers considered, along with their relative energy ( $\text{kJ mol}^{-1}$ , zero-point correction included). All structures are of  $C_s$  symmetry. Two other possibilities,  $H_3CCCCl$  and  $ClH_2CCCCH$ , are not shown; they both lie  $\sim 200 \text{ kJ mol}^{-1}$  to higher energy. It can be concluded that the sample likely contains ClBa, while ClBb and/or ClBc may comprise a smaller fraction. [11]

## 2.8 EXPERIMENTAL TRICKS & TREATS

When ions are deposited for a longer period of time, a space charge builds, which deflects the ions subsequently arriving at the substrate. This is especially the case having a ‘cleaner’ vacuum—there are no residual impurities which would counteract the accumulating charge in the form of species such as  $N_2^+$ ,  $C_2^{+/-}$  or  $OH^-$ . Thus, an *electron scavenger* needs to be introduced.

In order to suppress the neutralization of *cations* during deposition, a mixture of chloromethane with neon in a ratio of 1:20 000 was used to produce the host matrix.  $CH_3Cl$  has a high electron affinity ( $\sim 3 \text{ eV}$ ) and captures electrons efficiently, dissociating thereby to  $Cl^-$  ions and  $CH_3^\bullet$  radicals. [24] The latter remain

in matrix cages and, because of the low concentration, do not interfere with the trapped cations, while the  $\text{Cl}^-$  anions reduce the space charge. Moreover, neither of these species ( $\text{CH}_3\text{Cl}$ ,  $\text{CH}_3^\bullet$ ,  $\text{Cl}^-$ ) has an absorption in the 200–1100 nm spectral range that would hinder measurements there. It was found that mixing additionally a small amount (~1:400) of argon into the neon results in matrices of better optical quality, probably allowing the deposited ions to occupy different sites in the crystal lattice by introducing defects. In the case of *anions*, another method should be considered ([Chapter 7](#)).

After the investigation of cations finish, one would want to have information on the corresponding neutrals, too; the appropriate technique for that is called *photo-bleaching*. Using a medium-pressure mercury (mpHg), halogen or xenon lamp, UV irradiation of the sample causes neutralization of the trapped charged species by electrons released from the  $\text{Cl}^-$  counterions from the scavenger. This process is operative only if the photon energy exceeds the detachment threshold of  $\text{Cl}^-$ . The electron affinity of chlorine is 3.61 eV in the gas phase, [25] which corresponds to photon wavelengths  $\lambda < 343$  nm. However, the threshold is expected to be ~0.5 eV higher in solid neon due to an interaction with the environment, that is, around 300 nm. Cut-off or band-pass filters for the bleaching are often chosen in consideration of this. Of course, such a radical treatment of some sensitive ion or species may result in different ‘light-induced’ chemical processes, *e.g.*, isomerization ([Appendix A](#)) or fragmentation. For anions, the same method can be used; they simply lose their extra electron upon irradiation. As a rough generalization it can be said that ionic features drop and (corresponding) neutrals gain intensity upon bleaching.

Lastly, by providing a modest amount of thermal energy to the matrix sample, diffusion starts to play a role and the embedded species, drawing on their increased mobility, can reorganize and take the most stable site(s). The procedure is called *annealing*; it is done by slowly (~0.2–0.5 K min<sup>-1</sup>) heating the sample to a temperature around 0.3  $T_m$  of neon, 7.3 K, for ca. 10–30 minutes. However, this method had to be dropped from the routine work steps because of the temperature oscillations caused by the two-stage helium cryostat ([Chapter 7](#)). It might be substituted by a ‘hole-burning’ implementation of a laser, *e.g.*, on the example of the highly structured origin bands of  $\text{C}_6\text{H}_4^+$  isomers ([Section A.3](#), [Appendix A](#)).

## 2.9 THEORETICAL SUPPORT

A clever combination of the methods and techniques described in this chapter are the basis for the characterization of a chosen species. The interpretation of spectra, however, much relied on—most commonly—(TD) DFT calculations, [26,27] which were carried out with the GAUSSIAN 03 software suite. [28] Hückel matrix diagonalizations [29] were absolved with the MATHEMATICA symbolic algebra package. [30] Higher-level computations were done in collaborations.

## Bibliography

- [1] See, *e.g.*, R. Nagarajan, J.P. Maier. *Electronic spectra of carbon chains and derivatives*. *Int. Rev. Phys. Chem.* **2010**, 29(3): 521–554.
- [2] S. Cradock, A.J. Hinchcliffe. *Matrix isolation: A technique for the study of reactive inorganic species*. New York: Cambridge University Press, **1975**.
- [3] I.R. Dunkin. *Matrix-isolation techniques: A practical approach*. Eds.: L.M. Harwood, C.J. Moody. New York: Oxford University Press, **1998**.
- [4] B. Meyer. *Low temperature spectroscopy*. New York: Elsevier, **1971**.
- [5] M.E. Jacox. *The spectroscopy of molecular reaction intermediates trapped in the solid rare gases*. *Chem. Soc. Rev.* **2002**, 31(2): 108–115.
- [6] (a) *A Bibliography of matrix isolation spectroscopy: 1954–1985*. Eds.: D.W. Ball, Z.H. Kafafi, L. Fredin, R.H. Hauge, J.L. Margrave. Houston: Rice University Press, **1988**; (b) *A bibliography of matrix isolation spectroscopy: 1985–1997*. Eds.: D.W. Ochsner, D.W. Ball, Z.H. Kafafi. Washington: Naval Research Laboratory, **1998**.
- [7] *Matrix Isolation Digest by Electronic mail (MIDE)*. A free electronic publication sent out on behalf of the international matrix isolation community;  
<http://www.chem.mun.ca/mi/>.
- [8] *Physics and chemistry at low temperatures*. Ed.: L. Khriachtchev. Singapore: Pan Stanford Publishing, **2011**.
- [9] *Chemistry and Physics of matrix-isolated species*. Eds.: L. Andrews, M. Moskovits. Amsterdam: Elsevier Science Publishers, **1989**.
- [10] M.E. Jacox. *The infrared spectroscopy of the products of ion–molecule reactions trapped in the solid rare gases*. *Int. J. Mass Spectrom.* **2007**, 267(1–3): 268–276.
- [11] S. Chakrabarty, V. Rudnev, J. Fulara, R. Dietsche, A. Nagy, I. Garkusha, F.J. Mazzotti, C.A. Rice, J.P. Maier. *Electronic spectra of C<sub>4</sub>H<sub>3</sub>Cl<sup>+</sup> isomers*. *Mol. Phys.* **2012**, 110(24): 3077–3084.
- [12] D.M. Lindsay, F. Meyer, W. Harbich. *Neutralization and matrix deposition experiments on mass-selected silver atoms and clusters*. *Z. Phys. D* **1989**, 12(1–4): 15–18.
- [13] W. Harbich, S. Fedrigo, F. Meyer, D.M. Lindsay, J. Lignieres, J.C. Rivoal, D. Kreisle. *Deposition of mass selected silver clusters in rare gas matrices*. *J. Chem. Phys.* **1990**, 93(12): 8535–8543.
- [14] M.S. Sabo, J. Allison, J.R. Gilbert, G.E. Leroi. *Bridging the gap between what mass spectrometrists want and what spectroscopists can do: An instrument for spectroscopic investigation of matrix-isolated, mass-selected ions*. *Appl. Spectrosc.* **1991**, 45(4): 535–542.
- [15] T.M., Halasinski, J.T. Godbout, J. Allison, G.E. Leroi. *Infrared detection of matrix-isolated, mass-selected ions*. *J. Phys. Chem.* **1994**, 98(15): 3930–3932.

- [16] J.T. Godbout, T.M. Halasinski, G.E. Leroi, J. Allison. *Matrix isolation of mass-selected cations: Are counterions present and how are they formed?* **J. Phys. Chem.** **1996**, 100(8): 2892–2899.
- [17] See Ph.D. theses from the V.E. Bondybey group at the Technical University of Munich, Faculty of Chemistry, e.g.: (a) M. Lorenz. *Matrix-isolation spectroscopy of mass-selected ions*, **2000**; (b) M. Frankowski. *Spectroscopy of unstable and charged species in cryogenic solids*, **2004**.
- [18] A.M. Smith-Gicklhorn, M. Lorenz, M. Frankowski, R. Kołos, V.E. Bondybey. *C<sub>5</sub>N<sub>2</sub> revisited: Mass-selective matrix isolation and DFT studies*. **Chem. Phys. Lett.** **2002**, 351(1–2): 85–91.
- [19] M. Frankowski, Z. Sun, A.M. Smith-Gicklhorn. *Unraveling the possible isomers of CH<sub>4</sub>CN<sup>+</sup> and CH<sub>2</sub>CN<sup>+</sup> through FT-IR matrix-isolation spectroscopy of mass-selected ions and DFT theory*. **Phys. Chem. Chem. Phys.** **2005**, 7(5): 797–805.
- [20] T.L. Haslett, K.A. Bosnick, S. Fedrigo, M. Moskovits. *Resonance Raman spectroscopy of matrix-isolated mass-selected Fe<sub>3</sub> and Ag<sub>3</sub>*. **J. Chem. Phys.** **1999**, 111(14): 6456–6461.
- [21] P. Ayotte, G.H. Weddle, J. Kim, M.A. Johnson. *Mass-selected “matrix isolation” infrared spectroscopy of the I-(H<sub>2</sub>O)<sub>2</sub> complex: Making and breaking the inter-water hydrogen-bond*. **Chem. Phys.** **1998**, 239(1–3): 485–491.
- [22] See Ph.D. theses from this laboratory at the University of Basel, Faculty of Science: (a) D. Forney. *Optische Spektroskopie von Kationen in Neonmatrizen*, **1990**; (b) M. Jakobi. *Elektronische und vibratorische Spektroskopie an den Fullerenen C<sub>60</sub>, C<sub>70</sub> und deren Ionen in Edelgasmatrizen*, **1994**; (c) P. Freivogel. *Spektroskopie an massenselektierten Kohlenstoffketten in Neonmatrizen*, **1997**; (d) M. Grutter de la Mora. *Spectroscopy of mass selected carbon chains in neon matrices*, **1999**; (e) M. Wyss. *Matrixspektroskopie und ab initio Kohlenstoffverbindungen von astrophysikalischem Interesse*, **2001**; (f) E. Riaplov. *Spectroscopy of mass selected carbon and boron species in solid neon*, **2002**; (g) A. Batalov. *Absorption spectroscopy of mass-selected hydrocarbon and boron species in 6 K neon matrices*, **2006**; (h) I.G. Shnitko. *Absorption spectroscopy of carbon and sulfur chains in 6 K neon matrices*, **2008**; (i) I. Garkusha. *Electronic spectroscopy of mass-selected protonated polycyclic aromatic hydrocarbons in neon matrices*, **2012**; as well as publications from [Table 2.1](#).
- [23] L. Brandsma, H.D. Verkruijsse. *Synthesis of acetylenes, allenes and cumulenes: a laboratory manual*. Amsterdam–Oxford–New York: Elsevier, **1981**.
- [24] J.D.D. Martin, J.W.J. Hepburn. *Determination of bond dissociation energies by threshold ion-pair production spectroscopy: An improved D<sub>0</sub>(HCl)*. **J. Chem. Phys.** **1998**, 109(19): 8139–8142.
- [25] Z.Y. Zhou, Y.M. Xing, H. Gao. *Studies on the bond-breaking reaction of the CH<sub>3</sub>–X bond for DFT calculations in electron transfer*. **J. Mol. Struct.: THEOCHEM** **2001**, 542(1–3): 79–87.



- [26] F. Jensen. *Introduction to Computational Chemistry*. 2<sup>nd</sup> Edition; Chichester: John Wiley & Sons Ltd, 2007.
- [27] C.J. Cramer. *Essentials of Computational Chemistry: Theories and Models*. 2<sup>nd</sup> Edition; Chichester: John Wiley & Sons Ltd, 2004.
- [28] M.J. Frisch, G.W. Trucks, H.B. Schlegel, G.E. Scuseria, M.A. Robb, J.R. Cheeseman, J.A. Montgomery Jr., T. Vreven, K.N. Kudin, J.C. Burant, J.M. Millam, S.S. Iyengar, J. Tomasi, V. Barone, B. Mennucci, M. Cossi, G. Scalmani, N. Rega, G.A. Petersson, H. Nakatsuji, M. Hada, M. Ehara, K. Toyota, R. Fukuda, J. Hasegawa, M. Ishida, T. Nakajima, Y. Honda, O. Kitao, H. Nakai, M. Klene, X. Li, J.E. Knox, H.P. Hratchian, J.B. Cross, V. Bakken, C. Adamo, J. Jaramillo, R. Gomperts, R.E. Stratmann, O. Yazyev, A.J. Austin, R. Cammi, C. Pomelli, J.W. Ochterski, P.Y. Ayala, K. Morokuma, G.A. Voth, P. Salvador, J.J. Dannenberg, V.G. Zakrzewski, S. Dapprich, A.D. Daniels, M.C. Strain, O. Farkas, D.K. Malick, A.D. Rabuck, K. Raghavachari, J.B. Foresman, J.V. Ortiz, Q. Cui, A.G. Baboul, S. Clifford, J. Cioslowski, B.B. Stefanov, G. Liu, A. Liashenko, P. Piskorz, I. Komaromi, R.L. Martin, D.J. Fox, T. Keith, M.A. Al-Laham, C.Y. Peng, A. Nanayakkara, M. Challacombe, P.M.W. Gill, B. Johnson, W. Chen, M.W. Wong, C. Gonzalez, J.A. Pople, GAUSSIAN 03 (Revision C.01). Gaussian Inc., Wallingford CT, 2004; <http://www.gaussian.com>.
- [29] E. Heilbronner, H. Bock. *The HMO Model and its Application: 1) Basis and Manipulation*. London–New York–Sydney–Toronto: John Wiley & Sons Ltd, 1968.
- [30] MATHEMATICA 5.0 (Build: 5.0.1.0). Wolfram Research Inc., Oxfordshire UK, 2003; <http://www.wolfram.com>



Part II  
RESULTS



*“But if they don’t exist, how can a man see them?”*

Ken Kesey (1935–2001), *One Flew Over the Cuckoo’s Nest*

# 3

## HIGHER-ENERGY ELECTRONIC TRANSITIONS OF $\text{HC}_{2n+1}\text{H}^+$ ( $n = 2\text{--}7$ ) AND $\text{HC}_{2n+1}\text{H}$ ( $n = 4\text{--}7$ )

---

To demonstrate the capabilities of the fundamentally upgraded experimental apparatus described in [Chapter 2](#), first the electronic absorption spectra of linear  $\text{HC}_{2n+1}\text{H}^+$  ( $n = 2\text{--}7$ ) were re-recorded in 6 K neon matrices following their mass-selective deposition. The species have been studied earlier in these laboratories; however, four *new* band systems could be identified this time: The strongest,  $E\ ^2\Pi_{g/u} \leftarrow X\ ^2\Pi_{u/g}$ , lies in the UV and the second most intense,  $C\ ^2\Pi_{g/u} \leftarrow X\ ^2\Pi_{u/g}$ , is located in the visible range. The known  $A\ ^2\Pi_{g/u} \leftarrow X\ ^2\Pi_{u/g}$  absorption is an order of magnitude weaker than  $C\ ^2\Pi_{g/u} \leftarrow X\ ^2\Pi_{u/g}$ ; hence, the latter may be of more relevance for DIB research. Transitions to the *B* and *D* states are also discussed. The onset wavelengths of the  $\text{HC}_{2n+1}\text{H}^+$  ( $n = 2\text{--}7$ ) electronic systems obey a *linear relation* as a function of the size of the cations, similar to other carbon chains. The  $B\ ^3\Sigma_u^- \leftarrow X\ ^3\Sigma_g^-$  transition of neutral  $\text{HC}_{2n+1}\text{H}$  ( $n = 4\text{--}7$ ) was identified too, in the UV upon photobleaching the cations trapped in the matrices.

### 3.1 INTRODUCTION

Highly unsaturated hydrocarbon molecules,  $\text{C}_x\text{H}_y$  ( $y = 1,2$ ), are important intermediates in terrestrial environments, *e.g.*, in combustion under oxygen-deficient condition and discharges. [1] They are of astrophysical interest too as it is well-established that  $\text{C}_x\text{H}_y$  ( $y = 1,2$ ) chains are constituents of the ISM. [2,3] Furthermore, they are perhaps building blocks of larger organic systems such as PAHs.  $\text{C}_x\text{H}$  [4–7] and  $\text{C}_x\text{H}^-$  ( $x \leq 8$ ), [8–10] and  $\text{H}_2\text{C}_x$  ( $x \leq 6$ ) [11–13] have been detected by their pure rotational transitions in many astronomical objects.  $\text{HC}_{2n}\text{H}$  ( $n = 2,3$ ) polyacetylenes are also present in the ISM as their IR bands were detected in carbon-rich proto-planetary nebulae. [14]

Particularly interesting are members of the  $\text{HC}_x\text{H}$  series with  $x = \text{odd}$  number of carbons, because they are open-shell and their lowest-energy electronic transition falls in the visible and NIR—regions associated with the DIB forest.  $\text{HC}_{2n+1}\text{H}$  have been studied in the optical by direct absorption in neon [15] and nitrogen matrices, [16] and in the gas phase by CRDS [17,18] and REMPI. [19] They also have been investigated by *ab initio* methods. [20–24]

Much less is known about the even-long,  $\text{HC}_{2n+1}\text{H}^+$  ions. Apart from a few theoretical papers on the smaller representatives ( $n = 2\text{--}4$ ) of the homologous series, [25,26] there are only two spectroscopic reports on the lowest-energy electronic transition of  $\text{HC}_{2n+1}\text{H}^+$  ( $n = 2\text{--}7$ ). [15,27] Higher-energy absorptions of  $\text{HC}_{2n}\text{H}^+$  ( $n = 2\text{--}7$ ) have been obtained already in neon matrices. [28] The results presented here complement these information by four new absorption systems of  $\text{HC}_{2n+1}\text{H}^+$  ( $n = 2\text{--}7$ ) and a yet unknown UV transition of neutral  $\text{HC}_{2n+1}\text{H}$  ( $n = 4\text{--}7$ ).

### 3.2 $A\ ^2\Pi_{g/u} \leftarrow X\ ^2\Pi_{u/g}$ TRANSITION OF $\text{HC}_{2n+1}\text{H}^+$ ( $n = 2\text{--}7$ )

Co-deposition of the  $\text{HC}_{2n+1}\text{H}^+$  ( $n = 2\text{--}7$ ) cations with neon led to the detection of several electronic band systems that extend from the NIR to the UV. Figure 3.1 shows the lowest-energy,  $A\ ^2\Pi_b \leftarrow X\ ^2\Pi_a$  transition of  $\text{HC}_{2n+1}\text{H}^+$ , where  $a \equiv u$  and  $b \equiv g$  ('ungerade/gerade') for  $n = \text{even}$ , and *vice versa* for  $n = \text{odd}$ . This system has already been reported [15,27] but is included here for two reasons. Firstly, a higher S/N ratio was achieved and, consequently, more detail is seen in the spectra, *e.g.*, vibrationally excited levels of  $\text{HC}_3\text{H}^+$  and  $\text{HC}_7\text{H}^+$ . The second is to compare its relative intensity with those of the newly observed transitions.

The  $A\ ^2\Pi_b \leftarrow X\ ^2\Pi_a$  system is similar in appearance for all the  $\text{HC}_{2n+1}\text{H}^+$  ( $n = 2\text{--}7$ ) species (Figure 3.1). The origin band and a progression in  $\sim 2000\text{ cm}^{-1}$  that corresponds to the excitation of a  $\text{C}\equiv\text{C}$  stretching mode in the  $A$  state are characteristic. Wavelengths of the bands of the  $A\ ^2\Pi_b \leftarrow X\ ^2\Pi_a$  transition are given in Table 3.1. The onset shifts monotonically by  $\sim 90\text{ nm}$  towards longer wavelengths as the size of  $\text{HC}_{2n+1}\text{H}^+$  increases, in accordance with that reported earlier. [27] Another pattern is that the integrated intensity of the electronic system normalized to the same amount of deposited ion charge ( $1\ \mu\text{C}$ ) ascends from 0.06 through 0.14, 0.32 and 0.37 to 0.86 in the series  $n = 2$  to 6.

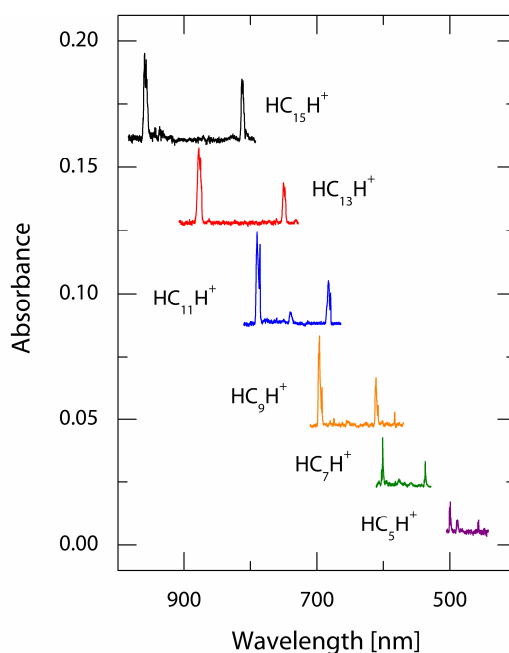


**Figure 3.1:** The  $A^2\Pi_{g/u} \leftarrow X^2\Pi_{u/g}$  electronic transition of  $\text{HC}_{2n+1}\text{H}^+$  ( $n = 2-7$ ) in a neon matrix, recorded following the deposition of mass-selected cations. They are of superior quality to those in Ref. [27].

The smaller members ( $n = 2-4$ ) of the  $\text{HC}_{2n+1}\text{H}^+$  series have been explored by *ab initio* methods. [25,26] The energy of the first dipole-allowed,  $A^2\Pi_b \leftarrow X^2\Pi_a$  transition is overestimated reasonably modest, by 0.1–0.3 eV. This transition can be classified as weak on the basis of its predicted oscillator strength ( $f = 0.004$ , 0.002 and 0.007 for  $n = 2$  to 4, respectively). However, the calculations foretell the  $f$ -values less accurately; *e.g.*, the experimental integrated (and normalized) intensity of  $\text{HC}_7\text{H}^+$  is  $2.3\times$  larger than for  $\text{HC}_5\text{H}^+$ , rather than two times weaker according to the theory.

### 3.3 VISIBLE SPECTRAL RANGE

The  $\text{HC}_{2n+1}\text{H}^+$  cations exhibit much richer electronic spectra than reported earlier. [15,27] Apart from  $A^2\Pi_b \leftarrow X^2\Pi_a$ , new absorptions are found in the visible (Figure 3.2) and UV (Section 3.4). The relative intensity of the bands in Figure 3.2 remains the same for a given mass in experiments carried out under different conditions and correlate well with the strength of the  $A$  system (Figure 3.1). This leads to the conclusion that the  $A$  absorptions and those in Figure 3.2 originate just from one isomer series, namely, linear  $\text{HC}_{2n+1}\text{H}^+$ .

**Table 3.1:** Observed band maxima ( $\lambda \pm 0.1$  nm) in the electronic absorption spectra of  $HC_{2n+1}H^+$  ( $n = 2-7$ ) and  $HC_{2n+1}H$  ( $n = 4-7$ ) species in 6 K neon matrices with their suggested assignments<sup>[a]</sup>

$\lambda$ [nm]	$\tilde{\nu}$ [ $cm^{-1}$ ]	$\Delta\tilde{\nu}$ [ $cm^{-1}$ ]	Assignment <sup>[b]</sup>
<b>HC<sub>5</sub>H<sup>+</sup></b>			
500.8	19 968	0	$0_0^0 A^2\Pi_g \leftarrow X^2\Pi_u$
490.0	20 408	440	$2\nu_8$
483.9	20 665	697	$\nu_3$
481.5	20 768	800	$4\nu_8$
475.8	21 017	1049	$2\nu_9$
471.8	21 195	1227	$2\nu_7$
458.3	21 820	1852	$\nu_2$
449.5	22 246	2278	$\nu_2 + 2\nu_8$
442.1	22 619	2651	$\nu_2 + 4\nu_8$
361.8	27 640	0	$0_0^0 B^2\Pi_g \leftarrow X^2\Pi_u$
355.2	28 153	513	$2\nu_8$
352.7	28 353	713	$\nu_3$
350.0	28 571	931	$2\nu_{10}$
345.7	28 927	1287	$2\nu_7$
344.2	29 053	1413	$2\nu_3$
339.0	29 499	1859	$\nu_2$
331.3	30 184	2544	$\nu_2 + \nu_3$
328.1	30 479	0	$0_0^0 C^2\Pi_g \leftarrow X^2\Pi_u$
323.0	30 960	481	$2\nu_8$
320.3	31 221	742	$\nu_3$
316.9	31 556	1077	$2\nu_9$
314.1	31 837	1358	$2\nu_7$
312.6	31 990	1511	$2\nu_3$
309.1	32 352	1873	$\nu_2$
302.3	33 080	2601	$\nu_2 + \nu_3$
292.5	34 188	3709	$2\nu_2$
<b>HC<sub>7</sub>H<sup>+</sup></b>			
599.8	16 672	0	$0_0^0 A^2\Pi_u \leftarrow X^2\Pi_g$
535.8	18 664	1992	$\nu_2$
448.4	22 302	0	$0_0^0 B^2\Pi_u \leftarrow X^2\Pi_g$
437.5	22 857	555	$\nu_4$
428.7	23 326	1024	$2\nu_4$
422.2	23 685	1383	
411.4	24 307	2005	$\nu_2$
407.0	24 570	0	$0_0^0 C^2\Pi_u \leftarrow X^2\Pi_g$
398.0	25 126	556	$\nu_4$
375.7	26 617	2047	$\nu_2$
368.0	27 174	2604	$\nu_2 + \nu_4$
231.8	43 141	0	$0_0^0 E^2\Pi_u \leftarrow X^2\Pi_g$

**Table 3.1:** (Continued.)

$\lambda$ [nm]	$\tilde{\nu}$ [ $cm^{-1}$ ]	$\Delta\tilde{\nu}$ [ $cm^{-1}$ ]	Assignment <sup>[b]</sup>
<b>HC<sub>9</sub>H<sup>+</sup></b>			
694.9	14 391	0	$0_0^0 A^2\Pi_g \leftarrow X^2\Pi_u$
609.9	16 396	2005	$\nu_3$
545.1	18 345	3954	$2\nu_3$
553.5	18 067	0	$0_0^0 B^2\Sigma_g^- \leftarrow X^2\Pi_u$
539.3	18 543	476	$\nu_5$
529.1	18 900	0	$0_0^0 C^2\Pi_g \leftarrow X^2\Pi_u$
517.2	19 335	435	$\nu_5$
491.1	20 362	1462	
480.7	20 803	1903	$\nu_3$
477.4	20 947	2047	$\nu_2$
467.7	21 381	2481	$\nu_2 + \nu_5$
455.3	21 964	3064	
437.9	22 836	3936	$2\nu_3$
434.7	23 004	4104	$2\nu_2$
426.8	23 430	4530	$2\nu_2 + \nu_5$
399.0	25 063	6163	$3\nu_2$
323.5	30 912	$0 + \delta$	$0_0^0 + \delta D^2\Theta_{u/g} \leftarrow X^2\Pi_u$
319.1	31 338	426	$\nu_5$
316.7	31 576	664	
312.3	32 020	1108	$\nu_4$
308.4	32 425	1513	$\nu_4 + \nu_5$
304.4	32 852	1940	$\nu_3$
301.7	33 146	2234	$2\nu_4$
299.0	33 445	2533	
295.5	33 841	2929	
269.5	37 106	0	$0_0^0 E^2\Pi_g \leftarrow X^2\Pi_u$
266.6	37 509	403	$\nu_5$
260.6	38 373	1267	$\nu_4$
<b>HC<sub>9</sub>H</b>			
241.0	41 494	0	$0_0^0 B^3\Sigma_u^- \leftarrow X^3\Sigma_g^-$
<b>HC<sub>11</sub>H<sup>+</sup></b>			
789.7	12 663	0	$0_0^0 A^2\Pi_u \leftarrow X^2\Pi_g$
681.9	14 665	2002	$\nu_3$
598.3	16 714	4051	$2\nu_3$
621.3	16 095	0	$0_0^0 B^2\Sigma_u^- \leftarrow X^2\Pi_g$
605.6	16 513	418	$\nu_6$
615.1	16 258	0	$0_0^0 C^2\Pi_u \leftarrow X^2\Pi_g$
547.2	18 275	2017	$\nu_3$
533.4	18 748	2490	
492.9	20 288	4030	$2\nu_3$
366.3	27 300	$0 + \delta$	$0_0^0 + \delta D^2\Theta_{g/u} \leftarrow X^2\Pi_g$
353.6	28 281	981	$\nu_5$
346.8	28 835	1535	$\nu_4$
342.2	29 223	1923	$\nu_3$
317.5	31 496	0	$0_0^0 E^2\Pi_u \leftarrow X^2\Pi_g$
314.0	31 847	351	$\nu_6$
310.2	32 237	741	$2\nu_6$
307.9	32 478	982	
305.5	32 733	1237	$\nu_5$
302.3	33 080	1584	$\nu_5 + \nu_6$
299.6	33 378	1882	$\nu_4$
294.2	33 990	2490	$2\nu_5$



**Table 3.1:** (Continued.)

$\lambda$ [nm]	$\tilde{\nu}$ [cm <sup>-1</sup> ]	$\Delta\tilde{\nu}$ [cm <sup>-1</sup> ]	Assignment <sup>[b]</sup>
<b>HC<sub>11</sub>H</b>			
266.4	37 538	0	$0_0^0 B^3\Sigma_u^- \leftarrow X^3\Sigma_g^-$
254.8	39 246	1708	$\nu_4$
<b>HC<sub>13</sub>H<sup>+</sup></b>			
876.9	11 404	0	$0_0^0 A^2\Pi_g \leftarrow X^2\Pi_u$
749.6	13 340	1936	$\nu_4$
659.2	15 170	3766	$2\nu_4$
690.5	14 482	0	$0_0^0 C^2\Pi_g \leftarrow X^2\Pi_u$
672.5	14 870	388	$\nu_7$
664.0	15 060	578	
609.6	16 404	1922	$\nu_4$
542.5	18 433	3951	$2\nu_4$
490.1	20 404	5922	$3\nu_4$
677.9	14 751	0	$0_0^0 B^2\Sigma_g^- \leftarrow X^2\Pi_u$
597.6	16 734	1983	$\nu_4$
406.0	24 631	$0 + \delta$	$0_0^0 + \delta D^2\Theta_{u/g} \leftarrow X^2\Pi_u$
393.3	25 426	805	
390.8	25 589	958	$\nu_6$
382.0	26 178	1547	$\nu_5$
378.1	26 448	1817	$\nu_4$
366.2	27 307	0	$0_0^0 E^2\Pi_g \leftarrow X^2\Pi_u$
362.3	27 601	294	$\nu_7$
359.2	27 840	533	
352.6	28 361	1054	$\nu_6$
350.7	28 514	1207	
347.7	28 760	1453	$\nu_5$
343.4	29 121	1814	$\nu_4$
340.4	29 377	2070	$\nu_3$
337.1	29 665	2358	$\nu_3 + \nu_7$
334.9	29 860	2553	$\nu_5 + \nu_6$
331.6	30 157	2850	$2\nu_5$
325.5	30 722	3415	$\nu_3 + \nu_5$
313.7	31 878	4571	
303.4	32 960	5653	
<b>HC<sub>13</sub>H</b>			
290.0	34 483	0	$0_0^0 B^3\Sigma_u^- \leftarrow X^3\Sigma_g^-$
276.0	36 232	1749	$\nu_4$

**Table 3.1:** (Continued.)

$\lambda$ [nm]	$\tilde{\nu}$ [cm <sup>-1</sup> ]	$\Delta\tilde{\nu}$ [cm <sup>-1</sup> ]	Assignment <sup>[b]</sup>
<b>HC<sub>15</sub>H<sup>+</sup></b>			
959.4	10 423	0	$0_0^0 A^2\Pi_u \leftarrow X^2\Pi_g$
812.7	12 305	1882	$\nu_4$ or $\nu_5$
702.7	14 231	3808	$2\nu_4$ or $2\nu_5$
784.1	12 753	0	$0_0^0 B^2\Sigma_u^- \leftarrow X^2\Pi_g$
711.3	14 059	1306	$\nu_6$
680.9	14 686	1933	$\nu_4$
603.8	16 562	3809	$2\nu_4$
759.1	13 173	0	$0_0^0 C^2\Pi_u \leftarrow X^2\Pi_g$
743.5	13 450	277	$\nu_8$
728.1	13 734	981	
667.0	14 993	1820	$\nu_5$
661.0	15 129	1956	$\nu_4$
590.3	16 941	3768	$\nu_4 + \nu_5$
585.8	17 071	3898	$2\nu_4$
575.7	17 370	4197	$2\nu_4 + \nu_8$
443.6	22 543	$0 + \delta$	$0_0^0 + \delta D^2\Theta_{g/u} \leftarrow X^2\Pi_g$
438.5	22 805	262	$\nu_8$
429.3	23 294	751	$\nu_7$
425.2	23 518	975	$\nu_7 + \nu_8$
405.4	24 667	2124	$\nu_3$
398.8	25 075	0	$0_0^0 E^2\Pi_u \leftarrow X^2\Pi_g$
393.5	25 413	338	$\nu_8$
389.8	25 654	579	
384.7	25 994	919	$\nu_7$
381.0	26 247	1172	$2 \times 579$
378.8	26 399	1324	$\nu_6$
375.3	26 645	1570	
371.6	26 911	1836	$\nu_5$
368.3	27 152	2077	$\nu_4$
363.6	27 503	2428	$\nu_4 + \nu_8$
354.0	28 249	3174	$\nu_5 + \nu_6$
344.8	29 002	3927	$\nu_4 + \nu_5$
332.7	30 057	4982	
<b>HC<sub>15</sub>H</b>			
313.1	31 939	0	$0_0^0 B^3\Sigma_u^- \leftarrow X^3\Sigma_g^-$
297.8	33 580	1641	$\nu_5$

[a] Based on  $\sigma_g^+$  totally symmetric (stretching) frequencies (cm<sup>-1</sup>) in the ground electronic state of HC<sub>2n+1</sub>H<sup>+</sup>, calculated with DFT at the B3YLP/cc-pVTZ level: HC<sub>5</sub>H<sup>+</sup> 3383, 2052, 783; HC<sub>7</sub>H<sup>+</sup> 3400, 2135, 1698, 572; HC<sub>9</sub>H<sup>+</sup> 3413, 2155, 2064, 1275, 450; HC<sub>11</sub>H<sup>+</sup> 3430, 2156, 2143, 1791, 1070, 373; HC<sub>13</sub>H<sup>+</sup> 3436, 2195, 2124, 2057, 1461, 917, 317; HC<sub>15</sub>H<sup>+</sup> 3441, 2223, 2128, 2075, 1820, 1289, 802, 276. [b]  $\Xi$  and  $\Theta$  mean either  $\Pi$  or  $\Phi$  symmetry (see text).

The spectrum of  $\text{HC}_5\text{H}^+$  and  $\text{HC}_7\text{H}^+$  in [Figure 3.2](#) are similar. Two bands (labeled *B* and *C*) dominate; they are separated by 2813 and 2268  $\text{cm}^{-1}$  for  $\text{HC}_5\text{H}^+$  and  $\text{HC}_7\text{H}^+$ , respectively. This spacing is too large to be due to (single, intense) vibrational excitation; therefore, *B* and *C* are assigned as the onsets of two different electronic systems. Multi-reference double-excitation configuration interaction (MRD-CI) calculations have predicted the excitation energy to the  $(2)^2\Pi_g$  and  $(3)^2\Pi_g$  electronic states of  $\text{HC}_5\text{H}^+$  at 3.75 and 3.85 eV, and at 3.14 and 3.17 eV to  $(2)^2\Pi_u$  and  $(3)^2\Pi_u$  of  $\text{HC}_7\text{H}^+$ . [25] These values are quite near the *B* and *C* bands of the respective cations (at 3.43/3.78 eV and 2.77/3.05 eV). However, the computed oscillator strength to the  $(2)^2\Pi_b$  state is 250 and 90 $\times$  smaller than to  $(3)^2\Pi_b$  of  $\text{HC}_5\text{H}^+$  and  $\text{HC}_7\text{H}^+$ , respectively, while the integrated intensity of system *B* is about two times lower than that of *C* for both cations. Weak bands on the high-energy side of *B* and *C* are assigned to vibrational excitation within the electronic transitions ([Table 3.1](#)).

The absorptions of  $\text{HC}_9\text{H}^+$  in the visible are more alike those of the larger cations in the series than the smaller ones. A regular intensity distribution of the strongest bands (*C* in [Figure 3.2](#)) is apparent. The most intense feature on the lower-energy edge of the spectrum is assigned as the onset of a new electronic transition; other absorptions are due to two fundamental modes of energy 1903 and 2047  $\text{cm}^{-1}$ , and their overtones, active in the excited electronic state. These are attributed to the  $\nu_3$  and  $\nu_2$  totally-symmetric vibrations of  $\text{HC}_9\text{H}^+$  on the basis of DFT calculations of the ground-state frequencies for this cation at the B3LYP/cc-pVTZ level of theory. Computed energy of the  $\sigma_g^+$  modes of the entire  $\text{HC}_{2n+1}\text{H}^+$  ( $n = 2-7$ ) series is listed in footnote [a] of [Table 3.1](#).

In addition to the strong *C* band system, the spectrum of  $\text{HC}_9\text{H}^+$  exhibits several weak absorptions at the low-energy side ([Figure 3.2](#)). For the visible, *ab initio* MRD-CI has located two excited electronic states that are dipole-accessible from  $X^2\Pi_u$  of  $\text{HC}_9\text{H}^+$ :  $(2)^2\Pi_g$  and  $(3)^2\Pi_g$ ; the energies to these are 2.72 and 2.81 eV. [26] The stronger transition is to  $(2)^2\Pi_g$  with an oscillator strength 0.2; that to  $(3)^2\Pi_g$  is predicted much weaker, with  $f \approx 0.0001$ . The origin band of the strong *C* absorption system lies at 529.1 nm (2.34 eV) and the weak, longest-wavelength feature in [Figure 3.2](#), *B*, at 553.5 nm (2.24 eV). The discrepancy between the calculated and experimental energies of the visible transitions of  $\text{HC}_9\text{H}^+$  is larger ( $\sim 0.5$  eV) than for the smaller members ( $n = 2,3$ ) of the same  $\text{HC}_{2n+1}\text{H}^+$  family.

Because of this and as the  $(2)^2\Pi_g$  and  $(3)^2\Pi_g$  states of  $\text{HC}_9\text{H}^+$  lie close to each other according to the theory, it is likely that their order is also reversed and, consequently, the transition moment to the lower-energy state  $(2)^2\Pi_g$  is in fact the lower and not to  $(3)^2\Pi_g$ . Thus, the strong band system of  $\text{HC}_9\text{H}^+$  (C in Figure 3.2) is assigned to the same  $\text{C } ^2\Pi_b$  state as for the higher-energy transition of those to B and C of  $\text{HC}_{2n+1}\text{H}^+$  ( $n = 2,3$ ).

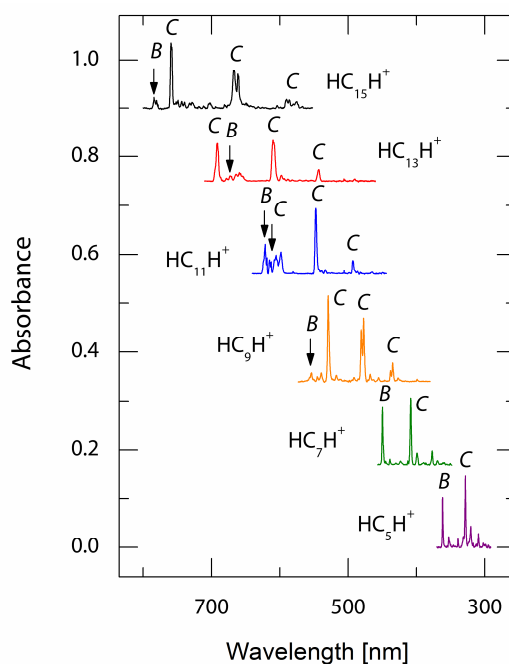


**Figure 3.2:** A visible section of the electronic absorption spectra measured following mass-selective deposition of  $\text{HC}_{2n+1}\text{H}^+$  ( $n = 2-7$ ) into a neon matrix. The two observed new band systems B and C are assigned to the  $B^2\Pi_{g/u} \leftarrow X^2\Pi_{u/g}$  and  $C^2\Pi_{g/u} \leftarrow X^2\Pi_{u/g}$  electronic transitions, respectively.

The absorption spectra of  $\text{HC}_{13}\text{H}^+$  and  $\text{HC}_{15}\text{H}^+$  in the visible (Figure 3.2) look much alike  $\text{HC}_9\text{H}^+$ . Two systems, the strong C and the much weaker B, are discernible. The onset of B changes with respect to that of C passing from  $\text{HC}_9\text{H}^+$  to  $\text{HC}_{15}\text{H}^+$ . In the case of  $\text{HC}_9\text{H}^+$  it lies on the long-wavelength side of the origin band of C, for  $\text{HC}_{13}\text{H}^+$  it is blue-shifted, while for  $\text{HC}_{15}\text{H}^+$  it is again to the red.

The electronic spectrum of  $\text{HC}_{11}\text{H}^+$  in Figure 3.2 looks peculiar in comparison to those of other members of the  $\text{HC}_{2n+1}\text{H}^+$  series. The band at 547.2 nm dominates

and a weaker one at 492.9 nm (separated by  $2013\text{ cm}^{-1}$ ) accompanies it. If the wavelength of the origin band of the strong,  $C\ ^2\Pi_b \leftarrow X\ ^2\Pi_a$  transition of  $\text{HC}_{2n+1}\text{H}^+$  in the visible is plotted as a function of the number of carbon atoms, a linear dependence is seen (Figure 3.3), as has been noted for the  $A\ ^2\Pi_{g/u} \leftarrow X\ ^2\Pi_{u/g}$  transition and for other carbon chains. [29,30] The band at 547.2 nm of  $\text{HC}_{11}\text{H}^+$  departs somewhat from this linearity, which suggests that it is not the onset of its  $C\ ^2\Pi_u \leftarrow X\ ^2\Pi_g$  transition. A common character of the C band system of all the  $\text{HC}_{2n+1}\text{H}^+$  cations is a strong progression due to the excitation of  $\text{C}\equiv\text{C}$  stretching modes. In this regard  $\text{HC}_{11}\text{H}^+$  is not an exception, because a vibrational band of  $2013\text{ cm}^{-1}$  is observed at 492.9 nm. On closer inspection of the moderately intense group of bands red-shifted from the strongest one (at 547.2 nm), a feature at 615.1 nm was discovered, which is separated from the 547.2 nm peak by  $2017\text{ cm}^{-1}$ . Therefore, the absorption at 615.1 nm is assigned as the onset of the C system of  $\text{HC}_{11}\text{H}^+$ ; the peak at 547.2 nm corresponds to the excitation of a fundamental and that at 492.9 nm is the overtone. The moderately intense group of bands around 620 nm is attributed to the weaker system B. The closeness of the two electronic states B and C leads to their interaction and, as a result, the weaker  $B\ ^2\Pi_u \leftarrow X\ ^2\Pi_g$  transition gains intensity. B of  $\text{HC}_{11}\text{H}^+$  is therefore much stronger than observed for the other members of this series, while the origin band of  $C\ ^2\Pi_b \leftarrow X\ ^2\Pi_a$  becomes exceptionally weak compared to the case of the other  $\text{HC}_{2n+1}\text{H}^+$  cations.

In summary, the strong C system of  $\text{HC}_{2n+1}\text{H}^+$  ( $n = 5-7$ ) is assigned as the  $(3)^2\Pi_b \leftarrow X\ ^2\Pi_a$  transition by an analogy to the smaller members ( $n = 2-4$ ) of this series. The weaker B can be ordered to  $(2)^2\Pi_b \leftarrow X\ ^2\Pi_a$ ; however, calculations for  $\text{HC}_9\text{H}^+$  predict another state,  $(1)^2\Phi_g$ , to lie close to  $(2)^2\Pi_g$ . [26] Although the former is not dipole-allowed from the ground electronic state ( $\Sigma \not\leftarrow \Phi \times \{\Sigma, \Pi\} \times \Pi$  in  $D_{\infty h}$ ), it may become available via vibronic mixings due to the vicinity of the states. The symmetry of the B state is thus left open and is marked by  $\Xi$  in Table 3.1 and Figure 3.3, denoting either  $\Pi$  or  $\Phi$ . The onset wavelengths of the transitions to B and C of  $\text{HC}_{2n+1}\text{H}^+$  as a function of the number of carbon atoms rest on least-squares fitted lines shown in Figure 3.3. The linear fit for the transitions to B and C is somewhat worse than in the case of  $A\ ^2\Pi_b \leftarrow X\ ^2\Pi_a$  (the regression coefficient  $R$  is 0.9958 and 0.9962 vs. 0.9995). A reason could be an interaction of the B and C states, or broadening due to the lifetime and matrix effects.

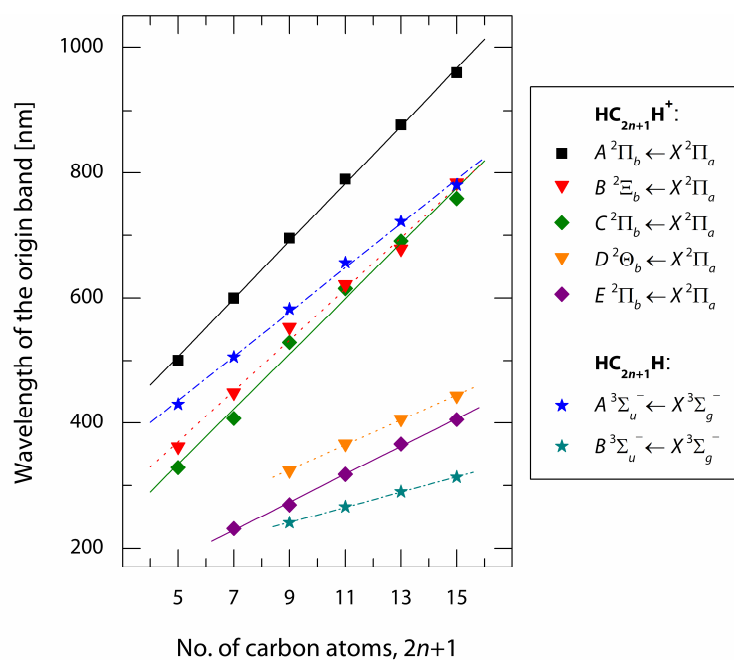


**Figure 3.3:** Origin wavelength of observed electronic transitions of  $\text{HC}_{2n+1}\text{H}^+$  and  $\text{HC}_{2n+1}\text{H}$  ( $n = 2-7$ ), plotted against the number of carbon atoms of the absorbing species.  $A^3\Sigma_u^- \leftarrow X^3\Sigma_g^-$  data of  $\text{HC}_{2n+1}\text{H}$  is reproduced from Ref. [15].  $a \equiv u/g$  and  $b \equiv g/u$  for  $n = \text{even/odd}$ ;  $\Xi$  and  $\Theta$  denote either  $\Pi$  or  $\Phi$  symmetry (see text).

### 3.4 UV DOMAIN

The UV section of the electronic absorption spectra of  $\text{HC}_{2n+1}\text{H}^+$  ( $n = 3-7$ ) is shown in Figure 3.4. For each cation but  $\text{HC}_7\text{H}^+$  two spectra are depicted: The upper was recorded after the deposition of mass-selected ions and the lower after irradiation of the matrix with UV photons from a mpHg lamp. Absorptions diminishing upon bleaching and some, marked by stars, which grow in intensity are distinguishable. The latter are due to neutrals (Chapter 2).

The focus is laid first on the region where the strongest absorptions of  $\text{HC}_{2n+1}\text{H}^+$  ( $n = 3-7$ ) are. The corresponding spectra are labeled a, c, e, g and i in Figure 3.4. Two band systems are discernible: The first one (*D*) lies at lower wavelengths and is weak, whereas the second (*E*) bears large intensity. In the case of  $\text{HC}_7\text{H}^+$ , there is a strong, broad absorption centered at around 232 nm which rises steeply from the high-energy side and then falls gradually. The short-wavelength edge of this band is obscured by scattered UV light in the matrix. For  $\text{HC}_9\text{H}^+$ , the *E* band

is drifted by  $\sim 38$  nm towards the red in comparison to  $HC_7H^+$  and a multiplet structure is apparent.  $E$  of  $HC_{11}H^+$  is shifted bathochromically by  $\sim 48$  nm with respect to  $HC_9H^+$  and the structure is even more evolved. This pattern is observed also for  $HC_{13}H^+$  and  $HC_{15}H^+$ . The  $E$  system of the latter two cations spans over 60 nm and has a complex structure. If the wavelength of the  $E$  band of  $HC_{2n+1}H^+$  ( $n = 3-5$ ) is plotted against the number of carbon atoms, the onset for  $HC_{13}H^+$  and  $HC_{15}H^+$  (vertical arrow on the left of the transition in Figure 3.4) lies also on this line (Figure 3.3).

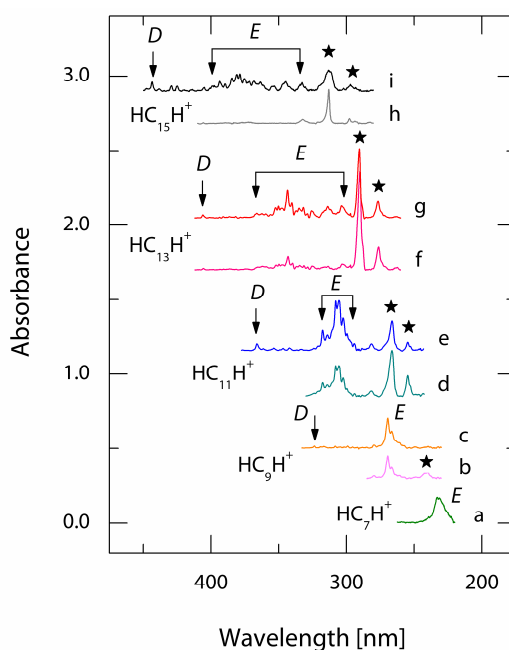


**Figure 3.4:** UV range of the electronic absorption spectra of  $HC_{2n+1}H^+$  ( $n=3-7$ ) in a neon matrix. (a), (c), (e), (g) and (i) were measured after deposition; (b), (d) and (f) after subsequent photobleaching. In (h) the spectrum was recorded after growing the  $HC_{15}H^+$  sample matrix under continuous irradiation with UV photons from a mpHg lamp. Stars mark bands of neutral  $HC_{2n+1}H$  ( $n = 4-7$ ).

Although the shape of system  $E$  changes on passing from  $HC_7H^+$  to  $HC_{15}H^+$ , it can nevertheless be assigned to the same electronic transition on the basis of its large intensity and the wavelength dependence on size. For the smaller ( $n = 2-4$ )  $HC_{2n+1}H^+$  members, MRD-CI calculations predict a strong transition to the  $(4)^2\Pi_b$  state at 7.02, 6.01 and 5.47 eV, respectively. [25,26] The  $E$  band system for  $HC_5H^+$

was not observed, because according to the linear plot (Figure 3.3) it should lie at  $\sim 188$  nm, not accessible in the neon matrix experiments. The experimental energy of the onset of the  $E$  band system of  $\text{HC}_7\text{H}^+$  is at 5.35 eV (231.8 nm), and 4.60 eV (269.5 nm) for  $\text{HC}_9\text{H}^+$ ; therefore, it is assigned to the predicted  $(4)^2\Pi_b \leftarrow X^2\Pi_a$  transition. [25,26]

The vibrational structure of  $E^2\Pi_b \leftarrow X^2\Pi_a$  of  $\text{HC}_{2n+1}\text{H}^+$  is more complex than for the lower-energy transitions. In the case of larger members ( $n = 6,7$ ), the system extends  $5000\text{ cm}^{-1}$  beyond the weak origin band. This is a signature of a geometry change in  $E^2\Pi_b$  with respect to the ground state. Thus, a tentative assignment of features of this system to  $\sigma_g^+$  modes is given in Table 3.1.

A rather weak band system ( $D$  in Figure 3.4) can be seen to the red of  $E$  for  $\text{HC}_{2n+1}\text{H}^+$  ( $n = 4-7$ ). The onset wavelength *versus* the number of carbon atoms shows a linear dependence (Figure 3.3) with  $R = 0.9996$ . MRD-CI predicts several states between  $C$  and  $E$  for  $\text{HC}_7\text{H}^+$  and  $\text{HC}_9\text{H}^+$ , but the transitions from the ground state to these are dipole-forbidden. [25,26] Therefore, it is difficult to deduce the  $D$  state symmetry and whether the transition appears because of vibronic interaction and/or if it is not adequately described by theory. This is left open and the  $D$  system is designated as  $D^2\Theta_{a/b} \leftarrow X^2\Pi_a$ , where  $^2\Theta_{a/b}$  could be  $^2\Pi$  or  $^2\Phi$ , and would have the same ( $a$ ) or the opposite ( $b$ ) to the ground state parity depending on whether it is vibronically induced or optically allowed transition, respectively. The onset of this transition is marked as  $0_0^0 + \delta$  in Table 3.1,  $\delta$  being the frequency of a non-totally symmetric vibration in the first case, while it equals zero for the second.

### 3.5 $B^3\Sigma_u^- \leftarrow X^3\Sigma_g^-$ OF $\text{HC}_{2n+1}\text{H}$ ( $n = 4-7$ )

Bands of neutral  $\text{HC}_{2n+1}\text{H}$  ( $n = 4-7$ ) are identified in the UV region; they are marked with stars in the spectra recorded after deposition of mass-selected  $\text{HC}_{2n+1}\text{H}^+$  (Figure 3.4). They grow in intensity upon UV irradiation of the matrix. The spectra measured after photobleaching the  $n = 4$  to 6 representatives of the  $\text{HC}_{2n+1}\text{H}^+$  series are denoted with letters b, d and f in Figure 3.4. That labeled h was recorded after continuous UV irradiation of the matrix during the deposition of  $\text{HC}_{15}\text{H}^+$ . The UV spectra of  $\text{HC}_{2n+1}\text{H}$  are simple; they exhibit two bands only: a strong origin and a weaker vibrational band  $\sim 1700\text{ cm}^{-1}$  above. In the case of

$\text{HC}_9\text{H}$ , only the origin band is seen (Figure 3.4). The onset wavelength of this transition of  $\text{HC}_{2n+1}\text{H}$  follows linearity as a function of the number of carbon atoms (bottom line in Figure 3.3). Though the UV system of  $\text{HC}_{2n+1}\text{H}$  dominates the spectra shown in Figure 3.4, their known long-wavelength  $A^3\Sigma_u^- \leftarrow X^3\Sigma_g^-$  transition [15] could be barely seen. In the case of  $\text{HC}_{11}\text{H}$ , where the strongest bands of  $A^3\Sigma_u^- \leftarrow X^3\Sigma_g^-$  are discernible, the ratio of the strength of the UV band system to the visible one is evaluated  $280 \pm 30$ . From the change of the intensity of the neutral and ionic forms of  $\text{HC}_{11}\text{H}$  upon UV bleaching, the relative intensity of the strong UV transition of these species can also be estimated—they are almost equal ( $\text{HC}_{11}\text{H}/\text{HC}_{11}\text{H}^+ = 0.95 \pm 0.10$ ).

$\text{HC}_{2n+1}\text{H}$  ( $n = 3-6,9$ ) have been studied in the gas phase by means of a resonant two-color, two-photon ionization technique. [19] The wavelength of the origin band of  $\text{HC}_{13}\text{H}$  has been found at 281.82 nm; it is at 290.0 nm in neon. Smaller members ( $n = 2-4$ ) of  $\text{HC}_{2n+1}\text{H}$  have been investigated by *ab initio* CASSCF and MRD-CI methods. [19,22-24] These predict a strong transition,  $B^3\Sigma_u^- \leftarrow X^3\Sigma_g^-$ . MRD-CI excitation to this state of, *e.g.*,  $\text{HC}_9\text{H}$  is at 5.91 eV, [23] while the present experimental data gives 5.51 eV (241.0 nm). The band system of  $\text{HC}_{2n+1}\text{H}$  ( $n = 4-7$ ) seen in Figure 3.4 is therefore assigned to the  $B^3\Sigma_u^- \leftarrow X^3\Sigma_g^-$  electronic transition. Wavelengths of the observed bands of  $\text{HC}_{2n+1}\text{H}$  and their assignment are in Table 3.1.

### 3.6 COMPARISON OF THE ELECTRONIC TRANSITIONS OF $\text{HC}_{2n+1}\text{H}^+$ AND $\text{HC}_{2n}\text{H}^+$ ( $n = 2-7$ )

Even- and odd-carbon members of the neutral  $\text{HC}_x\text{H}$  series,  $\text{HC}_{2n}\text{H}$  and  $\text{HC}_{2n+1}\text{H}$ , differ considerably in their electronic structure due to the presence of a half-filled  $\pi$  orbital for the latter species. As a consequence,  $\text{HC}_{2n+1}\text{H}$  have triplet ground state in contrary to the singlet for  $\text{HC}_{2n}\text{H}$ . The lowest-energy electronic transition of the odds falls into the visible and NIR, while for the evens it lies in the UV. Another consequence is a triple/single bond alternation in the case of  $\text{HC}_{2n}\text{H}$  and a complex character for odd polyacetylenes (Figure 3.5). Theoretical studies reveal that the  $\text{HC}_{2n+1}\text{H}$  series splits into two subgroups,  $\text{HC}_{4z+1}\text{H}$  and  $\text{HC}_{4z+3}\text{H}$ , having similar geometrical structure within. [20,24,31] Such a behavior may be expected for the cations of polyacetylenes, too, where both odd and even members have doublet ground state resulting from the unpaired  $\pi$  electron.



[25,26,32] Therefore, it is worthwhile to compare electronic transitions of  $x = \text{even}$  and odd representatives of  $\text{HC}_x\text{H}^+$  with each other.

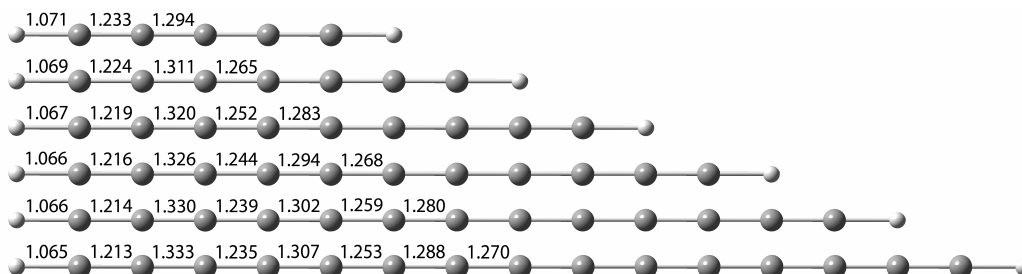


**Figure 3.5:** Bond length alternation in the odd-number carbon members of the  $\text{HC}_x\text{H}^+$  polyacetylene series. The values indicated ( $\text{\AA}$ ) are reproduced from the DFT calculations at the B3LYP/cc-pVTZ level of Ref. [33].

Electronic transitions from the ground to higher excited electronic states of the even,  $\text{HC}_{2n}\text{H}^+$  ( $n = 2-7$ ) series have been studied in neon matrices. [28] These cations exhibit  $A \ ^2\Pi \leftarrow X \ ^2\Pi$  electronic transition in the visible and NIR, and a strong  $E \ ^2\Pi \leftarrow X \ ^2\Pi$  system in the UV. The latter is an order of magnitude more intense than the former. Three much weaker transitions to the states  $B$ ,  $C$  and  $D$  lie between  $A$  and  $E$  in energy and have also been detected in those studies. Cations belonging to the  $\text{HC}_{2n+1}\text{H}^+$  series mimic to some extent the  $\text{HC}_{2n}\text{H}^+$  ones. The strongest electronic transition,  $E \ ^2\Pi \leftarrow X \ ^2\Pi$  is also in the UV, the next most intense to state  $C$  is in the visible.  $A \ ^2\Pi \leftarrow X \ ^2\Pi$  is an order of magnitude weaker than the latter.

The energies of the electronic transitions of the even  $\text{HC}_{2n}\text{H}^+$  [27,28] and odd  $\text{HC}_{2n+1}\text{H}^+$  (this work) sets are compared in Table 3.2. There is a striking similarity between the transition energy of two neighboring cations,  $\text{HC}_4\text{H}^+$  and  $\text{HC}_5\text{H}^+$ , ...,  $\text{HC}_{14}\text{H}^+$  and  $\text{HC}_{15}\text{H}^+$ ; the origin bands of each such couple lie near each other. As it has been shown earlier, [27] this regularity can be explained in the framework of the HMO theory where such a pair of molecules are described as having exactly the same excitation energy. Moreover, homologous series of linear chain molecules allows a reliable prediction of the origin band of unknown members of the series. Although the  $p_x$  orbital distribution of the carbons in the HOMO of  $\text{HC}_{2n+1}\text{H}$  may suggest so, [31] in the case of the  $\text{HC}_{2n+1}\text{H}^+$  set neither the linear

**Table 3.2:** Comparison of  ${}^2\Pi \leftarrow X^2\Pi$  electronic transition energies (eV) of  $HC_{2n}H^+$  and  $HC_{2n+1}H^+$  ( $n = 2-7$ ) (**bold**) in neon matrices with theoretical CASPT2/cc-pVTZ values (*italic*). Integrated intensities of the presently observed band systems and experimentally determined oscillator strengths are also included.<sup>[a]</sup>

Species	Transition					Label <sup>[b]</sup>
	<i>A</i> ← <i>X</i>	<i>B</i> ← <i>X</i>	<i>C</i> ← <i>X</i>	<i>D</i> ← <i>X</i>	<i>E</i> ← <i>X</i>	
$HC_4H^+$	2.44	—	3.69			ee
	2.62	—	3.93	4.53	5.21	ec
$HC_5H^+$	<b>2.48</b>	<b>3.43</b>	<b>3.78</b>			<b>oe</b>
	2.59	3.49	3.57			oc
	1.7	18	51			ii
	0.00075	0.0076	0.022			f
$HC_6H^+$	2.05	(2.54)	2.97			ee
	2.14	—	2.99	3.46	3.97	ec
$HC_7H^+$	<b>2.07</b>	<b>2.77</b>	<b>3.05</b>	—	<b>5.35</b>	<b>oe</b>
	2.11	2.88	2.89			oc
	4.1	44	90		750 <sup>[c]</sup>	ii
	0.0018	0.019	0.039		0.32	f
$HC_8H^+$	1.74	2.18	2.50	—	5.11	ee
	1.81	2.40	2.76	3.20		ec
$HC_9H^+$	<b>1.78</b>	<b>2.24</b>	<b>2.34</b>	<b>3.84</b>	<b>4.60</b>	<b>oe</b>
	1.87	2.22	2.51			oc
	9.3	11	130	32	420	ii
	0.004	0.0046	0.057	0.014	0.18	f
$HC_{10}H^+$	1.51	1.91	2.19	—	4.50	ee
	1.52	1.98	2.23	2.60		ec
$HC_{11}H^+$	<b>1.57</b>	<b>2.00</b>	<b>2.02</b>	<b>3.38</b>	<b>3.90</b>	<b>oe</b>
	1.65	1.95	2.18			oc
	11	45	58	54	980	ii
	0.0046	0.020	0.025	0.023	0.43	f
$HC_{12}H^+$	1.33	1.70	(1.96)	2.30	4.01	ee
	1.35	1.75	1.98	2.32		ec
$HC_{13}H^+$	<b>1.41</b>	<b>1.80</b>	<b>1.83</b>	<b>3.05</b>	<b>3.39</b>	<b>oe</b>
	1.49	1.74	1.96			oc
	25	41	190	63	1850	ii
	0.11	0.018	0.081	0.027	0.79	f
$HC_{14}H^+$	1.18	1.54	—	2.03	3.62	ee
	1.22	1.65	1.85	2.16		ec
$HC_{15}H^+$	<b>1.29</b>	<b>1.58</b>	<b>1.63</b>	<b>2.79</b>	<b>3.11</b>	<b>oe</b>
	1.35	1.57	1.78			oc
	0.031	0.017	0.265	0.075	1.00 <sup>[d]</sup>	ii

[a] See the text for the  $\Phi$  symmetry possibilities of the *B* and *D* excites states.

[b] ee experimental [27,28] and ec computed [32] excitation energies of  $HC_{2n}H^+$ ;

**oe** neon matrix (this work) and *oc* calculated [33] energies of  $HC_{2n+1}H^+$ ;

ii: integrated intensity ( $10^6 \text{ m mol}^{-1}$ ) of the systems; f: experimentally determined

oscillator strengths. [c] Not corrected for the broadening due to strong UV light

scattering in the matrix. [d] Intensities are scaled taken that of the strongest

transition,  $E^2\Pi \leftarrow X^2\Pi$  of  $HC_{15}H^+$  as 1.00.

dependence of the electronic transition onsets on the chain length (Figure 3.3) nor the bond length variations (Figure 3.5) show any peculiarity that would support a difference between subgroups  $\text{HC}_{4z+1}\text{H}^+$  and  $\text{HC}_{4z+3}\text{H}^+$ . The same can be said about categories  $\text{HC}_{4z}\text{H}^+$  and  $\text{HC}_{4z+2}\text{H}^+$ , [28] and, likely, for neutral polyacetylenes and other linear (hydro)carbon chains, too.

This is a simple manifestation of the 1D particle-in-a-box (PIB) model, [34–37] that is, the energy levels of such a system can be described as

$$E_k = \frac{h^2 k^2}{8m_e L^2} \quad , \quad (3.1)$$

where  $m_e$  is the rest mass of the electron and  $h$  stands for the Planck constant. Because the neighboring levels  $k$  and  $k+1$  involved in the (first allowed) transition (HOMO, and LUMO for singlets or SOMO for doublets), and the length  $L$  of the ‘box’ are both (roughly) proportional to the number of carbon atoms  $x$ , the followings can be written:

$$\tilde{\nu} = 1/\lambda = \frac{E_{k+1} - E_k}{hc} = \frac{h(k+k+1)}{8m_e c L^2} \propto 1/x \quad \Rightarrow \quad \lambda \propto x \quad , \quad (3.2)$$

where  $\lambda$  denotes the wavelength (maximum or origin) of the transition and  $c$  is the speed of light in vacuum. Specifically, for the investigated open-shell, odd-carbon  $\text{HC}_{2n+1}\text{H}^+$  cations, the total number of valence electrons distributed over the chain are the same as the number of carbon atoms,  $2n+1$ ; thus, according to the Pauli exclusion principle, the relevant (initial and final) orbitals  $k$  and  $k+1$  can be expressed as  $n$  and  $n+1$ , respectively. Consequently, the conjugation model can then be evaluated by calculating the effective box length

$$L_{\text{eff}} = \sqrt{\frac{h(2n+1)\lambda}{8m_e c}} \quad (3.3)$$

using the experimentally observed absorption data; [38] it can also be used to make predictions on the spectra of unknown members of the series. Analog considerations may be valid for higher excited electronic states, providing an explanation for the similarity in the gradient trend of different transitions within the same family of species (Figure 3.3).

During the course of these investigations, a paper on the excited electronic states of the  $\text{HC}_{2n+1}\text{H}^+$  series has appeared. [33] Energies of the first excited,  $A\ ^2\Pi_b$  state for  $n = 2$  to 7 have been compared with experimental data for the known long-wavelength  $A\ ^2\Pi_b \leftarrow X\ ^2\Pi_a$  transition of these cations. A good agreement is apparent (Table 3.2). Their calculated excitation energies of  $\text{HC}_{2n+1}\text{H}^+$  for higher-lying electronic states are also included in the table. The predicted positions of the  $B$  and  $C$  states agree well with the present experimental data. Similar calculations fit even better for the electronic states of the known  $\text{HC}_{2n}\text{H}^+$  cations (Table 3.2). [28,32]

### 3.7 OSCILLATOR STRENGTH OF THE OBSERVED TRANSITIONS OF $\text{HC}_{2n+1}\text{H}^+$ ( $n = 2-6$ )

Measuring the current at the substrate surface and, thereby, counting the total charge of the ions deposited into a neon matrix allows a comparison of electronic transitions strength. Integrated intensity of the band systems of  $\text{HC}_{2n+1}\text{H}^+$  ( $n = 2-7$ ) is in Table 3.2. The accuracy is estimated to be ca.  $\pm 10\%$  within the same cation, while for two different species this could be somewhat worse. The integrated intensity of a given band system is proportional to the oscillator strength  $f$  of the transition. The dimensionless  $f$ -values can be evaluated using

$$f = \frac{4\varepsilon_0 m_e c^2 \ln 10}{N_A e^2} \int_{\tilde{\nu}_1}^{\tilde{\nu}_2} \varepsilon(\tilde{\nu}) d\tilde{\nu} \quad , \quad (3.4)$$

where  $\varepsilon_0$ ,  $m_e$ ,  $c$ ,  $N_A$  and  $e$  are fundamental physical constants and  $\varepsilon(\tilde{\nu})$  is the molar extinction coefficient.  $\varepsilon(\tilde{\nu})$  can be approximated from the concentration of the cations deposited into the matrix ( $\propto$  accumulated charge  $Q_{\text{dep}}$ ) and its volume ( $V_{\text{mtx}} \approx 2 \times 2 \times 0.015 \text{ cm}^3$ ) by the Beer–Lambert law,

$$A(\tilde{\nu}) = -\lg(I/I_0) = \varepsilon(\tilde{\nu}) \frac{Q_{\text{dep}} N_A}{e V_{\text{mtx}}} l \quad . \quad (3.5)$$

The path length was  $l \approx 2 \text{ cm}$ .

To test how reliable  $f$  can be from the experimental data, the  $A$ ,  $B$  and  $C$  band systems of  $\text{HC}_5\text{H}^+$  were chosen as for these the integrated intensities and the theoretical oscillator strengths resemble each other the most. The values obtained are  $f(A) = 7.5 \times 10^{-4}$ ,  $f(B) = 7.6 \times 10^{-3}$  and  $f(C) = 0.022$ , while calculations give 0.0005, 0.034 and 0.06, respectively. [33] Experiments provide a lower bound to oscillator

strengths of cations because losses due to charge neutralization during deposition of the matrix are not taken into account. It is assumed that this can lower  $f$  by a factor of about two as the UV band system of neutral  $\text{HC}_{2n+1}\text{H}$  has an intensity comparable to the cationic one in the spectra recorded. The experimentally determined  $f$ -values for all the band systems for  $\text{HC}_{2n+1}\text{H}^+$  are given in [Table 3.2](#).

### 3.8 CONCLUSIONS

By locating several new electronic systems of an unsaturated hydrocarbon series that was studied earlier in this laboratory, [15,27] the capabilities of the upgraded apparatus is evident. The quality improvement is a result of a number of advancements ranging from the better end vacuum through the appropriate electron scavenger choice to a fast, sensible detection system, as described in [Chapter 2](#). The strong band systems of  $\text{HC}_{2n+1}\text{H}^+$  and  $\text{HC}_{2n+1}\text{H}$  presented here provide more a sensitive means of detection of such species in gas-phase experiments and, perhaps, in astrophysical environments than it was possible before via their weaker,  $A^2\Pi_{g/u} \leftarrow X^2\Pi_{u/g}$  or  $A^3\Sigma_u^- \leftarrow X^3\Sigma_g^-$  transitions, respectively. For  $\text{HC}_{2n+1}\text{H}$  ( $n = 4-7$ ) this is the  $B^3\Sigma_u^- \leftarrow X^3\Sigma_g^-$  electronic transition; in the case of the smaller  $\text{HC}_{2n+1}\text{H}^+$  cations ( $n = 3-5$ ) appropriate for this purpose is  $E^2\Pi_{g/u} \leftarrow X^2\Pi_{u/g}$ , whereas for the larger ones ( $n = 6,7$ ) the most suitable is probably the  $C^2\Pi_{g/u} \leftarrow X^2\Pi_{u/g}$  system. These findings have been published in *The Journal of Chemical Physics*. [39]



## Bibliography

- [1] K.-H. Homann. *Fullerenes and soot formation—New pathways to large particles in flames*. *Angew. Chem. Int. Ed.* **1998**, 37(18): 2434–2451; and references therein.
- [2] M.B. Bell, P.A. Feldman, J.K.G. Watson, M.C. McCarthy, M.J. Travers, C.A. Gottlieb, P. Thaddeus. *Observations of long  $C_nH$  molecules in the dust cloud TMC-1*. *Astrophys. J.* **1999**, 518(2): 740–747.
- [3] T.J. Millar, E. Herbst, R.P.A. Bettens. *Large molecules in the envelope surrounding IRC+10216*. *Mon. Not. R. Astron. Soc.* **2000**, 316(1): 195–203.
- [4] M. Guélin, S. Green, P. Thaddeus. *Detection of the  $C_4H$  radical toward IRC +10216*. *Astrophys. J.* **1978**, 224(1): L27–L30.
- [5] H. Suzuki, M. Ohishi, N. Kaifu, S. Ishikawa, T. Kasuga, S. Saito, K. Kawaguchi. *Detection of the interstellar  $C_6H$  radical*. *Publ. Astron. Soc. Japan* **1986**, 38(6): 911–917.
- [6] M. Guélin, J. Cernicharo, M.J. Travers, M.C. McCarthy, C.A. Gottlieb, P. Thaddeus, M. Ohishi, S. Saito, S. Yamamoto. *Detection of a new linear carbon chain radical:  $C_7H$* . *Astron. Astrophys.* **1997**, 317(1): L1–L4.
- [7] J. Cernicharo, M. Guélin. *Discovery of the  $C_8H$  radical*. *Astron. Astrophys.* **1996**, 309(2): L27–L30.
- [8] J. Cernicharo, M. Guélin, M. Agúndez, K. Kawaguchi, M. McCarthy, P. Thaddeus. *Astronomical detection of  $C_4H^-$ , the second interstellar anion*. *Astron. Astrophys.* **2007**, 467(2): L37–L40.
- [9] M.C. McCarthy, C.A. Gottlieb, H. Gupta, P. Thaddeus. *Laboratory and astronomical identification of the negative molecular ion  $C_6H^-$* . *Astrophys. J.* **2006**, 652(2): L141–L144.
- [10] S. Brünken, H. Gupta, C.A. Gottlieb, M.C. McCarthy, P. Thaddeus. *Detection of the carbon chain negative ion  $C_8H^-$  in TMC-1*. *Astrophys. J.* **2007**, 664(1): L43–L46.
- [11] J. Cernicharo, C.A. Gottlieb, M. Guélin, T.C. Killian, P. Thaddeus, J.M. Vrtilék. *Astronomical detection of  $H_2CCCC$* . *Astrophys. J. Lett.* **1991**, 368(2): L43–L45.
- [12] J. Cernicharo, C.A. Gottlieb, M. Guélin, T.C. Killian, G. Paubert, P. Thaddeus, J.M. Vrtilék. *Astronomical detection of  $H_2CCC$* . *Astrophys. J. Lett.* **1991**, 368(2): L39–L41.
- [13] W.D. Langer, T. Velusamy, T.B.H. Kuiper, R. Peng, M.C. McCarthy, M.J. Travers, A. Kovács, C.A. Gottlieb, P. Thaddeus. *First astronomical detection of the cumulene carbon chain molecule  $H_2C_6$  in TMC-1*. *Astrophys. J. Lett.* **1997**, 480(1): L63–L66.
- [14] J. Cernicharo, A.M. Heras, A.G.G.M. Tielens, J.R. Pardo, F. Herpin, M. Guélin, L.B.F.M. Waters. *Infrared Space Observatory's discovery of  $C_4H_2$ ,  $C_6H_2$ , and benzene in CRL 618*. *Astrophys. J.* **2001**, 546(2): L123–L126.
- [15] J. Fulara, P. Freivogel, D. Forney, J.P. Maier. *Electronic absorption spectra of linear carbon chains in neon matrices. III.  $HC_{2n+1}H$* . *J. Chem. Phys.* **1995**, 103(20): 8805–8810.

- [16] N.P. Bowling, R.J. Halter, J.A. Hodges, R.A. Seburg, P.S. Thomas, C.S. Simmons, J.F. Stanton, R.J. McMahon. *Reactive carbon-chain molecules: Synthesis of 1-diazo-2,4-pentadiyne and spectroscopic characterization of triplet pentadiynylidene ( $H-C\equiv C-\ddot{C}-C\equiv C-H$ )*. *J. Am. Chem. Soc.* **2006**, 128(10): 3291–3302.
- [17] C.D. Ball, M.C. McCarthy, P. Thaddeus. *Laser spectroscopy of the carbon chains  $HC_7H$  and  $HC_9H$* . *Astrophys. J.* **1999**, 523(1): L89–L91.
- [18] C.D. Ball, M.C. McCarthy, P. Thaddeus. *Cavity ringdown spectroscopy of the linear carbon chains  $HC_7H$ ,  $HC_9H$ ,  $HC_{11}H$ , and  $HC_{13}H$* . *J. Chem. Phys.* **2000**, 112(23): 10149–10155.
- [19] H. Ding, T.W. Schmidt, T. Pino, A.E. Boguslawskiy, F. Güthe, J.P. Maier. *Gas phase electronic spectra of the linear carbon chains  $HC_{2n+1}H$  ( $n=3-6,9$ )*. *J. Chem. Phys.* **2003**, 119(2): 814–819.
- [20] R.A. Seburg, R.J. McMahon, J.F. Stanton, J. Gauss. *Structures and stabilities of  $C_5H_2$  isomers: Quantum chemical studies*. *J. Am. Chem. Soc.* **1997**, 119(44): 10838–10845.
- [21] L. Horný, N.D.K. Petraco, H.F. Schaefer III. *Odd carbon long linear chains  $HC_{2n+1}H$  ( $n = 4-11$ ): Properties of the neutrals and radical anions*. *J. Am. Chem. Soc.* **2002**, 124(49): 14716–14720.
- [22] G. Mpourmpakis, M. Mühlhäuser, G.E. Froudakis, S.D. Peyerimhoff. *Importance of multi-reference configuration interaction for  ${}^3\Sigma_u^- \leftarrow X {}^3\Sigma_g^-$  transitions of linear  $HC_7H$* . *Chem. Phys. Lett.* **2002**, 356(3–4): 398–402.
- [23] M. Mühlhäuser, J. Haubrich, S.D. Peyerimhoff. *The electronic spectrum of linear  $HC_9H$* . *Chem. Phys.* **2002**, 280(3): 205–210.
- [24] C. Zhang, Z. Cao, H. Wu, Q. Zhang. *Linear and nonlinear feature of electronic excitation energy in carbon chains  $HC_{2n+1}H$  and  $HC_{2n}H$* . *Int. J. Quantum Chem.* **2004**, 98(3): 299–308.
- [25] M. Mühlhäuser, J. Haubrich, G. Mpourmpakis, A. Mavrandonakis, G.E. Froudakis. *Ab initio MR-Cl investigation of linear  $HC_6H^+$  and  $HC_7H^+$* . *Internet Electron. J. Mol. Des.* **2003**, 2(9): 578–588.
- [26] M. Mühlhäuser, J. Haubrich, S.D. Peyerimhoff. *The electronic spectrum of linear  $HC_9H^+$* . *Int. J. Quantum Chem.* **2004**, 100(1): 53–58.
- [27] P. Freivogel, J. Fulara, D. Lessen, D. Forney, J.P. Maier. *Absorption spectra of conjugated hydrocarbon cation chains in neon matrices*. *Chem. Phys.* **1994**, 189(2): 335–341.
- [28] J. Fulara, M. Grutter, J.P. Maier. *Higher excited electronic transitions of polyacetylene cations  $HC_{2n}H^+$   $n = 2-7$  in neon matrixes*. *J. Phys. Chem. A* **2007**, 111(46): 11831–11836.
- [29] P. Freivogel, J. Fulara, M. Jakobi, D. Forney, J.P. Maier. *Electronic absorption spectra of linear carbon chains in neon matrices. II.  $C_{2n}^-$ ,  $C_{2n}$ , and  $C_{2n}H$* . *J. Chem. Phys.* **1995**, 103(1): 54–59.



- [30] D. Forney, P. Freivogel, J. Fulara, J.P. Maier. *Electronic absorption spectra of cyano-substituted polyacetylene cations in neon matrices*. **J. Chem. Phys.** **1995**, 102(4): 1510–1514.
- [31] Q. Fan, G.V. Pfeiffer. *Theoretical study of linear  $C_n$  ( $n=6-10$ ) and  $HC_nH$  ( $n=2-10$ ) molecules*. **Chem. Phys. Lett.** **1989**, 162(6): 472–478.
- [32] J. Zhang, X. Guo, Z. Cao. *Electronic spectra of the linear polyynes cations  $HC_{2n}H^+$  ( $n = 2-8$ ): An ab initio study*. **J. Chem. Phys.** **2009**, 131(14): 144307/1–7.
- [33] J. Zhang, X. Guo, Z. Cao. *Theoretical studies on structures and electronic spectra of linear  $HC_{2n+1}H^+$  ( $n = 2-7$ )*. **Int. J. Mass Spectrom.** **2010**, 290(2–3): 113–119.
- [34] H. Kuhn. 194. *Elektronengasmodell zur quantitativen Deutung der Lichtabsorption von organischen Farbstoffen I*. **Helv. Chim. Acta** **1948**, 31(6): 1441–1445.
- [35] H. Kuhn. *Free electron model for absorption spectra of organic dyes*. **J. Chem. Phys.** **1948**, 16(8): 840–841.
- [36] H. Kuhn. *A quantum-mechanical theory of light absorption of organic dyes and similar compounds*. **J. Chem. Phys.** **1949**, 17(12): 1198–1212.
- [37] G. Calzaferri. *Particle in a one-dimensional box as a model for the description of conjugated systems*. **Chimia** **1987**, 41(7–8): 248–250.
- [38] D. Zhao, H. Linnartz, W. Ubachs. *The electronic spectrum of the  $C_s-C_{11}H_3$  radical*. **J. Chem. Phys.** **2012**, 136(5): 054307/1–8.
- [39] J. Fulara, A. Nagy, I. Garkusha, J.P. Maier. *Higher energy electronic transitions of  $HC_{2n+1}H^+$  ( $n=2-7$ ) and  $HC_{2n+1}H$  ( $n=4-7$ ) in neon matrices*. **J. Chem. Phys.** **2010**, 133(2): 024304/1–9.



*“Many years later, as he faced the firing squad,  
Colonel Aureliano Buendía was to remember that distant afternoon  
when his father took him to discover ice.”*  
Gabriel García Márquez (b. 1927), *One Hundred Years of Solitude*

# 4

## ON THE C<sub>7</sub>H<sub>7</sub><sup>+</sup> BENZYLIIUM/TROPYLIUM ION DICHOTOMY

---

In this chapter, the investigations of open-chain hydrocarbons are extended to aromatics. This was preceded by and partially thanks to the recording of a variety of simple organic precursors ([Chapter 5](#) and [Appendix A](#)). Specifically, two of the smallest representatives of cyclic structures with  $4x + 2$  valence electrons were targeted at first, and electronic absorption spectra of mass-selected benzylium (Bz<sup>+</sup>) and tropylium (Tr<sup>+</sup>) cations embedded in solid neon are reported herein. These are the first vibrationally resolved electronic spectra of these two species, serving as a reliable starting point for high-resolution, gas-phase investigations. They reveal a weak,  $(1)^1B_1 \leftarrow \tilde{X}^1A_1$  visible and a much stronger,  $(1)^1A_1 \leftarrow \tilde{X}^1A_1$  UV transition for Bz<sup>+</sup> (*C*<sub>2v</sub> symmetry), and the lowest dipole-allowed,  $^1A_2'' \leftarrow \tilde{X}^1A_1'$  absorption in the UV for Tr<sup>+</sup> (*D*<sub>7h</sub>).

### 4.1 INTRODUCTION

C<sub>7</sub>H<sub>7</sub><sup>+</sup> hydrocarbon cations have been the focus of attention ever since Tr<sup>+</sup> was predicted to be highly stable. [1,2] It fulfills Hückel's rule and is the most common textbook example for aromaticity after benzene. However, the rivalry with its energetically close-lying isomer, Bz<sup>+</sup>, still poses diverse challenges ([Figure 4.1](#)). For instance, physical organic chemists have been debating the mass spectrometry data regarding the formation and automerization pathways of these two species generated upon electron impact, photodissociation, ionization/charge transfer or collisional activation of precursors such as toluene, halotoluenes, benzyl derivatives or cycloheptatriene (CHT). [3–9] Detection schemes were based mainly on the reactivity difference of Bz<sup>+</sup> and Tr<sup>+</sup> in ion–molecule reactions, in particular with toluene.

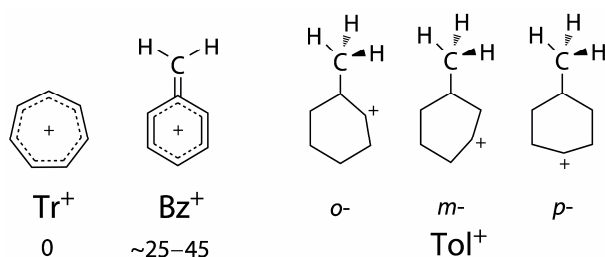
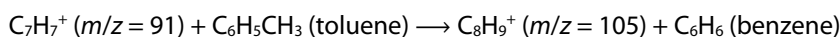


**Figure 4.1:** Left: The two most stable structural isomers of C<sub>7</sub>H<sub>7</sub><sup>+</sup> with their relative energy (kJ mol<sup>-1</sup>), taken from Refs. [9–17]. The three tolylium cations (CH<sub>3</sub>C<sub>6</sub>H<sub>4</sub><sup>+</sup>) on the right are significantly higher in energy, by ~200 kJ mol<sup>-1</sup> or more. [12–15]

It is assumed from branching ratios and heats of formation that the process



proceeds only if the reacting partner is Bz<sup>+</sup>; it is ‘inactive’ for Tr<sup>+</sup>. [3] The results from these kinetic studies have been, however, often inconsistent depending on the experimental method. Complications arise primarily due to the fact that the energy of these two ions is computed to differ only by 0.2–0.5 eV (Tr<sup>+</sup> being the global minimum); [9–17] furthermore, the activation barrier for unimolecular isomerization is low (~3 eV) and believed to involve a large variety of transition states. [9–12]

Straightforward structural information can be obtained by spectroscopic means, and even though such studies on C<sub>7</sub>H<sub>7</sub><sup>+</sup> date back sixty years, it is a far less explored alternative to the mass spectrometric investigations. The first reported Tr<sup>+</sup> spectrum revealed a broad UV absorption in a low-pH water solution of its bromide salt. [18] The following decades have produced only a sparse number of further experimental results on the excited states of the cations in question, including photoelectron spectroscopy for Tr<sup>+</sup>; [19] whereas direct absorption in acidic solutions, [20–22] pulse radiolysis (PR) [23–25] and laser flash photolysis (LFP) [26,27] in liquids, and a photoionization (PI) study in an argon matrix [28] were used to determine Bz<sup>+</sup> electronic transitions. Despite these efforts, the spectroscopic knowledge of C<sub>7</sub>H<sub>7</sub><sup>+</sup> is ambiguous, which is well illustrated by the fact that the nine studies on Bz<sup>+</sup> listed above assign all kinds of spectral features at about every 30 nm in the 300–500 nm window to this species. [20–28] For the first time, *reliable* electronic absorption spectra of Bz<sup>+</sup> and Tr<sup>+</sup>, recorded after mass-selective trapping of cations in 6 K neon matrices, are presented here.

## 4.2 VISIBLE SPECTRA

Figure 4.2a shows the absorption spectrum obtained after deposition of mass-selected  $C_7H_7^+$  ions produced from CHT as precursor into a neon matrix. It is dominated by an extended series of broad bands between ca. 400–520 nm. Several sharp peaks commencing at ~450 nm are imposed onto them. The use of toluene, benzyl chloride (BzCl) or 1,6-heptadiyne as starting material resulted in essentially the same spectra. The broad features lose and the sharp ones gain intensity upon broadband UV irradiation of the matrix, whereas no additional bands appear (Figure 4.2b). UV photons induce electron recombination in the matrix (Chapter 2); hence, the decreasing bands are due to cations, while the ones growing belong to neutral species.

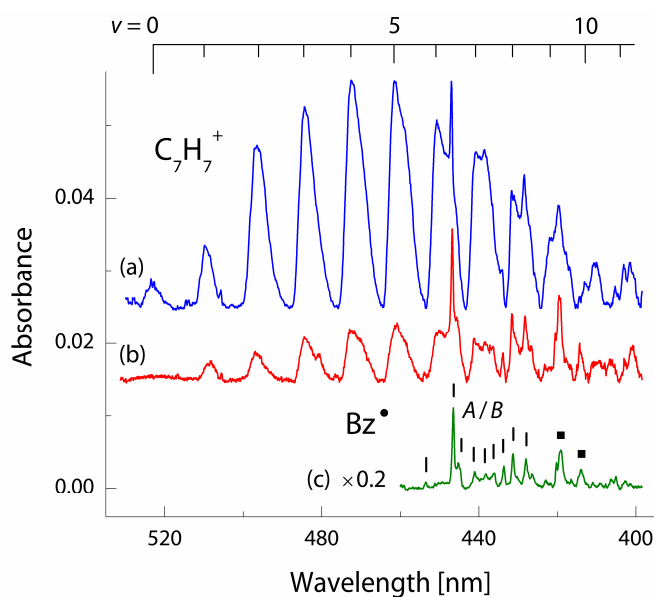


**Figure 4.2:** Electronic spectrum observed in the visible spectral region after: (a) deposition of mass-selected  $C_7H_7^+$  ions produced from CHT into a 6 K neon matrix (vibrational progression in the  $\nu_{13}$  fundamental of  $Bz^+$  is given above) and (b) subsequent UV irradiation of the matrix. Deposition of the cations without using an electron scavenger (trace c) results in rapid charge neutralization and the formation of benzyl radical,  $Bz^\bullet$  (indicated are the known, vibronically coupled  $\tilde{A}^2A_2 / \tilde{B}^2B_2 \leftarrow \tilde{X}^2B_2$  transitions). [29–33] Note that the ionic bands in the latter case are absent and the spectrum was downscaled for comparison. Squares mark absorptions likely due to a different  $C_7H_7^\bullet$  isomer (Section 4.6).

The system of narrow bands with the strongest peak at 447 nm is recognized to contain the visible spectrum of the benzyl neutral radical (Bz<sup>•</sup>), reported from low-temperature matrices [29–31] and in the gas phase. [32,33] Although chloromethane, which works as an electron scavenger (Chapter 2), was added to the neon host, the bands of Bz<sup>•</sup> are weakly seen in Figure 4.2a. They result from partial charge neutralization of the deposited C<sub>7</sub>H<sub>7</sub><sup>+</sup> cations. Scavengers suppress neutralization by capturing free electrons and equilibrating space charge that develops from cation accumulation during matrix growth (Chapter 2). [34] In experiments carried out without CH<sub>3</sub>Cl (Figure 4.2c), the bands of Bz<sup>•</sup> are stronger than in spectra recorded with the scavenger; the absence of the broad, structured absorptions of Figure 4.2a is a further indication of the cationic nature of their carrier.

For these reasons and because a mass-selective method was used for cation trapping, the new electronic absorption system (Figure 4.2a) with an origin band at 523 nm belongs to C<sub>7</sub>H<sub>7</sub><sup>+</sup>. Furthermore, depositing the ions with the smallest kinetic energy possible quenched the C<sub>7</sub>H<sub>7</sub><sup>+</sup> fragmentation at the surface—neither C<sub>5</sub>H<sub>5</sub><sup>+</sup>, the easiest accessible channel as shown by dissociation techniques, [35,36] nor a number of other small fragment species that were studied in this laboratory (Appendix A), [37] appeared in any of the experiments.

The visible system of C<sub>7</sub>H<sub>7</sub><sup>+</sup> has a regular, bell-like Franck–Condon (FC) profile (Figure 4.2a). It is formed by a number of bands separated from each other by ~510 cm<sup>-1</sup>. Its maximum lies around 460–470 nm and corresponds to 4 or 5 quanta excitation of the mode above in the upper electronic state. The intensity of the system normalized to the same deposited charge of C<sub>7</sub>H<sub>7</sub><sup>+</sup> does not depend on the precursor used for cation production; therefore, the structure of the C<sub>7</sub>H<sub>7</sub><sup>+</sup> species can not be deduced from the topology of the precursor molecules.

### 4.3 UV RANGE

Apart from the visible systems shown in Figure 4.2, several absorptions have been detected in the UV range (Figure 4.3a). The bands marked with arrows and asterisks decreased upon UV irradiation of the matrix and thus have cationic origin; the others stem from neutral species because they gained intensity under the same conditions (Figure 4.3b). The neutral absorptions with onsets around

305 and 248 nm are identical with the literature UV spectrum of  $\text{Bz}^\bullet$ ; [29–31,38–42] they arise from its  $\tilde{C}^2\text{A}_2 \leftarrow \tilde{X}^2\text{B}_2$  and  $\tilde{D}^2\text{B}_2 \leftarrow \tilde{X}^2\text{B}_2$  transitions. In the present study, due to the high intensity of the  $\tilde{C}^2\text{A}_2 \leftarrow \tilde{X}^2\text{B}_2$  system of  $\text{Bz}^\bullet$ , it was possible to detect several weak vibrational bands not reported in earlier studies. Positions of the band maxima and their assignment are collected in Table 4.1. The strong absorptions of  $\text{Bz}^\bullet$  obscure bands of the cations. To better visualize the features originating from  $\text{C}_7\text{H}_7^+$ , absorptions of the radical species (Figure 4.3b) have been subtracted, after proper scaling, from the spectrum shown in Figure 4.3a. The resulting trace is Figure 4.3c.

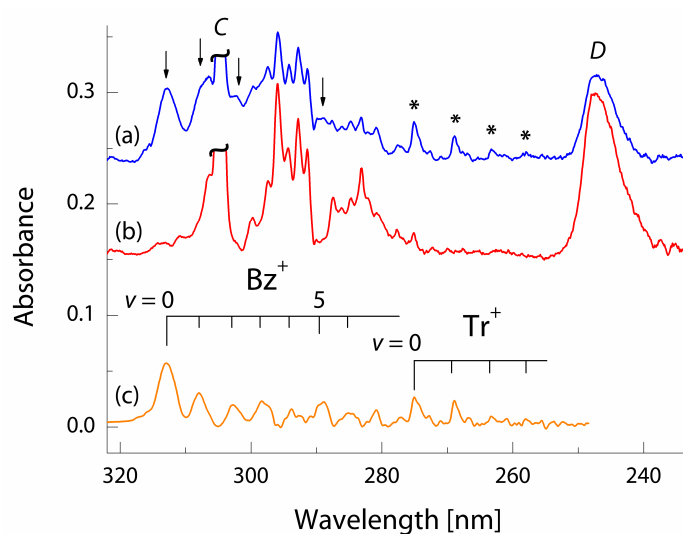


**Figure 4.3:** Electronic spectra in the UV observed after: (a) deposition of  $\text{C}_7\text{H}_7^+$  and (b) photobleaching the matrix. Bands labeled C and D belong to known transitions of  $\text{Bz}^\bullet$ ; [29–31,38–42] while asterisks and arrows mark cationic absorptions. In (c), trace b was subtracted from trace a after scaling it by an appropriate factor to match the intensity of band C.

Two band systems of  $\text{C}_7\text{H}_7^+$  can be discerned in Figure 4.3c. The first comprises broad, regularly-spaced ( $\sim 510 \text{ cm}^{-1}$ ) absorptions starting at 313 nm. The second one with an onset at 275 nm is formed by narrower bands separated by  $\sim 840 \text{ cm}^{-1}$ . The relative intensity of these two systems varies with the precursors used for the production of  $\text{C}_7\text{H}_7^+$  cations; however, the absorptions in the visible with an onset around 523 nm and the UV system at 313 nm preserve the same ratio using different starting materials, indicating a common origin. The absorptions commencing at 275 nm were almost absent in the case of  $\text{BzCl}$ , while the visible

system and that in the UV at 313 nm were quite strong. Therefore, it is concluded that the former and the two latter systems originate from two isomers of C<sub>7</sub>H<sub>7</sub><sup>+</sup>. Moreover, the fact that only one isomer was produced from BzCl indicates that this is Bz<sup>+</sup>, because using benzyl chloride for the generation of C<sub>7</sub>H<sub>7</sub><sup>+</sup> ensures the mildest discharge conditions in the ion source. It is expected that the C–Cl bond dissociates readily, leading to Bz<sup>•</sup>, which then forms Bz<sup>+</sup> upon ionization. Concluding, the band systems with onsets near 523 and 313 nm belong to Bz<sup>+</sup>.

**Table 4.1:** Observed band maxima ( $\lambda_{\text{Ne}} \pm 0.1$  nm) of electronic transitions of the benzyl radical compared with previous studies  $\lambda_{\text{air}}$ , and their assignments

$\lambda_{\text{Ne}}$ [nm]	$\lambda_{\text{air}}$ [nm]	$\tilde{\nu}^{\text{[a]}}$ [cm <sup>-1</sup> ]	$\Delta\tilde{\nu}$ [cm <sup>-1</sup> ]	Assignment
454.1	454.5	22 022	0	$0_0^0 \bar{A}^2A_2 / \bar{B}^2B_2 \leftarrow \bar{X}^2B_2^{\text{[b]}}$
447.0	447.9 / 446.7	22 371	349	$A^1 / A^2$
445.7	445.8	22 437	415	$6 a_0^1$
441.6	442.2	22 645	623	$A^3$
438.7	439.3	22 795	773	$B^3$
436.5	437.0	22 910	888	$A^4$
434.3	434.8	23 026	1004	$A^5$
	433.7			$A^6$
431.9	432.8	23 154	1132	$A^7$
428.5	429.4 / 429.3	23 337	1315	$A^8 / A^9$
305.4	305.2	32 744	0	$0_0^0 \bar{C}^2A_2 \leftarrow \bar{X}^2B_2^{\text{[c]}}$
300.5	300.4	33 278	534	$v_{13}$
297.7	297.9	33 591	847	$v_{12}$
296.5	296.7 / 296.4	33 727	983	$v_{11}$
294.9	294.8	33 910	1166	$v_9$
293.5	293.7	34 072	1328	$v_8$
292.1	292.2	34 235	1491	$v_{13} + v_{11}$
288.0		34 722	1978	$2v_{11}$
286.6		34 892	2148	$v_{11} + v_9$
285.1		35 075	2331	$2v_9$
283.6		35 261	2517	$v_8 + v_9$
282.5		35 398	2654	$v_{13} + v_{11} + v_9$
281.2		35 562	2818	
278.2		35 945	3201	
275.7		36 271	3527	
273.2		36 603	3859	$2v_8 + v_9$
247.5	253.0 <sup>[d]</sup>	40 404	0	$0_0^0 \bar{D}^2B_2 \leftarrow \bar{X}^2B_2$

[a]  $\tilde{\nu}$  is calculated as  $1/\lambda_{\text{Ne}}$ , thereby—for there are more influential matrix effects such as band shifts and inhomogeneous broadening—neglecting refractive indices of neon and air, and dispersion. [b] Bz<sup>•</sup> exhibits strong vibronic coupling in its nearly degenerate  $\bar{A}^2A_2$  and  $\bar{B}^2B_2$  electronic states—see Ref. [32] for labeling of the bands of the transition in the visible. [c] Bands of the near UV system are assigned tentatively after Ref. [38] and theoretical calculations similar to those for the investigated cations (see text). [d] Ref. [42].



## 4.4 COMPUTATIONAL SUPPORT

In order to support an interpretation, ground-state energy and vibrational frequencies of the two lowest-lying isomers of  $C_7H_7^+$ ,  $Tr^+$  and  $Bz^+$ , have been calculated with DFT at the BLYP/6-311G(d,p) level of theory. Results are included as footnote [a] in Table 4.2. They confirm earlier studies that  $Tr^+$  is the most stable form of  $C_7H_7^+$ ;  $Bz^+$  lies 42 kJ mol<sup>-1</sup> above the global minimum. Although thermal equilibrium in the source during the production of the ions may not be reached, tolylium cations ( $CH_3C_6H_4^+$ , Figure 4.1) and adventitious open-chain or bicyclic structures are excluded from consideration on the basis that they are significantly higher in energy than  $Tr^+$  and  $Bz^+$ . [12–15]

The lowest-frequency totally symmetric vibrational fundamental of  $Bz^+$  (in  $C_{2v}$ ) is  $\nu_{13}$  at 523 cm<sup>-1</sup>, a benzene ring distortion mode, which is in agreement with the ~510 cm<sup>-1</sup> mode observed in both the visible and UV spectra of  $Bz^+$  (Table 4.2).  $Tr^+$  ( $D_{7h}$  symmetry) has only two totally symmetric fundamentals,  $\nu_1 = 3113$  (C–H stretch) and  $\nu_2 = 847$  cm<sup>-1</sup> (ring breathing). The absorption system of  $C_7H_7^+$  with an origin at 275 nm shows a simple progression of energy ~840 cm<sup>-1</sup> (Table 4.2). Therefore, this system is likely due to  $Tr^+$ .

More relevant to the present experimental studies are the excitation energies of  $Bz^+$  and  $Tr^+$ . They were calculated using time-dependent (TD) DFT method with the BLYP functional and the 6-311G(d,p) basis set. Results of these calculations are collected in Table 4.2. For  $Bz^+$ , a moderately intense electronic transition is predicted in the visible around 453 nm (oscillator strength  $f \approx 0.02$ ), which is within the expected vicinity of the origin band at 523 nm using the TD DFT method. Two other transitions are located in the UV range; the strongest ( $f \approx 0.2$ ) near 281 nm and a very weak one ( $f \approx 0.0002$ ) around 277 nm. The calculated excitation energy of the UV transition of  $Bz^+$  at 281 nm matches well the origin observed at 313 nm. The integrated intensity of the band system with an onset at 523 nm is about 5 times less than that of the UV one with origin at 313 nm; the calculations give an intensity ratio of the visible to the UV transition of 12. Based on these theoretical results, the absorptions starting at 523 and 313 nm are assigned to the  $(1)^1B_1 \leftarrow \tilde{X}^1A_1$  and  $(1)^1A_1 \leftarrow \tilde{X}^1A_1$  transitions of  $Bz^+$ , respectively.

TD DFT computations carried out on Tr<sup>+</sup> (Table 4.2) revealed two allowed electronic transitions from the  $\tilde{X}^1A_1'$  ground state; a weaker one ( $f \approx 0.002$ ) around 225 nm to a  $^1A_2''$  state and a much stronger ( $f \approx 0.6$ ) around 202 nm to one with  $^1E_1'$  symmetry. If the absorptions with onset at 275 nm originate from Tr<sup>+</sup>, then the calculations overestimate its excitation energy by  $\sim 1$  eV. This discrepancy can partially result from the fact that calculations give the vertical excitation energy; the other reason could be a multi-reference character of the  $^1A_2''$  state. The predicted  $^1E_1' \leftarrow \tilde{X}^1A_1'$  transition around 202 nm could not be detected in the present study due to strong light scattering precluding measurements there.

From a theoretical point of view, it is to be noted that by setting up the Hückel determinants of Bz<sup>+</sup> and Tr<sup>+</sup>, and numerically solving the corresponding polynomial equation, a good approximation for the first allowed transition of these two species can be given. For example, the secular equation of Bz<sup>+</sup> would take the form

$$\|B_{\mu\nu} - \delta_{\mu\nu}x\| = \begin{vmatrix} -x & 1 & 0 & 0 & 0 & 0 & 0 \\ 1 & -x & 1 & 0 & 0 & 0 & 1 \\ 0 & 1 & -x & 1 & 0 & 0 & 0 \\ 0 & 0 & 1 & -x & 1 & 0 & 0 \\ 0 & 0 & 0 & 1 & -x & 1 & 0 \\ 0 & 0 & 0 & 0 & 1 & -x & 1 \\ 0 & 1 & 0 & 0 & 0 & 1 & -x \end{vmatrix} = 0 \quad , \quad (4.1)$$

where  $\mathbf{B} = [B_{\mu\nu}]$  is the Hückel 'incidence' matrix,  $\mu, \nu = 1, \dots, Z$  run over the carbon atoms ('aromatic centers') of the system (Figure 4.4, top right),  $\delta_{\mu\nu}$  stands for the Kronecker delta and  $x = (\varepsilon - \alpha)/\beta$ . The expanded polynomial is of the seventh degree and provides the roots  $x_J = +2.101, +1.259, +1.000, 0.000, -1.000, -1.259$  and  $-2.101$ . A similar procedure for Tr<sup>+</sup> results in the following solutions to the eigenvalue coefficients:  $x_J = +2.000, +1.247$  (2 $\times$ ),  $-0.445$  (2 $\times$ ) and  $-1.802$  (2 $\times$ ). Using the formula  $\varepsilon_J = \alpha + x_J \beta$  ( $J = 1, \dots, Z$ ) for the energy levels and taking an estimated resonance integral of *benzene*,  $|\beta| := 20\,000 \text{ cm}^{-1}$ , the HOMO  $\rightarrow$  LUMO transition of Bz<sup>+</sup> and Tr<sup>+</sup> are predicted at 500 and 294 nm (Figure 4.4), not unreasonable compared to the observed values of 523 and 275 nm, respectively. In fact, they are in a significantly better agreement with the experimental results than the DFT values (Table 4.2); however, this is not the case for and upward from the second allowed transition.

**Table 4.2:** Observed band maxima ( $\lambda_{\text{Ne}} \pm 0.1$  nm) of electronic transitions of  $\text{C}_7\text{H}_7^+$  cations and their assignments. The results are compared with computed vertical excitation energies  $\Delta E$  and transition oscillator strengths  $f$  (*italic*) from the ground- to the lowest excited states.

$\lambda_{\text{Ne}}$ [nm]	$\Delta E^{[a]}$ [eV] ( <i>f</i> )	$\tilde{\nu}^{[b]}$ [ $\text{cm}^{-1}$ ]	$\Delta\tilde{\nu}$ [ $\text{cm}^{-1}$ ]	Assignment <sup>[c]</sup>
<b>Bz<sup>+</sup></b>				
523.2 <sup>[d]</sup>	2.73 ( <i>0.0193</i> )	19 113	0	$0_0^0$ ( $1^1\text{B}_1 \leftarrow \tilde{X}^1\text{A}_1$ )
509.6		19 623	510	$\nu_{13}$ (ring distortion)
496.3		20 149	1036	$2\nu_{13}$
484.1		20 657	1544	$3\nu_{13}$
472.3		21 173	2060	$4\nu_{13}$
461.4		21 673	2560	$5\nu_{13}$
450.7		22 188	3075	$6\nu_{13}$
440.6		22 696	3583	$7\nu_{13}$
430.5		23 229	4116	$8\nu_{13}$
421.1		23 747	4634	$9\nu_{13}$
410.2		24 378	5265	$10\nu_{13}$
402.9		24 820	5707	$11\nu_{13}$
312.9	4.42 ( <i>0.2257</i> )	31 959	0	$0_0^0$ ( $1^1\text{A}_1 \leftarrow \tilde{X}^1\text{A}_1$ )
308.0		32 468	509	$\nu_{13}$
303.0		33 003	1044	$2\nu_{13}$
298.4		33 512	1553	$3\nu_{13}$
293.8		34 037	2078	$4\nu_{13}$
289.3		34 566	2607	$5\nu_{13}$
285.0		35 088	3129	$6\nu_{13}$
<b>Tr<sup>+</sup></b>				
280.8		35 613	-737	
275.1	5.51 ( <i>0.0024</i> )	36 350	0	$0_0^0$ ( $1^1\text{A}_2'' \leftarrow \tilde{X}^1\text{A}_1'$ )
268.9		37 189	839	$\nu_2$ (ring breathing)
263.3		37 979	1629	$2\nu_2$
258.0		38 760	2410	$3\nu_2$

[a] Transition energies were obtained from TD DFT calculations at the BLYP/6-311G(d,p) level of theory. For  $\text{Tr}^+$ , excited states were assumed to keep the  $D_{7h}$  molecular symmetry; however, they may be affected by Jahn–Teller distortion and split into  $C_{2v}$  resonance structures (see Refs. [43,44] for the case of the tropyli neutral radical). [b] See footnote a of Table 4.1. [c] Vibrational assignment in the excited states is based on totally symmetric modes ( $\text{cm}^{-1}$ ) in the ground state of  $\text{Bz}^+$  ( $a_1$  in  $C_{2v}$ ): 3137, 3119, 3112, 3070, 1605, 1538, 1456, 1346, 1183, 990, 975, 798, 523; and of  $\text{Tr}^+$  ( $a_1'$  in  $D_{7h}$ ): 3113, 847; obtained with DFT at the BLYP/6-311G(d,p) level of theory. Energies ( $E_h$ , not corrected for ZPE) are as follows: -270.603 38 ( $\text{Bz}^+$ ) and -270.619 28 ( $\text{Tr}^+$ ). [d] See Section 4.6 for fluorescence data.

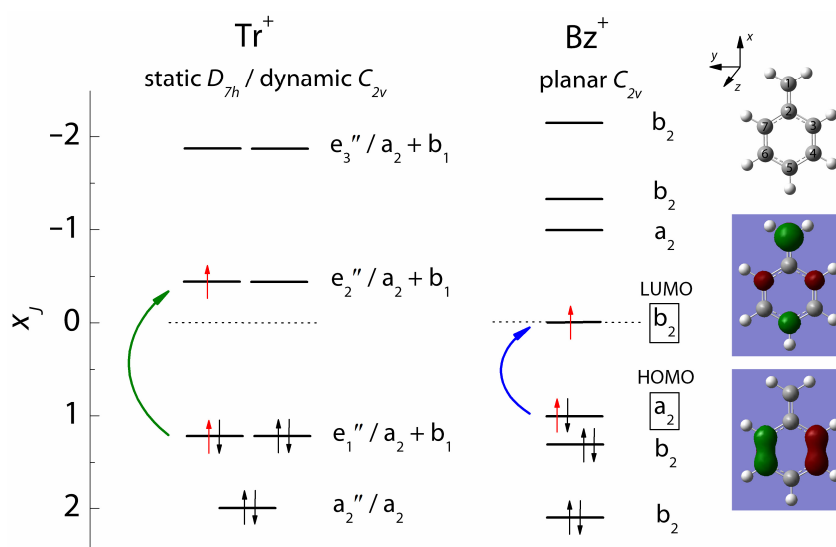


**Figure 4.4:** Hückel MO diagram of tropylium and benzylium. The first allowed transitions are marked by *green* and *blue* arrows, respectively. On the *far right*, the isosurfaces of the HOMO and LUMO of Bz<sup>+</sup> are shown in color; they imply charge redistribution upon electron promotion and a geometry change in the excited state.

#### 4.5 EARLIER EXPERIMENTAL RESULTS

A photoelectron study on the tropyli radical, generated by the pyrolysis of bitropyli, revealed that the first excited state of Tr<sup>+</sup> is <sup>3</sup>E<sub>3</sub>', lying 3.4 eV higher than the ground state. [19] Upon examination of the reported spectrum, there is another band spaced ~4.4 eV (~284 nm) above the ground state of the cation; it agrees well with the origin of the second isomer of C<sub>7</sub>H<sub>7</sub><sup>+</sup> observed at 275 nm. Hence, results of that study validate the present quantum chemical calculations and lead to the conclusion that the absorptions with an onset at 275 nm originate from Tr<sup>+</sup>. Furthermore, the reported UV spectrum of Tr<sup>+</sup> in strong acidic solutions has a maximum at 275 nm. [18,36]

UV electronic transitions of Bz<sup>+</sup> have been studied in the past using different methods: low-pH solutions, [20–22] PR [23–25] and LFP [26,27] in liquids, and PI in solid argon. [28] The spectra obtained did not agree with each other. The most plausible results were obtained at room-temperature (RT) in a PR experiment on liquid BzCl containing O<sub>2</sub>, ethanol or pyrrole as radical or ion interceptors; [23] these quenched the transient absorptions to a different extent. Two broad,

structureless absorptions of  $\text{Bz}^+$  with maxima at 304 (strongest) and 500 nm have been reported. [23] The spectrum agrees well with the present matrix data; however, neon is a less perturbing environment and reveals well-resolved vibrational structure (Figure 4.5).

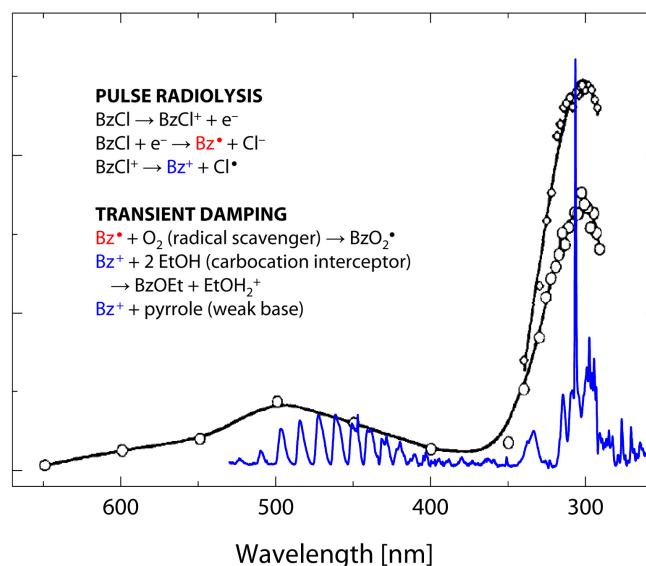


**Figure 4.5:** A pulse radiolysis experiment of liquid  $\text{BzCl}$  at RT (black trace) [23] compared to the UV/Vis transitions of  $\text{Bz}^+$  and  $\text{Bz}^\bullet$  in solid neon (blue, this study). The process equations and the reactions involved in the scavenging of the short-lived species as employed in the PR paper are indicated.

#### 4.6 CONCLUDING REMARKS

In summary, the two most stable  $\text{C}_7\text{H}^+$  isomers,  $\text{Bz}^+$  and  $\text{Tr}^+$ , were trapped and identified in neon matrices. Hitherto, electronic spectroscopy of these species was not fully understood. This study, drawing on the advantages of a combination of mass selection with matrix isolation, revealed a weak,  $(1)^1\text{B}_1 \leftarrow \tilde{\text{X}}^1\text{A}_1$  and a much stronger,  $(1)^1\text{A}_1 \leftarrow \tilde{\text{X}}^1\text{A}_1$  transition for  $\text{Bz}^+$ , and the lowest dipole-allowed,  $^1\text{A}_2'' \leftarrow \tilde{\text{X}}^1\text{A}_1'$  absorption for  $\text{Tr}^+$ . The findings described here were published (in a slightly different form) in the *Angewandte Chemie International Edition*. [45]

Recently, a paper has appeared on the simulation of FC profiles for closed-shell, PAH-related cations including  $\text{Bz}^+$  and whether these species could be held responsible for some DIBs. [46] The agreement between the computed spectrum

and the experimental trace in Figure 4.2a is excellent (Figure 4.6). However, their conclusion is that the large FC envelope of Bz<sup>+</sup> is inconsistent with DIBs and such cations larger than fluorenylium (triple-ring system with the constitutional formula C<sub>13</sub>H<sub>9</sub><sup>+</sup>) may only have the spectral properties (excitation and ionization energies, and low FC activity) required to carry DIBs. Nevertheless, a detailed gas-phase analysis of especially the weak, (1)<sup>1</sup>B<sub>1</sub> ←  $\tilde{X}^1$ A<sub>1</sub> visible system of Bz<sup>+</sup> is called for.

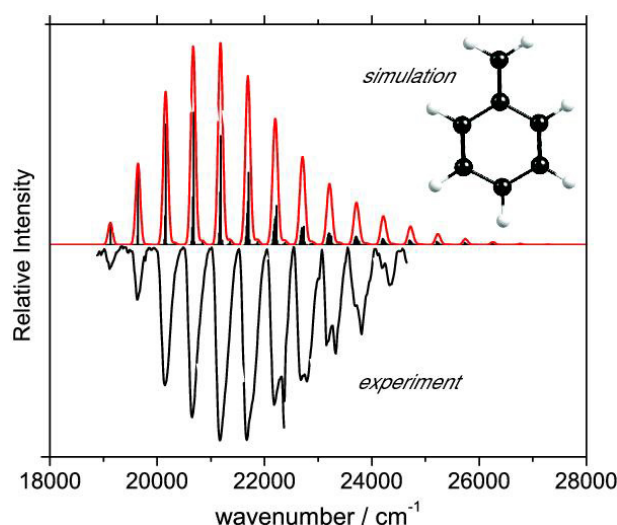


**Figure 4.6:** Top: Calculated FC profile of the S<sub>1</sub> ← S<sub>0</sub> transition of Bz<sup>+</sup>, depicted as sticks convolved with a 100 cm<sup>-1</sup> FWHM Gaussian profile (red) Bottom: The experimental trace from Figure 4.2a. The figure is reproduced from Ref. [46].

There are three additional aspects worth mentioning here. First, effort was dedicated to the assignment of some additional features in the red part of the visible spectrum (Figure 4.7a). The onset is around 801 nm with the ‘main’ vibrational progression taking place in ~1560 cm<sup>-1</sup> (methylene, conjugated C–C or aromatic C=C stretch) in the excited state; they did not grow or decay upon UV irradiation, which indicates their neutral origin (Chapter 2). These absorptions were weakly present in most experiments; however, they were about 2–3× stronger when 1,6-heptadiyne was used as the precursor of C<sub>7</sub>H<sub>7</sub><sup>+</sup>. The bands do not belong to Bz<sup>+</sup>, Tr<sup>+</sup> or their neutral counterparts because of intensity disrelations with assigned systems of these species; their origin as fragmentation products could also be ruled out. [37] Thus, the features are tentatively inferred

as being caused by a neutral  $C_7H_7^\bullet$  isomer which results from a ring-opening reaction in combination with charge neutralization upon some  $C_7H_7^+$  arriving at the matrix surface. Although DFT calculations performed on the ground-state energy and electronic transitions of a number of such structural possibilities could narrow down the options to a few isomers (Figure 4.7a, inset), the best predictions for an excitation came around 550–650 nm ( $\Delta \sim 0.4\text{--}0.7$  eV) and it would be speculative to assign the absorptions based on such an amount of information. Similar ambiguity is posed by assignment attempts of features to  $Tr^\bullet$ , one group of strong candidates being those marked by squares in Figure 4.2a, starting at ca. 420 nm. These bands seem not to belong to  $Bz^\bullet$  on the basis of gas-phase investigations; [32,33] however, an electronic transition of  $Tr^\bullet$  ( ${}^2E_3'' \leftarrow \tilde{X}{}^2E_2''$ ) as reported by REMPI at 388.8 nm [47] is far off to be due to a ‘common’ matrix/gas-phase shift. The question as to the origin of both these spectral features is left open.

Secondly, in the course of the continuous development of the apparatus, fluorescence studies became possible (Chapter 2). The spectrum of  $C_7H_7^+$  was thereby re-measured and  $Bz^+$  was found to *weakly* emit ( $S_1 \rightarrow S_0$ ) upon the excitation to its first excited state (e.g., at 461.4 nm—below that  $Bz^\bullet$  starts to fluoresce particularly strong and complex), with event counts an order of magnitude or more lower than for  $C_{11}H_9^+$  (Chapter 5) or protonated PAHs (Appendix A). [48] Nevertheless, two broad emission bands around 512 and 538 nm were clearly seen (not shown as separate figure). This suggests that the origin band of the  $(1){}^1B_1 \leftarrow \tilde{X}{}^1A_1$  transition of  $Bz^+$  may in fact be that at ca. 510 nm and not the one located  $\sim 523$  nm (Table 4.2); the latter would then be an artifact present in a dozen experiments carried out on this species. Also, the difference between the two observed fluorescence features, about  $950\text{--}980\text{ cm}^{-1}$ , is lower than  $2 \times 510\text{ cm}^{-1}$ ; this implies different modes being perhaps active in the ground than in the excited state. Such a hint is carried by the asymmetric profile of some of the bands of this system (Figure 4.2a); however, this latter may simply be due to inhomogeneous broadenings in neon.

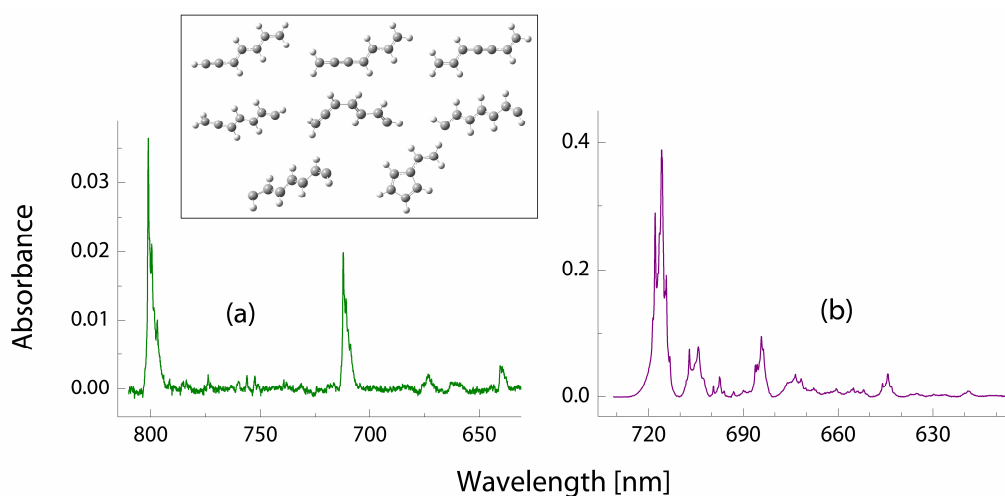


**Figure 4.7:** Additional electronic spectra related to the present Bz<sup>+</sup>/Tr<sup>+</sup> study. (a) Neutral absorptions observed after depositing C<sub>7</sub>H<sub>7</sub><sup>+</sup> produced from 1,6-heptadiyne into neon. Some possible C<sub>7</sub>H<sub>7</sub><sup>+</sup> structures perhaps responsible for the spectrum are shown in the inset. (b) Electronic absorption spectrum recorded after the trapping of C<sub>6</sub>H<sub>5</sub>SiH<sub>2</sub><sup>+</sup> (*m/z* = 107) cations using phenylsilane as the precursor and subsequent bleaching of the sample.

The third point was a project initiative: the measurement of a ligand heteroatom series with the constitutional formula C<sub>6</sub>H<sub>5</sub>X<sup>+</sup>, X being SiH<sub>2</sub>, NH, PH, O or S. The common feature in these species is that they are (valence) isoelectronic with Bz<sup>+</sup>. They contain Group 14–16 elements, which—depending on their electronegativity and size (Table 4.3)—could provide general information of aromatic characteristics. Such measures include assessment of the kinetic stability/reactivity by the so-called absolute chemical hardness,  $\eta = (\epsilon_{\text{LUMO}} - \epsilon_{\text{HOMO}})/2$ , [49] or of the relative aromaticity via the nucleus-independent chemical shift. [50] Suitable precursors such as aniline, phenol or phenylsilane are commercially available. Because the (1)<sup>1</sup>B<sub>1</sub> ←  $\tilde{X}$ <sup>1</sup>A<sub>1</sub> transition of Bz<sup>+</sup> is along the C<sub>2</sub> axis ( $\Gamma(\hat{\mu})$  is of B<sub>1</sub> symmetry, corresponding to the *x*-direction translation) and the lowest-energy vibrational mode corresponds to a ‘swimming’ motion on this axis, there is no reason to assume that the absorption features would not come around the same place in the spectra of these analog species. Calculations confirm these expectations (Table 4.3). Especially promising was the C<sub>6</sub>H<sub>5</sub>NH<sup>+</sup> ion which shows a broad, structureless absorption centered at ~500 nm and ca. ±100 nm in breadth, [51] greatly resembling the solution data from the PR study on Bz<sup>+</sup>. [23]



A number of depositions were done for  $X = \text{SiH}_2$ ,  $\text{NH}$  and  $\text{O}$  with reasonable ion currents; however, the only useful spectrum was recorded depositing  $\text{C}_6\text{H}_5\text{SiH}_2^+$  (Figure 4.7b). It shows an electronic system with a strong, structured onset at  $\sim 718$  nm and an extended vibrational progression. It is of neutral origin, because it grew upon mpHg bleaching. Since it is present in the same, red region of the spectrum as the unassigned  $\text{C}_7\text{H}_7^{\bullet}$  feature (Figure 4.7a), it is likely to have a similar, open-chain structure. This, unfortunately, could not be deduced from a short REMPI confirmation attempt. [52]

**Table 4.3:** Comparison of  $\text{C}_6\text{H}_5\text{X}^+$  species valence isoelectronic with  $\text{Bz}^{+[\text{a}]}$

Group 14 ( $\text{C}_{2v}, \tilde{X}^1\text{A}_1$ )			Group 15 (planar $\text{C}_s, \tilde{X}^1\text{A}'$ )			Group 16 ( $\text{C}_{2v}, \tilde{X}^1\text{A}_1$ )		
$\chi$	$r_c$ [Å]	$\Delta E^{(1)}$ [eV] ( <i>f</i> )	$\chi$	$r_c$ [Å]	$\Delta E^{(1)}$ [eV] ( <i>f</i> )	$\chi$	$r_c$ [Å]	$\Delta E^{(1)}$ [eV] ( <i>f</i> )
$\text{C}_6\text{H}_5\text{CH}_2^+$			$\text{C}_6\text{H}_5\text{NH}^+$			$\text{C}_6\text{H}_5\text{O}^+$		
2.55	0.76	2.73 (0.0193)	3.04	0.71	2.51 (0.0219)	3.44	0.66	2.29 (0.0216)
$\text{C}_6\text{H}_5\text{SiH}_2^+$			$\text{C}_6\text{H}_5\text{PH}^+$			$\text{C}_6\text{H}_5\text{S}^+$		
1.90	1.11	2.47 (0.0043)	2.19	1.07	2.05 (0.0045)	2.58	1.05	1.77 (0.0049)

[a] Indicated are the molecular and ground-state symmetry of the species, Pauling electronegativity  $\chi$  and covalent radius  $r_c$  of the ligand heteroatoms (**bold**), and first allowed transition  $\Delta E^{(1)}$  and corresponding oscillator strength *f* (*italic*) calculated with DFT at the BLYP/6-311G(d,p) level of theory.

These efforts show that although the matrix apparatus is robust for hydrocarbons, additional side effects such as fragmentation, neutralization or rearrangements may overtake the primary role once heteroatoms (other than C and H) are introduced into the molecular systems to be measured (Appendix A), and improvements should be considered (Chapter 7).



## Bibliography

- [1] E. Hückel. *Quantum-theoretical contributions to the benzene problem. I. The electron configuration of benzene and related compounds.* **Z. Physik** **1931**, 70(3–4): 204–286.
- [2] J.L. Franklin, F.H. Field. *The resonance energies of certain organic free radicals and ions.* **J. Am. Chem. Soc.** **1953**, 75(12): 2819–2821.
- [3] C. Lifshitz. *Tropylium ion formation from toluene: Solution of an old problem in organic mass spectrometry.* **Acc. Chem. Res.** **1994**, 27(5): 138–144; and references therein.
- [4] E.-L. Zins, C. Pepe, D. Schröder. *Methylene-transfer reactions of benzylium/tropylium ions with neutral toluene studied by means of ion-trap mass spectrometry.* **Faraday Discuss.** **2010**, 145(0, Frontiers in Physical Organic Chemistry): 157–169.
- [5] M. Malow, M. Penno, K.-M. Weitzel. *The kinetics of methyl loss from ethylbenzene and xylene ions: The tropylium versus benzylium story revisited.* **J. Phys. Chem. A** **2003**, 107(49): 10625–10630.
- [6] M. Schwell, F. Dulieu, C. Gée, H.-W. Jochims, J.-L. Chotin, H. Baumgärtel, S. Leach. *Photoionization mass spectrometry of six isomers of C<sub>7</sub>H<sub>8</sub> in the 7–22 eV photon energy range.* **Chem. Phys.** **2000**, 260(1–2): 261–279.
- [7] S.K. Shin, B. Kim, R.L. Jarek, S.-J. Han. *Product-resolved photodissociations of iodotoluene radical cations.* **Bull. Kor. Chem. Soc.** **2002**, 23(2): 267–270.
- [8] J.H. Moon, J.C. Choe, M.S. Kim. *Kinetic energy release distribution in the dissociation of toluene molecular ion. The tropylium vs benzylium story continues.* **J. Phys. Chem. A** **2000**, 104(3): 458–463.
- [9] T.D. Fridgen, J. Troe, A.A. Viggiano, A.J. Midey, S. Williams, T.B. McMahon. *Experimental and theoretical studies of the benzylium<sup>+</sup>/tropylium<sup>+</sup> ratios after charge transfer to ethylbenzene.* **J. Phys. Chem. A** **2004**, 108(26): 5600–5609.
- [10] K.W. Bullins, T.T.S. Huang, S.J. Kirkby. *Theoretical investigation of the formation of the tropylium ion from the toluene radical cation.* **Int. J. Quantum Chem.** **2009**, 109(6): 1322–1327.
- [11] B.J. Smith, N.E. Hall. *G2(MP2,SVP) study of the relationship between the benzyl and troyl radicals, and their cation analogs.* **Chem. Phys. Lett.** **1997**, 279(3–4): 165–171.
- [12] I.S. Ignatyev, T. Sundius. *Competitive ring hydride shifts and tolyl-benzyl rearrangements in tolyl and silatolyl cations.* **Chem. Phys. Lett.** **2000**, 326(1–2): 101–108.
- [13] S.-J. Kim, C.-H. Shin, S.K. Shin. *Ab initio quantum mechanical investigation of the reaction mechanisms for the formation of C<sub>7</sub>H<sup>+</sup> from o-, m-, and p-chlorotoluene radical cations.* **Mol. Phys.** **2007**, 105(19–22, A Special Issue in Honour of Péter Pulay): 2541–2549.
- [14] C.-H. Shin, K.-C. Park, S.-J. Kim, B. Kim. *Theoretical approach for the equilibrium structures and relative energies of C<sub>7</sub>H<sup>+</sup> isomers and the transition states between o-, m-, and p-tolyl cations.* **Bull. Kor. Chem. Soc.** **2002**, 23(2): 337–345.

- [15] S.K. Shin. *Relative stabilities of ortho-, meta- and para-tolyl cations*. *Chem. Phys. Lett.* **1997**, 280(3–4): 260–265.
- [16] J.C. Choe. *Formation of C<sub>7</sub>H<sub>7</sub><sup>+</sup> from benzyl chloride and chlorotoluene molecular ions: A theoretical study*. *J. Phys. Chem. A* **2008**, 112(27): 6190–6197.
- [17] J.C. Choe. *Isomerization and dissociation of ethylbenzene and xylene molecular ions: A DFT study*. *Chem. Phys. Lett.* **2007**, 435(1–3): 39–44.
- [18] W. von E. Doering, L.H. Knox. *The cycloheptatrienylium (tropylium) ion*. *J. Am. Chem. Soc.* **1954**, 76(12): 3203–3206.
- [19] T. Koenig, J.C. Chang. *Helium(I) photoelectron spectrum of troyl radical*. *J. Am. Chem. Soc.* **1978**, 100(7): 2240–2242.
- [20] G.A. Olah, C.U. Pittman Jr., R. Waack, M. Doran. *The electronic spectra of carbonium ions in strongly acidic solutions*. *J. Am. Chem. Soc.* **1966**, 88(7): 1488–1495.
- [21] I. Hanazaki, S. Nagakura. *Electronic spectra and electronic structures of the benzyl cation and its methyl derivatives*. *Tetrahedron* **1965**, 21(9): 2441–2452.
- [22] J.A. Grace, M.C.R. Symons. *194. Unstable intermediates. Part VI. Spectra of certain aryl carbinols and olefins in strongly acidic and weakly acid media*. *J. Chem. Soc.* **1959**, (0): 958–562.
- [23] N. Fujisaki, P. Comte, T. Gäumann. *Ultraviolet absorption spectrum of the benzyl cation observed by the pulse radiolysis of benzyl chloride*. *J. Chem. Soc. Chem. Commun.* **1993**, (10): 848–849.
- [24] L.M. Dorfman, R.J. Sujdak, B. Bockrath. *Fast reaction studies of carbanions and carbocations in solution*. *Acc. Chem. Res.* **1976**, 9(10): 352–357.
- [25] R.L. Jones, L.M. Dorfman. *Submicrosecond formation and observation of reactive carbonium ions*. *J. Am. Chem. Soc.* **1974**, 96(18): 5715–5722.
- [26] F.L. Cozens, V.M. Kanagasabapathy, R.A. McClelland, S. Steenken. *Lifetimes and UV-visible absorption spectra of benzyl, phenethyl, and cumyl carbocations and corresponding vinyl cations. A laser flash photolysis study*. *Can. J. Chem.* **1999**, 77(12): 2069–2082.
- [27] R.A. McClelland, C. Chan, F. Cozens, A. Modro, S. Steenken. *Laser flash photolysis generation, spectra, and lifetimes of phenylcarbenium ions in trifluoroethanol and hexafluoroisopropyl alcohol. On the UV spectrum of the benzyl cation*. *Angew. Chem. Int. Ed. Engl.* **1991**, 30(10): 1337–1339.
- [28] L. Andrews, B.W. Keelan. *Ultraviolet absorption spectra and photochemical rearrangements of benzyl and tropylium cations in solid argon*. *J. Am. Chem. Soc.* **1981**, 103(1): 99–103.
- [29] L. Andrews, J.H. Miller, B.W. Keelan. *Absorption spectra and photochemistry of the toluene cation and benzyl radical in solid argon*. *Chem. Phys. Lett.* **1980**, 71(2): 207–210.
- [30] D.M. Friedrich, A.C. Albrecht. *The visible excitation spectra of benzyl, benzyl-d<sub>7</sub> and p-methylbenzyl in rigid solution at 77 K*. *Chem. Phys.* **1974**, 6(3): 366–372.

- [31] G. Porter, E. Strachan. *The electronic spectra of benzyl*. *Spectrochim. Acta* **1958**, 12(4): 299–304.
- [32] G.C. Eiden, J.C. Weisshaar. *Vibronic coupling mechanism in the  $\tilde{A}^2A_2 - \tilde{B}^2B_2$  excited states of benzyl radical*. *J. Chem. Phys.* **1996**, 104(22): 8896–8912.
- [33] K. Tonokura, M. Koshi. *Cavity ring-down spectroscopy of the benzyl radical*. *J. Phys. Chem. A* **2003**, 107(22): 4457–4461; and references therein.
- [34] J. Fulara, A. Nagy, I. Garkusha, J.P. Maier. *Higher energy electronic transitions of  $HC_{2n+1}H^+$  ( $n=2-7$ ) and  $HC_{2n+1}H$  ( $n=4-7$ ) in neon matrices*. *J. Chem. Phys.* **2010**, 133(2): 024304/1–9.
- [35] P. Lablanquie, K. Ohashi, N. Nishi. *Laser photodissociation of  $C_7H_7^+$  created through multiphoton ionization of para-chlorotoluene*. *J. Chem. Phys.* **1993**, 98(1): 399–408; and references therein.
- [36] D.A. McCrery, B.S. Freiser. *Gas phase photodissociation of  $C_7H_7^+$* . *J. Am. Chem. Soc.* **1978**, 100(9): 2902–2904.
- [37] Unpublished results include electronic absorption spectra of  $C_7H_{\gamma}^{+/0}$  ( $\gamma = 4-6$ ),  $C_5H_{\gamma}^{+/0}$  ( $\gamma = 3-6$ ) ([Appendix A](#)) and other cationic/neutral hydrocarbons.
- [38] B. Ward. *Absorption spectra of aromatic free radicals: A vibrational analysis of the 3050 Å absorption spectrum of benzyl and a new transition of phenoxyl*. *Spectrochim. Acta Part A* **1968**, 24A(7): 813–818.
- [39] M. Margraf, B. Noller, C. Schröter, T. Schultz, I. Fischer. *Time- and frequency-resolved photoionization of the  $C^2A_2$  state of the benzyl radical,  $C_7H_7$* . *J. Chem. Phys.* **2010**, 133(7): 074304/1–5.
- [40] F. Markert, P. Pagsberg. *UV spectra and kinetics of radicals produced in the gas phase reactions of Cl, F and OH with toluene*. *Chem. Phys. Lett.* **1993**, 209(5–6): 445–454.
- [41] N. Ikeda, N. Nakashime, K. Yoshihara. *Formation and relaxation of hot benzyl radicals in the gas phase*. *J. Phys. Chem.* **1984**, 88(24): 5803–5806.
- [42] M.A. Hoffbauer, J.W. Hudgens. *Multiphoton ionization detection of gas-phase benzyl radicals*. *J. Phys. Chem.* **1985**, 89(24): 5152–5154.
- [43] V.L. Stakhursky, I. Sioutis, Gy. Tarczay, T.A. Miller. *Computational investigation of the Jahn–Teller effect in the ground and excited electronic states of the tropylium radical. Part I. Theoretical calculation of spectroscopically observable parameters*. *J. Chem. Phys.* **2008**, 128(8): 084310/1–13.
- [44] I. Sioutis, V.L. Stakhursky, Gy. Tarczay, T.A. Miller. *Experimental investigation of the Jahn–Teller effect in the ground and excited electronic states of the tropylium radical. Part II. Vibrational analysis of the  $\tilde{A}^2E_3 - \tilde{X}^2E_2$  electronic transition*. *J. Chem. Phys.* **2008**, 128(8): 084311/1–18.
- [45] A. Nagy, J. Fulara, I. Garkusha, J.P. Maier. *On the benzylium/tropylium ion dichotomy: electronic absorption spectra in neon matrices*. *Angew. Chem. Int. Ed.* **2011**, 50(13): 3022–3025.

- [46] T.P. Troy, S.H. Kable, T.W. Schmidt, S.A. Reid. *On the electronic spectroscopy of closed-shell cations derived from resonance-stabilized radicals: Insights from theory and Franck–Condon analysis*. *Astron. Astrophys.* **2012**, 541: A8/1–6.
- [47] T. Pino, F. Güthe, H. Ding, J.P. Maier. *Gas-phase electronic spectrum of the tropylium C<sub>7</sub>H<sub>7</sub><sup>+</sup> radical*. *J. Phys. Chem. A* **2002**, 106(42): 10022–10026.
- [48] I. Garkusha. *Electronic spectroscopy of mass-selected protonated polycyclic aromatic hydrocarbons in neon matrices*. Ph.D. thesis, University of Basel, Faculty of Science, **2012**.
- [49] Z. Zhou, R.G. Parr. *New measures of aromaticity: Absolute hardness and relative hardness*. *J. Am. Chem. Soc.* **1989**, 111(19): 7371–7379.
- [50] Z. Chen, C.S. Wannere, C. Corminboeuf, R. Puchta, P.v.R. Schleyer. *Nucleus-independent chemical shifts (NICS) as an aromaticity criterion*. *Chem. Rev.* **2005**, 105(10): 3842–3888; and references therein.
- [51] J. Wang, J. Kubicki, M.S. Platz. *An ultrafast study of phenyl azide: The direct observation of phenylnitrenium ion*. *Org. Lett.* **2007**, 9(20): 3973–3976.
- [52] Unpublished results.

*“ ‘Hey, there’s something falling down in there,’ said the chief clerk.  
Gregor tried to suppose to himself that what had happened to him  
might some day also happen to the chief clerk.  
There was no denying that anything was possible.”*  
Franz Kafka (1883–1924), *The Metamorphosis*

## FORMATION OF AROMATICS IN DISCHARGES: ABSORPTION AND FLUORESCENCE OF C<sub>11</sub>H<sub>9</sub><sup>+</sup>

---

# 5

To proceed on the path in the study of PAH-related compounds that has been laid by the results presented in [Chapter 4](#), a set of other small, prototypical arenes (phenylacetylene, indene and naphthalene cations, and C<sub>11</sub>H<sub>9</sub><sup>+</sup> isomers) was produced, deposited in solid neon and studied spectroscopically. This project initiated itself somewhat incidentally—it was noted that, using the updated setup and a hot-cathode discharge source ([Chapter 2](#)), 2,4-hexadiyne (2,4-HDy) vapor diluted in helium has a particularly interesting mass spectrum ([Figure 5.1a](#)). Although it is expected that, depending strongly on the experimental conditions, species with higher  $m/z$  ratios than for the initial material are ‘synthesized’ upon parallel ionization, fragmentation and ion–molecule reactions in the source, such a behavior as for 2,4-HDy (a regular progression in mass and intensity, as well as relatively high ion yields) is not at all common for other unsaturated hydrocarbon chains. A random example for this is presented in [Figure 5.1b](#), showing the mass spectrum of another linear precursor (mixture) investigated in this laboratory.

A closer look at the prominent peaks of [Figure 5.1a](#) and that the parent of 2,4-HDy ( $m/z = 78$ ) is isoelectronic with benzene cation hints the formation of cyclic structures ([Figure 5.2](#)). Therefore, mass-selected ions with  $m/z = 91, 102, 115$  and  $128$  were co-deposited with neon at 6 K and investigated by electronic spectroscopy in absorption. It became apparent that fused-ring species are readily produced from an open-chain precursor in the chemistry under such discharge circumstances: The first and third mass belong to the aromatics C<sub>7</sub>H<sub>7</sub><sup>+</sup> ([Chapter 4](#)) and C<sub>9</sub>H<sub>7</sub><sup>+</sup> ([Chapter 6](#)), respectively; the remaining two recorded spectra are of

the cyclic phenylacetylene and naphthalene radical cations,  $C_8H_6^{*+}$  (Figure A.10, Appendix A) and  $C_{10}H_8^{*+}$  (Figure 5.3), both known from earlier studies.<sup>1,2</sup>

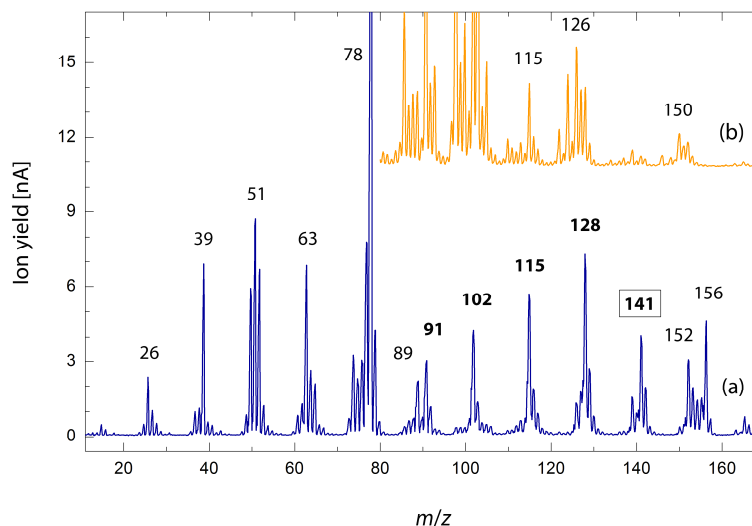


**Figure 5.1:** Mass spectra as produced in a hot-cathode discharge source from (a) 2,4-hexadiyne vapor and (b) a butatriene/diacetylene open-chain precursor mixture, diluted in helium. The clear progression in  $\sim 12$ – $14$  mass units in the former suggests PAH growth not only via the commonly accepted hydrogen abstraction/ $C_2H_2$  addition route<sup>3</sup> but also by incorporation of  $CH_y$  ( $y = 0$ – $2$ ) groups into smaller intermediates. Those indicated in **bold** were deposited in neon and their electronic absorption spectra recorded, which confirms the formation of aromatic species.

However, there has been little known spectroscopic data on the species with the formula  $C_{11}H_9^+$  ( $m/z = 141$ , for which another constitutional alternative would be the fully saturated decylium,  $C_{10}H_{21}^+$ , unlikely to be produced considering the

<sup>1</sup> (a) T. Pino, S. Douin, N. Boudin, Ph. Bréchnignac. *J. Phys. Chem. A* **2007**, *111*(51): 13358–13364;

(b) H. Xu, P.M. Johnson, T.J. Sears. *J. Phys. Chem. A* **2006**, *110*(25): 7822–7825.

<sup>2</sup> (a) N. Boudin, T. Pino, Ph. Bréchnignac. *J. Mol. Struct.* **2001**, *563–564*: 209–214; (b) L. Andrews, B.J. Kelsall, T.A. Blankenship. *J. Phys. Chem.* **1982**, *86*(15): 2916–2926; (c) F. Salama, L.J. Allamandola. *J. Chem. Phys.* **1991**, *94*(11): 6964–6977; (d) F. Negri, M.Z. Zgierski. *J. Chem. Phys.* **1994**, *100*(2): 1387–1399.

<sup>3</sup> (a) H. Bockhorn, F. Fetting, H.W. Wenz. *Ber. Bunsen-Ges. Phys. Chem.* **1983**, *87*(11): 1067–1073;

(b) M. Frenklach, D.W. Clary, W.C. Gardiner, S.E. Stein. *Proc. 20<sup>th</sup> Symp. (Intl.) Combust.* **1985**,

*20*(1): 887–901; (c) H. Wang, M. Frenklach. *Combust. Flame* **1997**, *110*(1–2): 173–221.



nature of the precursor) and corresponding neutrals C<sub>11</sub>H<sub>9</sub><sup>•</sup>.<sup>4</sup> Thus, the focus was directed onto these.

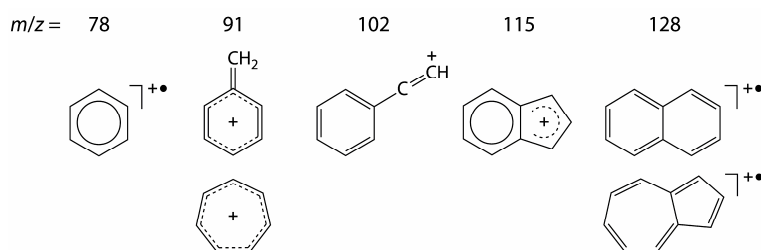


**Figure 5.2:** Expected mono- and bicyclic structures for some of the stronger mass peaks of Figure 5.1a.

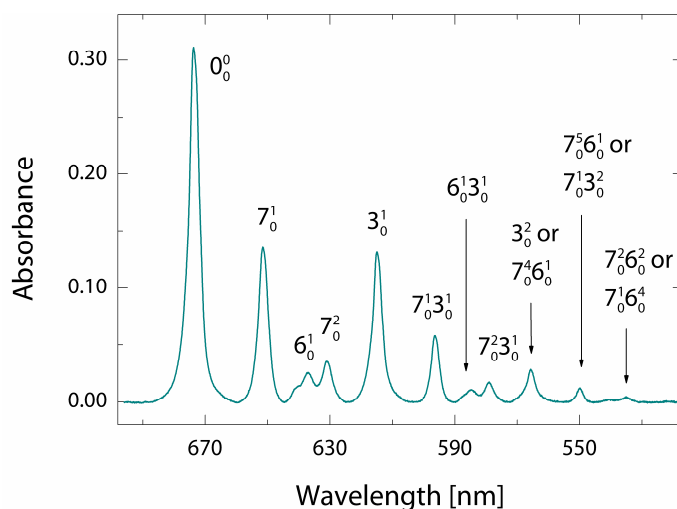


**Figure 5.3:** The  $(1)^2B_{2g} \leftarrow \tilde{X}^2A_u$  electronic transition of naphthalene<sup>•+</sup> radical cation in a neon matrix. The spectrum is identical to those published in Ref. (2). The assignment is taken from Ref. (2c).

<sup>4</sup> (a) Kh.I. Mamedov, I.K. Nasibov. *Opt. Spectrosc.* **1971**, 30(6): 565–567; (b) N. Chalyavi, T.P. Troy, M. Nakajima, B.A. Gilbson, K. Nauta, R.G. Sharp, S.H. Kable, T.W. Schmidt. *J. Phys. Chem. A* **2011**, 115(27): 7959–7965; (c) G. Naville, H. Strauss, E. Heilbronner. *Helv. Chim. Acta* **1960**, 43(5): 1221–1243.

5.1 DIVERSITY OF  $C_{11}H_9^+$  AND  $C_{11}H_9^\bullet$  ISOMERS

It has been discussed in previous chapters that the main ‘limitation’ of mass selection is that several structural isomers can be deduced for a given chemical formula, which are produced and trapped parallel in a matrix. Taken that the compounds  $C_{11}H_9^+$  and  $C_{11}H_9^\bullet$  contain twenty atoms and 5–8-membered rings may become resonance-stabilized with the right number of electrons, there are a number of geometries to consider (Figure 5.4).

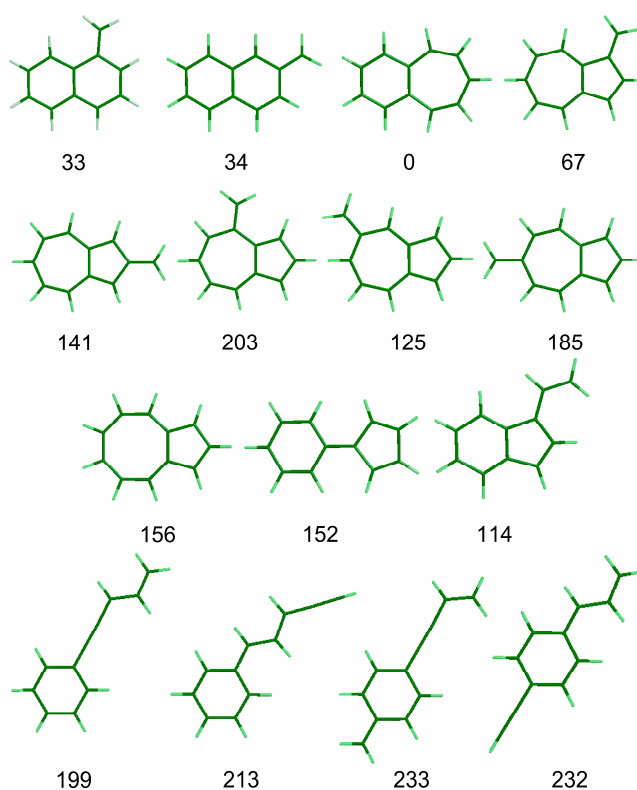


**Figure 5.4:** Optimized ground-state structure and relative energy ( $\text{kJ mol}^{-1}$ ) of some considered  $C_{11}H_9^+$  isomers calculated with DFT at the BLYP/6-31G(d,p) level of theory. All configurations are of planar  $C_s$  or, where applicable,  $C_{2v}$  symmetry.

On the other hand, the species formed do undergo partial thermalization in the ion source, because the voltage of  $\sim 50$  V applied on the cylindrical anode limits the energy to which they have access (Chapter 2). Experience shows that multiple isomers of a mass-selected ion can be embedded in such neon matrices in copious

amounts in two cases: if (a) they have energy within ~50 kJ mol<sup>-1</sup> of the most stable form or (b) the product can be directly derived from the precursor by simple chemical reactions (*e.g.*, breaking or formation of one bond). This means that two closely-related species, 1- and 2-naphthylmethyl cation (1- and 2-NyMe<sup>+</sup>), and a third, benzotropylium (BzTr<sup>+</sup>), were expected to be the 'main' deposited C<sub>11</sub>H<sub>9</sub><sup>+</sup> forms (first three geometries in [Figure 5.4](#)).

However, in order to get unambiguous structural information, the electronic spectrum of the trapped species had to be understood. Deciphering such a complex spectrum ([Figure 5.5a](#)) with several absorbing molecules and systems can rely only on a very limited number of crutches:

- Earlier experimental studies. Commonly, for the last several decades, reactive species have been studied in solutions, which may give some information as to where they absorb. However, these are often shifted and broadened because of extensive interaction with each other as well as the solvent. Such an example was shown in [Chapter 4](#). Specifically, for C<sub>11</sub>H<sub>9</sub><sup>+</sup> and C<sub>11</sub>H<sub>9</sub><sup>•</sup>, there is a lack of literature data.<sup>4</sup>
- Computed transition energies. The C<sub>11</sub>H<sub>9</sub><sup>+</sup> cations and their corresponding neutrals are relatively large electronic systems (74/75 electrons); hence, because of the problem of electron correlation, they cannot be treated easily with high-level, *ab initio* methods. This means that only lower-level approximations are affordable (TD DFT, CC2, CASSCF, *etc.*). It is, however, not forthcoming because these methods (and, as a matter of fact, *any* computational approach) often overestimate the transition energy by ~0.5 eV or more, even for systems with just a few atoms.<sup>5</sup> Furthermore, frequencies in the excited states are not those in the electronic ground state due to eventual geometric change upon excitation. Therefore, even using *in silico* options, both the onset of transitions and vibrational patterns observed in a spectrum may remain difficult to assign.

---

<sup>4</sup> See, *e.g.*, (a) J.F. Stanton. *Faraday Discuss.* **2011**, *150*(Frontiers in Spectroscopy): 331–343; and (b) R.C. Fortenberry, R.A. King, J.F. Stanton, T.D. Crawford. *J. Chem. Phys.* **2010**, *132*(14): 144303/1–10 for recent examples.

- Precursor selectivity. Though the energetics of isomers largely determine the ions that can be produced and embedded in neon as stated above the production ratio of different species can be influenced by the choice of starting materials.
- Photobleaching. Providing UV photons to the matrix induces photodetachment of electrons from the scavenger and their recombination with the deposited cations to form corresponding neutrals (Chapter 2). This is, however, not an 'absolute' mean of deciding whether a particular species is of neutral or ionic origin; selected instances of accompanying light-induced processes are described in Appendix A.

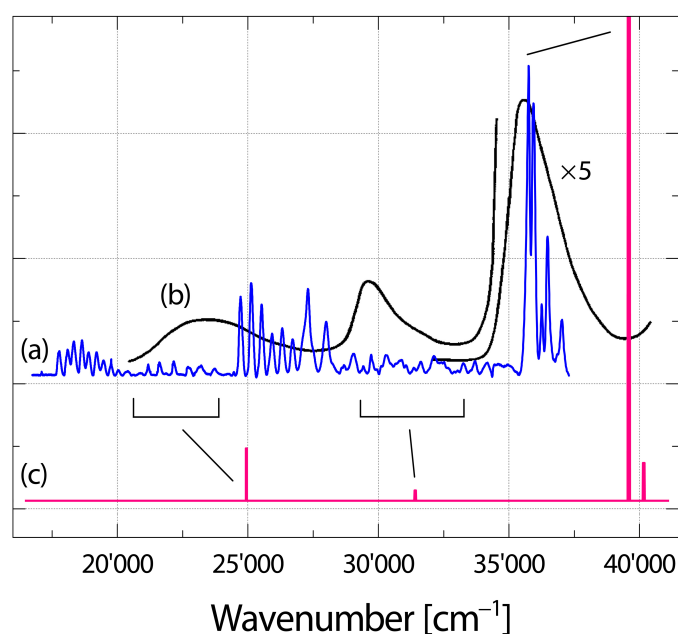


**Figure 5.5:** (a) Overview plot of electronic absorption spectra of  $C_{11}H_9^+$  (and  $C_{11}H_9^\bullet$ ) recorded after depositing mass-selected ions into a neon matrix, compared to (b) a direct absorption spectrum of  $BzTr^+$  in a concentrated (60 %) sulfuric acid solution at  $RT^{4c}$  and (c) a stick diagram representing calculated values for the same species at the CC2//MP2/cc-pVTZ level.

For the measurements of  $C_{11}H_9^+$  and  $C_{11}H_9^\bullet$ , these points were drawn on.  $BzTr^+$ , and 1- and 2-naphthylmethyl neutrals have been studied in strong acidic solutions and in the gas phase by REMPI, respectively.<sup>4</sup> DFT and MP2 methods

were employed for ground-state optimization and harmonic frequency calculations, while TD DFT and CC2 for vertical excitation energies. The ‘collaboration’ of these first two bullet points is illustrated on the example of BzTr<sup>+</sup> in [Figure 5.5](#). A variety of precursors (1- and 2-methyl-naphthalene, 1-phenyl-4-penten-1-yne, phenylacetylene + propyne, benzyl chloride + diacetylene and 2,4-HDy + acetylene) was tried and compared for band intensity distribution. Irradiation of the cationic matrices was also performed every case. However, without introducing at this time an important additional experimental configuration option, *fluorescence* ([Chapter 2](#)), the following results section could not be written.

## 5.2 RESULTS AND OUTLOOK

Altogether, *seventeen* (!) electronic systems due to different C<sub>11</sub>H<sub>9</sub><sup>+</sup> and neutral C<sub>11</sub>H<sub>9</sub><sup>•</sup> radicals were identified; these were present in the absorption spectra *simultaneously*. However, it was found that transitions of two isomers, BzTr<sup>+</sup> and 2-NyMe<sup>+</sup>, dominate ([Figures 5.5](#) and [5.6](#)), regardless of the hydrocarbon used for ion production. These two species emit (S<sub>1</sub> → S<sub>0</sub>) upon laser excitation. The expected third C<sub>11</sub>H<sub>9</sub><sup>+</sup> species, 1-NyMe<sup>+</sup>, could not be detected. BzTr<sup>+</sup> and 2-NyMe<sup>+</sup> are also in the obtained spectra using open-chain and ring–chain initial materials, indicating that isomerization of C<sub>11</sub>H<sub>9</sub><sup>+</sup> does take place in the source.

BzTr<sup>+</sup> is the most stable structure on the potential energy surface of C<sub>11</sub>H<sub>9</sub><sup>+</sup>; hence, it was not surprising that for all precursors it was present. 1- and 2-NyMe<sup>+</sup> have similar energies in the ground state; however, distinct absorptions of only the latter were observed, even when 1-methyl-naphthalene (1-MetN) was used as the starting material. The weak oscillator strength of transitions of 1-NyMe<sup>+</sup> does not account for this anomaly.

An explanation is the following. The 1-NyMe<sup>+</sup> cation initially formed from 1-MetN in the source rearranges, producing BzTr<sup>+</sup> and 2-NyMe<sup>+</sup>. This would involve hydrogen shifts and scrambling of carbon atoms; of course, more complex plasma processes must play a significant role in a discharge. Because no photoconversion of isomers was observed upon UV irradiation, the barrier for isomerization of C<sub>11</sub>H<sub>9</sub><sup>+</sup> should be higher than optical excitations. However, there is no obvious reason why this would differ from the case of C<sub>6</sub>H<sub>4</sub><sup>+</sup> or protonated

naphthalenes (Appendix A), where (reversible) photoisomerization and even a quantum tunneling phenomenon have been observed. Thus, the 1-/2-NyMe<sup>+</sup> automerization pathway and transition states call for high-level, quantum chemical exploration.

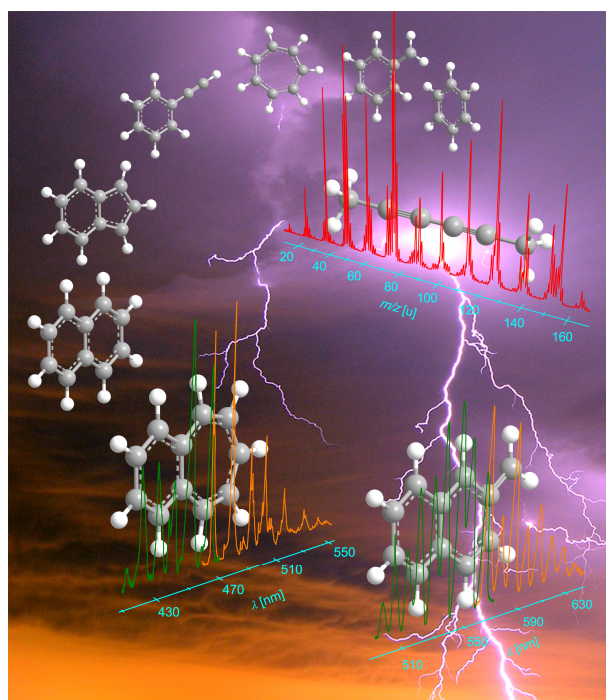


**Figure 5.6:** Impression on the growth of PAHs in a discharge plasma from an open-chain precursor, 2,4-hexadiyne. Species of interest ( $m/z = 141$ , that is,  $C_{11}H_9^+$  isomers) were identified by spectroscopic means, direct absorption and fluorescence emission, after mass-selectively sampling them into 6 K neon matrices.

Absorptions of three other isomers of  $C_{11}H_9^+$ , besides those of BzTr<sup>+</sup> and 2-NyMe<sup>+</sup>, were detected following deposition of the cations produced from acyclic precursors. In these isomers a benzene ring is fused with a chain. Calculations predict strong single transitions ( $f \sim 1$ ) in the visible for such cations and their corresponding neutrals, raising a considerable question on the relevance of ring-chain hydrocarbons in the DIB saga.

On a side note: Figure 5.1a shows a few intense masses besides those discussed, e.g., 63, 152 and 156 u. The former is of  $C_5H_3^+$ , a member of the  $C_5H_y^+$  series

(Appendix A). The latter two originate from  $C_{12}H_8^+$  and  $C_{12}H_{12}^+$ , which likely belong to ionic derivatives of the PAHs acenaphthylene, and heptalene and/or biphenyl. It is again interesting, that diagonalizing the Hückel energy matrix  $\mathbf{B}$  (Chapter 4) for  $BzTr^+$ , 1- and 2-NyMe<sup>+</sup> leads to HOMO/LUMO dimensionless level eigenvalue coefficients  $x_j = 0.802$  and  $-0.226$ ,  $0.799$  and  $0.000$ , and  $0.676$  and  $0.000$ , respectively. Taking again the exchange integral value of benzene,  $\beta_{\mu\nu} \approx 20\,000\text{ cm}^{-1}$ , similarly to the case of  $C_7H_7^+$  (Chapter 4), gives for the first allowed transition of the three species an energy of 486, 626 and 740 nm. This is somewhat better than those calculated with CC2, and comparable with the values from the TD DFT approximation and the experiments, which proves the robustness of the HMO method for simple, classical arenes with  $4x + 2$  valence electrons. It is also worth mentioning that though the DFT optimization of *c*- $C_{11}H_9^+$  restrained in  $C_2$  molecular symmetry converges with one imaginary frequency at the BLYP/6-31G(d,p) level, its energy is as much as  $\sim 400\text{ kJ mol}^{-1}$  above  $BzTr^+$ . Therefore, the approach described herein is likely not the way to go for the investigation of Möbius aromatics (possessing  $4x$  electrons).<sup>6</sup>

This work revealed that PAH-related compounds may form from acyclic precursors (Figure 5.6). Besides giving relevant mass spectrometric and spectroscopic information in an undeveloped field—namely, direct observation of formation of aromatic structures in aliphatic hydrocarbon discharges—, it extended for the first time the UV/Vis and IR capabilities of the matrix apparatus with LIF (Chapter 2). The recorded electronic spectra will serve as a starting point for gas-phase surveys and provide a means of direct monitoring of intermediate steps in kinetic experiments on PAH formation. An astronomical relevance of the observed ‘main’ cationic species as DIB carriers is, in view of their broad FC profile (Figure 5.5), unlikely.<sup>7</sup> These findings were reported in detail in the *Journal of the American Chemical Society*;<sup>8</sup> the paper is appended below.

---

<sup>6</sup> See, e.g., (a) E. Heilbronner. *Tetrahedron Lett.* **1964**, 5(29): 1923–1928; (b) M. Mauksch. *Ph.D. thesis*, University of Erlangen-Nürnberg, Faculty of Science, **1999**; and (c) E.-K. Mucke, F. Köhler, R. Herges. *Org. Lett.* **2010**, 12(8): 1708–1711 for theoretical descriptions of such species, and (d) D. Ajami, O. Oeckler, A. Simon, R. Herges. *Nature* **2003**, 426: 819–821 for a synthesis attempt.

<sup>7</sup> T.P. Troy, S.H. Kable, T.W. Schmidt, S.A. Reid. *Astron. Astrophys.* **2012**, 541: A8/1–6.

<sup>8</sup> A. Nagy, J. Fulara, J.P. Maier. *J. Am. Chem. Soc.* **2011**, 133(49): 19796–19806.





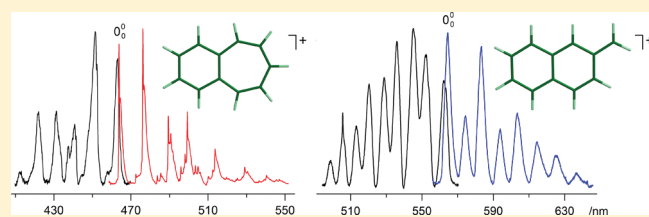
# Formation of Aromatic Structures from Chain Hydrocarbons in Electrical Discharges: Absorption and Fluorescence Study of $C_{11}H_9^+$ and $C_{11}H_9^\bullet$ Isomers in Neon Matrices

Adam Nagy, Jan Fulara,<sup>†</sup> and John P. Maier<sup>\*</sup>

Department of Chemistry, University of Basel, Klingelbergstrasse 80, CH-4056 Basel, Switzerland

**S** Supporting Information

**ABSTRACT:** A set of arenes (phenylacetylene, indene, and naphthalene cations and  $C_{11}H_9^+$  isomers) was produced from 2,4-hexadiyne diluted in helium in a hot-cathode discharge source. The mass-selected ions were codeposited with neon at 6 K and investigated by electronic absorption spectroscopy. This reveals that fused-ring species are readily formed from an acyclic precursor in such a source. After photobleaching of matrices containing  $C_{11}H_9^+$ , neutral  $C_{11}H_9^\bullet$  radicals were also characterized. Assignment of the observed transitions to different  $m/z = 141$  cationic and corresponding neutral isomers is given and supported by experiments using other precursors, fluorescence measurements, and time-dependent density functional and second-order approximate coupled cluster calculations.



## 1. INTRODUCTION

Aromaticity not only is a core concept in organic chemistry but also is of astrophysical interest. For instance, polycyclic aromatic hydrocarbons (PAHs) and their derivatives have raised attention since they were proposed as carriers of diffuse interstellar<sup>1</sup> as well as unidentified infrared bands.<sup>2</sup> They are also assumed to play an important role in young Earth-like planetary atmospheres such as that of Titan.<sup>3</sup>

It is generally agreed that the initial step in the growth of PAHs is the ring closure of two propargyl units to benzene.<sup>4–6</sup> Two mechanisms have been put forward for the formation of larger species. The first involves stepwise hydrogen abstraction from the reacting hydrocarbon followed by acetylene addition (HACA);<sup>7–9</sup> the other considers resonance-stabilized free radicals to be the key compounds toward PAHs.<sup>10–13</sup> Both these routes originate from combustion or premixed flame studies, where PAHs are believed to be intermediates in soot formation.<sup>14,15</sup> Although the interstellar medium lacks the two single most important characteristics of the latter environments, high pressure and temperature, the long time scales may compensate for the lower reaction rates in cold, vacuum conditions.

In order to identify such species unambiguously, rather than restrict oneself to mass spectrometric investigations and chemical models, spectroscopic studies on PAH derivatives are desirable. However, these are often hindered by the unavailability of suitable precursors and alternative “synthesis” methods need to be employed. Among others,<sup>16–18</sup> diagnosis of open-chain and cyclic molecules in discharges have suggested the production of PAH-related compounds.<sup>19,20</sup> In this contribution, a series of (fused-)ring hydrocarbon cations was produced from acyclic precursors and trapped in 6 K neon matrices. The reported electronic absorption and fluorescence spectra of  $C_{11}H_9^+$  and

$C_{11}H_9^\bullet$  may support a better understanding of intermediate steps of PAH formation.

## 2. METHODOLOGY

The setup employed has been described.<sup>21</sup> Cations of interest were produced in a hot-cathode discharge source from precursor mixtures with helium. The source is similar to conventional electron impact except that the electrons emitted from a hot ( $\sim 2000$  °C) tungsten filament are confined to a central region by a voltage of  $\sim 50$  V applied on a cylindrical anode, and an electromagnetic coil. Chemistry occurs in the resulting plasma, where ionization, fragmentation, and ion–molecule reactions take place.

After extraction from the source, ions were guided using a series of electrostatic lenses through a  $90^\circ$  static deflector, where they were separated from neutrals, to a quadrupole mass filter. Cations mass selected at approximately  $\pm 0.5$  u resolution were codeposited with a mixture of neon and an electron scavenger (chloromethane)<sup>21,22</sup> for a few hours onto a rhodium-coated sapphire substrate kept at 6 K to build a matrix of  $\sim 150$   $\mu\text{m}$  in thickness.

The detection system consists of a halogen or a high-pressure xenon light source, a spectrograph equipped with three gratings blazed at different wavelengths, and two range-specific CCD cameras. Absorption spectra were recorded in the 250–1100 nm region by propagating broadband light through the matrix parallel to its surface in a “waveguide” manner. The effective path length was about 20 mm. Light exiting the sample was collected and transferred with a bundle of 50 optical fibers to the spectrograph. Cut-off filters were used during recording of the spectra to eliminate possible photoconversion of the trapped species by the broadband light. Furthermore, scans were started from the near-IR and continued into the UV; the procedure was later repeated to test

Received: July 13, 2011

Published: October 17, 2011

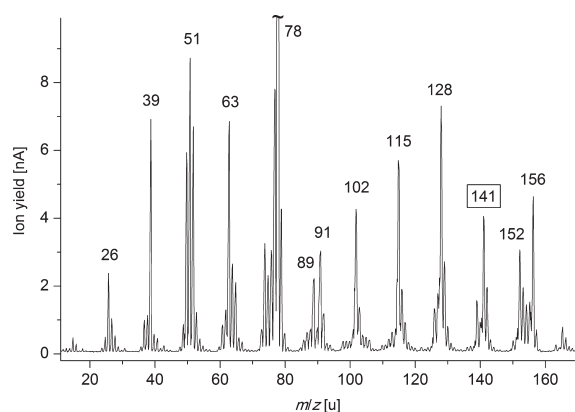


**Figure 1.** Mass spectrum produced from 2,4-hexadiyne in a hot-cathode discharge ion source.

whether the species were light-sensitive. Subsequently, the matrix was irradiated for 30–60 min with water-filtered radiation of a medium-pressure mercury (mpHg) lamp to neutralize the trapped cations (“photobleaching”), and spectra were recorded anew.

Wavelength-dispersed fluorescence spectra were obtained by exciting the species embedded in neon at an angle of incidence  $\sim 45^\circ$  with a pulsed,  $\text{Nd}^{3+}$ :YAG-pumped, tunable optical parametric oscillator laser with bandwidth  $3\text{--}8\text{ cm}^{-1}$  and energies  $2\text{--}30\text{ mJ}$ . The emission data were collected perpendicular to the matrix surface—the light was focused with a short-focus lens into the optical fiber bundle and transmitted to the same spectrograph and cameras as were used for the absorption measurements. Fluorescence spectra were recorded in  $50\text{--}60\text{ nm}$  overlapping sections by exciting each distinct absorption band seen obtained after depositing  $\text{C}_{11}\text{H}_9^+$  cations. The signal was accumulated over  $\sim 1000$  laser shots per section. The excitations were started from the longest-wavelength absorptions and continued to the UV. The fluorescence was measured starting  $2\text{ nm}$  from the excitation wavelength upward to avoid saturation of the CCDs with scattered laser light and continued to  $\sim 650\text{ nm}$ .

Ground-state harmonic frequencies and excitation energies were computed at different levels of theory using the Gaussian 03 or Turbomole program suites.<sup>23,24</sup>

### 3. EXPERIMENTAL OBSERVATIONS

Mass spectra of a number of hydrocarbons were recorded to search for precursors for the synthesis of unsaturated carbon chains. Under certain experimental conditions, besides the parent and fragment cations, a growth in the size of ions was observed. For example, in the mass spectrum of 2,4-hexadiyne (2,4-HDy), several prominent peaks corresponding to heavier species than the parent  $\text{C}_6\text{H}_6^+$  ( $m/z = 78$ ) are present (Figure 1). They form a series in which neighboring members differ notably by 24 or 26 mass units. These are at 102, 128, 152, and 156 u and correspond to  $\text{C}_8\text{H}_6^+$ ,  $\text{C}_{10}\text{H}_8^+$ ,  $\text{C}_{12}\text{H}_8^+$ , and  $\text{C}_{12}\text{H}_{12}^+$ , respectively. Because the parent of 2,4-HDy is isoelectronic with the benzene cation, the question as to the structure of these ions produced from the acyclic precursor arises. The  $m/z = 102$  and  $128$  species generated from 2,4-HDy were selectively deposited into neon matrices and their absorptions recorded. In the case of  $\text{C}_8\text{H}_6^+$ , the spectrum obtained contains phenylacetylene<sup>25–27</sup> whereas the trapping of  $\text{C}_{10}\text{H}_8^+$  resulted in bands of naphthalene cation, known from previous matrix isolation and gas-phase studies<sup>27–30</sup> (Figure S1, Supporting Information). These experiments show that small-sized PAH<sup>+</sup>s are produced from an open-chain precursor in ion–molecule reactions that take place in the discharge-type

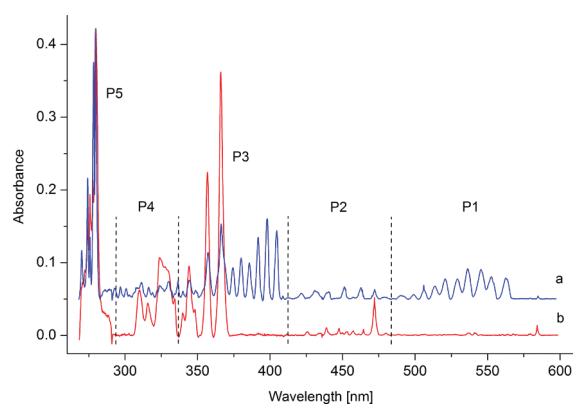


**Figure 2.** Overview plots of electronic absorption spectra recorded after deposition of  $\text{C}_{11}\text{H}_9^+$  cations ( $m/z = 141$ ) produced from 1-methyl-naphthalene as precursor into a neon matrix (a) containing  $\text{CH}_3\text{Cl}$  and (b) without an electron scavenger. Regions P1–P3 and P5 are shown in detail in Figures 3–6.

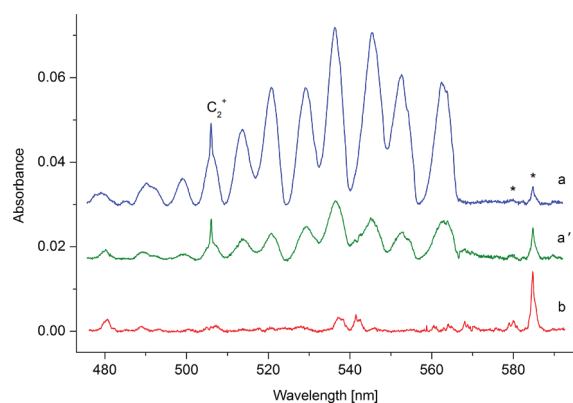


**Figure 3.** P1 part of the electronic absorption spectrum of  $\text{C}_{11}\text{H}_9^+$  produced from 1-methyl-naphthalene recorded after (a) deposition into neon and (a') irradiating the matrix with a medium-pressure mercury lamp. Trace b was obtained from the same precursor in an experiment without an electron scavenger. Weak neutral  $\text{C}_{11}\text{H}_9^+$  bands in trace a are marked with asterisks.  $\text{C}_2^+$  is a common impurity.

source. This is consistent with the HACA sequence of PAH growth.<sup>4–6</sup>

However, in the mass spectrum of 2,4-HDy (Figure 1) between the bands corresponding to PAH<sup>+</sup>s with an even number of carbon atoms, there are peaks differing from these by 12–14 u. They are at 89, 91, 115, and 141 u and belong to  $\text{C}_7\text{H}_5^+$ ,  $\text{C}_7\text{H}_7^+$ ,  $\text{C}_9\text{H}_7^+$ , and  $\text{C}_{11}\text{H}_9^+$ , respectively. Their presence indicates that the growth of PAHs proceeds by incorporation of  $\text{CH}_x$  ( $x = 0\text{--}2$ ) groups into smaller intermediates. Apart from minor intensity gain of a few peaks (e.g., those at 26 and 116 u), the mass spectrum remains identical to Figure 1 after mixing acetylene to the 2,4-HDy precursor.

$\text{C}_7\text{H}_7^+$  was studied recently in 6 K neon matrices and two isomers were detected: tropylium and benzylum.<sup>31</sup>  $\text{C}_9\text{H}_n^+$  ( $n = 7\text{--}9$ ) species are the topic of ongoing investigations.<sup>32</sup> In this contribution, the structure of the  $\text{C}_{11}\text{H}_9^+$  cations is the focus.

**3.1. Absorption Measurements.** Several electronic band systems have been detected in the  $250\text{--}600\text{ nm}$  range following the deposition of  $m/z = 141$  cations produced from 1-methyl-naphthalene (1-MetN) into a neon matrix containing a small

admixture of chloromethane (Figure 2a). Normally, during the trapping of cations, corresponding neutrals are also formed in the matrix via recombination of the ions with free electrons ejected from metal surfaces.<sup>21,22</sup> To distinguish absorptions of cations from those of neutrals,  $C_{11}H_9^+$  generated from the same precursor was deposited also into a “pure” neon matrix. The spectrum obtained is Figure 2b; it corresponds to neutral  $C_{11}H_9^\bullet$ , because the neutralization of cations is highly efficient in cases when no electron scavenger is used.<sup>21,22</sup> The spectra of  $C_{11}H_9^+$  and its neutral radical are quite complex and likely originate from more than one species. Five distinct regions (P1–P5) can be recognized (Figure 2).

The P1 part is in Figure 3 and shows the absorptions measured after deposition of  $C_{11}H_9^+$  produced from 1-MetN (upper trace), the change of the spectrum upon UV irradiation of the matrix with a mpHg lamp (middle), and the bands of neutral  $C_{11}H_9^\bullet$  recorded for the same precursor in a “pure” neon matrix (bottom). The peak labeled  $C_2^+$  is a minor fragmentation product of some of the mass-selected ions which arrive with high kinetic

**Table 1. Observed Absorption Band Maxima ( $\lambda_{Ne} \pm 0.1$  nm) of Electronic Transitions of  $C_{11}H_9^+$  Cationic Isomers in 6 K Neon Matrices and Assignments**

$\lambda_{Ne}$ (nm)	$\nu$ ( $cm^{-1}$ )	$\Delta\nu$ ( $cm^{-1}$ )	assignment <sup>d</sup>
2-Naphthylmethylium (2-NyMe <sup>+</sup> )			
562.2 <sup>b</sup>	17 787	0	$0_0^0$ $1^1A' \leftarrow X^1A'$
552.1	18 113	326	$\nu_{37}$
546.0	18 315	528	$\nu_{34}$ [or $\nu_{33}$ ]
536.1	18 653	866	$\nu_{30}$ [or $\nu_{37} + 528$ ]
528.9	18 907	1120	$\nu_{26}$ [or $2 \times 528$ ]
520.4	19 216	1429	$\nu_{16}$ [or $2 \times 528 + \nu_{37}$ ]
513.4	19 478	1691	[ $3 \times 528$ ]
505.7	19 775	1988	$\nu_{26} + \nu_{30}$ [or $3 \times 528 + \nu_{37}$ ]
498.7	20 052	2265	
490.7	20 379	2592	
404.5	24 722	0	$0_0^0$ $2^1A' \leftarrow X^1A'$
398.0	25 126	404	$\nu_{36}$
391.7	25 530	808	$2\nu_{36}$
385.5	25 940	1218	$3\nu_{36}$
379.9	26 323	1601	$4\nu_{36}$
374.2	26 724	2002	$5\nu_{36}$
369.1	27 093	2371	$6\nu_{36}$
363.5	27 510	2788	$7\nu_{36}$
Benzotropylium (BzTr <sup>+</sup> )			
462.6 <sup>b</sup>	21 617	0	$0_0^0$ $1^1B_1 \leftarrow X^1A_1$
451.1	22 168	551	$\nu_{18}$
440.1	22 722	1105	$2\nu_{18}$
430.9	23 207	1590	$3\nu_{18}$ [or $\nu_6$ ]
421.8	23 708	2091	$4\nu_{18}$ [or $\nu_{18} + 1590$ ]
336.3	29 735	0	$0_0^0$ $1^1A_1 \leftarrow X^1A_1$
329.9	30 312	577	$\nu_{18}$
325.9	30 684	949	$\nu_{15}$
321.8	31 075	1340	$\nu_{10}$
278.4	35 920	0	$0_0^0$ $2^1A_1 \leftarrow X^1A_1$
274.2	36 470	550	$\nu_{18}$
267.4	37 397	1477	$\nu_8$

**Table 1. Continued**

$\lambda_{Ne}$ (nm)	$\nu$ ( $cm^{-1}$ )	$\Delta\nu$ ( $cm^{-1}$ )	assignment <sup>d</sup>
Ring–Chain Cations <sup>c</sup>			
457.5	21 858	0	isomer C <sup>+</sup>
436.9	22 889	0	isomer A <sup>+</sup>
430.5	23 229	340	
421.3	23 736	847	
417.5	23 952	1063	
412.0	24 272	1383	
404.5	24 722	1833	
391.7	25 530	0	isomer B <sup>+</sup>

<sup>a</sup>Vibrational assignment in the excited states is based on totally symmetric modes ( $cm^{-1}$ ) in the ground state of 2-NyMe<sup>+</sup> ( $a'$  in  $C_s$ ), 3170, 3135, 3128, 3123, 3114, 3112, 3110, 3105, 3077, 1604, 1583, 1547, 1513, 1485, 1453, 1439, 1399, 1369, 1360, 1334, 1277, 1237, 1196, 1175, 1157, 1126, 1012, 987, 930, 882, 740, 712, 614, 505, 452, 406, and 275, and BzTr<sup>+</sup> ( $a_1$  in  $C_{2v}$ ), 3134, 3117, 3111, 3093, 3083, 1570, 1504, 1488, 1468, 1378, 1250, 1192, 1179, 1034, 946, 889, 688, 563, and 406, calculated with DFT at the BLYP/cc-pVTZ level of theory (unscaled), as well as on fluorescence measurements (in square brackets, see section 3.2). See the Supporting Information for the frequencies of 1-NyMe<sup>+</sup>. <sup>b</sup>Based on the combined absorption and fluorescence (section 3.2) data, the zero-phonon lines of the onsets of the referred electronic transitions are at 563.2 (2-NyMe<sup>+</sup>) and 463.8 nm (BzTr<sup>+</sup>). <sup>c</sup>These features were observed only when chain or ring–chain precursors were used for the production of  $C_{11}H_9^+$ . Assignment of the transitions to different isomers is given in section 4.1.

energy at the substrate surface.<sup>33</sup> UV photons bleach the absorptions with onset at 562.2 nm indicating the cationic nature of the system. These bands were also observed using several different precursors or precursor mixtures for the generation of  $C_{11}H_9^+$  cations, e.g., 2-methyl-naphthalene (2-MetN), 1-phenyl-4-penten-1-yne (PPey), phenylacetylene + propyne, benzyl chloride + diacetylene, or 2,4-HDy + acetylene. The relative band intensity of the 562 nm system remained the same in all experiments illustrating a common origin. It has an extended vibrational progression, which is built on five normal modes of energy 326, 528, 866, 1120, and 1429  $cm^{-1}$  and their combinations. Wavelengths of the cationic absorption band maxima are collected in Table 1.

In the top trace of Figure 3, absorptions of neutral  $C_{11}H_9^\bullet$  are also seen; these are the band at 584.2 nm and a very weak one at 579.6 nm. They grow in intensity upon UV irradiation of the matrix (middle trace) and are better discernible when no electron scavenger was used for the trapping of cations (bottom). In the latter spectrum, there are more neutral bands; they lie 136, 504, 632, 740, 1371, and 1512  $cm^{-1}$  above the origin at 584.2 nm. Wavelengths of the observed  $C_{11}H_9^\bullet$  absorptions are listed in Table 2.

In the past,  $C_{11}H_9^\bullet$  radicals produced by the UV photolysis of 1- or 2-MetN in frozen *n*-paraffin glassy solutions were studied by luminescence methods—wavelength-dispersed phosphorescence and fluorescence spectra of 1- and 2-naphthylmethyl (1- and 2-NyMe<sup>•</sup>) have been reported.<sup>34</sup> The origin band of transitions of the former and latter species in *n*-hexane lies at 588 and 598 nm, respectively, spaced  $\sim 290$   $cm^{-1}$  from one another. Several vibrational frequencies have also been derived from their structured emission; they are, among others, 519, 1389, and 1598  $cm^{-1}$  for 2-NyMe<sup>•</sup>, which are close to observed ones for  $C_{11}H_9^\bullet$  embedded in neon (Table 2), though the former refer to

**Table 2. Absorption Band Maxima ( $\lambda_{\text{Ne}} \pm 0.1$  nm) of Electronic Transitions of  $\text{C}_{11}\text{H}_9^+$  Neutral Radicals in 6 K Neon Matrices and Assignments**

$\lambda_{\text{Ne}}$ (nm)	$\nu$ ( $\text{cm}^{-1}$ )	$\Delta\nu$ ( $\text{cm}^{-1}$ )	assignment <sup>a</sup>
2-Naphthylmethyl (2-NyMe <sup>•</sup> )			
584.2	17 117	0	$0_0^0$ $1^2A' \leftarrow X^2A''$
579.6	17 253	136	$\nu_{37}$
567.5	17 621	504	$\nu_{34}$
563.4	17 749	632	$\nu_{33}$
560.0	17 857	740	$\nu_{31}$
540.9	18 488	1371	$\nu_{17}$
536.8	18 629	1512	$\nu_{12}$
506.5	19 743	2626	
488.4	20 475	3358	
479.9	20 838	3721	
472.2	21 177	0	$0_0^0$ $2^2A' \leftarrow X^2A''$
464.5	21 529	352	$\nu_{36}$
457.4	21 863	686	$\nu_{32}$
453.5	22 051	874	$\nu_{30}$
447.6	22 341	1164	$\nu_{23}$
438.9	22 784	1607	
366.4	27 293	0	$0_0^0$ $6^2A' \leftarrow X^2A''$
357.0	28 011	718	$\nu_{32}$
348.4	28 703	1410	$2\nu_{32}$
344.4	29 036	1743	
340.0	29 412	2119	$3\nu_{32}$
334.6	29 886	2593	
330.7	30 239	2946	
323.8	30 883	3590	
315.9	31 656	4363	
310.2	32 237	4944	
1-Naphthylmethyl (1-NyMe <sup>•</sup> )			
579.6	17 253	0	$0_0^0$ $1^2A' \leftarrow X^2A''$
357.0	28 011	0	$0_0^0$ $3^2A' \leftarrow X^2A''$
Ring–Chain Neutrals <sup>b</sup>			
485.5	20 597	0	isomer A <sup>•</sup>
464.5	21 529	0	isomer B <sup>•</sup>
447.6	22 341	0	isomer C <sup>•</sup>
Benzocycloheptadienyl (BzCh <sup>•</sup> )			
280.2	35 689	0	$0_0^0$ $4^2A_1 \leftarrow X^2B_1$
277.8	35 997	308	$\nu_{19}$
275.9	36 245	556	$\nu_{18}$
274.2	36 470	781	$\nu_{16}$ or $\nu_{17}$
272.2	36 738	1049	$\nu_{14}$

<sup>a</sup> See the Supporting Information for ground-state harmonic frequencies. <sup>b</sup> These features were detected only when chain or ring–chain starting materials were used for the production of  $\text{C}_{11}\text{H}_9^+$ , followed by neutralization. Assignment of the observed transitions to different isomers is given in section 4.2.

the ground state of the radical. This suggests that the neutral system with onset at 584.2 nm in a neon matrix originates from 2-NyMe<sup>•</sup> and the weak band  $136\text{ cm}^{-1}$  below (at 579.6 nm) belongs to 1-NyMe<sup>•</sup>.

This assignment is corroborated by a recent resonance-enhanced multiphoton ionization study on the 1- and 2-NyMe<sup>•</sup>

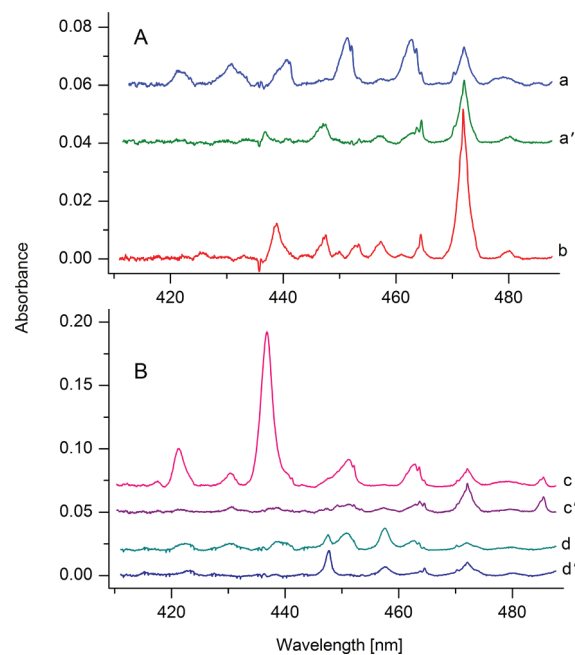


**Figure 4.** P2 part of the electronic absorption spectrum of  $\text{C}_{11}\text{H}_9^+$ . (A) The cations were produced from 1-methyl-naphthalene and the spectra recorded after (a) deposition and (a') irradiation; trace b was obtained from the same precursor without an electron scavenger. (B)  $\text{C}_{11}\text{H}_9^+$  was generated from 1-phenyl-4-penten-1-yne or a 2,4-hexadiyne + acetylene mixture, and the spectra were measured after (c, d) deposition and (c', d') subsequent UV bleaching, respectively.

radicals generated from 1- or 2-MetN.<sup>35</sup> Both isomers of NyMe<sup>•</sup> have been formed from each precursor. The onset of the electronic transition of 2-NyMe<sup>•</sup> (at 583.6 nm) lies close to the origin band of  $\text{C}_{11}\text{H}_9^+$  at 584.2 nm in a neon matrix. The onset of 1-NyMe<sup>•</sup> in the gas phase is located at somewhat shorter wavelength,  $106\text{ cm}^{-1}$  from that of 2-NyMe<sup>•</sup>. This value is close to the one extracted from the neon matrix spectrum ( $136\text{ cm}^{-1}$ ) for the weak band next to the origin at 584.2 nm. The spacing of  $290\text{ cm}^{-1}$  obtained from the separation of the emissions of the two NyMe<sup>•</sup> isomers in frozen *n*-hexane<sup>34</sup> is larger due to a more perturbative environment.

To summarize, neutralization of  $\text{C}_{11}\text{H}_9^+$  produced from 1-MetN leads to the formation of both 1- and 2-NyMe<sup>•</sup> radicals in the matrix; absorptions of the latter are stronger than that of the former. This reflects a higher concentration of 2-NyMe<sup>•</sup> than 1-NyMe<sup>•</sup> in the neon matrices of the present study or a larger oscillator strength of its transition or both. It can also be concluded that both naphthylmethyl cations (1- and 2-NyMe<sup>+</sup>) should be present trapped in the matrix in these experiments and that 1-NyMe<sup>+</sup> formed from 1-MetN isomerizes in the ion source, because a 1-/2-NyMe<sup>•</sup> rearrangement in the rigid matrix as alternative is hindered.

In the P2 range, weak absorptions have been detected following the deposition of  $\text{C}_{11}\text{H}_9^+$  produced from 1-MetN (Figure 4A, upper trace). The same bands were observed in spectra obtained for all other precursors used for the generation of the cations, including 2,4-HDy. That at 462.6 nm and four accompanying ones at shorter wavelengths decay after UV irradiation of the matrix (Figure 4A, middle trace). Their similar shape (a broad feature and a sharp, long-wavelength shoulder) and identical behavior upon photobleaching indicate that they belong to a system of one

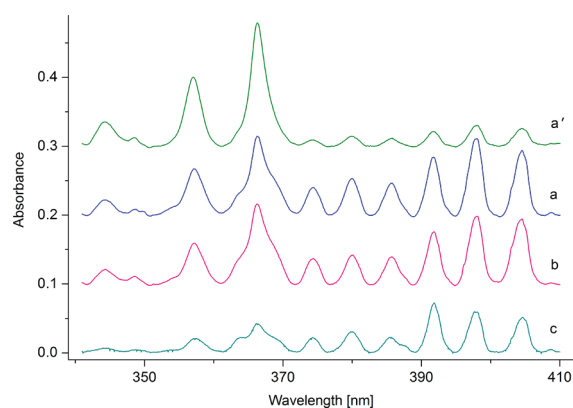


**Figure 5.** P3 part of the electronic absorption spectrum of  $C_{11}H_9^+$  produced from (a) 1-methyl-naphthalene, (b) 1-phenyl-4-penten-1-yne, and (c) 2,4-hexadiyne + acetylene. Trace a' was measured after irradiating the matrix corresponding to trace a.

isomer of  $C_{11}H_9^+$ . The spectrum looks simple; the 462.6 nm band is the onset and those at higher energies are the fundamental and overtone vibrations of  $551\text{ cm}^{-1}$ . The relative intensity of this 463 nm system and the 562 nm one (Figure 3) varied in spectra obtained under different discharge conditions in the source and with the precursors used; hence, they belong to two  $C_{11}H_9^+$  isomers.

Apart from the cationic absorptions, neutral ones are also present in trace a of Figure 4A. Their intensity increases at the expense of the photoneutralized  $C_{11}H_9^+$  cations (trace a'). The most prominent (origin) band of neutral  $C_{11}H_9^+$  was detected at 472.2 nm in this part of the spectrum. It is also present, together with weaker absorptions at shorter wavelengths, in the spectra obtained for every starting material studied and is better seen in trace b, measured in a neon matrix without  $CH_3Cl$ . The band at 464.5 nm forms another system, because its ratio to that at 472.2 nm varied in different experiments. However, the 472.2 nm peak and that at 584.2 nm of 2-NyMe $^{\bullet}$  (Figure 3b) preserved a constant intensity rate in every recording.

Besides the cationic and neutral systems discussed above, new absorptions, unique to some of the precursors used, have been detected in the P2 spectral range (Figure 4B). When the  $C_{11}H_9^+$  cations were generated from PPey and embedded into a neon matrix, a strong cationic system with onset at 436.9 nm (trace c) appeared that decayed upon UV irradiation. Simultaneously, a neutral absorption at 485.5 nm grew (trace c'). These two features were also seen, although weaker, in experiments using 1,6-heptadiyne + diacetylene, phenylacetylene + propyne, or benzyl chloride + diacetylene mixtures for ion production. The conclusion is that the plausible structure of this  $C_{11}H_9^+$  isomer and its respective radical is a benzene ring fused with an aliphatic chain.

Other new absorptions have also been detected, characteristic for the 2,4-HDy + acetylene mix as the precursor of  $C_{11}H_9^+$  (Figure 4B). The onset of a cationic system lies at 457.5 nm (trace d) and that of a neutral one at 447.6 nm (trace d'). These  $C_{11}H_9^{\bullet}$  and  $C_{11}H_9^+$  isomers likely have similar "head-and-tail" structure to the pair above (a chain attached to benzene), because their bands lie in the same spectral region.

In the 340–410 nm range (P3 part of the spectrum), strong, structured absorptions have been detected following the deposition of  $C_{11}H_9^+$  produced from 1-MetN into neon (Figure 5, trace a). The system with origin at 404.5 nm has a long, regular progression

built on the  $404\text{ cm}^{-1}$  mode and decreases in intensity upon irradiation of the matrix with UV photons (trace a'). Concurrently, another system with onset at 366.4 nm becomes stronger. The 366.4 nm band has two broad, long- and short-wavelength shoulders, which belong to the 404 nm cationic system, because they behave in a similar way upon irradiation. The band at 357.0 nm gains intensity upon exposure to UV photons, however, not as much as that at 366.4 nm does. The reason could be a wavelength coincidence of the former absorption with another cationic system or it may be the onset of an electronic transition of another isomer of neutral  $C_{11}H_9^{\bullet}$ . Both the 404 cationic and 366 nm neutral systems were present in the spectra obtained for all precursors used for generation of the ions. The former maintained a constant intensity ratio with the 562 nm system, whereas the strength of the bands starting at 366.4 nm of neutral  $C_{11}H_9^{\bullet}$  correlated well with the absorption of 2-NyMe $^{\bullet}$  at 584.2 nm and the 472 nm system.

Because of this coherence and that in earlier studies fluorescence of 2-NyMe $^{\bullet}$  in frozen *n*-hexane was observed when the 2-MetN sample was excited with the 365 nm mercury line,<sup>34</sup> the 366 nm system is assigned to the 2-NyMe $^{\bullet}$  radical. From that study, it can also be expected that 1-NyMe $^{\bullet}$  has a transition in the same region, because its emission was observed upon excitation with the same mercury line. The best candidate for this transition in solid neon is the 357.0 nm band, whose intensity changes in a different manner to that at 366.4 nm. In glassy matrices, bands are broader and shifted in comparison to solid neon; therefore, it was possible to excite both isomers of NyMe $^{\bullet}$  using the same mercury line. At  $\sim 357\text{ nm}$  lies also the first vibrational band of the 366 nm system of 2-NyMe $^{\bullet}$  ( $718\text{ cm}^{-1}$  to the blue of the origin), because its first overtone at  $1410\text{ cm}^{-1}$  can be well discerned in the neon matrix spectrum. The onset of the transition of 1-NyMe $^{\bullet}$  is likely hidden underneath this band.

The relative intensity of the first three absorption bands of the 404 nm system varies with the precursor used. In most experiments, the intensity pattern was as Figure 5, trace a, shows for 1-MetN: the second band is the strongest. However, in the case of PPey, the first and second have similar strength (trace b), because a vibrational band of the 437 nm system (Figure 4B, trace c) overlaps with the origin of the 404 nm transition. In the case of 2,4-HDy + acetylene, the third band at 391.7 nm is the strongest in this part of the spectrum (Figure 5c); this could be the onset of the second transition of the  $C_{11}H_9^+$  isomer for which the first system is observed at 457.5 nm (Figure 4B, trace d) or it is due to another isomer of  $C_{11}H_9^+$ .

The P4 part of the spectra of  $C_{11}H_9^+$  (Figure 2, 290–340 nm range) has a number of weak, cationic absorptions as well as some of neutral origin. Due to their low intensity and complexity, it is difficult to associate them with any of the systems discussed above.

The strongest absorptions have been detected in the P5 UV range after deposition of  $C_{11}H_9^+$  produced from 1-MetN (Figure 6, blue trace). Two systems can be seen: a cationic with onset at 278.4 nm and one associated with neutral  $C_{11}H_9^{\bullet}$  commencing at 280.2 nm. The former loses intensity, while the latter becomes stronger upon UV irradiation (green trace). The 278 nm system of  $C_{11}H_9^+$  is more discernible in an experiment using a phenylacetylene + propyne precursor mixture (magenta); three vibrational bands are apparent. An accurate measure of band intensities is problematic in the UV because of the strong light scattering in neon matrices—the optical path (and, thus, the absorbance) changes with the wavelength of the probing light. Additionally, in most experiments carried out in this study, the

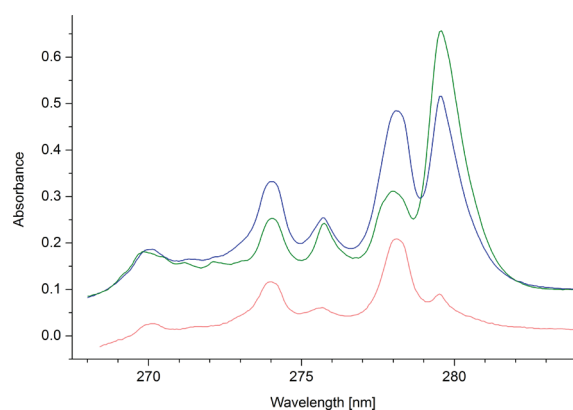


**Figure 6.** P5 part of the electronic absorption spectrum of  $C_{11}H_9^+$  produced from 1-methyl-naphthalene after deposition (blue trace) and after photobleaching the matrix (green). Cationic bands are better discernible in the spectrum from another experiment using a phenyl-acetylene + propyne precursor mixture (magenta).

absorptions in this region were saturated due to the high oscillator strength of transitions of the trapped species. Moreover, the bands of  $C_{11}H_9^+$  and  $C_{11}H_9^*$  overlap. All these effects preclude a rational comparison of their intensity with the systems discussed previously.

**3.2. Fluorescence Spectra.** All the prominent bands in the absorption spectrum recorded after depositing  $m/z = 141$  cations produced from PPey into neon have been excited with a pulsed, tunable laser in order to obtain wavelength-dispersed emission of the trapped species. PPey was chosen as the precursor of  $C_{11}H_9^+$  for the fluorescence studies because it shows all the systems that were observed using 1-MetN (Figure 2a); additionally, the 437 nm system, specific for chain and ring–chain precursors, is also present (Figure 4B, trace c). The search for emission features was started by exciting the longest-wavelength prominent absorption band at 562.2 nm (Figure 3) and continued toward the UV.

The excitation at 562.2 nm resulted in a structured emission starting at  $\sim 574$  nm. The (origin) band at around 562 nm could not be observed in this case, because measurements were started at a wavelength 2 nm longer than the excitation one in order to avoid overexposure of the CCD from the strong laser scatter. Upon exciting the next absorption band of the 562 nm system, an emission at 564.8 nm, together with the features seen before, appeared. The spectrum obtained for the excitation wavelength 536.8 nm, along with the 562 nm absorption system, is shown in Figure 7. The two are similar; the fluorescence corresponds to the 562 nm system of  $C_{11}H_9^+$ . Origins of the emission and absorption spectra overlap in the region where the bands have weak short- or long-wavelength shoulders, respectively, at 563.2 nm. This is the zero-phonon line (ZPL) of the onsets of the two spectra.

The 565 nm fluorescence system of  $C_{11}H_9^+$  has a regular pattern: strong and weak bands alternate. The former is based on the fundamental and overtone vibrations of the mode  $573\text{ cm}^{-1}$ , which is active in the ground state of  $C_{11}H_9^+$ . The weaker ones are associated with the  $311\text{ cm}^{-1}$  vibration (first band) and its combinations with the  $573\text{ cm}^{-1}$  fundamental (the remaining ones). In absorption, the first two bands correspond to modes of  $326$  and  $528\text{ cm}^{-1}$ , respectively. However, this latter system of  $C_{11}H_9^+$  is more complicated than the fluorescence. The third

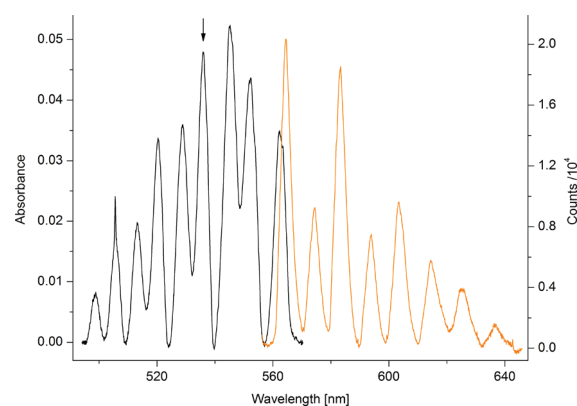


**Figure 7.** Electronic absorption (left) and fluorescence (right) spectra of  $C_{11}H_9^+$  recorded after depositing the cations produced from 1-phenyl-4-penten-1-yne into a neon matrix. The emission trace was obtained upon exciting the 536.8 nm feature (arrow) of the 562 nm absorption system. The intersection of the two spectra shows that the zero-phonon line of the origin bands is at 563.2 nm.

band lies  $866\text{ cm}^{-1}$  above the origin; it is  $14\text{ cm}^{-1}$  higher in energy than the combination of the two modes above. The fourth absorption corresponds to a  $1120\text{ cm}^{-1}$  vibration, which exceeds the overtone value of the  $528\text{ cm}^{-1}$  mode by  $64\text{ cm}^{-1}$ . Likely, more fundamentals are active in the 562 nm absorption system than in the corresponding fluorescence one (Tables 1 and 3), but not all are well-resolved, for example, between every second band of the former spectrum the absorbance does not reach the baseline. The absorption measurements showed that the intensity of the 562 nm system correlates well with that of starting at  $404.5\text{ nm}$ ; however, no emission has been detected upon excitation of individual bands of the latter system.

Another strong emission with onset at  $\sim 464\text{ nm}$  has been detected when the laser was scanned across the moderately intense absorption system with origin at  $462.6\text{ nm}$ . The first three absorption bands of this system have a sharp long-wavelength shoulder (ZPL) imposed onto a broad feature (Figure 8, top left trace). The emission obtained for the excitation of the ZPL of the second absorption band (at  $452.1\text{ nm}$ ) is shown in the top right trace of the figure. The red trace on the right shows the emission recorded when the maximum of this absorption band ( $451.1\text{ nm}$ ) was excited instead of its ZPL. These two fluorescence spectra have similar appearance and look like mirror images of the  $463\text{ nm}$  absorption system. The onset of the first one has a strong, narrow short-wavelength feature preceding a broad one (ZPL and phonon sideband). ZPLs of the origins of the emission and absorption spectra overlap at  $463.8\text{ nm}$ . The fluorescence spectrum recorded when the  $452.1\text{ nm}$  vibrational band ZPL was excited reveals more detail than that obtained from exciting the maximum of the same band. Many weak, narrow features (ZPLs of the individual vibrations) are resolved in this spectrum; they become smeared out in the second one.

The vibrational energies derived from the ZPL positions of individual fluorescence bands of the  $464\text{ nm}$  system (Figure 8, top right) are collected in Table 3. The most prominent emission features originate from relaxation to the two fundamental modes of energy  $561$  and  $1533\text{ cm}^{-1}$  in the ground state of  $C_{11}H_9^+$  and their overtones and combinations. The weaker peaks in this spectrum correspond to five other fundamentals:  $401$ ,  $887$ ,  $1182$ ,  $1396$ , and  $1485\text{ cm}^{-1}$ , which also form combination bands with the two mentioned above. All the bands (even the weakest ones

**Table 3. Fluorescence Band Maxima ( $\lambda_{\text{Ne}} \pm 0.1$  nm) of Electronic Transitions of  $\text{C}_{11}\text{H}_9^+$  Cationic Isomers in 6 K Neon Matrices and Assignments<sup>a</sup>**

$\lambda_{\text{Ne}}$ (nm)	$\nu$ ( $\text{cm}^{-1}$ )	$\Delta\nu$ ( $\text{cm}^{-1}$ )	assignment <sup>b</sup>
2-Naphthylmethylium (2-NyMe <sup>+</sup> )			
564.8 <sup>c</sup>	17 705	0	$0_0^0$ $X^1A' \leftarrow 1^1A'$
574.9	17 394	311	$\nu_{37}$
583.7	17 132	573	$\nu_{33}$
594.3	16 827	878	$\nu_{33} + \nu_{37}$
603.8	16 562	1143	$2\nu_{33}$
614.8	16 265	1440	$2\nu_{33} + \nu_{37}$
625.8	15 980	1725	$3\nu_{33}$
637.9	15 676	2029	$3\nu_{33} + \nu_{37}$
Benzotropylium (BzTr <sup>+</sup> ) <sup>d</sup>			
463.8 s	21 561	0	$0_0^0$ $X^1A_1 \leftarrow 1^1B_1$
472.6	21 160	401	$\nu_{19}$
476.2 s	21 000	561	$\nu_{18}$
483.7	20 674	887	$\nu_{16}$
485.5	20 597	964	$\nu_{18} + \nu_{19}$
489.4 m	20 433	1128	$2\nu_{18}$
490.7	20 379	1182	$\nu_{12}$
495.9	20 165	1396	$\nu_{10}$
498.1	20 076	1485	$\nu_8$
499.3 m	20 028	1533	$\nu_6$
503.5	19 861	1700	$3\nu_{18}$
504.9	19 806	1755	$\nu_{12} + \nu_{18}$
510.3	19 596	1965	$\nu_{10} + \nu_{18}$
512.5	19 512	2049	$\nu_8 + \nu_{18}$
513.7 m	19 467	2094	$\nu_6 + \nu_{18}$
519.6	19 246	2315	$2\nu_{18} + \nu_{12}$
522.4	19 142	2419	$\nu_6 + \nu_{16}$
524.4	19 069	2492	$\nu_6 + \nu_{18} + \nu_{19}$
525.2	19 040	2521	$2\nu_{18} + \nu_{10}$
529.1 w	18 900	2661	$2\nu_{18} + \nu_6$
530.5	18 850	2711	$\nu_6 + \nu_{12}$
536.6	18 636	2925	$\nu_6 + \nu_{10}$
539.3	18 543	3018	$\nu_6 + \nu_8$
540.5 w	18 501	3060	$2\nu_6$
545.5	18 332	3229	$3\nu_{18} + \nu_6$
547.0	18 282	3279	$\nu_6 + \nu_{12} + \nu_{18}$

<sup>a</sup> Fluorescence studies were carried out using 1-phenyl-4-penten-1-yne as precursor for the production of  $\text{C}_{11}\text{H}_9^+$ . <sup>b</sup> See footnote a of Table 1 for the totally symmetric vibrational fundamentals. <sup>c</sup> Based on the absorption (section 3.1) and fluorescence measurements, the zero-phonon line of the referred transition is at 563.2 nm. <sup>d</sup> Main spectral features (Figure 8, right) correspond to the two “most active” modes of energy 561 and 1533  $\text{cm}^{-1}$  in the ground state of BzTr<sup>+</sup>; their intensity is indicated as strong, medium, or weak (all others are very weak).

present) can be assigned to specific overtones or combinations of these seven modes. In the case of the 463 nm absorption system, the bands are broader and were recorded at a lower signal-to-noise ratio; as a consequence, only the most prominent bands, corresponding to the excitation based on the two vibrations 551 and 1590  $\text{cm}^{-1}$ , have been detected.

The same 464 nm fluorescence system has been seen when weak absorptions in the 290–340 nm range (Figure 8,

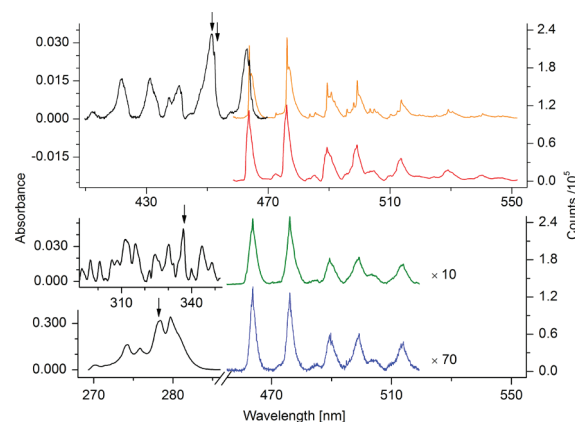


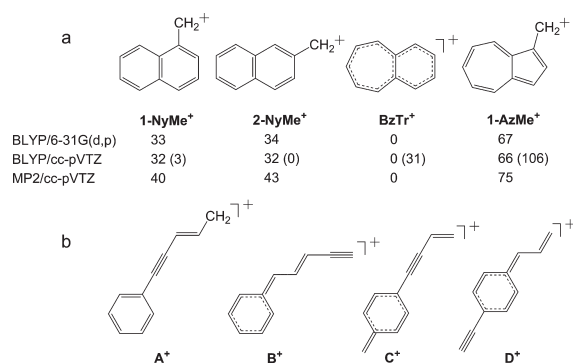
**Figure 8.** Electronic absorption (left) and fluorescence (right) spectra of  $\text{C}_{11}\text{H}_9^+$  recorded after depositing the cations produced from 1-phenyl-4-penten-1-yne into a neon matrix. Excitation wavelengths of the recorded emission traces are indicated on the corresponding absorption plots with arrows. The orange and red plots were obtained upon exciting the zero-phonon line at 452.1 or the band maximum at 451.1 nm, respectively.

middle left trace) or the strong one at 278.4 nm (bottom left) were excited. The resulting emission spectra, which belong to the excitation of the 336.3 and 278.4 nm absorption bands of  $\text{C}_{11}\text{H}_9^+$ , are shown in green and blue traces, respectively, of the same figure. Their intensity is about 10 and 70 times weaker than that for the excitation of the 463 nm visible absorption system, although the spectra were not normalized for the laser power, which is about an order of magnitude lower in the second harmonic regime,  $\lambda < 420$  nm.

These fluorescence measurements prove that the three absorption systems with onsets at 462.6,  $\sim 340$ , and 278.4 nm belong to the same  $\text{C}_{11}\text{H}_9^+$  isomer. It was not possible to deduce this on the basis of the recorded absorption spectra only, because the intensity of the second system was too modest to reliably relate it to others. Furthermore, the third, strong system with onset at 278.4 nm lies in the UV, where scattering in the matrix has a significant influence on the absorbance measurements; hence, the comparison of its intensity with other ones was also hindered.

The positions of the three correlating absorption systems lie near the wavelengths of broad absorptions of the benzotropylium cation (BzTr<sup>+</sup>) reported in an acidic solution at 425, 338, and 282 nm.<sup>36</sup> In that study, BzTr<sup>+</sup> was produced by dissolving the  $\text{LiAlH}_4$  reduction product of benzotropone, the pseudobase  $\text{C}_{11}\text{H}_9\text{OH}$ , in concentrated (60 %) sulfuric acid. Though somewhat different methods were applied for the synthesis of tropylium cation,<sup>37,38</sup> its spectrum in a strong sulfuric acid solution<sup>36,37</sup> agrees well with the one obtained in a 6 K neon matrix following mass-selective ( $m/z = 91$ ) deposition of  $\text{C}_7\text{H}_7^+$  cations.<sup>31</sup> Therefore, the three absorption systems with onsets at 462.6,  $\sim 340$ , and 278.4 nm are assigned to BzTr<sup>+</sup>.

In summary, the present absorption and emission studies on  $\text{C}_{11}\text{H}_9^+$  and  $\text{C}_{11}\text{H}_9^\bullet$  embedded in neon matrices reveal band systems that originate from several cationic and neutral species. Three absorption systems and the corresponding fluorescence spectrum have been assigned to BzTr<sup>+</sup>. Absorptions of neutral 1- and 2-NyMe<sup>•</sup> have also been identified; their cationic counterparts should also be present in the spectra. There are several systems that remained unassigned; in order to do so, theoretical

**Chart 1. Structures of (a) the Four Most Stable and (b) Four Considered Ring–Chain Isomers of  $C_{11}H_9^+$ <sup>a</sup>**

<sup>a</sup>All species are of planar  $C_s$  symmetry except BzTr<sup>+</sup> (planar  $C_{2v}$ ). Relative ground-state energies ( $\text{kJ mol}^{-1}$ , not corrected for zero-point vibrations) of the first four cations as well as the corresponding neutrals (in parentheses) are given at different levels of theory.

calculations on excitation energies of different isomers of  $C_{11}H_9^+$  and their neutrals were needed.

## 4. COMPUTATIONAL RESULTS

**4.1.  $C_{11}H_9^+$  Cations.** The  $C_{11}H_9^+$  cations and their corresponding neutrals are relatively large electronic systems (74/75 electrons); hence, they cannot be treated easily with high-level, *ab initio* methods. However, past work from this laboratory has shown that multiple isomers of a mass-selected ion can be trapped in solid neon in copious amounts in two cases: (a) if they partially relax thermally in the ion source and, thus, have energy within  $\sim 50 \text{ kJ mol}^{-1}$  of the most stable form or (b) if the product can directly be derived from the precursor by simple chemical reactions. Therefore, in order to select first the lowest-energy isomers of  $C_{11}H_9^+$ , geometries of expected as well as exotic structures were optimized with density functional theory (DFT) using the BLYP functional<sup>39,40</sup> and a small basis set, 6-31G(d,p). The four most stable structures, BzTr<sup>+</sup>, 1-NyMe<sup>+</sup>, 2-NyMe<sup>+</sup>, and 1-azulenylmethylmethylium (1-AzMe<sup>+</sup>), are shown together with their relative ground-state energies in Chart 1a. Other possible, higher-energy structures are collected in Chart S1 (Supporting Information).

The geometry of these four fused-ring isomers was then optimized with the same functional and a larger (cc-pVTZ) basis set. The calculations reveal that BzTr<sup>+</sup> is the lowest-energy structure on the  $C_{11}H_9^+$  potential energy surface. Two closely related species, 1- and 2-NyMe<sup>+</sup>, have nearly the same energy, lying  $32 \text{ kJ mol}^{-1}$  above BzTr<sup>+</sup>. The fourth isomer, 1-AzMe<sup>+</sup>, is  $66 \text{ kJ mol}^{-1}$  less stable than BzTr<sup>+</sup>. The ground-state energies computed using the small basis set agree well with the results obtained with the larger one (Chart 1a); thus, further discussion is restricted to these four most stable isomers.

Vibrational fundamentals were calculated with DFT at the BLYP/cc-pVTZ level of theory for the optimized structures. They can be compared directly with the experimental values derived from the emission spectra of  $C_{11}H_9^+$  (Table 3). For instance, in the case of BzTr<sup>+</sup>, seven modes ( $401, 561, 887, 1182, 1396, 1485, \text{ and } 1533 \text{ cm}^{-1}$ ) have been observed in the fluorescence spectrum (Figure 8, top right). Calculated totally symmetric fundamentals corresponding to the values above are

$406, 563, 889, 1179 \text{ or } 1192, 1378, 1488, \text{ and } 1504 \text{ or } 1570 \text{ cm}^{-1}$  (Table 1, footnote a). The  $1192 \text{ and } 1570 \text{ cm}^{-1}$  theoretical values are better candidates for the experimental  $1182 \text{ and } 1533 \text{ cm}^{-1}$  vibrations than the lower-energy ones, because calculations usually overestimate frequencies. The agreement is good and confirms the assignment. The other fluorescence system with onset at  $564.8 \text{ nm}$  (Figure 7) has a simpler structure based on two vibrations,  $306 \text{ and } 571 \text{ cm}^{-1}$ . The latter also forms overtones and combinations with the former one. The calculations predict frequencies  $297/567 \text{ and } 275/614 \text{ cm}^{-1}$  for 1- and 2-NyMe<sup>+</sup>, respectively. Although the former values are closer to the observation, it would be speculative to assign the  $565 \text{ nm}$  system to 1-NyMe<sup>+</sup> based on such small number of vibrations. The calculated frequencies can also be used as a guide for the assignment of vibrational bands of the electronic absorption systems observed in a neon matrix; however, a worse agreement is expected because the latter correspond to the excited state (Table 1).

Knowledge of the electronic energy levels and transition moments of a specific ion is crucial for the assignment of observed electronic systems to that species. Therefore, vertical excitation energies of the four aromatic isomers discussed above (Chart 1a) were calculated using time-dependent (TD) DFT method<sup>41</sup> with the same BLYP functional and cc-pVTZ basis set as for their ground state. In addition, the excitation energies were also obtained employing the second-order approximate coupled cluster (CC2) model<sup>42</sup> from ground-state geometries optimized at the second-order Møller–Plesset perturbation theory (MP2) level. The resolution-of-identity approximation was used also, which replaces four-center, two-electron integrals by three-center ones.<sup>43</sup> The excitation energies of BzTr<sup>+</sup> and 1- and 2-NyMe<sup>+</sup> computed using these two methods are collected along with their oscillator strengths in Table 4 and compared with the experimental values. A rough correlation can be seen; however, discrepancies are not exceptional even for quite small molecules using state-of-the-art theoretical approaches.<sup>44,45</sup> Although the TD DFT results show a somewhat better match with the observed transition energies, the higher-level CC2 data were considered for comparison; these are shown as stick diagrams together with the absorption spectrum of  $C_{11}H_9^+$  in Figure 9. The results for 1-AzMe<sup>+</sup> are listed in Table S1 (Supporting Information).

The theoretical excitation energies of BzTr<sup>+</sup> can be used to test their reliability, because the electronic systems of this cation have already been assigned on the basis of experiments only. The strongest transition has an energy  $4.91 \text{ eV}$  (around  $253 \text{ nm}$ , oscillator strength  $f = 0.91$ ) calculated by CC2; it is overestimated by  $0.46 \text{ eV}$  with respect to that detected at  $278.4 \text{ nm}$ . If a similar shift is applied to the two other, low-energy transitions calculated, then the origins of these weak systems are expected at around  $471 \text{ and } 361 \text{ nm}$ . These are close to those observed at  $463.8 \text{ and } \sim 340 \text{ nm}$ . In the latter case, the origin likely lies at somewhat lower wavelength and is masked by other absorptions.

Of the two NyMe<sup>+</sup> cations, the stick diagram of 2-NyMe<sup>+</sup> (Figure 9, trace b) resembles more the remaining two “main” band systems of  $C_{11}H_9^+$ . The predicted intense transition of 2-NyMe<sup>+</sup> at  $3.66 \text{ eV}$  ( $339 \text{ nm}$ ,  $f = 0.37$ ) needs to be shifted by  $-0.59 \text{ eV}$  to match the observed strong origin band at  $404.5 \text{ nm}$ . The other, weaker transition of energy  $2.24 \text{ eV}$  ( $554 \text{ nm}$ ) agrees well with the observed system origin at  $562.2 \text{ nm}$ . Thus, the two systems with onset at  $562.2 \text{ and } 404.5 \text{ nm}$ , for which good intensity correlation has been observed in all experiments, are assigned to 2-NyMe<sup>+</sup>. Because the weak band at  $579.6 \text{ nm}$  was identified as the origin band of a transition of neutral 1-NyMe<sup>0</sup>, it



**Table 4. Excited-State Symmetries, Vertical Excitation Energies ( $\Delta E$ ) and Transition Oscillator Strengths ( $f$ ) Computed with Two Methods for the Three Most Stable Isomers of  $C_{11}H_9^+$ , and Comparison with Experimental Data**

excited state	TD DFT//BLYP/cc-pVTZ		CC2//MP2/cc-pVTZ		expt <sup>a</sup> (eV)
	$\Delta E$ (eV)	$f$	$\Delta E$ (eV)	$f$	
1-NyMe <sup>+</sup> ( $X^1A'$ , planar $C_s$ )					
1 <sup>1</sup> A'	2.21	0.029	2.65	0.12	
2 <sup>1</sup> A'	2.60	0.083	2.90	0.091	
3 <sup>1</sup> A'	4.21	0.052	4.84	0.20	
4 <sup>1</sup> A'	4.43	0.060	5.13	0.0014	
5 <sup>1</sup> A'	4.66	0.0041	5.21	0.029	
6 <sup>1</sup> A'	5.09	0.099	5.71	0.050	
7 <sup>1</sup> A'	5.69	0.14			
8 <sup>1</sup> A'	5.84	0.58			
2-NyMe <sup>+</sup> ( $X^1A'$ , planar $C_s$ )					
1 <sup>1</sup> A'	1.82	0.027	2.24	0.064	2.21
2 <sup>1</sup> A'	3.35	0.0020	3.66	0.37	3.07
3 <sup>1</sup> A'	3.39	0.18	4.09	0.052	
4 <sup>1</sup> A'	4.67	0.10	5.42	0.064	
5 <sup>1</sup> A'	4.86	0.0077	5.47	0.53	
6 <sup>1</sup> A'	4.93	0.61	5.58	0.39	
7 <sup>1</sup> A'	5.40	0.013			
8 <sup>1</sup> A'	5.67	0.29			
BzTr <sup>+</sup> ( $X^1A_1$ , planar $C_{2v}$ )					
1 <sup>1</sup> B <sub>1</sub>	2.71	0.014	3.09	0.025	2.68
1 <sup>1</sup> A <sub>1</sub>	3.50	0.0009	3.89	0.0049	3.69
2 <sup>1</sup> B <sub>1</sub>	4.46	0.0051	4.98	0.018	
2 <sup>1</sup> A <sub>1</sub>	4.63	0.64	4.91	0.91	4.45
3 <sup>1</sup> A <sub>1</sub>	5.18	0.021	5.85	0.017	
3 <sup>1</sup> B <sub>1</sub>	5.26	0.21	5.83	0.30	
4 <sup>1</sup> B <sub>1</sub>	5.62	0.044			
4 <sup>1</sup> A <sub>1</sub>	5.76	0.054			

<sup>a</sup> Origin band of electronic transitions of  $C_{11}H_9^+$  observed in 6 K neon matrices of this study.

suggests that the 1-NyMe<sup>+</sup> cation should also be present. However, its absorptions could not be identified in the experiments; they are probably too weak or hidden underneath strong ones. The energetically least stable cationic isomer of the four in Chart 1a, 1-AzMe<sup>+</sup>, is unlikely to be present in the neon matrices of this study.

Apart from the absorptions of BzTr<sup>+</sup> and 2-NyMe<sup>+</sup>, three other cationic systems with onset at 457.5, 436.9, and 391.7 nm have been detected. These are precursor-specific: the first and last come together and are only present when a mixture of 2,4-HDy + acetylene was used for generation of the cations; the 437 nm system was the strongest when PPey was used. The structure of  $C_{11}H_9^+$  produced mostly from PPey must closely resemble the precursor; namely, constructed from a benzene ring and a hydrocarbon chain (Chart 1b, isomer A<sup>+</sup>). The other isomer(s) associated with the 2,4-HDy + acetylene mix should have similar, "head-and-tail" structure; three possibilities (B<sup>+</sup>–D<sup>+</sup>) are also shown in the same figure.

TD DFT and CC2 calculations were carried out to determine the excitation energies of these four considered ring–chain  $C_{11}H_9^+$

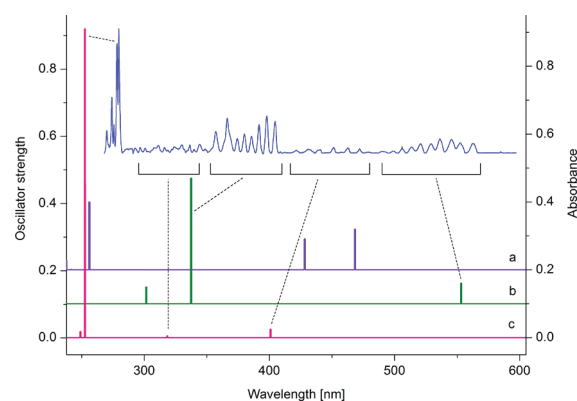


**Figure 9.** Comparison of the experimentally observed absorptions of  $C_{11}H_9^+$  (blue trace) with values calculated at the CC2//MP2/cc-pVTZ level of theory for (a) 1-naphthylmethyl cation, (b) 2-naphthylmethyl cation, and (c) benzotropylium.

isomers. The results are listed in Table S1 (Supporting Information). All isomers have a strong transition in the blue; D<sup>+</sup> has two. The CC2 excitation energies and oscillator strengths are as follows: A<sup>+</sup> (3.00 eV/413 nm,  $f = 1.3$ ); B<sup>+</sup> (3.23/384, 1.2); C<sup>+</sup> (2.94/422, 1.1); and D<sup>+</sup> (3.20/387, 0.57; 3.27/379, 0.59). The excitation energy of A<sup>+</sup> is not far from the onset of the 437 nm system, and because it has similar structure to the precursor used, PPey, the absorptions are assigned to this cation. The remaining two systems (onsets at 457.5 and 391.7 nm) are tentatively assigned to the C<sup>+</sup> and B<sup>+</sup> isomers, respectively, because the former has transition at longer wavelength than the latter.

**4.2.  $C_{11}H_9^{\bullet}$  Neutrals.** In contrast to  $C_{11}H_9^+$  with singlet ground state, the corresponding neutrals are open-shell systems; hence, they are more problematic objects for quantum chemical calculations. Nevertheless, all  $C_{11}H_9^{\bullet}$  isomers of the cations shown in Chart 1 were studied by (TD) DFT and CC2//MP2 methods. As opposed to the cations, the most stable isomer is the 2-NyMe<sup>•</sup> radical. Next is 1-NyMe<sup>•</sup>, predicted 3 kJ mol<sup>-1</sup> to higher energy, and the benzocycloheptadienyl (BzCh<sup>•</sup>) radical is at 31 kJ mol<sup>-1</sup> (Chart 1a). Apart from the ground-state energies, harmonic vibrational frequencies were also calculated with DFT at the BLYP/cc-pVTZ level of theory for the considered  $C_{11}H_9^{\bullet}$  structures. Those of the three "main" bicyclic isomers are collected in footnote a of Table S2 (Supporting Information). These cannot be compared directly with experimental ones, because fluorescence of neutrals has not been detected in this study. However, they were used as a guide for the assignment of the observed electronic absorption spectra of  $C_{11}H_9^{\bullet}$  (Table 2).

The optically allowed electronic transitions from the ground state of  $C_{11}H_9^{\bullet}$  were calculated using TD DFT and CC2 methods, the former with cc-pVTZ and the latter with cc-pVDZ basis set. The excitation energies and oscillator strengths are compiled in Tables S2 and S3 (Supporting Information). Energies of the lowest excited electronic state of 1- and 2-NyMe<sup>•</sup> predicted by CC2 are 3.27 and 3.33 eV (379 and 372 nm,  $f = 0.0009$  and 0.0036); they should be compared with the observed ones at 579.6 and 584.2 nm for the former and the latter isomers. The calculations overestimate the energy of these transitions by as much as  $\sim 1.2$  eV. The agreement between the computed and experimental excitation energies is worse than in the case of  $C_{11}H_9^+$ . The  $\sim 3$  times larger value of the so-called *D1* diagnostic<sup>46</sup> for the neutrals than for cations indicates the multireference character of the ground state of the radicals. Therefore, TD DFT calculations are also

expected to describe electronic transitions of neutral  $C_{11}H_9^\bullet$  worse than those of the cations.

However, TD DFT predicts a weak transition at 2.21 eV (561 nm) with oscillator strength  $f = 0.0004$  for 1-NyMe $^\bullet$  and at 2.06 eV (602 nm,  $f = 0.0015$ ) for 2-NyMe $^\bullet$ , which agree well with the observed ones in a neon matrix at 579.6 and 584.2 nm, respectively. A stronger transition ( $f = 0.035$ ) of 2-NyMe $^\bullet$  is predicted at 2.63 eV (472 nm), exactly where a medium-intensity neutral system is detected in a neon matrix. The calculated density of states in the experimentally accessible wavelength domain is higher for  $C_{11}H_9^\bullet$  than in the case of  $C_{11}H_9^+$ . According to the theory, the strongest transitions of 2-NyMe $^\bullet$  are located in the UV at 3.76, 4.73, and 4.78 eV (330, 262, and 259 nm) with  $f$  values 0.11, 0.29, and 0.14, respectively. The former matches the observed intense system with onset at 366.4 nm, the latter two were not seen in the experiments due to strong scattering in that region. Consequently, the three systems around 584, 472, and 366 nm, which preserved a constant intensity ratio in all recorded spectra, are assigned to the 2-NyMe $^\bullet$  radical.

The strongest transitions of 1-NyMe $^\bullet$  are predicted around 2.85, 3.17, 4.59, and 4.62 eV (435, 391, 270, and 268 nm) with  $f = 0.059, 0.048, 0.040,$  and  $0.043,$  respectively. These  $f$  values are smaller than the ones calculated for 2-NyMe $^\bullet$ . Only one weak band at 579.6 nm has been assigned to 1-NyMe $^\bullet$ . Another candidate is an absorption underneath the first vibrational band of the 366 nm system of 2-NyMe $^\bullet$ , at 357.0 nm. The weaker oscillator strengths and lower concentration of 1-NyMe $^\bullet$  in a neon matrix than for 2-NyMe $^\bullet$  are the reasons that no distinct band of this radical could be detected in the spectra.

The most intense neutral absorptions of the overview spectrum, Figure 2b, are in the P5 part (Figure 6). TD DFT foretells the strongest transition of the third "main" neutral isomer, BzCh $^\bullet$ , at 4.43 eV (280 nm,  $f = 0.29$ ) and several weaker ones around 2.57, 2.81, 3.56, and 4.23 eV (482, 441, 348, and 293 nm) with  $f$  values 0.018, 0.0083, 0.0037, and 0.0040, respectively. Exactly at the wavelength predicted for the strong transition of BzCh $^\bullet$  is observed the onset of the most intense absorption system of  $C_{11}H_9^\bullet$  at 280.2 nm in neon; therefore, it is assigned to this radical. Two much weaker transitions predicted around 482 and 441 nm are in the region where the medium-intensity 472 nm system of 2-NyMe $^\bullet$  is present and they likely overlap with it. The next calculated weak transition (348 nm) of BzCh $^\bullet$  corresponds to absorptions of neutrals present in part P4 of the spectrum recorded without an electron scavenger in the matrix (Figure 2b).

The precursor-dependent bands of  $C_{11}H_9^\bullet$  neutrals at 485.5, 464.5, and 447.6 nm have already been associated with the cationic transitions at 436.9, 457.5, and 391.7 nm, respectively, based on the absorption measurements. The latter three have been assigned tentatively to exotic  $C_{11}H_9^+$  isomers, namely, A $^+$ , C $^+$ , and B $^+$  (Chart 1b). TD DFT calculations predict strong, singular transitions at 3.39, 3.07, and 3.48 eV (366, 404, and 356 nm,  $f = 0.80, 0.67,$  and  $0.84$ ) for the belonging radicals (Table S3, Supporting Information). The excitation energies are thus overestimated by  $\sim 0.8$  eV for isomers A $^\bullet$  and B $^\bullet$  and by 0.3 eV for C $^\bullet$ .

## 5. CONCLUDING REMARKS

Transitions of two isomers, benzotropylium (BzTr $^+$ ) and 2-naphthylmethylum (2-NyMe $^+$ ), dominate the absorption spectra recorded after deposition of  $C_{11}H_9^+$  into neon matrices, regardless of the hydrocarbon used for ion production. The 1-methyl-naphthalene (1-MetN) precursor is not an exception;

however, any distinct band that would belong to 1-naphthylmethylum (1-NyMe $^+$ ) should be detected at least in this case. The absorptions of BzTr $^+$  and 2-NyMe $^+$  are present also in spectra obtained using open-chain and ring-chain initial materials; this indicates that isomerization of  $C_{11}H_9^+$  takes place in the ion source. BzTr $^+$  is the most stable structure on the potential energy surface of  $C_{11}H_9^+$ ; hence, it is not surprising that the absorptions of this cation are seen in the spectra for all precursors. 1- and 2-NyMe $^+$  have similar energies in the ground state; however, distinct absorptions of only 2-NyMe $^+$  have been observed instead of the expected 1-NyMe $^+$  for the 1-MetN precursor. Weak oscillator strengths of transitions of the latter does not fully explain this anomaly.

The 1-NyMe $^+$  cation initially formed from 1-MetN in the source rearranges producing BzTr $^+$  and 2-NyMe $^+$ . The reaction pathway and transition states call for a high-level, quantum chemical exploration. Unimolecular isomerization of simple aromatics such as benzene or naphthalene has been studied earlier by experimental and theoretical methods. Hydrogen shift as well as scrambling of isotope-labeled  $^{13}C$  carbon atoms have been observed.<sup>47</sup> Mechanisms were proposed to explain the automerization;<sup>47,48</sup> of course, more complex processes may play a significant role in discharges. The barrier for the isomerization of  $C_{11}H_9^+$  is likely higher than optical excitations (greater than  $\sim 4.5$  eV), because no photoconversion of the isomers has been observed upon UV irradiation of the matrices. BzTr $^+$  and 2-NyMe $^+$ , once excited, decay radiatively.

Absorptions of three other isomers of  $C_{11}H_9^+$ , besides those of BzTr $^+$  and 2-NyMe $^+$ , have been detected following deposition of the cations produced from 1-phenyl-4-penten-1-yne or a 2,4-hexadiyne + acetylene mixture. In these isomers, a benzene ring is fused with acyclic chain(s). TD DFT and CC2 calculations predict strong single transitions ( $f \sim 1$ ) in the visible for such cations and their corresponding neutrals.

The present work reveals that PAH-related compounds are readily formed from acyclic precursors. The reported electronic spectra serve as a starting point for gas-phase surveys and provide a means of direct monitoring in kinetic experiments on PAH formation.

## ■ ASSOCIATED CONTENT

**S Supporting Information.** Electronic absorption spectra of phenylacetylene and naphthalene cations, scheme of considered  $C_{11}H_9^+$  structures and their relative ground-state energy, calculated harmonic frequencies and vertical excitation energies of selected  $C_{11}H_9^+$  and  $C_{11}H_9^\bullet$  isomers and complete ref 23. This information is available free of charge via the Internet at <http://pubs.acs.org/>.

## ■ AUTHOR INFORMATION

### Corresponding Author

[j.p.maier@unibas.ch](mailto:j.p.maier@unibas.ch)

<sup>†</sup>Permanent address: Institute of Physics, Polish Academy of Sciences, Al. Lotników 32–46, PL-02668 Warsaw, Poland.

## ■ ACKNOWLEDGMENT

This work has been financed by the Swiss National Science Foundation (Project No. 200020-124349/1).

## REFERENCES

- (1) Cox, N. L. J. In *PAHs and the Universe: A Symposium to Celebrate the 25th Anniversary of the PAH Hypothesis*; Joblin, C., Tielens, A. G. G. M., Eds.; EAS Publications Series, Vol. 46; EDP Sciences: Les Ulis, France, 2011; p 349.
- (2) Tielens, A. G. G. M. In *PAHs and the Universe: A Symposium to Celebrate the 25th Anniversary of the PAH Hypothesis*; Joblin, C., Tielens, A. G. G. M., Eds.; EAS Publications Series, Vol. 46; EDP Sciences: Les Ulis, France, 2011; p 3.
- (3) Waite, J. H.; Young, D. T.; Cravens, T. E.; Coates, A. J.; Cray, F. J.; Magee, B. A.; Westlake, J. *Science* **2007**, *316*, 870.
- (4) Miller, J. A.; Klippenstein, S. J. *J. Phys. Chem. A* **2001**, *105*, 7254.
- (5) McEnally, C. S.; Pfefferle, L. D.; Atakan, B.; Kohse-Höinghaus, K. *Prog. Energy Combust. Sci.* **2006**, *32*, 247.
- (6) Richter, H.; Howard, J. B. *Prog. Energy Combust. Sci.* **2000**, *26*, 565.
- (7) Bockhorn, H.; Fetting, F.; Wenz, H. W. *Ber. Bunsen-Ges. Phys. Chem.* **1983**, *87*, 1067.
- (8) Frenklach, M.; Clary, D. W.; Gardiner, W. C.; Stein, S. E. *Proc. Combust. Inst.* **1984**, *20*, 887.
- (9) Wang, H.; Frenklach, M. *Combust. Flame* **1997**, *110*, 173.
- (10) Miller, J. A. *Proc. Combust. Inst.* **1996**, *20*, 461.
- (11) D'Anna, A.; Violi, A.; D'Allesio, A. *Combust. Flame* **2000**, *121*, 418.
- (12) Marinov, N. M.; Pitz, W. J.; Westbrook, C. K.; Lutz, A. E.; Vincentore, A. M.; Senkan, S. M. *Proc. Combust. Sci.* **1998**, *27*, 605.
- (13) Appel, J.; Bockhorn, H.; Frenklach, M. *Combust. Flame* **2000**, *121*, 122.
- (14) Wen, J. Z.; Thomson, M. J.; Lightstone, M. F.; Rogak, S. N. *Energy Fuels* **2006**, *20*, 547.
- (15) McKinnon, J. T.; Howard, J. B. *Proc. Combust. Inst.* **1992**, *24*, 965.
- (16) Ascenzi, D.; Aysina, J.; Tosi, P.; Maranzana, A.; Tonachini, G. *J. Chem. Phys.* **2010**, *133*, No. 184308.
- (17) Shukla, B.; Koshi, M. *Phys. Chem. Chem. Phys.* **2010**, *12*, 2427.
- (18) Garkusha, I.; Fulara, J.; Sarre, P. J.; Maier, J. P. *J. Phys. Chem. A* **2011**, *115*, 10972.
- (19) Newby, J. J.; Stearns, J. A.; Liu, C.-P.; Zwier, T. S. *J. Phys. Chem. A* **2007**, *111*, 10914.
- (20) Güthe, F.; Ding, H.; Pino, T.; Maier, J. P. *Chem. Phys.* **2001**, *269*, 347.
- (21) Fulara, J.; Nagy, A.; Garkusha, I.; Maier, J. P. *J. Chem. Phys.* **2010**, *133*, No. 024304.
- (22) Garkusha, I.; Fulara, J.; Nagy, A.; Maier, J. P. *J. Am. Chem. Soc.* **2010**, *132*, 14979.
- (23) Frisch, M. J.; et al. *Gaussian 03*, Revision C.01; Gaussian, Inc.: Wallingford, CT, 2004.
- (24) *Turbomole*, version 6.2, 2010; a development of University of Karlsruhe and Forschungszentrum Karlsruhe GmbH, 1989–2007, Turbomole GmbH, since 2007; available from <http://www.turbomole.com>.
- (25) Pino, T.; Douin, S.; Boudin, N.; Bréchnignac, Ph. *J. Phys. Chem. A* **2007**, *111*, 13358.
- (26) Xu, H.; Johnson, P. M.; Sears, T. J. *J. Phys. Chem. A* **2006**, *110*, 7822.
- (27) Boudin, N.; Pino, T.; Bréchnignac, Ph. *J. Mol. Struct.* **2001**, *563*, 209.
- (28) Andrews, L.; Kelsall, B. J.; Blankenship, T. A. *J. Phys. Chem.* **1982**, *86*, 2916.
- (29) Salama, F.; Allamandola, L. J. *J. Chem. Phys.* **1991**, *94*, 6964.
- (30) Negri, F.; Zgierski, Z. *J. Chem. Phys.* **1994**, *100*, 1387.
- (31) Nagy, A.; Fulara, J.; Garkusha, I.; Maier, J. P. *Angew. Chem., Int. Ed.* **2011**, *50*, 3022.
- (32) Nagy, A.; Garkusha, I.; Fulara, J.; Maier, J. P. 2011, manuscript in preparation.
- (33) Forney, D.; Althaus, H.; Maier, J. P. *J. Phys. Chem.* **1987**, *91*, 6458.
- (34) Mamedov, Kh. I.; Nasibov, I. K. *Opt. Spectrosc.* **1971**, *30*, 565.
- (35) Chalyavi, N.; Troy, T. P.; Nakajima, M.; Gilbson, B. A.; Nauta, K.; Sharp, R. G.; Kable, S. H.; Schmidt, T. W. *J. Phys. Chem. A* **2011**, *115*, 7959.
- (36) Naville, G.; Strauss, H.; Heilbronner, E. *Helv. Chim. Acta* **1960**, *43*, 1221.
- (37) Doering, W. v. E.; Knox, L. H. *J. Am. Chem. Soc.* **1954**, *76*, 3203.
- (38) Dewar, M. J. S.; Pettit, R. *J. Chem. Soc.* **1956**, 2021.
- (39) Becke, A. D. *Phys. Rev. A* **1988**, *38*, 3098.
- (40) Lee, C.; Yang, W.; Parr, R. G. *Phys. Rev. B* **1988**, *37*, 785.
- (41) Burke, K.; Werschnik, J.; Gross, E. K. U. *J. Chem. Phys.* **2005**, *123*, No. 062206.
- (42) Christiansen, O.; Koch, H.; Jørgensen, P. *Chem. Phys. Lett.* **1995**, *243*, 409.
- (43) Hättig, C.; Weigend, F. *J. Chem. Phys.* **2000**, *113*, 5154.
- (44) Stanton, J. F. *Faraday Discuss.* **2011**, *150*, 331.
- (45) Fortenberry, R. C.; King, R. A.; Stanton, J. F.; Crawford, T. D. *J. Chem. Phys.* **2010**, *132*, No. 144303.
- (46) Janssen, C. L.; Nielsen, I. M. B. *Chem. Phys. Lett.* **1998**, *290*, 423.
- (47) Bettinger, H. F.; Schreiner, P. R.; Schaefer, H. F., III; Schleyer, P. v. R. *J. Am. Chem. Soc.* **1998**, *120*, 5741.
- (48) Schwarz, H.; Bohlmann, B. *Org. Mass Spectrom.* **1973**, *7*, 23.



*"We shall meet in the place where there is no darkness."*

George Orwell (1903–1950), Nineteen Eighty-Four

# 6

## THE INDENE-BASED CATION FAMILY $C_9H_y^+$ ( $y = 7-9$ )

---

Besides the  $C_7H_7^+$  (Chapter 4) and  $C_{11}H_9^+$  (Chapter 5) systems, the study of another aromatic(-related) set of cations was undertaken, and electronic spectra of the indene-motif bicyclic hydrocarbon derivatives  $C_9H_y^+$  ( $y = 7-9$ ) are presented. In absorption, the spectra reveal transitions in the visible and near UV domains with onsets at 458.3 and 259.0 nm for 1-indenylum,  $C_9H_7^+$ ; 723.6, and 579.7 and 355.5 nm for  $\alpha$ - and  $\beta$ -indene radical cations ( $C_9H_8^{\bullet+}$ ), respectively; and 471.8 and 315.2 nm for 2-protonated indene,  $C_9H_9^+$ . Corresponding neutrals,  $C_9H_y$ , were identified by photobleaching matrices containing the cations. A complicated spectral pattern in the ~400–480 nm region due to overlapping systems (of different species) has been deciphered using the earlier introduced fluorescence method (Chapter 2). Chemical processes such as photoconversion between the two indene $^{\bullet+}$  isomers, and upon irradiation  $H_2$  loss of  $C_9H_9^{\bullet}$  were also observed. Assignments are given and supported by DFT computations.

### 6.1 INTRODUCTION

Although mass selectivity as described earlier (Chapter 2) is indeed a crucial tool in the characterization of transient species, numerous different structures can still be drawn with one particular constitutional formula, which is especially the case when  $m/z$  is large enough. An example for this has been presented in Chapter 5. Equilibrium is not (or only partially) established in the discharge-type sources employed (Chapter 2). Co-existing isomers can be produced by similar chemistry and detected, *e.g.*, via reaction rates; recent IR work shows that the emerging ion abundances do not necessarily represent stability trends.<sup>1</sup> Furthermore, neutralization rates may differ in the matrix environment. However, past work from

---

<sup>1</sup> See, *e.g.*, studies from the research group of M.A. Duncan, J.M. Lisy or M.A. Johnson.

this laboratory as well as results described in earlier chapters of the present work have shown that multiple isomers of a given mass-selected ion can be trapped in neon only if (a) they have a relative internal energy within ~50 kJ mol<sup>-1</sup> of the most stable form, or (b) the product can be directly derived from the precursor by simple bond-breaking or formation processes. These clues are reliable initializations for the restriction of isomers to be considered. In this chapter, electronic spectra of a series of cations built on an indene skeleton (Figure 6.1) are described. These provide another archetype of fused-ring aromatics and reveal again the complexity of the study of these species.

## 6.2 1-INDENYLIUM, C<sub>9</sub>H<sub>7</sub><sup>+</sup>

The hydrocarbon C<sub>9</sub>H<sub>7</sub><sup>+</sup> is an abundant fragment of a number of organic precursors; it is also formed in ion–molecule reactions.<sup>2</sup> Its *m/z* = 115 peak is seen in the mass spectra of naphthalene and dihydro-naphthalene,<sup>3</sup> biphenyl, from a mixture of linear hydrocarbons (Chapter 5),<sup>4</sup> and many more from this laboratory.<sup>5</sup> As it is produced from such a variety of starting materials and found ‘among’ (that is, differing by a CH unit) stable, cyclic-skeleton ions such as *m/z* = 102 (phenylacetylene<sup>•+</sup>) and 128 (naphthalene<sup>•+</sup>) (Chapter 5), it is expected to be the most stable isomer on the C<sub>9</sub>H<sub>7</sub><sup>+</sup> PES. An MS study has shown that the cation has the same structure generated from various C<sub>10</sub>H<sub>10</sub> compounds or indene by low-energy electron ionization.<sup>6</sup>

For these reasons, in order to select the relevant isomer(s) of C<sub>9</sub>H<sub>7</sub><sup>+</sup>, the geometry of expected as well as exotic structures was optimized with DFT using the B3LYP functional and a small basis set, 6-31G(d,p). Considered species are listed in Figure 6.2 with their relative ground-state energy. These calculations predict that the most stable isomer is the anticipated 1-indenylium cation (labeled **115+** from this point onward) (Figure 6.1). In order to confirm this, spectroscopy is needed.

---

<sup>2</sup> See, *e.g.*, (a) P.M. Lalli, Y.E. Corilo, P.V. Abdelnur, M.N. Eberlin, K.K. Laali. *Org. Biomol. Chem.* **2010**, 8(11): 2580–2585; (b) S.-T. Lin, M.-L. Lin, W.-C. Lin. *Org. Mass Spectrom.* **2005**, 25(12): 667–670.

<sup>3</sup> I. Garkusha, A. Nagy, J. Fulara, M.F. Rode, A.L. Sobolewski, J.P. Maier. *J. Phys. Chem. A* **2012**, published online; doi: 10.1021/jp310612j.

<sup>4</sup> A. Nagy, J. Fulara, J.P. Maier. *J. Am. Chem. Soc.* **2011**, 133(49): 19796–19806.

<sup>5</sup> Unpublished results (Appendix A).

<sup>6</sup> C. Dass, M.L. Gross. *Org. Mass Spectrom.* **1983**, 18(12): 542–546.

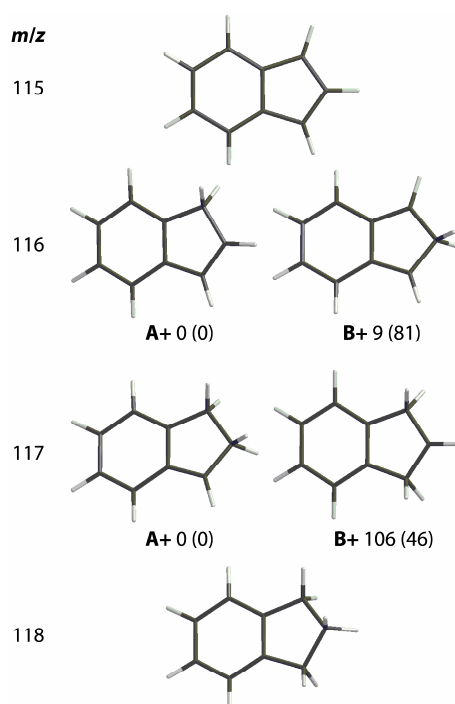


**Figure 6.1:** Graphical representation of the considered 'main' isomers of  $C_9H_y^+$  ( $y = 7-10$ ) of the present study. Relative ground-state energy ( $\text{kJ mol}^{-1}$ , corrected for ZPE) of the indene and protonated indene cations and corresponding neutrals (in parentheses) was calculated with DFT at the (u)BLYP/cc-pVDZ level of theory.

$C_9H_7^+$  cations were produced from indene vapor and selectively deposited to form a matrix sample; the spectrum obtained is shown in [Figure 6.3a](#). Several sharp peaks alternating with broad bands dominate in the 390–470 nm range. The system of broad features with an origin at 458.2 nm lost, whereas the sharp ones starting at 464.7 nm gained intensity after irradiation with an mpHg lamp; no new bands appeared ([Figure 6.3b](#)). Because of the mass selection, the use of an electron scavenger and the observed behavior upon irradiation, the broad absorptions are of cationic  $C_9H_7^+$  and the narrow ones belong to neutral  $C_9H_7^\bullet$ . Bands of the neutrals can be subtracted to better visualize the features originating from  $C_9H_7^+$ ; this was done after properly scaling trace b to the same intensity of the 465 nm peak on trace a. The resulting cationic net curve is [Figure 6.3c](#).

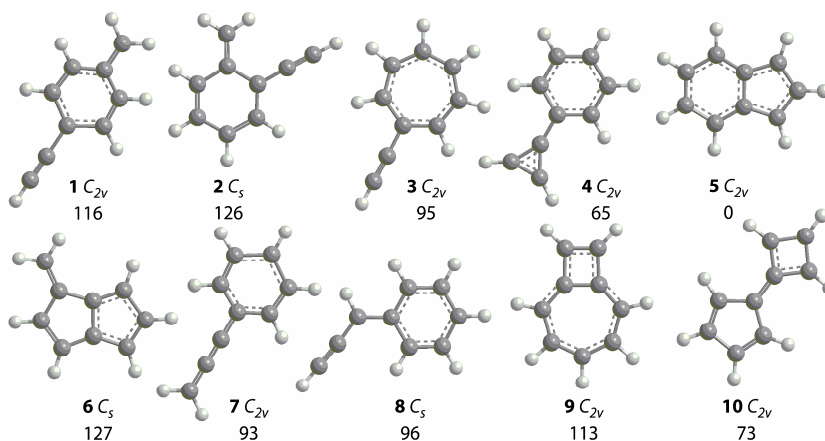


**Figure 6.2:** Scheme and group symmetry of some considered  $C_9H_7^+$  ( $m/z = 115$ ) cations. The indicated relative ground-state energy ( $\text{kJ mol}^{-1}$ , corrected for zero-point vibrations) of the isomers was calculated with DFT at the B3LYP/6-31G(d,p) level. As seen, no structure is within  $50 \text{ kJ mol}^{-1}$  of 1-indenylium, "5".

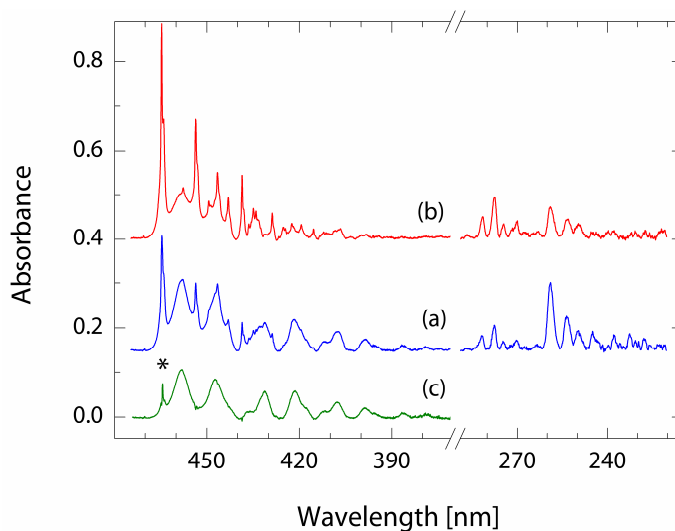


**Figure 6.3:** Electronic absorption spectra recorded after (a) mass-selective deposition of  $C_9H_7^+$  ( $m/z = 115$ ) cations, produced from indene vapor diluted with helium in a hot-cathode discharge source, into a 6 K neon matrix and (b) subsequent 1 h irradiation of the matrix sample with a mpHg lamp. The cationic features of the visible spectral domain are better discernible in trace c, which was obtained by subtracting trace a from b after proper intensity scaling. Asterisk denotes 'residual' neutral absorption due to a peak shoulder in trace a.



**Table 6.1:** Absorption band maxima ( $\lambda_{\text{Ne}} \pm 0.1$  nm) of electronic transitions of  $\text{C}_9\text{H}_7^+$  and  $\text{C}_9\text{H}_7^\bullet$  observed in 6 K neon matrices and their assignment

$\lambda_{\text{Ne}}$ [nm]	$\tilde{\nu}$ [a] [ $\text{cm}^{-1}$ ]	$\Delta\tilde{\nu}$ [ $\text{cm}^{-1}$ ]	Assignment <sup>[b]</sup>
<b><math>\text{C}_9\text{H}_7^+</math> 115+</b>			
458.2	21 822	0	$0_0^0$ (1) <sup>1</sup> A <sub>1</sub> ← $\tilde{X}$ <sup>1</sup> A <sub>1</sub>
447.3	22 356	534	$\nu_{15}$ (benzene distortion)
436.5	22 909	1087	$2\nu_{15}$ or $\nu_{11}$
431.3	23 186	1364	$\nu_8$ (two-ring distortion)
421.5	23 725	1903	$\nu_{15} + \nu_8$
412.2	24 262	2440	$\nu_8 + 1087$
407.7	24 528	2706	$2\nu_8$
398.7	25 084	3262	$2\nu_8 + \nu_{15}$
386.4	25 879	4057	$3\nu_8$
258.9	38 620	0	$0_0^0$ (2) <sup>1</sup> A <sub>1</sub> ← $\tilde{X}$ <sup>1</sup> A <sub>1</sub>
253.6	39 440	820	$\nu_{13}$
249.6	40 067	1447	$\nu_7$
244.9	40 827	2207	
<b><math>\text{C}_9\text{H}_7^\bullet</math> 115<sup>[c]</sup></b>			
464.7 s	21 520	0	$0_0^0$ (1) <sup>2</sup> A <sub>1</sub> ← $\tilde{X}$ <sup>2</sup> A <sub>2</sub>
457.7	21 850	330	
453.6 s	22 045	525	$\nu_{15}$
449.4	22 252	732	$\nu_{14}$
446.6 s	22 394	874	$\nu_{13}$
443.0 m	22 571	1051	$2\nu_{15}$ or $\nu_{11}$
438.6 s	22 801	1281	
436.4	22 914	1394	$\nu_{15} + \nu_{13}$
434.9	22 995	1475	$\nu_6$
434.1	23 038	1518	
433.0	23 092	1572	$3\nu_{15}$
428.8 m	23 322	1802	$\nu_{15} + 1281$
425.2	23 519	1999	
422.5	23 670	2150	
419.4	23 845	2325	$2\nu_{15} + 1281$
415.4	24 075	2555	$2 \times 1281$
281.6	35 516	0	$0_0^0$ (4) <sup>2</sup> B <sub>1</sub> ← $\tilde{X}$ <sup>2</sup> A <sub>2</sub>
277.7	36 014	498	$\nu_{15}$
274.6	36 415	899	$\nu_{13}$
271.8	36 787	1271	
270.2	37 017	1501	

[a]  $\tilde{\nu} = 1/\lambda_{\text{Ne}}$ . [b] Vibrational assignments in the excited states are based on ground-state fundamentals calculated with DFT at the (u)BLYP/cc-pVDZ level of theory, and listed in Table 6.2. [c] s: strong; m: medium; all other bands are weak.

The cationic system commencing at 458 nm consists of several broad bands extending to below 400 nm. The vibrational progression in the excited state is built on two ‘main’ modes of energy 534 and 1364  $\text{cm}^{-1}$  (Table 6.1). The sharp peaks of neutral origin are piled onto these (Figure 6.3, traces a and b); their wavelength maxima are also listed in the same table.

Besides these visible systems, two additional were detected in the UV range. First, starting at 258.9 nm is one of neutral origin as it turns stronger after mpHg bleaching; the next with an onset at 281.6 nm is due to cations because it decreased in intensity upon UV irradiation of the matrix (Figure 6.3, traces a and b).

The 458 and 259 nm absorption systems shall be of the same cationic C<sub>9</sub>H<sub>7</sub><sup>+</sup>, **115+** (Figure 6.1); the 465 and 282 nm systems are then of the corresponding neutral C<sub>9</sub>H<sub>7</sub><sup>•</sup>, **115**. This is inferred from the facts that (a) the two cationic systems decay at the same rate as well as the neutrals grow similarly upon bleaching, (b) no other absorptions were seen in the spectra—except C<sub>9</sub>H<sub>8</sub><sup>•+</sup> cations due to a lower than ±0.5 u mass resolution and/or the <sup>13</sup>C/<sup>12</sup>C natural isotopic ratio (~1.1 %); see Section 6.3—and (c) computational results (Section 6.5). These together provide sufficient basis for the designation of the systems (Table 6.1), even though only one precursor was used, no fluorescence was observed upon exciting the absorptions, and neutrals and cations were found both relatively photostable. Furthermore, the neutral at 465 nm is likely not the one detected in the gas phase,<sup>7</sup> where a neutral C<sub>9</sub>H<sub>7</sub><sup>•</sup> species (1-phenylpropargyl, corresponding to structure “8” in Figure 6.2) was found to absorb at 476, 459.4, 456.2 and 455.2 nm, and emit strongly at 476 and 503 nm. The origin in the gas phase is at 21 007 cm<sup>-1</sup>, red shifted by as much as 815 cm<sup>-1</sup> from the neon matrix value (Table 6.1), as well as its relative energy is out of the ‘right’, 50 kJ mol<sup>-1</sup> frame (Figure 6.2). Moreover, the neutral absorption at 465 nm is a fragment of protonated indene upon UV irradiation, involving neutralization and H<sub>2</sub> loss (Section 6.4). This provides an additional confirmation of the inferred stable, bicyclic structure. An assignment of the systems is given in Table 6.1; it is based on TD DFT results (Section 6.5) and totally symmetric ground-state frequencies (Table 6.2).

---

<sup>7</sup> N.J. Reilly, D.L. Kokkin, M. Nakajima, K. Nauta, S.H. Kable, T.W. Schmidt. *J. Am. Chem. Soc.* **2008**, *130*(10): 3137–3142.

**Table 6.2:** Ground-state totally symmetric ( $a'$  in  $C_5$  or  $a_1$  in  $C_{2v}$ ) vibrational fundamentals ( $\text{cm}^{-1}$ , unscaled) of  $C_9H_y^+$  cations and  $C_9H_y$  neutrals ( $y = 7-10$ ) calculated with DFT at the (u)BLYP/cc-pVDZ level of theory

Nr.	Cations						Neutrals						
	$C_9H_7^+$		$C_9H_8^{*+}$		$C_9H_9^+$		$C_9H_7^*$		$C_9H_8$		$C_9H_9^*$		$C_9H_{10}$
	<b>115+</b>	<b>116A+</b>	<b>116B+</b>	<b>117A+</b>	<b>117B+</b>	<b>118+</b>	<b>115</b>	<b>116A</b>	<b>116B</b>	<b>117A</b>	<b>117B</b>	<b>118</b>	
1	3186	3159	3153	3140	3136	3137	3158	3143	3143	3124	3129	3110	
2	3148	3144	3142	3129	3126	3124	3131	3119	3114	3116	3114	3083	
3	3143	3143	3128	3125	3117	3053	3119	3115	3092	3103	3088	3015	
4	3125	3134	2932	3117	2870	2976	3093	3102	2925	3089	2866	2989	
5	1618	3130	1517	3114	1551	2968	1571	3090	1524	3083	1571	2959	
6	1490	3121	1465	2966	1432	2861	1441	3084	1490	2955	1458	2919	
7	1442	2949	1399	2931	1349	1503	1427	2937	1398	2911	1385	1571	
8	1372	1600	1349	1595	1269	1437	1340	1595	1335	1558	1338	1458	
9	1180	1497	1292	1536	1201	1411	1185	1579	1316	1534	1258	1433	
10	1159	1457	1214	1492	1185	1349	1138	1547	1205	1452	1190	1411	
11	1055	1415	1156	1443	1147	1326	1041	1442	1134	1420	1138	1339	
12	981	1390	992	1398	1008	1253	1003	1437	961	1413	1015	1257	
13	843	1379	925	1369	899	1194	844	1368	913	1393	903	1201	
14	725	1346	819	1361	809	1150	731	1357	813	1370	791	1181	
15	527	1326	715	1316	710	1119	534	1308	708	1313	691	1139	
16		1274	529	1279	523	970		1265	532	1261	519	1023	
17		1228		1275		962		1202		1258		1014	
18		1196		1225		929		1186		1204		917	
19		1142		1173		878		1143		1158		888	
20		1134		1171		791		1135		1144		839	
21		1096		1147		748		1091		1127		743	
22		1049		1096		708		1044		1076		729	
23		981		996		611		1011		1003		603	
24		921		989		510		927		985		507	
25		840		903		392		844		892		416	
26		802		848		215		817		847		251	
27		711		797		118		721		782		144	
28		576		703				585		690			
29		508		574				527		573			
30		380		521				376		521			
31				376						373			

Although **115+** has eight ( $= 4x$ ) valence electrons and, thereby, is anti-aromatic, it is a planar hydrocarbon with a fused-ring skeleton and is worthwhile to probe its Hückel transition energy. The relevant eigenvalue coefficients are  $x_j = +0.729$  (HOMO),  $+0.295$  (LUMO) and  $-0.902$ ; thus, the energy of the intense transition (Figure 6.3) is predicted to be  $(0.729 + 0.902) \times 20\,000\text{ cm}^{-1}$ , that is, 307 nm. This is a poor estimate for the observed value at 458 nm in neon (Table 6.1), which—after showing reasonable matches for two aromatics,  $C_7H_7^+$  (Chapter 4) and  $C_{11}H_9^+$  (Chapter 5)—finally indicates the defects/breakdown of the HMO method, too.

6.3 INDENE RADICAL CATIONS,  $C_9H_8^{\bullet+}$ 

Figure 6.4a depicts the spectrum of  $m/z = 116$  cations produced from an indene/helium mixture. Besides the cationic features commencing at  $\sim 458$  nm and neutrals at ca. 465 nm—absorptions of **115+** and **115** as already identified (Section 6.2)—, several new systems are in the spectrum. **115+** and **115** are present because of a mass resolution somewhat worse than  $\pm 0.5$  u and/or partial fragmentation upon deposition. All the other systems are of cationic origin, because their intensity decreased after irradiation with a mpHg lamp (not shown in the figure). Their onsets are at around 724, 580 and 356 nm (Table 6.3).

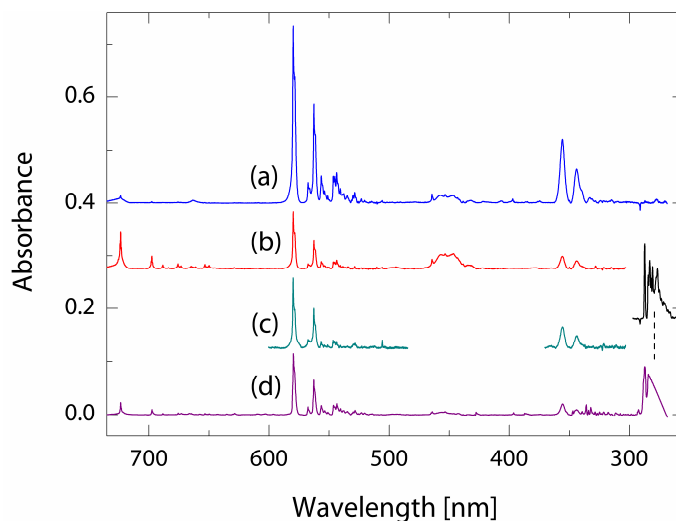


**Figure 6.4:** Electronic absorption spectra recorded after (a) mass-selective trapping of  $C_9H_8^{\bullet+}$  ( $m/z = 116$ ), produced from indene, in a neon matrix and (b) subsequent 15 min,  $308 < \lambda < 390$  nm irradiation of the sample with a Xe arc. In (c)  $C_9H_8^{\bullet+}$  was synthesized from a mixture of linear hydrocarbon precursors in the ion source ( $\times 0.5$ ), whereas for (d) in a  $CH_2^+$  (normalized to 25  $\mu$ C deposited charge) + indene ionization reaction taking place upon matrix formation (see text). The black trace corresponds to a spectrum measured after direct deposition of indene vapor mixed with neon in a low concentration.

The lowest energy absorption is at 723.6 nm (Figure 6.4a); it is the weakest one. Only one band was found to belong to a vibrational progression in the excited state, spaced  $515\text{ cm}^{-1}$  from the origin. These two have the same multiplet structure, having a side band  $\sim 10\text{--}12\text{ cm}^{-1}$  from the maximum. After selective UV bleaching with a  $308 < \lambda < 390$  nm bandpass filter, the system grew at the expense

of the 580 and 356 nm absorptions (Figure 6.4b). Its vibrational structure is much more pronounced in this case: Several additional modes such as 704, 809 and 976  $\text{cm}^{-1}$ , their overtones and combinations are active (Table 6.3).

**Table 6.3:** Observed absorption band maxima ( $\lambda_{\text{Ne}} \pm 0.1$  nm) of electronic transitions of  $\text{C}_9\text{H}_8^{\bullet+}$  isomers in neon matrices and the assignments

$\lambda_{\text{Ne}}$ [nm]	$\tilde{\nu}$ [a] [ $\text{cm}^{-1}$ ]	$\Delta\tilde{\nu}$ [ $\text{cm}^{-1}$ ]	Assignment <sup>[b]</sup>
<b><math>\text{C}_9\text{H}_8^{\bullet+}</math> 116B+</b>			
723.6	13 819	0	$0_0^0$ ( $1$ ) <sup>2</sup> B <sub>2</sub> ← $\tilde{X}$ <sup>2</sup> A <sub>2</sub>
703.2	14 220	401	
697.6	14 334	515	$\nu_{16}$
688.6	14 523	704	$\nu_{15}$
683.6	14 628	809	$2 \times 401$ or $\nu_{14}$
675.9	14 795	976	
673.2	14 854	1035	$2\nu_{16}$
664.8	15 042	1223	$\nu_{16} + \nu_{15}$ or $\nu_{10}$
661.1	15 126	1307	$\nu_{16} + \nu_{14}$ or $\nu_9$
657.0	15 221	1402	$2\nu_{15}$ or $\nu_7$
653.5	15 303	1484	$\nu_{16} + 976$ or $\nu_6$
650.1	15 383	1564	
645.0	15 504	1685	$\nu_{15} + 976$
<b><math>\text{C}_9\text{H}_8^{\bullet+}</math> 116A+</b>			
579.7	17 249	0	$0_0^0$ ( $2$ ) <sup>2</sup> A' ← $\tilde{X}$ <sup>2</sup> A''
567.6	17 619	370	$\nu_{30}$
562.7	17 771	522	$\nu_{29}$
556.5	17 970	721	$\nu_{27}$
553.7	18 059	810	$\nu_{26}$
551.0	18 149	900	$\nu_{30} + \nu_{29}$
546.4	18 303	1054	$\nu_{22}$
545.1	18 344	1095	$\nu_{30} + \nu_{27}$ or $\nu_{21}$
543.5	18 399	1150	$\nu_{20}$
540.4	18 503	1254	$\nu_{29} + \nu_{27}$ or $\nu_{17}$
538.6	18 566	1317	$\nu_{29} + \nu_{26}$
537.7	18 598	1349	$\nu_{15}$
534.6	18 705	1456	
531.1	18 829	1580	$\nu_{29} + \nu_{22}$
529.9	18 870	1621	$2 \nu_{26}$ or $\nu_{30} + 1254$ or $\nu_8$
528.4	18 925	1676	$\nu_{29} + \nu_{20}$
525.6	19 026	1777	$\nu_{29} + 1254$ or $\nu_{27} + \nu_{22}$
522.9	19 123	1874	$\nu_{29} + \nu_{15}$
355.5	28 128	0	$0_0^0$ ( $5$ ) <sup>2</sup> A' ← $\tilde{X}$ <sup>2</sup> A''
343.8	29 086	958	$\nu_{24/23}$
339.5	29 452	1324	$\nu_{16/15}$
332.7	30 054	1926	$2\nu_{24/23}$

[a]  $\tilde{\nu} = 1/\lambda_{\text{Ne}}$ . [b] Vibrational assignments in the excited states are based on ground-state modes calculated with DFT at the uBLYP/cc-pVDZ level (Table 6.2).

The second system is the strongest of the spectrum (Figure 6.4a), starting at 579.7 nm. The most intense feature is the origin, followed by an extended vibrational progression with several bands of alternating intensity and involving numerous low-energy modes (Table 6.3). The highest-energy transition detected in the spectrum consists of several bands with an onset at 355.9 nm (Figure 6.4a). They are broader but still resolved: spaced 958, 1324 and 1926 cm<sup>-1</sup> from the origin (Table 6.3).

The same cationic absorptions are present in the spectra obtained from a linear hydrocarbon precursor mixture, 2,4-hexadiyne and acetylene (Figure 6.4c; see Chapter 5), as well as from the fragmentation of indane (not shown). They are also produced when neutral indene vapour was directly deposited in a neon matrix and, simultaneously, bombarded by CH<sub>2</sub><sup>+</sup> from the discharge ion source (Figure 6.4d). This implies that CH<sub>2</sub><sup>+</sup> and indene do not react with each other in the classical sense in such an experimental configuration, but rather a single ionization takes place such as it was in the case of impacting naphthalene with H<sup>+</sup> or H<sub>3</sub><sup>+</sup> (Appendix A).

UV irradiation of the matrix with a Xe light source during measurement induced changes in the spectra, reducing the intensity of the 580 and 356 nm systems; at the same time that at 724 nm became stronger. The broad bump at 475 nm, underneath **115+** and **115**, got more intense, too. These effects are better seen after 10–20 min irradiation of the matrix with the same xenon lamp confined in the 310–390 nm range (Figure 6.4b). Relative intensity of the 580 and 356 nm systems correlate well from different precursors; their decay upon irradiation do so perfectly. Thus, the absorptions at 724, and 580 and 356 nm are assigned to two different isomers of C<sub>9</sub>H<sub>8</sub><sup>+</sup>, **116B+** and **116A+**, respectively (Table 6.3). The presence of both these in the spectra is not surprising in view of their similar stability (Figure 6.2).

The irradiation scheme **116A+** → **116B+** is a photo-induced isomerization process similar to that of planar C<sub>6</sub>H<sub>4</sub><sup>+</sup> species and protonated naphthalenes, HN<sup>+</sup>s (Appendix A). ‘Pump-back’ attempts were done to convert the isomer whose absorptions start at 724 nm (**116B+**) back into the by ca. ~9 kJ mol<sup>-1</sup> more stable **116A+** form (Figure 6.2). Several irradiation schemes such as λ > 570 nm Hlg or Xe, 15 min λ > 480 nm Xe, and 40 min λ > 510 nm mpHg were tried. Intensity

decrease of the 724 nm system was seen; however, no direct correlation could be found with the other isomer, not as in the cases of  $C_6H_4^+$  and  $HN^+$  (Appendix A).

#### 6.4 2-PROTONATED INDENE, $C_9H_9^+$

In Figure 6.5, the spectrum of  $m/z = 117$  cations produced from an indane/helium vapor mixture and deposited with  $CH_3Cl$  (trace a) is compared to that recorded without an electron scavenger (trace b); the latter was scaled to match the intensity of the neutral 471 nm system in the former. Two cationic systems can be identified. The first, weak one consists of a series of absorptions with an onset at 475.8 nm. Its bands are broad, asymmetric and several sharp peaks imposed onto them are apparent (Figure 6.5a). As is seen from Figure 6.5b, neutrals and cations overlap; their features can not be distinguished everywhere from each other, neither can zero-phonon lines (ZPLs) and side bands be discriminated. Therefore, in Table 6.4 a selection of the recorded values are given—only the maxima for several bands of the vibrational progression.

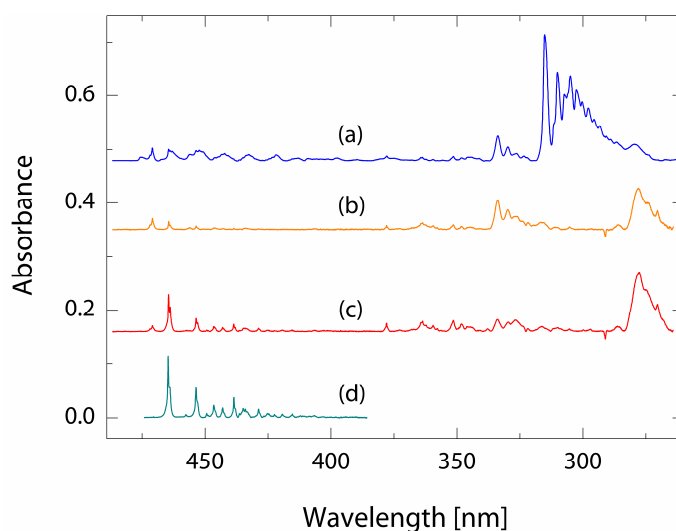


**Figure 6.5:** Electronic absorption spectra recorded after mass-selective deposition of  $C_9H_9^+$  ( $m/z = 117$ ) cations, produced from indane vapor in a discharge-type source, into a 6 K neon matrix (a) mixed with  $CH_3Cl$  and (b) without an electron scavenger, the latter scaled to the strength of the neutral absorption around 471 nm in trace a. Trace c was obtained after irradiating the matrix that corresponds to trace b. In (d) the visible part of the spectrum of neutral  $C_9H_7^\bullet$  ( $m/z = 115$ ) is shown.

**Table 6.4:** Absorption band maxima ( $\lambda_{\text{Ne}} \pm 0.1$  nm) of electronic transitions of C<sub>9</sub>H<sub>9</sub><sup>+</sup> and C<sub>9</sub>H<sub>9</sub><sup>•</sup> observed in 6 K neon matrices and their assignment

$\lambda_{\text{Ne}}$ [nm]	$\tilde{\nu}$ [a] [cm <sup>-1</sup> ]	$\Delta\tilde{\nu}$ [cm <sup>-1</sup> ]	Assignment <sup>[b]</sup>
<b>C<sub>9</sub>H<sub>9</sub><sup>+</sup> 117A<sup>+</sup></b>			
475.8 <sup>[c]</sup>	21 017 max	0	0 <sub>0</sub> <sup>0</sup> (1) <sup>1</sup> A' ← $\bar{X}$ <sup>1</sup> A'
467.6	21 385	368	v <sub>31</sub>
463.0	21 597 max	580	v <sub>29</sub>
456.6	21 899	882	v <sub>26</sub>
452.3	22 109 max	1092	v <sub>22</sub>
450.8	22 185	1168	2v <sub>29</sub> OR v <sub>21</sub>
443.6	22 545	1528	v <sub>10</sub>
442.2	22 614 max	1597	v <sub>8</sub>
440.8	22 688	1671	v <sub>29</sub> + v <sub>22</sub>
433.8	23 051	2034	v <sub>26</sub> + 1168
432.5	23 119 max	2102	v <sub>29</sub> + v <sub>10</sub>
431.3	23 184	2167	2v <sub>22</sub> OR v <sub>29</sub> + v <sub>8</sub>
423.4	23 617	2600	
422.0	23 696 max	2679	v <sub>22</sub> + v <sub>8</sub>
415.3	24 081	3064	
414.0	24 152 max	3135	
413.0	24 213	3196	
315.2	31 726	0	0 <sub>0</sub> <sup>0</sup> (2) <sup>1</sup> A' ← $\bar{X}$ <sup>1</sup> A'
311.6	32 096	370	v <sub>31</sub>
310.2	32 246	520	v <sub>30</sub>
307.4	32 529	803	v <sub>27</sub>
305.0	32 780	1054	2v <sub>30</sub> OR v <sub>22</sub>
302.6	33 042	1316	v <sub>30</sub> + v <sub>27</sub> OR v <sub>16</sub>
300.3	33 296	1570	3v <sub>30</sub> OR v <sub>8</sub>
298.0	33 563	1837	v <sub>30</sub> + 1316
295.6	33 831	2105	2 × 1054
293.3	34 091	2365	1054 + 1316
290.7	34 395	2669	
286.6	34 895	3169	
<b>C<sub>9</sub>H<sub>9</sub><sup>•</sup> 117A</b>			
470.9 <sup>[c]</sup>	21 235	0	0 <sub>0</sub> <sup>0</sup> (3) <sup>2</sup> A' ← $\bar{X}$ <sup>2</sup> A''
456.2	21 918	683	v <sub>28</sub>
450.5	22 199	964	v <sub>24</sub>
333.8	29 960	0	0 <sub>0</sub> <sup>0</sup> (5) <sup>2</sup> A' ← $\bar{X}$ <sup>2</sup> A''
329.8	30 322	362	v <sub>31</sub>
327.3	30 556	596	
326.6	30 623	663	v <sub>28</sub>
326.0	30 671	711	2v <sub>31</sub>
323.4	30 918	958	v <sub>31</sub> + 596
322.1	31 042	1082	3v <sub>31</sub>

[a]  $\tilde{\nu} = 1/\lambda_{\text{Ne}}$ ; 'max' denotes band maximum of broad features. [b] Vibrational assignments in the excited states are based on ground-state modes calculated with DFT at the (u)BLYP/cc-pVDZ level (Table 6.2). [c] See Table 6.5 for the emission values corresponding to ZPLs.

The other set of absorptions due to C<sub>9</sub>H<sub>9</sub><sup>+</sup> cations—absent in no-CH<sub>3</sub>Cl experiments as shown in Figure 6.5b—is the strongest of the spectrum, with an origin



band located at 315.2 nm. Its integrated intensity is ~10–12 times larger than that of the 476 nm system. The strongest feature is the onset, followed by an extended vibrational profile (Table 6.4).

The same cationic absorptions with a similar intensity ratio as in Figure 6.5a were present in the spectrum obtained from an indene/ethanol mixture (not shown), involving a proton transfer reaction described for the synthesis of protonated PAHs thereby producing the most stable alternative (Appendix A).<sup>3</sup> The relative band intensity is the same for the two (476 and 315 nm) systems in different experiments; thus, they are assigned to 2-protonated indene, **117A+**, for it is the more stable isomer of the two of relevance (Figure 6.1).

Features of a neutral species are also discernible in Figure 6.5. A weak band at 471 nm (trace c) is more intense in spectra recorded without an electron scavenger (trace d). The absence of the broad absorptions of cationic nature in the latter case allowed the detection of two more bands contributing to its vibrational progression, 683 and 964  $\text{cm}^{-1}$  above the origin (Table 6.4). Another system of neutral origin becomes also stronger without  $\text{CH}_3\text{Cl}$ , with an origin at 334 nm, and vibrational bands at 362 and 596  $\text{cm}^{-1}$ , their overtones and combinations (Figure 6.5d and Table 6.4). It correlates well with the former system in experiments using different precursors. Because neutral  $\text{C}_9\text{H}_9^\bullet$  radicals are formed by the neutralization of  $\text{C}_9\text{H}_9^+$  in the matrix and this process normally retains the structure of the cations, the 471 and 334 nm systems should belong to 1-indanyl radical, **117A**.

In order to decipher the complex absorption system between ~400–480 nm (of overlapping, simultaneously present **117A+** and **117A** species; see Figure 6.5a reproduced in Figure 6.6, blue trace), all the bands seen in absorption recorded after the deposition of  $\text{C}_9\text{H}_9^+$  (produced from an indene/ethanol mixture) have been excited with a laser to detect fluorescence. Excitation of the band at ~476 nm of cationic origin resulted in trace red of Figure 6.6. The origin is not seen because scans were started ~2 nm above the excitation wavelength to avoid saturation of the detector with intense laser scatter (Chapter 2). The spectrum is a mirror image of the cationic system, with sharper bands piling onto broad features. A wealth of peaks can be distinguished; even the weak absorption band at 368  $\text{cm}^{-1}$  is present in emission, at 375  $\text{cm}^{-1}$ . The fluorescence values given in Table 6.5 are

the ZPLs. Excitation to the origin of the neutral species (at ~471 nm) gave rise to the spectrum shown as green trace. As was seen from the absorption measurements, the two systems of neutral **117A** and cationic **117A**<sup>+</sup> overlap in the visible. Laser excitation to any band in the 465–415 nm range resulted in an emission as is shown in Figure 6.6, orange trace, where both systems are present, though different relative intensities were observed upon varying the excitation wavelength.

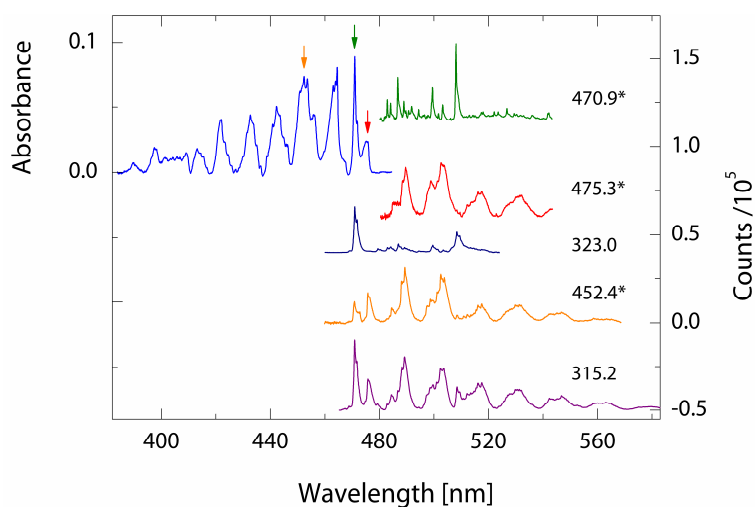


**Figure 6.6:** The ~400–480 nm system of overlapping absorptions of **117A**<sup>+</sup> and **117A** species (left), and corresponding fluorescence spectra (right). Excitation wavelength for the recorded emission traces is given in nm and those marked with an asterisk are also indicated by arrows on the absorption curve. For details, see the text.

The neutrals have been identified as follows: The visible one at 471 nm is the  $\tilde{A}^2A'' \leftarrow \tilde{X}^2A''$  transition of 1-indanyl, reported from gas-phase studies.<sup>8</sup> Its origin in the gas phase is at 21 159 cm<sup>-1</sup>, and at 21 235 cm<sup>-1</sup> in a neon matrix (Table 6.4), corresponding to a modest, 76 cm<sup>-1</sup> red shift. Ground-state frequencies have been derived; they are 377, 529, 583, 700, 794, 1018 cm<sup>-1</sup> and others. These can be compared directly to the fluorescence data obtained in neon—378, 527, 579, 693, 788 and 1016 cm<sup>-1</sup> (Table 6.5)—and those calculated using DFT (Table 6.2). The agreement is excellent.

<sup>8</sup> T.P. Troy, M. Nakajima, N. Chalyavi, R.G.C.R. Clady, K. Nauta, S.H. Kable, T.W. Schmidt. *J. Am. Chem. Soc.* **2009**, *113*(38): 10279–10283.

**Table 6.5:** Fluorescence band maxima ( $\lambda_{\text{Ne}} \pm 0.1$  nm) of an electronic transition of  $\text{C}_9\text{H}_9^+$  and  $\text{C}_9\text{H}_9^\bullet$  observed in a neon matrix and the assignment

$\lambda_{\text{Ne}}$ [nm]	$\tilde{\nu}^{\text{[a]}}$ [ $\text{cm}^{-1}$ ]	$\Delta\tilde{\nu}$ [ $\text{cm}^{-1}$ ]	Assignment <sup>[b]</sup>
<b><math>\text{C}_9\text{H}_9^+</math> 117A+</b>			
475.7	21 020	0	$0_0^0$ (1) <sup>1</sup> A' ← $\tilde{X}^1$ A'
484.4	20 645	375	$\nu_{31}$
488.0	20 491	529	$\nu_{30}$
489.2	20 442	578	$\nu_{29}$
497.2	20 112	908	$\nu_{25}$
498.5	20 059	961	
501.0	19 962	1058	$\nu_{23/24}$ or $2\nu_{30}$
502.3	19 908	1112	$\nu_{22}$
503.6	19 857	1163	$\nu_{21}$
510.7	19 581	1439	$\nu_{12/11}$
512.1	19 526	1494	$\nu_{10}$
513.4	19 476	1544	$\nu_9$
516.2	19 374	1646	$\nu_{22} + \nu_{30}$
517.5	19 322	1698	$\nu_{22} + \nu_{29}$
527.1	18 972	2048	
528.4	18 927	2093	
529.8	18 875	2145	
530.6	18 848	2172	$\nu_{22} + \nu_{23/24}$
531.3	18 821	2199	
532.1	18 794	2226	$2\nu_{22}$
545.2	18 342	2678	
546.8	18 288	2732	
558.4	17 909	3111	
562.2	17 786	3234	
575.1	17 389	3631	
<b><math>\text{C}_9\text{H}_9^\bullet</math> 117A</b>			
471.1	21 228	0	$0_0^0$ (3) <sup>2</sup> A' ← $\tilde{X}^2$ A''
479.6	20 850	378	$\nu_{31}$
483.1	20 701	527	$\nu_{30}$
484.3	20 649	579	$\nu_{29}$
487.0	20 535	693	$\nu_{28}$
489.2	20 440	788	$\nu_{27}$
491.0	20 368	860	$\nu_{26}$
492.2	20 319	909	$\nu_{25}$
494.8	20 212	1016	
496.9	20 126	1102	
498.2	20 072	1156	
499.9	20 004	1224	
502.1	19 915	1313	
503.7	19 852	1376	
508.5	19 664	1564	
517.8	19 312	1916	
522.5	19 139	2089	
523.9	19 086	2142	
527.2	18 970	2258	
529.8	18 875	2353	

[a]  $\tilde{\nu} = 1/\lambda_{\text{Ne}}$ . [b] Vibrational assignment is based on a *direct* comparison with ground-state totally symmetric frequencies (a' in  $C_s$ ) calculated with DFT at the BLYP/cc-pVDZ level of theory (Table 6.2).

Excitation of the bands of the 334 nm absorption system resulted in identical fluorescence to the one seen from that at 471 nm (not shown). Bands are broader but all discernible, conforming their common origin with the visible system of the 1-indanyl radical **117A**. Using the next absorption system as the subject of excitation (namely, its strong origin at 315.2 nm), the emission pattern is similar as was in the visible: neutrals and cations are both present (Figure 6.6, purple trace). Thus, the assignment of 476 and 315 nm transitions to the same **117A**+ cation is ratified.

In addition, it was found that irradiation of matrices containing **117A**+ with a mpHg lamp destroys all its discussed features: Cations and the two neutral systems are all decreasing; however, a system originating at 465 nm increases substantially. This absorption has been identified as the 1-indenyl radical, **115**, in Section 6.2. The process involved is  $H_2$  loss, one of the fragmentation channels of small PAHs.<sup>9</sup> Observing this photo-induced reaction provides further confirmation of the assignments to the discussed fused-ring species,  $C_9H_y^+$  ( $y = 7-9$ ). The process was seen in matrices both with and without  $CH_3Cl$ , suggesting that the abstraction reaction involves radicals.

It is to be mentioned here that there are additional, weak absorptions of a neutral in the UV, around 380–340 nm. No fluorescence was observed from these; thus, it should belong to another isomer than **117A**. A logical inference would be the other relevant  $C_9H_y^\bullet$  isomer, **117B**; however, its relative energy does not fit in the required  $50 \text{ kJ mol}^{-1}$  window for deposition (Figure 6.1). Perhaps H migration or ring opening may be associated with this species and its spectral features.

## 6.5 COMPUTATIONS

TD DFT calculations, similar to those in earlier chapters, were carried out at the (u)BLYP/cc-pVDZ level of theory to support the interpretation of the observed spectra; these are listed and compared with the experimental data in Table 6.6 and Figure 6.7. It can be said that, in general, these are sufficient to describe matrix data once (expected) shifts are taken into account for all electronic transitions. The predicted spectra are, however, complex and there are a few discre-

---

<sup>9</sup> See, e.g., V. Le Page, T.P. Snow, V.M. Bierbaum. *Astrophys. J.* **2009**, *704*(1): 274–280.

pancies; hence, higher-level calculations (CC2 and CASPT2) are underway. Gas-phase investigations are also called for in view of the fact that the radicals **115** and **116A+** of this study possess strong, (in a matrix sense) narrow absorptions in the 400–600 nm spectral region (Figure 6.7). A manuscript containing these findings, along with an overview on the recent developments of the mass-selective matrix isolation apparatus (Chapter 2), is being prepared for submission as a Perspective article in the *Physical Chemistry Chemical Physics*.<sup>10</sup>

It is to note that effort was paid to obtain the electronic spectra of the indane cation **118+** and neutral **118** (Figure 6.1); however, this was unsuccessful. The computational results predict that the neutral absorbs in the deep UV, a region inaccessible because of strong light scattering there, whereas that the cation should show a complex spectral pattern was not validated by the experiments.

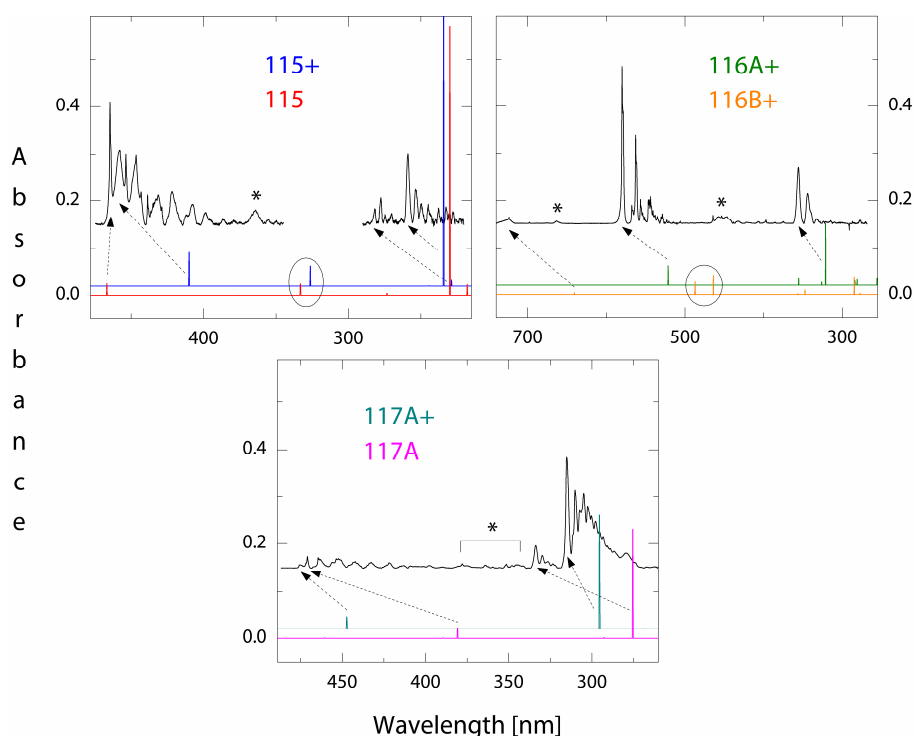


**Figure 6.7:** Electronic absorption spectra of  $C_9H_y^{+/0}$  ( $y = 7-9$ ) species observed in 6 K neon matrices (black; see Figures 6.3–6.5) and compared with colored stick diagrams representing TD DFT calculations at the (u)BLYP/cc-pVDZ level. Features marked by asterisks or circles are not or only tentatively assigned (Table 6.6).

<sup>10</sup> A. Nagy, I. Garkusha, J. Fulara, J.P. Maier. (Phys. Chem. Chem. Phys.) 2012, in preparation.

**Table 6.6:** Excited-state symmetries, vertical excitation energies  $\Delta E < 5.8$  eV (or maximum eight) and oscillator strengths  $f$  calculated for  $C_9H_y^+$  cationic and  $C_9H_y$  neutral ( $y = 7-10$ ) isomers with TD DFT at the (u)BLYP/cc-pVDZ level, and comparison with experimental data

Cations				Neutrals			
Exc. St.	$\Delta E$ /eV	$f$	Expt. <sup>[a]</sup> /eV	Exc. St.	$\Delta E$ /eV	$f$	Expt. <sup>[a]</sup> /eV
$C_9H_7^+ \mathbf{115}^+$ , $\tilde{X}^1A_1$ , planar $C_{2v}$				$C_9H_7 \mathbf{115}$ , $\tilde{X}^2A_2$ , planar $C_{2v}$			
$^1B_1$	1.03	0.0002		$^2B_1$	1.31	0.0001	
$^1A_1$	3.02	0.072	2.71	$^2A_1$	2.66	0.025	2.67
$^1B_1$	3.80	0.043	(3.40)	$^2B_1$	3.30	0.0005	
$^1B_2$	3.83	0.0001		$^2A_1$	3.69	0.0003	
$^1B_2$	5.07	0.0006		$^2B_1$	3.72	0.024	(*)
$^1A_1$	5.29	0.58	4.79	$^2B_2$	4.48	0.0001	
$^1B_1$	5.42	0.012		$^2B_1$	4.53	0.0043	4.40
$^1B_2$	5.76	0.0003		$^2B_1$	4.82	0.0001	
$C_9H_8^{2+} \mathbf{116A}^+$ , $\tilde{X}^2A''$ , $C_s$ (0)				$C_9H_8 \mathbf{116A}$ , $\tilde{X}^1A'$ , $C_s$ (0)			
$^2A'$	0.95	0.0001		$^1A'$	4.37	0.0090	
$^2A'$	2.38	0.042	2.14	$^1A'$	4.63	0.14	
$^2A'$	3.49	0.015		$^1A'$	5.16	0.14	
$^2A'$	3.80	0.0066		$^1A'$	5.58	0.0004	
$^2A'$	3.86	0.13	3.49				
$^2A'$	4.37	0.0091					
$^2A'$	4.41	0.012					
$^2A'$	4.85	0.014					
$C_9H_8^{2+} \mathbf{116B}^+$ , $\tilde{X}^2A_2$ , $C_{2v}$ (9)				$C_9H_8 \mathbf{116B}$ , $\tilde{X}^1A_1$ , $C_{2v}$ (81)			
$^2B_2$	1.94	0.0036	1.71	$^1B_1$	2.71	0.046	(2.72)
$^2A_1$	2.55	0.027	(*)	$^1B_1$	4.26	0.0053	
$^2B_2$	2.67	0.041	(*)	$^1A_1$	4.31	0.012	
$^2B_2$	3.48	0.0019		$^1B_2$	5.28	0.0003	
$^2A_1$	3.57	0.0096		$^1B_1$	5.32	0.0006	
$^2A_1$	4.35	0.038					
$^2B_2$	4.47	0.0027					
$^2B_1$	4.79	0.0002					

**Table 6.6:** (Continued.)

Cations				Neutrals			
Exc. St.	$\Delta E$ /eV	$f$	Expt. <sup>[a]</sup> /eV	Exc. St.	$\Delta E$ /eV	$f$	Expt. <sup>[a]</sup> /eV
$C_9H_9^+ \mathbf{117A}^+$ , $\tilde{X}^1A'$ , $C_s$ (0)				$C_9H_9 \mathbf{117A}$ , $\tilde{X}^2A''$ , $C_s$ (0)			
$^1A'$	2.77	0.026	2.61	$^2A'$	2.69	0.0010	
$^1A'$	4.20	0.24	3.93	$^2A'$	3.18	0.0011	
$^1A''$	4.23	0.0001		$^2A'$	3.26	0.022	2.63
$^1A''$	4.62	0.0003		$^2A'$	4.23	0.0014	
$^1A''$	5.12	0.0001		$^2A'$	4.50	0.23	3.71
$^1A''$	5.32	0.0027		$^2A''$	4.92	0.0003	
$^1A'$	5.37	0.070		$^2A'$	5.28	0.0007	
$^1A'$	5.60	0.12		$^2A''$	5.36	0.0001	
$C_9H_9^+ \mathbf{117B}^+$ , $\tilde{X}^1A_1$ , $C_{2v}$ (106)				$C_9H_9 \mathbf{117B}$ , $\tilde{X}^2B_1$ , $C_{2v}$ (46)			
$^1B_2$	0.81	0.0005		$^2A_1$	3.09	0.0014	
$^1A_1$	1.22	0.025		$^2B_2$	3.28	0.0029	
$^1B_1$	2.82	0.0003		$^2A_1$	3.49	0.0001	
$^1A_1$	3.51	0.0026		$^2B_2$	3.65	0.0003	
$^1B_1$	4.46	0.0009		$^2A_1$	5.02	0.010	
$^1A_1$	5.04	0.0009		$^2B_1$	5.07	0.0031	
$^1B_1$	5.22	0.0007		$^2B_1$	5.30	0.0022	
$^1B_2$	5.67	0.0001		$^2B_1$	5.60	0.0020	
$C_9H_{10}^{2+} \mathbf{118}^+$ , $\tilde{X}^2A'$ , $C_s$				$C_9H_{10} \mathbf{118}$ , $\tilde{X}^1A'$ , $C_s$			
$^2A''$	0.77	0.0005		$^1A'$	4.91	0.019	
$^2A'$	2.22	0.049		$^1A''$	5.62	0.010	
$^2A'$	2.46	0.019					
$^2A''$	2.55	0.0005					
$^2A'$	2.75	0.0071					
$^2A'$	3.32	0.0004					
$^2A''$	4.08	0.018					
$^2A'$	4.24	0.0006					

[a] Origin band position of transitions observed in neon matrices of this study. Tentatively assigned or predicted but missing (asterisk) features are in parentheses.

*“In fact, I’m beginning to fear that  
this confusion will go on for a long time.  
And all because he writes down what I said incorrectly.”*  
Mikhail Bulgakov (1891–1940), *The Master and Margarita*

# 7

## SUMMARY & OUTLOOK

---

Although matrix isolation is considered by many as an old-fashioned or even outdated spectroscopic method, it continues (and, likely, *will* continue) to bridge the gap between solutions and the intermolecular interaction-free environment of the gas phase. With it, reactive species can be embedded into a frozen, crystal-like structure and examined comfortably over a wide variety of spectral regions for days or longer. The obtained spectroscopic data can be interpreted usually with the support of theoretical calculations and used for predicting reliable band positions in high-resolution studies. These latter are then the basis of a comparison with astronomical observations. The advantages of the MI technique, especially in combination with mass selection, were illustrated on a number of examples in the framework of this thesis and are summarized below.

### 7.1 INVESTIGATED HYDROCARBONS

The main focus of this work lay in the characterization of carbonaceous cations, which are supposed to be of relevance for DIB research. These included unsaturated open-chain as well as aromatic hydrocarbons. As the experimental apparatus has received more serious improvements ([Chapter 2](#)), it seemed logical to start out with species whose (electronic) spectra were partially known from earlier studies.

Thus, one of the first projects was the re-investigation of the series  $\text{HC}_{2n+1}\text{H}^+$  ( $n = 2-7$ ) and their corresponding neutrals. By locating several new electronic systems with respect to those recorded previously from the same laboratory but with an older version of the setup, [\[1,2\]](#) the quality and data acquisition speed

advances due to the upgrades became evident. Though no DIB can be attributed to this set of linear hydrocarbons, thereby rejecting once again the carbon chain hypothesis, [3] the strong band systems in the UV presented herein provide more a sensitive means for the detection of such species in gas-phase experiments and, perhaps, in astrophysical environments than it was possible before via their transitions in the visible. Furthermore, theoretical approaches applied on these polyacetylenes are interesting in their own rights and they have been tested for decades. It was now shown that the available CASPT2 results [4] describe their electronic systems adequately, but was also confirmed that chemical pictures as simple as the particle-in-a-box model can be applied effectively to these kind of molecular systems. The onset wavelengths of the  $\text{HC}_{2n+1}\text{H}^{0/+}$  electronic transitions follow a linear relation as a function of the size of the cations, with a similar gradient for different groups of transitions ( $A,B,C$  and  $D,E \leftarrow X$ ) within the family (Chapter 3). [5] This also means that the more intense absorptions (to higher states) move into the range associated with the DIB forest,  $\sim 400\text{--}900$  nm, as the chain length grows; on the other hand, the cosmic abundance of these hydrocarbon chains is expected to drop in this direction.

Besides the spectra of open-chain species, aromatics were also investigated. First, two of the smallest representatives of cyclic structures with  $4x + 2$  valence electrons were targeted, and  $\text{C}_7\text{H}_7^+$  (benzylum,  $\text{Bz}^+$ , and tropylium,  $\text{Tr}^+$ ) cations were studied. This promised to be interesting for two reasons: (a)  $\text{Bz}^+$  has been studied by a number of methods for several decades, but a confusion as to which spectral features belong to this ion persisted and needed to be settled, and (b) there has been a very limited amount of experimental information on  $\text{Tr}^+$ , the prototype of closed-shell, classical Hückel-type cations. The difficulties with obtainability and reliability have originated in the energetic vicinity of  $\text{Bz}^+$  and  $\text{Tz}^+$  (separated in their ground electronic state only by  $\sim 25\text{--}45$  kJ mol $^{-1}$ ); on the contrary, this fact proved to be advantageous in the matrix and both isomers were possible to be trapped. The combination of mass-selective matrix isolation spectroscopy with (TD) DFT predictions allowed for an unambiguous assignment of the obtained spectra (Chapter 4). [6]

Another two aromatic studies carried out concerned  $\text{C}_{11}\text{H}_9^+$  (Chapter 5) [7] and  $\text{C}_9\text{H}_y^+$  ( $y = 7\text{--}9$ ) (Chapter 6). These two species/family are prototypes of small, fused-ring hydrocarbons. It was confirmed that there exists a structural diversity



for a given chemical formula as the size of the molecule grows, which results in the trapping of multiple isomers in a neon matrix and complicates the interpretation of spectra. However, the sensible combination of experimental (earlier solution data, selection of precursors, photobleaching, fluorescence/IR, *etc.*) and computational crutches complement each other in doing so. As for the latter, it is to be noted that TD DFT again proved to be a reasonable footing, as well as that another simple chemical model, the HMO method, is with limitations applicable for these modest-size aromatic species (Table 7.1).

**Table 7.1:** Comparison of the observed origin wavelength of electronic transitions of classical Hückel aromatics in neon ( $\lambda_{\text{Ne}}$ ) with solution band maxima  $\lambda_{\text{max}}$ , and values obtained from TD DFT calculations and with the HMO method<sup>[a]</sup>

Species/Transition	$\lambda_{\text{Ne}}$	$\lambda_{\text{max}}$	$\lambda_{\text{calc}}$	$\lambda_{\text{HMO}}$
<b>Benzylum</b> ( $C_{2v}$ )				
(1) <sup>1</sup> B <sub>1</sub> ← $\tilde{X}$ <sup>1</sup> A <sub>1</sub>	523	500	454	500
(1) <sup>1</sup> A <sub>1</sub> ← $\tilde{X}$ <sup>1</sup> A <sub>1</sub>	313	304	281	
<b>Tropylium</b> ( $D_{7h}$ )				
(1) <sup>1</sup> A <sub>2</sub> '' ← $\tilde{X}$ <sup>1</sup> A <sub>1</sub> '	275	275	225	294
<b>Benzotropylium</b> ( $C_{2v}$ )				
(1) <sup>1</sup> B <sub>1</sub> ← $\tilde{X}$ <sup>1</sup> A <sub>1</sub>	463	425	401	486
(1) <sup>1</sup> A <sub>1</sub> ← $\tilde{X}$ <sup>1</sup> A <sub>1</sub>	336	338	319	
(2) <sup>1</sup> A <sub>1</sub> ← $\tilde{X}$ <sup>1</sup> A <sub>1</sub>	278	282	253	
<b>1-Indenylium</b> <sup>[b]</sup> ( $C_{2v}$ )				
(1) <sup>1</sup> A <sub>1</sub> ← $\tilde{X}$ <sup>1</sup> A <sub>1</sub>	458	—	411	307
(2) <sup>1</sup> B <sub>1</sub> ← $\tilde{X}$ <sup>1</sup> A <sub>1</sub>	(365) <sup>[c]</sup>		326	
(2) <sup>1</sup> A <sub>1</sub> ← $\tilde{X}$ <sup>1</sup> A <sub>1</sub>	259		234	

[a] All in nm. [b] This C<sub>9</sub>H<sub>7</sub><sup>+</sup> isomer is similar to the structures above, but is anti-aromatic with eight valence electrons. [c] Tentative assignment.

A recent computational follow-up has suggested that the broad Franck–Condon profile of some of the investigated mid-sized aromatics makes them unlikely to be DIB responsables and only (closed-shell) arene cations larger than fluorine or so are worth to consider further. [8] Nevertheless, they will remain interesting from fundamental chemistry points of view. It is also to be mentioned that two open-shell species, 1-indenyl (C<sub>9</sub>H<sub>7</sub>•) and  $\alpha$ -indene radical cation (C<sub>9</sub>H<sub>8</sub>•<sup>+</sup>), do have spectral properties—narrow bands in the 400–600 nm region—that may be of relevance for DIB research in the gas phase.

Additional, rather exotic hydrocarbons characterized comprised planar  $C_6H_4^+$  isomers,  $C_5H_y^+$  and  $C_7H_y^+$  sets, and corannulene<sup>+</sup> among others (Appendix A). Some test experiments on the  $C_{60}^{0/+}$  and  $HC_{60}^{0/+}$  species were also carried out; however, no particularly useful (fluorescence) data could be obtained.

The interplay of different experimental methods, quantum simulations and astronomical observations culminated in the assignment of  $H_2CCC$  ( $l$ - $C_3H_2$ ) as a DIB carrier. [9] Although there is an ongoing debate [10,11] whether  $l$ - $C_3H_2$  can *really* be held responsible for the broad DIBs centered at 4881 and 5450 Å, [12–14] to date this is the most compelling example for correlating telescope data and laboratory spectra, and it triggers new studies. [15] The gas-phase characterization (Figure 7.1) of this species and a subsequent comparison with observed astronomical features [9] (not shown here) would not have been possible without the solid spectroscopic evidence provided by the neon matrix recordings (Figure 7.2). Indeed, the mass-selective matrix data allowed not only for tackling the origin of a previously observed but unassigned hydrocarbon molecule, [16] but also for predictions of gas-phase line positions (Table 7.2).

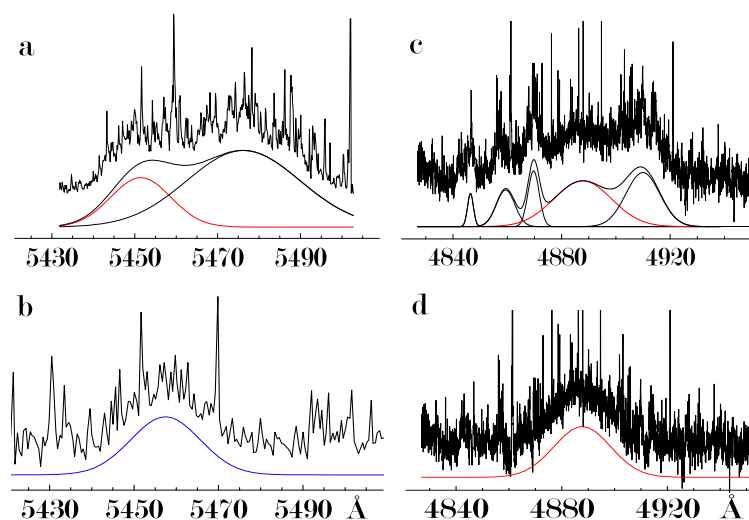


**Figure 7.1:** Gas-phase laboratory spectra recorded by CRDS in a supersonic slit jet expansion discharge using allene (traces a, c and d) and  $DC_2D$  (trace b) as precursors. The continuous, solid lines are Gaussians fitted to the data, after partial removal of the  $C_2$  lines and subtraction of the known  $l$ - $C_3H$  absorptions (trace c). Absorptions in red are due to  $l$ - $C_3H_2$  and match reasonably the DIBs at 4881 and 5450 Å. *Courtesy:* CRD Lab—R. Raghunandan and F.J. Mazzotti. [9]

**Table 7.2:** Absorption band maxima  $\lambda$  (Å) and integrated intensity  $I$  of  $l\text{-C}_3\text{H}_2$  and  $l\text{-C}_3\text{D}_2$  measured in a 6 K neon matrix and in the gas phase ( $K = 1 \leftarrow 0$ ) [9]

Neon matrix				Gas phase		Transition	Band
$\lambda(l\text{-C}_3\text{H}_2)$	$I$	$\lambda(l\text{-C}_3\text{D}_2)$	$I$	$\lambda(l\text{-C}_3\text{H}_2)$	$\lambda(l\text{-C}_3\text{D}_2)$		
6284	0.2	6260	0.4	6318.9		$\tilde{A}^1A_2 \leftarrow \tilde{X}^1A_1$	a
6219	0.3	6130	1.4	6251.7		"	b
6122	0.9	6093	1.5	6159.2		"	c
5445/5417 <sup>[a]</sup>	10	5412	10	5450(3)	5458(3)	$\tilde{B}^1B_1 \leftarrow \tilde{X}^1A_1$	$2_0^1$
5143	3	5160	3.5	5165–5185 <sup>[b]</sup>		"	$2_0^1 4_0^1$
4856	9	4857	12	4887(3)		"	$2_0^2$
4633	4.4			4645–4665 <sup>[b]</sup>		"	$2_0^2 4_0^1$
4412	4.7			4425–4445 <sup>[b]</sup>		"	$2_0^3$

[a] Most intense site. [b] Extrapolated values based on the neon matrix to gas phase shift of the  $2_0^1$  band.

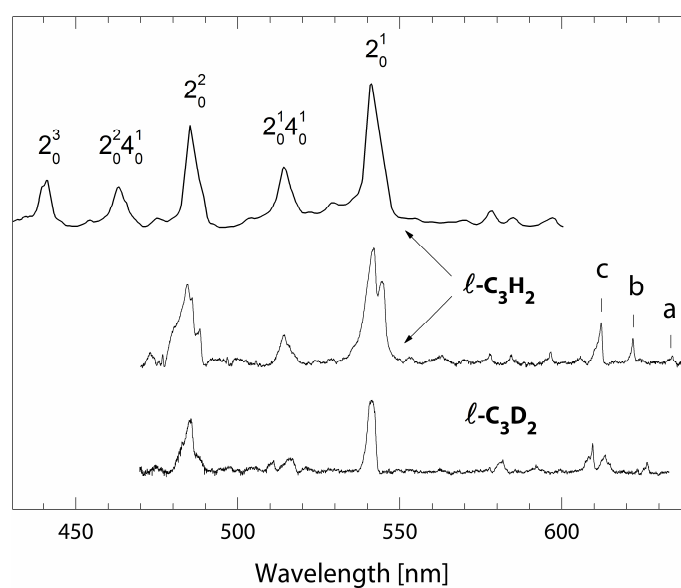


**Figure 7.2:** Absorption spectra of  $l\text{-C}_3\text{H}_2$  and  $l\text{-C}_3\text{D}_2$  recorded in neon matrices. [9] The top trace was obtained by 147 nm photolysis of allene embedded in the matrix (courtesy: J. Fulara); it is identical with the published spectrum in Ref. [17] generated by another chemical pathway. The middle and bottom traces were observed after mass-selective deposition of the corresponding cations. Labels a, b and c refer to the rotationally resolved gas-phase measurements. [18,19]

## 7.2 SPECIES FOR FUTURE CONSIDERATION &amp; UPGRADE POSSIBILITIES

The example of  $l\text{-C}_3\text{H}_2$  raises an obvious question: Could other members of the molecule group  $l\text{-C}_n\text{H}_2$  ( $n = \text{odd}$ ) exhibit similar spectroscopic patterns and, most importantly, be held responsible for DIBs? As these are neutral species and can be obtained via photobleaching of mass-selected ions (involving electron recombination or loss; see [Chapter 2](#)), it has to be decided whether the (thermal) stability of the corresponding cations *or* anions can be produced in the source in the first place. According to (unpublished) calculations, for the synthesis of  $\text{C}_3\text{H}_2$ ,  $\text{H}_2\text{CCC}^+$  is more stable than  $\text{HCCCH}^+$ , but for larger members of the series (including  $\text{C}_5\text{H}_2$ ),  $\text{H}_2\text{C}_n^+$  is significantly higher in energy than  $\text{HC}_n\text{H}^+$ . However, the opposite is valid for their negatively charged structures, which directs one's attention to anion spectroscopy. [20–22]

Negative ions also build a space charge upon deposition, which narrows their concentration and subsequent detection. In order to counteract this, measures have to be taken. A xenon<sup>+</sup> ion source was built and tested (in a straight configuration), which would allow for this ([Figure 7.3](#)).

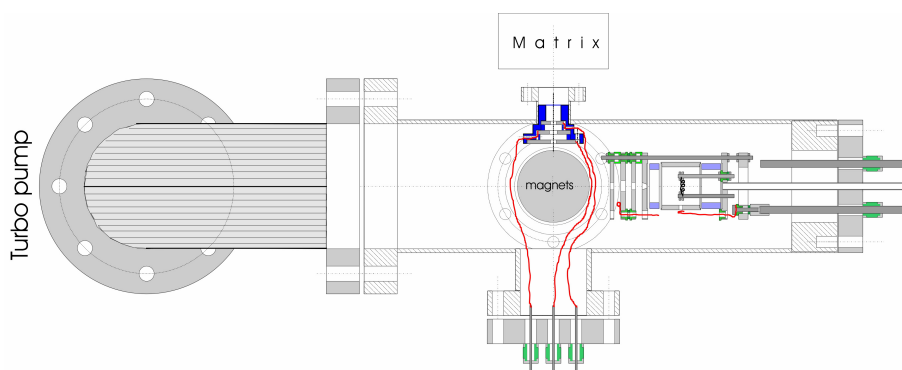


**Figure 7.3:** Top view drawing of the xenon counter-ion source (*courtesy*: J. Fulara). The noble gas enters on the right through a thin tubing, its atoms get ionized by electron impact and  $\text{Xe}^+$  is deflected by a pair of strong ( $\sim 0.1\text{--}1$  Tesla), permanent NdFeB magnets to be co-deposited with neon and the species under investigation onto the matrix substrate.

Another interesting project would be that of rhombic  $\text{C}_4$ , which has yet avoided spectroscopic detection despite considerable efforts. The case for this is the

reverse of that above: Cyclic  $C_4^+$  cation is within 50 kJ mol<sup>-1</sup> of the more stable  $l-C_4^+$  and could be trapped in neon, whereas  $c-C_4^-$  is by far higher in energy than its linear form (Table 7.3). This is promising in view of the example of  $C_6$  (same table): Both the linear and cyclic forms were possible to produce starting out with the deposition of  $C_6^+$ , [23] whereas only the linear species was seen from the anion. [24] Furthermore, it has been found using fully halogenated benzene precursors that solely  $c-C_6^+$  was formed from  $C_6Br_6$ , whereas  $C_6Cl_6$  produced both the cyclic and linear  $C_6^+$  isomers. [23] In order to urge such a selectivity, a similar precursor,  $c-C_4Br_6$ , should be synthesized from a commercially available material,  $c-C_4F_6$ , in a low-temperature (0 °C) distillation reaction: [25,26]

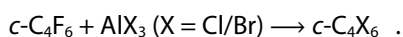


**Table 7.3:** Multiplicity  $M$ , molecular symmetry and relative ground-state energy (kJ mol<sup>-1</sup>, zero-point correction included) of charged and neutral  $C_4^{0/+/-}$  and  $C_6^{0/+/-}$  isomers calculated with DFT using the B3LYP or BLYP (in parentheses) functionals and the cc-pVTZ basis set

Species	$M$	Linear $D_{\infty h}$	Rhombic $D_{2h}$
$C_4^+$	2	<b>0</b> (3) <sup>[a]</sup>	22 (22) <sup>[b]</sup>
	4	27 ( <b>0</b> ) <sup>[c]</sup>	60 (88)
$C_4^-$	2	<b>0</b>	169
	4	272	415
$C_4$	1	75	67
	3	<b>0</b>	145
<b>Cyclic <math>D_{3h}</math></b>			
$C_6^+$	2	<b>0</b>	37
	4	66 <sup>[d]</sup>	143
$C_6^-$	2	<b>0</b>	170
	4	204	349
$C_6$	1	56	25
	3	<b>0</b>	145

[a] The symmetry is  $C_{2h}$  ('zig-zag') using BLYP. [b] The structure converges in  $C_{2v}$  with one negative frequency using B3LYP. [c]  $C_{2v}$  bent geometry using B3LYP. [d]  $C_{2h}$  symmetry.

Recently, the study of metal-terminated carbon chains has gained interest. Although the cesium sputtering source in Chapter 2 can in principle provide such, it has three main problems: (a) the current design does not include a precursor

gas inlet and the conductivity requirements of the probe significantly limits the choice of materials to be investigated; (b) the anion yield (current) is usually modest and subject to sputtering stability/ability issues, thereby confining the available cluster sizes; and (c) the sputtering material, cesium, is a highly flammable (liquid) alkali metal which is circumstantial to work with, making the maintenance operations time-consuming and demanding.

As an alternative, magnetron sputtering technology [27] has a capability of delivering fairly high and stable particle currents even in case of larger clusters. This property may be used not only to deposit various surface films for industrial purposes, [28–30] but also to produce targets to investigate for fundamental research laboratories. Groups have succeeded in producing certain type of clusters such as  $\text{Si}_n^-$  in the size range as large as  $n = 1000$  in detectable amount for PE studies. [31]

Initial steps were done to upgrade the machine in this direction and one possible scheme coupling a magnetron source with the existing mass-selective matrix isolation experiment is depicted in Figure 7.4. The soul of such a source is the sputtering head located in the aggregation chamber. It consists of a permanent ring magnet mounted behind the target (the negatively charged cathode), and their cylindrical holder (grounded anode). A voltage difference ( $\sim 300\text{--}500\text{ V}$ ) between the two electrodes creates—with the help of a sputtering gas (argon)—a plasma glow discharge and ionic complexes from the surface of the sample target are released due to energetic heavy ion ( $\text{Ar}^+$ ) bombardment. Secondary electrons are ‘trapped’ by the magnetic field and intensify the process. Helium is used for carrying the clusters through some irises towards extraction, continuously rinsing the production zone. Cooling water and liquid nitrogen are applied for reducing the high temperature inside the source. By varying a set of experimental conditions such as the target–first skimmer distance, the gas inlet pressure or the cathode voltage, the ion density as well as the aggregate size can be optimized. Differential pumping stages allow the operating pressure of the source to drop down stepwise from ca.  $1\text{--}10$  to  $\sim 10^{-6}$  mbar in the bending region. By properly choosing the target material and, eventually, dilute precursor gases into the He/Ar mixture, many different compounds will be possible to study.

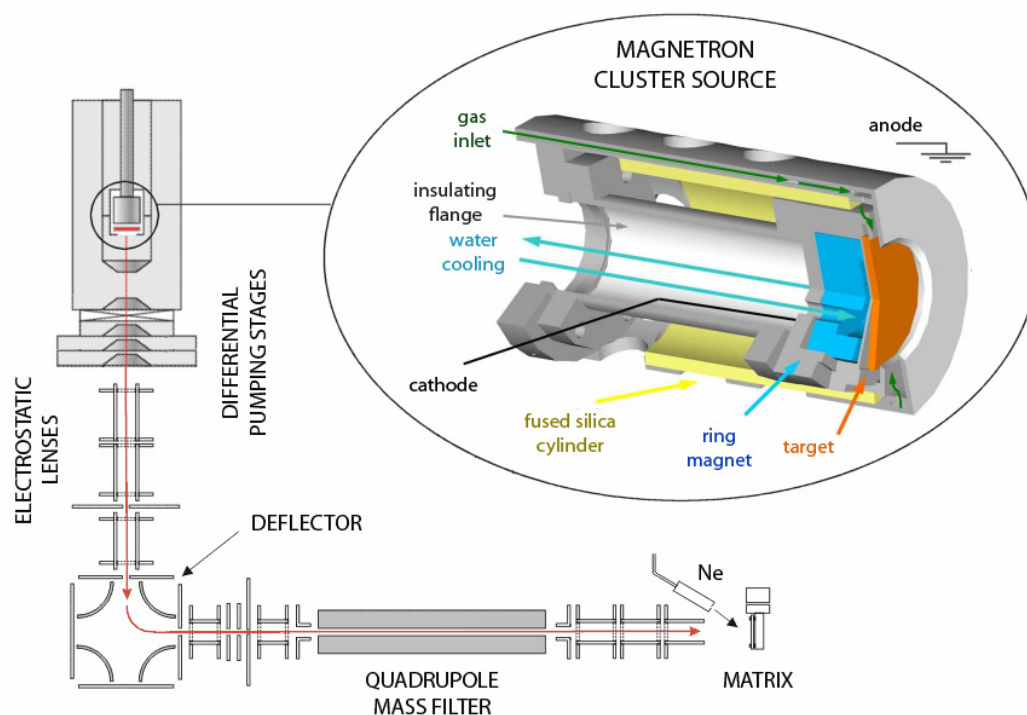


**Figure 7.4:** Scheme of a possible (horizontal) magnetron-coupled layout. *Courtesy to the research group of G.F. Ganteför at the University of Konstanz for the source drawing. [32]* Different types of design may rely on commercially available sputtering heads.

As for other upgrades: A major issue results from the new, Gifford–McMahon-type closed-cycle helium cryostat (Chapter 2). These kinds of instruments have a relatively simple design and are cheap; however, the up-and-down piston movement at a frequency of  $\sim 1$  Hz causes (well known) temperature oscillations of ca.  $\pm 0.4$  K between the base temperature of 2.5–3.5 and 10 K (Figure 7.5). [33–36] Because annealing is very sensitive to these changes (around the  $0.3 T_m$  point of neon), this otherwise useful method had to be dropped from the routine procedures of investigating a given frozen sample.

Basically, there exist two different solutions to this problem: (a) either the response time of the heater/controller pair should be decreased or (b) a temperature ‘buffer’ needs to be introduced between the substrate and the cold finger. For the first route, fast heater plates were mounted and a sophisticated pulse generator built, which latter would have counteracted the oscillations by setting the

threshold, intensity, position and width of heating pulses, synchronized with the frequency signal from a contact microphone mounted on the cryostat (Figure 7.5, green trace). However, tests showed that the improvement amounted unfortunately to not more than  $\sim 0.1$  K in precision. Another, simpler option could be the use of a faster temperature controller than the present one. For the second solution version, some copper (or aluminum) mass could be placed between the cold finger and the substrate. However, with a nominal cooling power of 1.0 W at 4.2 K, this would have to be a large amount (kilograms) of material, posing impractical re-design tasks. Another alternative could be a helium reservoir (a small, perfectly sealed copper pot filled with liquid helium), which would act as a heat ‘bath’ based of the large heat capacity of He.

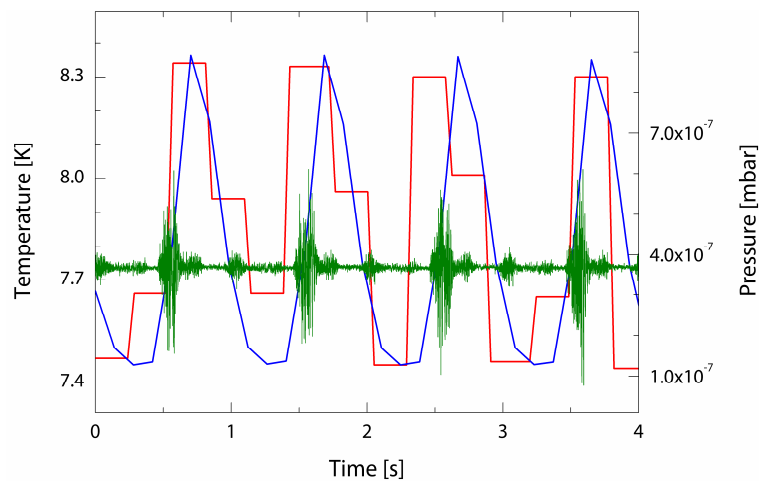


**Figure 7.5:** Demonstration of the temperature oscillations the matrix experiences due to the helium cryostat having only two (and no J–T) stages: Direct measurement of the  $T$  with a silicon diode placed in a copper holder between the substrate and the cold finger (red curve, controller readout rate:  $\sim 4$  Hz); indirect observation by monitoring  $p$  changes due to evaporating/freezing neon on a Penning gauge (blue, 7 Hz); and voltage signal on a 200 MHz digital scope using a contact microphone attached to the cryostat tower (green).

A related issue concerns the present temperature control/heating system of the substrate. Because it is possible to work with a neon matrix sample for multiple days, the matrix is kept overnight on a regular basis. As the controller in use (LakeShore 330) is too slow maintain an even temperature (at 6 K) and the common P(roportional)/I(ntegral)/D(erivative) autotuning makes these matters actually somewhat worse, continuous (DC) heating is applied. The cryostat has a



built-in shutdown security mechanism, which means that an accidental fallout of the electricity network would result in the switchback of the power supply only and, thus, may cause overheating (and damage to the cryostat beyond repair) over a certain period of time. This may well be beyond that 8–12 h the system would be unguarded; nevertheless, a switch-off relay (fuse) should be introduced.

Further improvement possibilities include the insertion of a gas flow controller. At present, the neon inflow is regulated manually (via a needle valve) while monitoring the pressure changes in the matrix chamber. However, the Penning gauge is located in a side arm of the cryostat tower, about 50–60 cm far from the substrate and, therefore, only approximately correlates with the *actual* pressure around the cold finger. This, plus eventual calibration/response time issues may result in a non-homogeneous matrix body and hinder the obtainment of quality spectra. The problem could be bypassed easily by letting the neon through an electronically driven flow regulator in a controlled, uniform manner (on the order of precision of mL h<sup>-1</sup>).

Another upgrade could be the introduction of a quartz defocusing lens (of focal length ~5 cm) right behind the laser beam entry window of the matrix chamber for the fluorescence experiments. Currently, the beam is directed on the matrix surface after allowing for merely a natural broadening of the beam profile, which results in a coverage of only a few mm<sup>2</sup> of the sample and low signal counts. With such a lens the whole of the matrix could be probed and, thus, weaker emissions observed faster.

Finally, a challenging idea would be the upgrade of the now complementary FTIR method. The main problem is that its effective path length is only  $l \approx 1$  mm, around 20 times smaller than for the UV/Vis spectral domain. Though the suggestion for the implementation of a similar, 'waveguide' configuration has been proposed nearly 20 years ago, [37] it remains a demanding task. In air, water absorptions would heavily contaminate the IR spectra; thus, modifications of the spectrometer would have to be carried out to direct the path of the beam from the 'light' source through the matrix back to the detector all the way vacuum tight. It is to be decided whether the gains are worth to undertake such customizations.



## Bibliography

- [1] J. Fulara, P. Freivogel, D. Forney, J.P. Maier. *Electronic absorption spectra of linear carbon chains in neon matrices. III. HC<sub>2n+1</sub>H*. **J. Chem. Phys.** **1995**, 103(20): 8805–8810.
- [2] P. Freivogel, J. Fulara, D. Lessen, D. Forney, J.P. Maier. *Absorption spectra of conjugated hydrocarbon cation chains in neon matrices*. **Chem. Phys.** **1994**, 189(2): 335–341.
- [3] A.E. Douglas. *Origin of diffuse interstellar lines*. **Nature** **1977**, 269(5624): 130–132.
- [4] J. Zhang, X. Guo, Z. Cao. *Theoretical studies on structures and electronic spectra of linear HC<sub>2n+1</sub>H<sup>+</sup> (n = 2–7)*. **Int. J. Mass Spectrom.** **2010**, 290(2–3): 113–119.
- [5] J. Fulara, A. Nagy, I. Garkusha, J.P. Maier. *Higher energy electronic transitions of HC<sub>2n+1</sub>H<sup>+</sup> (n=2–7) and HC<sub>2n+1</sub>H (n=4–7) in neon matrices*. **J. Chem. Phys.** **2010**, 133(2): 024304/1–9.
- [6] A. Nagy, J. Fulara, I. Garkusha, J.P. Maier. *On the benzylium/tropylium ion dichotomy: Electronic absorption spectra in neon matrices*. **Angew. Chem. Int. Ed.** **2011**, 50(13): 3022–3025; **Angew. Chem.** **2011**, 123(13): 3078–3081.
- [7] A. Nagy, J. Fulara, J.P. Maier. *Formation of aromatic structures from chain hydrocarbons in electrical discharges: Absorption and fluorescence study of C<sub>11</sub>H<sub>9</sub><sup>+</sup> and C<sub>11</sub>H<sub>9</sub><sup>\*</sup> isomers in neon matrices*. **J. Am. Chem. Soc.** **2011**, 133(49): 19796–19806.
- [8] T.P. Troy, S.H. Kable, T.W. Schmidt, S.A. Reid. *On the electronic spectroscopy of closed-shell cations derived from resonance-stabilized radicals: Insights from theory and Franck–Condon analysis*. **Astron. Astrophys.** **2012**, 541: A8/1–6.
- [9] J.P. Maier, G.A.H. Walker, D.A. Bohlender, F.J. Mazzotti, R. Raghunandan, J. Fulara, I. Garkusha, A. Nagy. *Identification of H<sub>2</sub>CCC as a diffuse interstellar band carrier*. **Astrophys. J.** **2011**, 726(1): 41/1–9.
- [10] T. Oka, B.J. McCall. *Disclosing identities in diffuse interstellar bands*. **Science** **2011**, 331(6015): 293–294.
- [11] J. Krelowski, G. Galazutdinov, R. Kołos. *Can H<sub>2</sub>CCC be the carrier of broad diffuse bands?* **Astrophys. J.** **2011**, 735(2): 124/1–6.
- [12] P. Jenniskens, F.-X. Désert. *A survey of diffuse interstellar bands (3800–8680 Å)*. **Astron. Astrophys. Suppl. Ser.** **1994**, 106(1): 39–78.
- [13] G.H. Herbig. *The diffuse interstellar bands*. **Annu. Rev. Astrophys.** **1995**, 33: 19–73.
- [14] L.M. Hobbs, D.G. York, T.P. Snow, T. Oka, J.A. Thorburn, M. Bishof, S.D. Friedman, B.J. McCall, B. Rachford, P. Sonnentrucker, D.E. Welty. *A catalog of diffuse interstellar bands in the spectrum of HD 204827*. **Astrophys. J.** **2008**, 680(2): 1256–1270.
- [15] J.F. Stanton, E. Garand, J. Kim, T.I. Yacovitch, C. Hock, A.S. Case, E.M. Miller, Y.-J. Lu, K.M. Vogelhuber, S.W. Wren, T. Ichino, J.P. Maier, R.J. McMahon, D.L. Osborn, D.M. Neumark, W.C. Lineberger. *Ground and low-lying excited states of*

- propadienylidene (H<sub>2</sub>C=C=C:) obtained by negative ion photoelectron spectroscopy.* **J. Chem. Phys.** **2012**, 136(13): 134312/1–16.
- [16] H. Linnartz, N. Wehres, H. Van Winckel, G.A.H. Walker, D.A. Bohlender, A.G.G.M. Tielens, T. Motylewski, J.P. Maier. *A coincidence between a hydrocarbon plasma absorption spectrum and the  $\lambda$ 5450 DIB.* **Astron. Astrophys.** **2010**, 511: L3/1–4.
- [17] J.A. Hodges, R.J. McMahon, K.W. Sattelmeyer, J.F. Stanton. *Electronic spectrum of propadienylidene (H<sub>2</sub>C=C=C:) and its relevance to the diffuse interstellar bands.* **Astrophys. J.** **2000**, 544(2): 838–842.
- [18] E. Achkasova, M. Araki, A. Denisov, J.P. Maier. *Gas phase electronic spectrum of propadienylidene C<sub>3</sub>H<sub>2</sub>.* **J. Mol. Spectrosc.** **2006**, 237(1): 70–75.
- [19] P. Birza, A. Chirokolava, M. Araki, P. Kolek, J.P. Maier. *Rotationally resolved electronic spectrum of propadienylidene.* **J. Mol. Spectrosc.** **2005**, 229(2): 276–282.
- [20] S.J. Blanksby, S. Dua, J.H. Bowie, D. Schröder, H. Schwarz. *Gas-phase syntheses of three isomeric C<sub>5</sub>H<sub>2</sub> radical anions and their elusive neutrals. A joint experimental and theoretical study.* **J. Phys. Chem. A** **1998**, 102(48): 9949–9956.
- [21] A. Mavrandonakis, M. Mühlhäuser, G.E. Froudakis, S.D. Peyerimhoff. *The electronic spectrum of linear pentadiynylidene in comparison with isomeric ethynylcyclopropenylidene.* **Phys. Chem. Chem. Phys.** **2002**, 4(14): 3318–3321.
- [22] R.A. Seburg, R.J. McMahon, J.F. Stanton, J. Gauss. *Structures and stabilities of C<sub>5</sub>H<sub>2</sub> isomers: Quantum chemical studies.* **J. Am. Chem. Soc.** **1997**, 119(44): 10838–10845.
- [23] J. Fulara, E. Riaplov, A. Batalov, I. Shnitko, J.P. Maier. *Electronic and infrared absorption spectra of linear and cyclic C<sub>6</sub><sup>+</sup> in a neon matrix.* **J. Chem. Phys.** **2004**, 120(16): 7520–7525.
- [24] M. Grutter, M. Wyss, E. Riaplov, J.P. Maier, S.D. Peyerimhoff, M. Hanrath. *Electronic absorption spectrum of linear C<sub>6</sub>, C<sub>8</sub> and cyclic C<sub>10</sub>, C<sub>12</sub> in neon matrices.* **J. Chem. Phys.** **1999**, 111(16): 7397–7401.
- [25] W.C. Solomon, L.A. Dee, D.W. Schults. *Heterogeneous defluorination of carbon.* **J. Org. Chem.** **1966**, 31(5): 1551–1553.
- [26] R. Criegee, R. Huber. *Tetrachlor- und Tetrabrom-cyclobutadien als Zwischenprodukte.* **Chem. Ber.** **2006**, 103(6): 1862–1866.
- [27] See, e.g., X. Yu, C. Wang, Y. Liu, D. Yu, T. Xing. *Recent developments in magnetron sputtering.* **Plasma Sci. Technol.** **2006**, 8(3): 337–343.
- [28] A. Majumdar, D. Köpp, M. Ganeva, D. Datta, S. Bhattacharyya, R. Hippler. *Development of metal nanocluster ion source based on dc magnetron plasma sputtering at room temperature.* **Rev. Sci. Instrum.** **2009**, 80(9): 095103/1–6.
- [29] S. Pratontep, S.J. Carroll, C. Xirouchaki, M. Streun, R.E. Palmer. *Size-selected cluster beam source based on radio frequency magnetron plasma sputtering and gas condensation.* **Rev. Sci. Instrum.** **2005**, 76(4): 045103/1–9.

- [30] H. Haberland, M. Karrais, M. Mall, Y. Thurner. *Thin films from energetic cluster impact: A feasibility study*. **J. Vac. Sci. Technol.** **1992**, 10(5): 3266–3271.
- [31] M. Astruc Hoffmann, G. Wrigge, B. v. Issendorff, J. Müller, G. Ganteför, H. Haberland. *Ultraviolet photoelectron spectroscopy of  $Si_4^-$  to  $Si_{1000}^-$* . **Eur. Phys. J. D** **2001**, 16(1–3): 9–11.
- [32] F. von Gynz-Rekowski. *Sauerstoffadsorption an freien und deponierten Clustern*. **Ph.D. thesis**, University of Konstanz, Faculty of Sciences, **2005**.
- [33] Y. Hasegawa, D. Nakamura, M. Murata, H. Yamamoto, T. Komine. *High-precision temperature control and stabilization using a cryocooler*. **Rev. Sci. Instrum.** **2010**, 81(9): 094901/1–4.
- [34] R. Li, A. Onishi, T. Satoh, Y. Kanazawa. *Temperature stabilization on cold stage of 4 K GM cryocoolers*. *Cryocoolers 9 (Proceedings of the 9<sup>th</sup> International Cryocooler Conference)* **1997**, pp. 765–771.
- [35] T. Shimazaki, K. Toyoda, O. Tamura. *Gifford–McMahon/Joule–Thomson cryocooler with high-flow-conductance counterflow heat exchanger for use in resistance thermometer calibration*. **Rev. Sci. Instrum.** **2006**, 77(3): 034902/1–6.
- [36] B. Igarashi, T. Christensen, E.H. Larsen, N.B. Olsen, I.H. Pedersen, T. Rasmussen, J.C. Dyre. *A cryostat and temperature control system optimized for measuring relaxations of glass-forming liquids*. **Rev. Sci. Instrum.** **2008**, 79(4): 045105/1–13.
- [37] M. Jakobi. *Elektronische und vibratorische Spektroskopie an den Fullerenen  $C_{60}$ ,  $C_{70}$  und deren Ionen in Edelgasmatrizen*. **Ph.D. thesis**, University of Basel, Faculty of Science, **1994**.



Part III

APPENDIX





*“There is a theory which states that if ever anyone discovers exactly what the Universe is for and why it is here, it will instantly disappear and be replaced by something even more bizarre and inexplicable. There is another which states that this has already happened.”*  
Douglas Adams (1952–2001), *The Restaurant at the End of the Universe*

A

## SIDE PROJECTS

---

During my Ph.D. studies at the *University of Basel* I worked on several other projects, some of which are briefly summarized below. This chapter intends to provide a complementary overview of further possibilities and topics using the mass-selective matrix isolation setup. The reader should note that two of these studies (on  $C_4H_3Cl^+$  and  $H_2CCC$ ) [1,2] have been discussed somewhat in [Chapters 2](#) and [7](#), while most of the remaining results were [3–9] or will be detailed elsewhere ([Section A.3](#)).

### A.1 PROTONATED BENZENE, NAPHTHALENES AND LARGER PAHS

Protonated polycyclic aromatic hydrocarbons (H-PAH<sup>+</sup>s) are one of the classes of species that have been suggested as carriers of DIBs as well as of unidentified infrared bands (UIRs). [10–13] Among other arene derivatives, H-PAH<sup>+</sup>s may play a role as intermediates toward soot formation in flames and combustion, [14–16] and in electrophilic substitution reactions of aromatics. [17]

H-PAH<sup>+</sup>s have been the focus of investigations for over half a century with spectroscopic techniques and theoretical approaches; however, the information obtained is limited. Their structure has been shown by NMR in superacidic solutions to be a  $\sigma$ - rather than a  $\pi$ -complex of the ‘excess’ hydrogen and the aromatic ring. [18,19] Secondly, ground-state vibrational spectra and electronic excitation energies have been calculated and the results used to make comparison with UIRs and DIBs. [13,20,21]

In the gas phase, the focus has been on IR methods. Different means have been employed for the generation of the H-PAH<sup>+</sup> cations: One is the chemical ionization of parent PAHs using CH<sub>5</sub><sup>+</sup> or C<sub>2</sub>H<sub>5</sub><sup>+</sup> as proton donors in an ion cyclotron resonance mass spectrometer; [22,23] in another, electron impact or a discharge was coupled with a supersonic expansion of PAHs seeded into a H<sub>2</sub>/carrier gas mixture. [24–26] These were used to produce protonated benzene and naphthalene, and their weakly-bound noble gas complexes, whereas larger H-PAH<sup>+</sup>s were made with electrospray ionization. [27,28] Their IR spectra were then obtained employing single- or multi-photon dissociation. As for electronic spectroscopy, only a few condensed-phase measurements had been available; [29–32] therefore, it was desirable to accumulate more such data.

#### A.1.1 Protonated benzene and fulvene, C<sub>6</sub>H<sub>7</sub><sup>+</sup>

Benzenium ion (PB<sup>+</sup>) represents the prototypical example of the fundamental class of organic ions above; it is the most stable isomer on the C<sub>6</sub>H<sub>7</sub><sup>+</sup> PES (Figure A.1). The cation has a ‘direct’ astrophysical relevance: It has been detected by mass spectrometry in the ionosphere of Titan. [33] In this context, the reactivity of ionized PAHs with atoms and simple molecular species were investigated [11,12] and found, *e.g.*, that benzene cations C<sub>6</sub>H<sub>6</sub><sup>+</sup> react readily with atomic hydrogen but not with H<sub>2</sub>. H-PAH<sup>+</sup>s are relatively stable towards the addition of a second H due to their closed-shell electronic structure.

C<sub>6</sub>H<sub>7</sub><sup>+</sup> cations have been studied as complexes with noble gas atoms by IR photodissociation (IRPD) spectroscopy. [24,25] These investigations have provided frequencies of several fundamentals of C<sub>6</sub>H<sub>7</sub><sup>+</sup>:Rg (rare gas) dimers in the range 750–3400 cm<sup>-1</sup>. A group of bands near 2800 cm<sup>-1</sup> was attributed to the aliphatic C–H stretch of the methylene group of benzenium. [24] Due to the weak interaction between C<sub>6</sub>H<sub>7</sub><sup>+</sup> and Rg atoms, the obtained IR frequencies should not differ much from those of the isolated ions.

However, multi-photon IRPD spectra of C<sub>6</sub>H<sub>7</sub><sup>+</sup>, which thereby undergo H<sub>2</sub> loss, differ from those mentioned above. [22] The observed bands are broadened and red shifted, and vary in intensity from single-photon dissociation data, which could be explained by the different nature of the fragmentation processes. These studies, in combination with calculations, have confirmed that PB<sup>+</sup> in its <sup>1</sup>A<sub>1</sub>

ground state ( $C_{2v}$  symmetry) is the favored form of  $C_6H_7^+$  (Figure A.1). The structure is planar with the exception of the  $CH_2$  hydrogens, which lie in a plane perpendicular to that of the benzene ring.

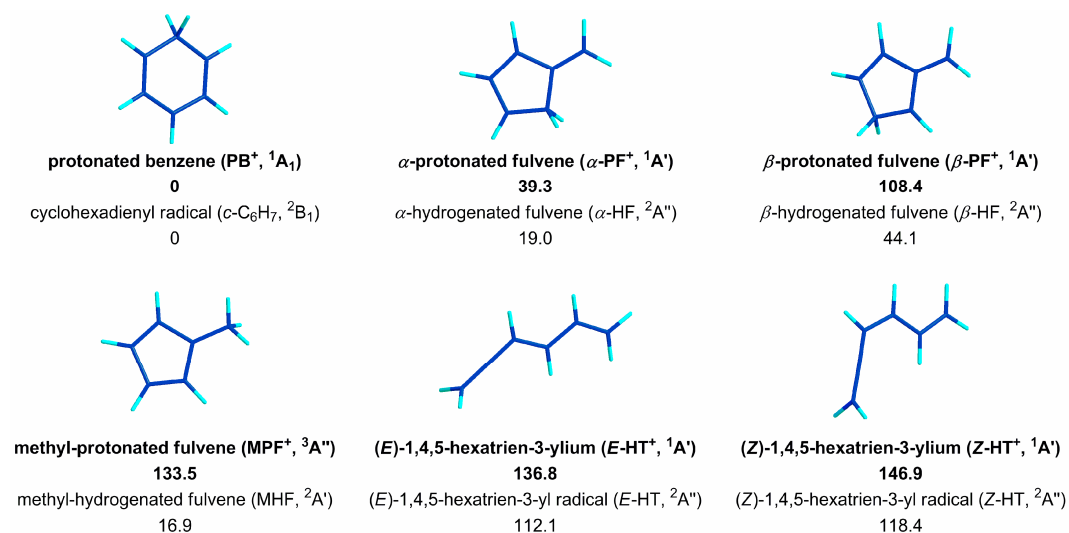


**Figure A.1:** Schematic representation of considered  $C_6H_7^+$  cations (**bold**) and their neutral counterparts (normal font). [3,5] Relative energy with respect to the most stable isomer are given in  $\text{kJ mol}^{-1}$ . The (ground-state) geometries were optimized with DFT at the B3LYP/cc-pVTZ level of theory.

Electronic spectroscopy on  $PB^+$  had been limited to absorption in superacidic solutions [32] and low-resolution UV photodissociation investigations. [34] The gas-phase spectrum revealed two broad, structureless transitions around 330 and 245 nm, which differ significantly from the solution spectra. *Ab initio* calculations on excited electronic states have provided an assignment for the UV spectrum. [35]

Not much had been known about other possible isomers of  $C_6H_7^+$ . Formation of  $\alpha$ - and  $\beta$ -protonated fulvenes ( $\alpha$ - and  $\beta$ - $PF^+$ ; see Figure A.1), in addition to benzenium, likely occurs upon dissociative ionization of a number of  $C_6H_8$  isomers [36,37] or by ion-molecule reactions; [37–41] however, there had been no spectroscopic data available.

In this contribution, [3,5] electronic transitions of  $C_6H_7^+$  trapped in neon matrices were investigated. Besides  $\tilde{A}^1B_2 \leftarrow \tilde{X}^1A_1$  of  $PB^+$  (which agrees well with the

earlier PD experiment), [34] the  $\tilde{A}^1A_1' \leftarrow \tilde{X}^1A_1'$  transition of  $\alpha$ -PF<sup>+</sup> was observed for the first time (Table A.1). They overlap, as well as both isomers formed concomitantly from a number of precursors such as cyclohexadienes, allene or methylcyclopentadiene (Figure A.2), which will hinder their future gas-phase spectroscopic studies. Several neutral C<sub>6</sub>H<sub>7</sub> (cyclohexadienyl radical and three other isomers) produced by the neutralization of C<sub>6</sub>H<sub>7</sub><sup>+</sup>, were also characterized (Table A.1). Furthermore, photoinduced isomerization of *c*-C<sub>6</sub>H<sub>7</sub> to an open-chain species and  $\alpha$ -hydrogenated fulvene radical was observed (Figure A.2). [3,5]

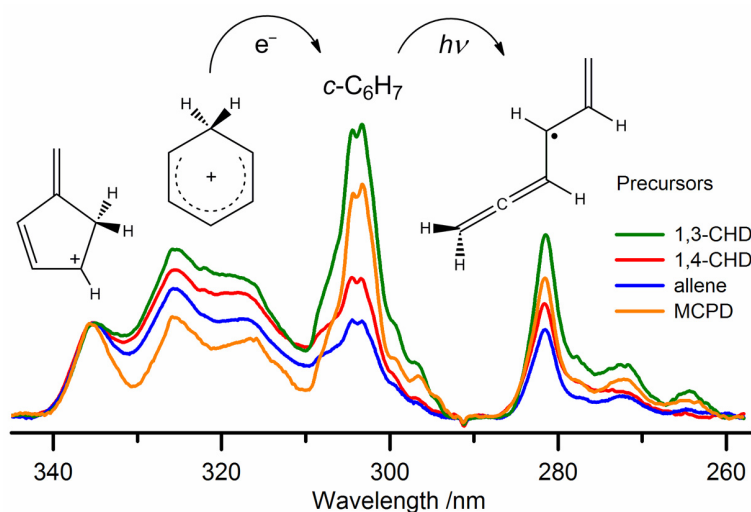


**Figure A.2:** Electronic transitions of protonated benzene ( $\tilde{A}^1B_2 \leftarrow \tilde{X}^1A_1$ , origin at 325 nm) and  $\alpha$ -protonated fulvene ( $\tilde{A}^1A' \leftarrow \tilde{X}^1A'$ , at 335 nm) as detected in 6 K neon matrices. [3,5] The cations were produced from several different precursors as indicated. After neutralization of the cations, systems of cyclohexadienyl (onsets at 549 and 310 nm) and  $\alpha$ -hydrogenated fulvene (532 and 326 nm) radicals were identified. Upon excitation of cyclohexadienyl to its  $\tilde{\beta}^2B_1$  state, it photoisomerizes to an open-chain structure (and  $\alpha$ -hydrogenated fulvene).

#### A.1.2 Protonated naphthalenes, C<sub>10</sub>H<sub>9</sub><sup>+</sup>

The next member of the H-PAH<sup>+</sup> family is that of protonated naphthalenes, the extra hydrogen being either in *alpha* or *beta* position ( $\alpha$ - and  $\beta$ -HN<sup>+</sup>). In fact, these species are the first 'real' representatives of the group above and are 'benzene-fused' analogues of PB<sup>+</sup>. As the constitutional formula C<sub>10</sub>H<sub>9</sub><sup>+</sup> implies, there are of course other isomers in need for consideration.

**Table A.1:** Observed onsets ( $\lambda_{\text{Ne}} \pm 0.1$  nm) and vibrational progressions within electronic transitions of  $\text{C}_6\text{H}_7^+$  cations and  $\text{C}_6\text{H}_7^\bullet$  neutral radicals in 6 K neon matrices [3,6]

Species	$\lambda_{\text{Ne}}$ [nm]	$\tilde{\nu}$ [ $\text{cm}^{-1}$ ]	$\Delta\tilde{\nu}$ [ $\text{cm}^{-1}$ ]	Assignment
<b><math>\alpha</math>-PF<sup>+</sup></b>	335.3	29 822	0	$0_0^0$ $\tilde{A}^1A' \leftarrow \tilde{X}^1A'$
<b>PB<sup>+</sup></b>	325.4	30 727	0	$0_0^0$ $\tilde{A}^1B_2 \leftarrow \tilde{X}^1A_1$
	316.3	31 619	892	$\nu_{11}$
<hr/>				
<b><math>\alpha</math>-HF</b>	532.4	18 782	0	$0_0^0$
	511.2	19 560	778	$\nu_{20}$
	326.1	30 661	0	$0_0^0$
	319.7	31 283	622	$\nu_{21}$ (or $5\nu_{14}$ of MHF)
	316.6	31 584	923	$\nu_{17}$
	313.6	31 886	1225	$\nu_{13}$
	312.3	32 017	1356	$\nu_{11}$
<b>MHF</b>	335.7	29 789	0	$0_0^0$
	332.1	30 111	322	$\nu_{14}$
	328.9	30 403	614	$2\nu_{14}$
	322.0	31 055	394	$4\nu_{14}$
<b>E-HT</b>	281.5	35 524	0	$0_0^0$
	272.3	36 718	1194	$\nu_{19}$
	263.6	37 930	2406	$2\nu_{19}$
<b>c-C<sub>6</sub>H<sub>7</sub></b>	548.9	18 217	0	$0_0^0$ $\tilde{A}^2A_2 \leftarrow \tilde{X}^2B_1$
	537.6	18 602	385	$2\nu_{23}$
	524.8	19 056	839	$\nu_{11}$
	520.5	19 212	995	$\nu_{10}$
	516.7	19 355	1138	$\nu_8$
	507.3	19 714	1497	$\nu_5$
	310.3	32 225	0	$0_0^0$ $\tilde{B}^2B_1 \leftarrow \tilde{X}^2B_1$
	308.4	32 430	205	$2\nu_{23}$
	306.4	32 642	417	$4\nu_{23}$
	304.5	32 843	618	$6\nu_{23}$
	302.8	33 021	796	$\nu_{11}$
	301.0	33 222	997	$\nu_{11} + 2\nu_{23}$
299.2	33 427	1202	$\nu_{11} + 4\nu_{23}$	
297.2	33 647	1422	$\nu_{11} + 6\nu_{23}$	

The experimental and theoretical methods described in earlier chapters of this work, one of which—fluorescence—developed first for the  $\text{C}_{11}\text{H}_9^+$  project (Chapter 5), were all needed and applied to draw some remarkable conclusions. [3,6] These are summarized below.

- Protonated PAHs are ‘synthesized’ efficiently via chemical ionization (proton transfer) of the parent PAH with suitable proton donors such as simple alcohols (in this case: MeOH). Such a reaction route prefers the production of the most stable H-PAH<sup>+</sup> isomer over other alternatives. The basis for selection of a particular donor is its proton affinity—it has to differ by ~50 kJ mol<sup>-1</sup> from that of the acceptor (the PAH) and then the H<sup>+</sup> is transferred over in the ion source productively. Whenever available, dihydro-PAHs can also be used as a precursor; they easily get ionized and fragmented (H loss) in discharge-type environments, and tend to form multiple structural isomers of the respective H-PAH<sup>+</sup>.
- $\alpha$ - and  $\beta$ -HN<sup>+</sup> possess moderately intense S<sub>1</sub>/S<sub>2</sub> ← S<sub>0</sub> transitions in the visible and UV spectral regions (calculated oscillator strengths  $f \sim 0.05$ – $0.3$ ), with origin bands located in a neon matrix at 502.1 and 396.1 nm for  $\alpha$ -HN<sup>+</sup>, and 534.5 and 322.3 nm in the case of  $\beta$ -HN<sup>+</sup> (Figure A.3; the UV transitions are not shown here). The excited states are of <sup>1</sup> $\pi\pi^*$  character.
- Another C<sub>10</sub>H<sub>9</sub><sup>+</sup> isomer, 2-indenylmethylum (2-IME<sup>+</sup>), was found to absorb with an onset at 377.8 nm. Though 1-azulenium was calculated to be more stable than 2-IME<sup>+</sup> and is within the rule-of-thumb (~50 kJ mol<sup>-1</sup>) energetic vicinity of the global minimum on the C<sub>10</sub>H<sub>9</sub><sup>+</sup> PES ( $\alpha$ -HN<sup>+</sup>) so that production (and trapping) of any structures should be possible, its absorptions were not seen. The reason could be the deterministic nature of the employed precursors (dihydro-naphthalene and 2-methyl-indene), that is, five- and, especially, six-membered rings, characteristic for all PAHs, have a damped ‘interest’ in giving up their resonance-stabilized structure.
- C<sub>10</sub>H<sub>9</sub> radicals corresponding to the detected cations reveal band systems with onsets at 528.1 and 330.9 nm for  $\alpha$ -, 516.2 nm for  $\beta$ -hydronaphthyl and 451.2 nm in the case of 2-methylene-indene. Upon irradiation, a similar  $\alpha \rightarrow \beta$  photoconversion likely takes place as for HN<sup>+</sup> (see below) with, on the contrary to the cations, additional naphthyl-motif  $\rightarrow$  indene-based species rearrangement, and requires further investigation.
- $\alpha$ -HN<sup>+</sup> was observed to fluoresce from its S<sub>1</sub> state upon both the excitation to S<sub>1</sub> and S<sub>2</sub>. Emission from no other form of the trapped C<sub>10</sub>H<sub>9</sub><sup>+</sup> or C<sub>10</sub>H<sub>9</sub> species was seen; this may be due to either the sensitivity of the approach or different relaxation processes.
- Selective irradiation ( $340 < \lambda < 390$  nm) of the S<sub>2</sub> ← S<sub>0</sub> absorption of  $\alpha$ -HN<sup>+</sup> induced tautomerization in the  $\alpha \rightarrow \beta$  direction. This photoprocess is fully

reversible:  $\beta$ -HN<sup>+</sup> relaxes rapidly into the by  $\sim 12$  kJ mol<sup>-1</sup> more stable *alpha* form both via quantum tunnelling of the ‘excess’ (liable) hydrogen/thermal excitation near the top of the ground-state barrier and—upon S<sub>1</sub>/S<sub>2</sub> ← S<sub>0</sub> excitation of  $\beta$ -HN<sup>+</sup>—through an out-of-plane conical intersection geometry (Figures A.3 and A.4). A backward pumping scheme  $\alpha \rightarrow \beta$  involving only the S<sub>0</sub> states might be possible to carry out with an IR laser below or above the transition-state barrier. Theoretical calculations on the electronic states of the HN<sup>+</sup> cations, vertical excitation and adiabatic energies, and minimum-energy pathways along the relevant  $r(\text{C-H})$  reaction coordinates revealed a high complexity even for this ‘simple’ H-PAH<sup>+</sup> system (Figure A.4). [3,6]

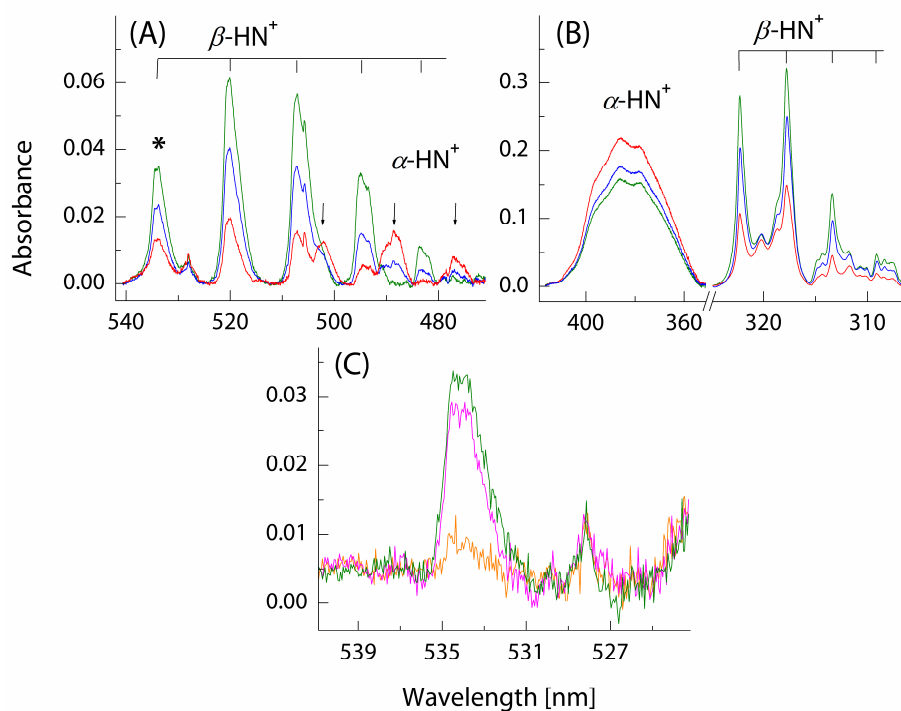


**Figure A.3:** Electronic absorption spectra of  $\alpha$ - and  $\beta$ -protonated naphthalenes illustrating the observed photophysical processes. [3,6] (A) Visible section of the spectra of C<sub>10</sub>H<sub>9</sub><sup>+</sup> cations produced from a naphthalene/MeOH mixture, recorded after UV measurements (red trace), subsequent 12 (blue) and 20 min (green) bleaching of the matrix with  $340 < \lambda < 390$  nm radiation. (B) UV part of the spectra measured reproducing the irradiation conditions used in panel A. (C) Origin band region of the 535 nm absorption system of  $\beta$ -HN<sup>+</sup> (asterisk in panel A) recorded using cut-off filters blocking the light below  $\sim 520$  nm. Green and magenta traces were measured in a  $\sim 2$  min sequence to demonstrate the intensity decay caused by the light used for recording the spectra, whereas the orange curve is after the matrix was left in the dark for  $\sim 30$  min.

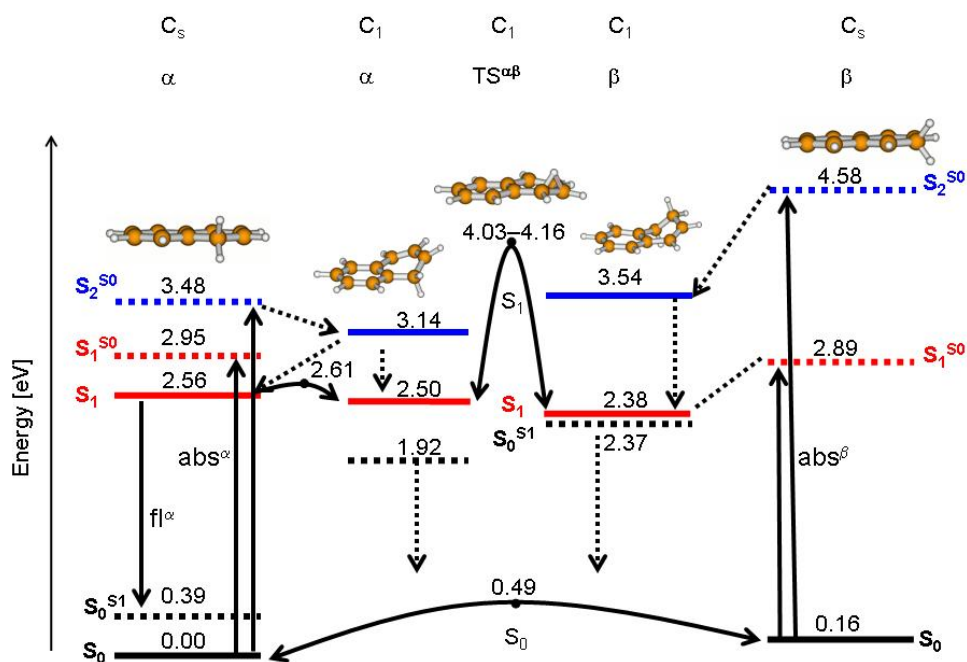


**Figure A.4:** Vertical (dashed lines) and adiabatic (solid) energies for the  $S_1 \leftarrow S_0$  and  $S_2 \leftarrow S_0$  transitions of  $\alpha$ - and  $\beta$ -protonated naphthalenes. [3,6] Ground-state energy computed at the optimized geometry of the first or second excited-state minimum is denoted as  $S_0^{S1}$  or  $S_0^{S2}$ , respectively. The energy (eV) of a given state is relative to the global minimum ( $S_0$  of  $\alpha$ -HN $^+$ ). The observed spectroscopic processes (absorption “abs” and fluorescence “fl”) are indicated by solid arrows, whereas the internal conversion by dashed ones.  $TS^{\alpha\beta}$  denotes the transition state of the  $\alpha$ - and  $\beta$ -HN $^+$  isomers. Energy barriers between the respective states are shown with arrows at each end.

A number of other aromatic and PAH derivatives were also studied. These include protonated anthracene and phenanthrene (an article is enclosed at the back of this appendix), [7] corannulene $^+$ ,  $\Phi$ - $C_{2n}H^+$  and  $(H)C_{60}^+$  among others, but the sets  $C_{2n}H_4^+$ ,  $C_5H_7^+$  and  $C_7H_9^+$  may contain cyclic structures, too (Section A.3). As already inferred in Chapter 7, these species continue to provide interesting topics for investigation.



## A.2 NON-CARBONACEOUS COMPOUNDS

As introduced in [Chapter 1](#), there are other elements than carbon being synthesized in large amounts in stars and novae, which then form molecules and ions constituting various objects of the ISM. Their cosmic abundance may be orders of magnitude lower than that of carbon; nevertheless, to measure the electronic spectra of species these atoms build is of fundamental (chemical) importance in terrestrial as well as space environments.

### A.2.1 Sulfur dimers and trimers, $S_{2,3}^{-/0}$

Sulfur and its compounds possess many interesting and unique properties. It sits below oxygen in the periodic table and has an extensive chemistry. Under normal conditions, sulfur atoms form cyclic octatomic molecules,  $S_8$ ; a soft, yellow, easily subliming solid with a faint odor ([Figure A.5a](#)). It is a multivalent non-metal and can act as either oxidant or reducing agent. Massive amounts of it can be found on Earth in minerals, bound gaseous as well as in pure, elemental forms. Sulfur has over 30 solid allotropes, second only to carbon, and 25 known isotopes. It is thought to be an essential (quantity) element for all life and is involved in a variety of biochemical processes. In space, it is the tenth most abundant element. S and  $S_2$  have been observed by the *Hubble Space Telescope* in the atmosphere of planet Jupiter's moon Io ([Figure A.5b](#)); [\[42,43\]](#) photochemical models predict that the eruption columns of its Pele-type volcanoes may contain sulfur clusters up to  $S_{10}$ . [\[44\]](#) These  $S_n$  species are also assumed to play a role in the photochemistry of the lower atmosphere of Venus [\[45,46\]](#) and in circumstellar shells of carbon-rich, evolved stars. [\[47\]](#) The smallest,  $n = 2-8$  neutrals have been studied experimentally by Raman, [\[48-51\]](#) IR, [\[52\]](#) microwave [\[53,54\]](#) and optical spectroscopies [\[55-60\]](#) in rare-gas matrices and the gas phase.

$S_n^-$  anions have also been the aim of numerous experimental [\[61-75\]](#) and theoretical studies; [\[74-79\]](#) most of these works concerned  $S_2^-$  and  $S_3^-$  only. The latter two species have been isolated in alkali halide or silicate matrices and characterized by means of ESR, [\[61-63\]](#) Raman, [\[64-68\]](#) and UV/Vis spectroscopies. [\[64,66-71\]](#) In addition to these matrix experiments, PD processes of gaseous  $S_2^-$  and  $S_3^-$  have been investigated, [\[72,73\]](#) as well as PE studies on  $S_n^-$  ( $n = 4-11$ ) revealed that the most stable isomers are ring-like up to  $S_5^-$ , chain-like for  $S_8^-$  and

$S_9^-$ , whereas  $S_6^-$  and  $S_7^-$  can occur in both forms. [74,75] The spectroscopic data which were the most relevant for this work came from emission and absorption studies of  $S_2^-$  embedded in alkali halide crystals, [66–71] and absorption of  $S_3^-$  in such crystals and basic solvents. [64,80]  $S_2^-$  has been reported to have a distinct band system with the onset at  $\sim 500$  nm, [70] whereas  $S_3^-$  has a strong broad absorption with a maximum around 620 nm; [64,80] the latter is responsible for the blue color of the mineral *lapis lazuli* and of synthetic ultramarine. [71]

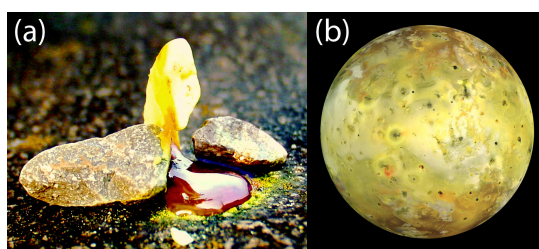


**Figure A.5:** (a) Yellow solid sulfur burns with a blue flame and melts to a red liquid. (b) True-color image of Io, the innermost of the four Galilean satellites of Jupiter, as photographed by the *Galileo* spacecraft. Surface paint is caused by gravitationally-driven volcanism resulting in plumes and lava flows largely of sulfur allotropes and compounds.

In this study, [4,8]  $S_2^-$  and  $S_3^-$  ( $n = 2,3$ ) anions were produced from a mixture of  $CS_2$  in argon in a hot-cathode discharge ion source—the anionic analogue of that described in Chapter 2—and mass-selectively embedded into a neon matrix at 6 K. A long progression with the excitation of up to 12 or more vibrational quanta was observed in the  $A\ ^2\Pi_u \leftarrow X\ ^2\Pi_g$  electronic transition of  $S_2^-$ , with the onset being at 467.1 nm (Figure A.6a). The inferred spectroscopic constants in the  $A\ ^2\Pi_u$  state are:  $\nu_{0-0} = (21\ 407 \pm 4)$   $cm^{-1}$ ,  $\omega_0' = (328.4 \pm 1)$   $cm^{-1}$ ,  $\omega_0'x_0' = (2.4 \pm 0.1)$   $cm^{-1}$ . The electronic spectrum of  $S_3^-$  exhibits a rich vibrational structure with a bimodal intensity distribution; this results from the overlap of two transitions,  $\tilde{C}^2A_2 \leftarrow \tilde{X}^2B_1$  and  $(\tilde{D}\text{ or } \tilde{E}) \leftarrow \tilde{X}^2B_1$ , with origins at 701.3 and 619.1 nm (Figure A.6c). The frequencies ( $cm^{-1}$ ) of the totally symmetric modes  $\nu_1$  and  $\nu_2$  are 466 and 184 in  $\tilde{C}^2A_2$ , and 446 and 177 in the  $(\tilde{D}\text{ or } \tilde{E})$  state. The matrices were then exposed to filtered ( $\lambda > 305$  nm) radiation from a mpHg lamp and spectra were recorded again to distinguish transitions of corresponding neutral species (Figure A.6, panels b and d) from the anions. [4,8]

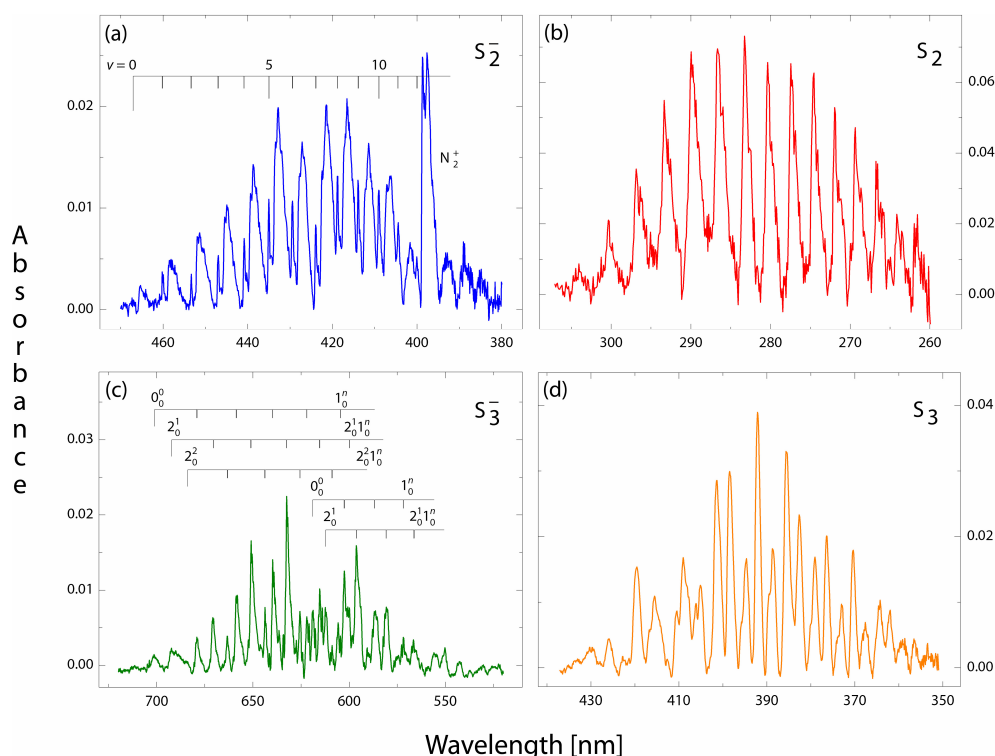


**Figure A.6:** Electronic transitions of  $S_n^{-/0}$  ( $n=2,3$ ) as recorded in absorption after selectively depositing the anions into 6 K neon matrices (*left*) and subsequent UV irradiation of the samples (*right*). (a)  $A^2\Pi_u \leftarrow X^2\Pi_g$  of  $S_2^-$ ; (b)  $B^3\Sigma_u^- \leftarrow X^3\Sigma_g^-$  of  $S_2$ ; (c)  $\tilde{C}^2A_2 \leftarrow \tilde{X}^2B_1$  and ( $\tilde{D}$  or  $\tilde{E}$ )  $\leftarrow \tilde{X}^2B_1$  of  $S_3^-$ ; (d)  $\tilde{A}^1B_2 \leftarrow \tilde{X}^1A_1$  of  $S_3$ . Vibrational progression in the excited states is shown above the spectra. Note that the absorbances on the x-axes are not proportionally scaled.  $N_2^+$  is due to residual nitrogen impurity in the vacuum chamber (Chapter 2). [4,8]

### A.2.2 Titanium dioxide, $TiO_2$

Spectral features of transition metal clusters are a particularly challenging topic to investigate because of the individual characteristics of the  $d$ -shell. Titanium is one of the most abundant transition metals in space; [81] it has been detected in stellar atmospheres of cool M-type stars (Figure A.7a) as titanium monoxide (TiO) and titanium hydride. [82] In fact, TiO is the main opacity source in these atmospheres in the visible and NIR regions and has extensively been studied spectroscopically. [83–87] According to modeling, titanium dioxide ( $TiO_2$ ) is believed to be present in similar environments where TiO is found. [88,89] It is interesting for more down-to-Earth reasons, too, having a wide range of applications from being memristor material to food coloring (Figure A.7b).

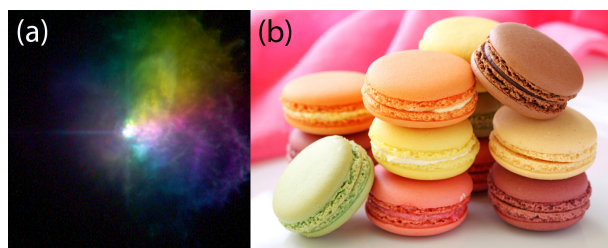


**Figure A.7:** (a) *Hubble Space Telescope* montage image of the M-type hypergiant VY Canis Majoris, the largest known star ( $R \sim 2000 R_{\odot}$ ), showing huge amounts of gas being ejected during its outbursts. (b) Artificial color additives [E100–E199] are recognized as an important part of practically all foods we consume.  $\text{TiO}_2$  is classified as E171 ('pure white').

The electronic absorption spectrum of  $\text{TiO}_2$  was investigated. [9]  $\text{TiO}_2^-$  anions were produced from  $\text{TiO}_2/\text{graphite}$  (2:1 ratio) composite rods in the cesium sputtering source mentioned in [Chapter 2](#) and, following mass selection, trapped in a neon matrix at 6 K. The spectra implied that both bent and linear forms of  $\text{TiO}_2$  were present in these matrices ([Figure A.8](#)), having the following characteristics: Two electronic systems of the bent oxo form ( $\text{O}=\text{Ti}=\text{O}$ ),  $\tilde{A}^1\text{B}_2 \leftarrow \tilde{X}^1\text{A}_1$  and  $\tilde{C}^1\text{B}_1 \leftarrow \tilde{X}^1\text{A}_1$ , were seen with origins at 524 and 368 nm; the linear isomer showed a transition with an onset at 628 nm ([Table A.2](#)). The obtained spectra were discussed with respect to PE studies [90] and theoretical calculations. [91] An astrophysical implication could be that there is an unidentified emission feature found towards VY Canis Majoris ([Figure A.7a](#)) at 530.538 nm. [92]

Subsequently, publications on the  $\text{TiO}_2$  molecule have appeared reporting high-resolution LIF and REMPI visible electronic spectra and detailed theoretical analyses. [93,94] Their interpretation suggests that the origin of  $\tilde{A}^1\text{B}_2 \leftarrow \tilde{X}^1\text{A}_1$  of the bent isomer (at  $17\,591\text{ cm}^{-1}$  in the gas phase) was too weak to be observed in the neon matrix spectrum ([Figure A.8](#)).

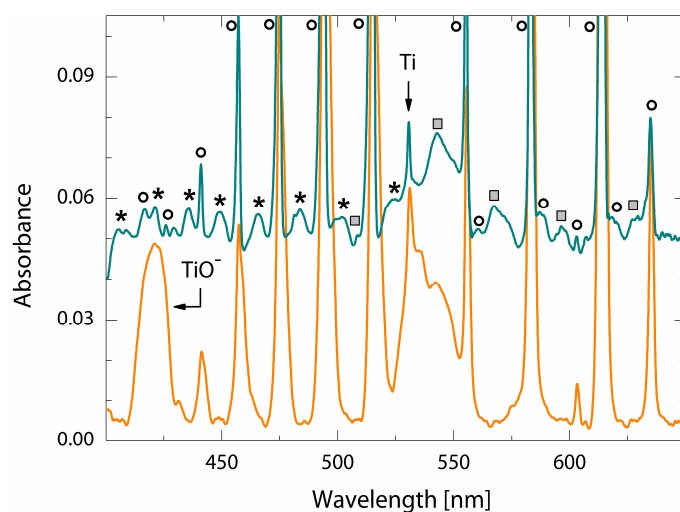


**Figure A.8:** Visible part of electronic absorption spectra recorded in a 6 K neon matrix after mass-selective deposition of  $\text{TiO}_2^-$  (*bottom*) and subsequent UV irradiation and annealing of the matrix (*top*). Asterisks represent bands of the  $\tilde{A}^1\text{B}_2 \leftarrow \tilde{X}^1\text{A}_1$  transition of bent  $\text{TiO}_2$ , squares stand for features of linear  $\text{TiO}_2$  and circles mark the absorptions of  $\text{TiO}$ . [9]

**Table A.2:** Observed bands  $\lambda_{\text{Ne}}$  in the electronic absorption spectra of  $\text{TiO}_2$  along with suggested assignments and reference data [9]

$\lambda_{\text{Ne}}$ [nm]	$\tilde{\nu}$ [ $\text{cm}^{-1}$ ]	$\Delta\tilde{\nu}$ [ $\text{cm}^{-1}$ ]	Assignment	Reference $\lambda$ [nm] PE / MRCI / TD DFT
<b>linear <math>D_{\infty h}</math></b>				
628	15 924	0	$0_0^0$	632
597	16 750	826	$\nu_1$	
568	17 606	1682	$2\nu_1$	
542	18 484	2560	$3\nu_1$	
509	19 646	3722	$4\nu_1 + \nu_3$	
<b>bent <math>C_{2v}</math></b>				
524	19 084	0	$0_0^0 \tilde{A}^1\text{B}_2 \leftarrow \tilde{X}^1\text{A}_1$	516 / 510 / 532
502	19 920	836	$\nu_1$	
497	20 121	1037	$\nu_1 + \nu_2$	
485	20 619	1535	$\nu_1 + \nu_2 + \nu_3$	
481	20 790	1706	$2\nu_1$	
465	21 505	2421	$3\nu_1$	
461	21 692	2608	$3\nu_1 + \nu_2$	
448	22 321	3237	$4\nu_1$	
433	23 095	4011	$5\nu_1$	
419	23 866	4782	$6\nu_1$	
405	24 691	5607	$7\nu_1$	
368	27 174	0	$0_0^0 \tilde{C}^1\text{B}_1 \leftarrow \tilde{X}^1\text{A}_1$	— / 347 / 339

## A.3 UNPUBLISHED RESULTS

To investigate a chosen species, first a suitable precursor has to be found. This is not as an easy task as it reads—besides the struggle for sufficient ion yields, different experimental conditions may cause unwanted isomerization or fragmentation. Such processes can be advantageous some times; an example was given in [Chapter 5](#).

For the study of the aromatics presented in this work, mass spectra of a large number of cyclic and open-chain hydrocarbons were recorded. The cation with  $m/z = 102$  is an intense band in several of these ([Table A.3](#) and [Figure A.9](#), panel A). The corresponding ion  $C_8H_6^+$  was produced from cyclooctatetraene (COT), deposited in neon and its electronic spectrum recorded. The feeding of a specific starting material into the source in combination with mass selection often suggests the structure of the trapped fragment; *e.g.*, in the case of COT the survival of the eight-membered ring upon the removal of two hydrogens might be expected. The harsh discharge conditions in the hot-cathode source, however, rearrange  $C_8H_6^+$  and the spectrum is identical with that of phenylacetylene<sup>•+</sup> ([Figure A.10](#)), in good agreement with Ref. [95].

**Table A.3:** Fragmentation data of selected hydrocarbons<sup>[a]</sup>

<b>naphthalene</b>							
<i>m/z</i>	129	128	127	<b>102</b>	64		
Rel. intensity	100	1000	108	<b>61</b>	68		
<b>azulene</b>							
<i>m/z</i>	129	128	127	<b>102</b>	51		
Rel. intensity	111	1000	124	<b>114</b>	66		
<b>cyclooctatetraene</b>							
<i>m/z</i>	104	103	<b>102</b>	78	77	51	50
Rel. intensity	1000	610	<b>105</b>	825	350	460	278
[a] The data are based on electron impact measurements and were retrieved from the <a href="#">NIST Mass Spectrometry Data Center</a> online databank.							

Focusing on the further fragmentation of phenylacetylene, spectra of the ions  $C_6H_2^+$  and  $C_6H_4^+$  ( $m/z = 74$  and  $76$ ; see [Figure A.9](#), panel B) were also recorded. In the first case, the benzene ring also opened up to form triacetylene cation, [96]

whereas the second revealed interesting spectroscopic information and is briefly discussed below.

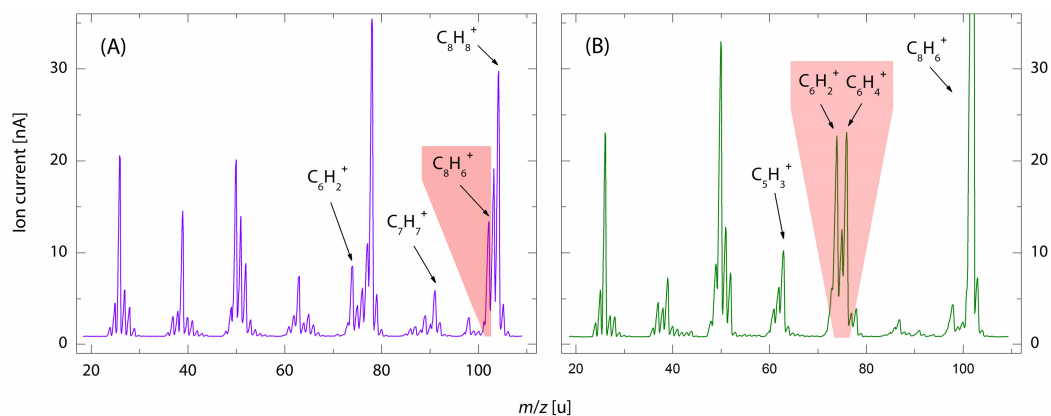


**Figure A.9:** Mass spectrum of (A) cyclooctatetraene and (B) phenylacetylene as produced in a hot-cathode discharge source. The respective parent ions and some other peaks of interest are indicated.

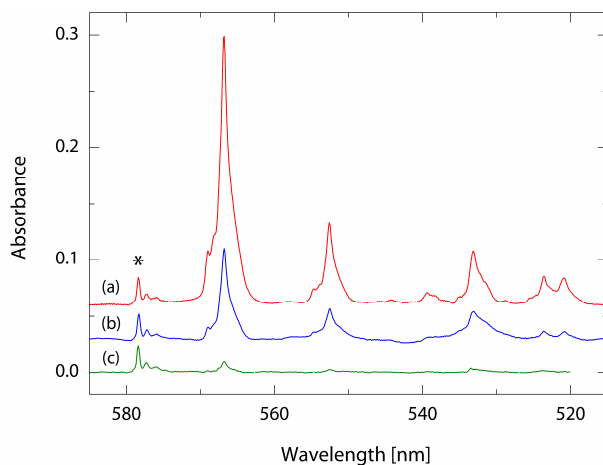


**Figure A.10:** Electronic absorption spectra of  $C_8H_6^+$  ( $m/z = 102$ ) produced from cyclooctatetraene, and recorded after (b) deposition and (c) subsequent UV irradiation. The decrease in absorption intensity in the latter indicates charged species. Trace a shows spectrum of the parent cation of phenylacetylene ( $\tilde{C}^2B_1 \leftarrow \tilde{X}^2B_1$  transition). [95] Asterisk belongs to an unidentified feature present when using  $O_2$  as an electron scavenger.

### A.3.1 Light-induced *cis/trans* isomerization of $C_6H_4^+$ species

It is often desirable to study *series* of carbon species such as  $C_{2n}H_4^+$ , because their spectral features may follow trends (Chapter 3) and the PIB model could be valid. Deposition of ions of the set above with  $n = 2-6$  was carried out, with (partial) electronic spectra of the first three members being known from earlier. [97–100]

Particularly interesting proved to be the cation  $C_6H_4^+$  for three reasons: (a) Apart from the known visible transition of two isomers around 600 nm, [98–100] there was to be resolved a complex pattern starting just below 380 nm, at least as strong as the formers (Figure A.11); (b) the constitutional formula  $C_6H_4^+$  describes benzyne cations too, the positively charged derivative of classical examples of the unique biradicals' class (structures **J+**, **K+** and **L+** in Figure A.12); and (c) two broad ( $\pm 5$  nm) 'bumps'—commonly associated with instrumental artifacts—, observed in the matrix spectra at ca. 630 and 390 nm, emerged as *real* spectroscopic features (the visible one is in Figure A.13). Not only that, these broad absorptions were actually found to belong—based on extensive irradiation schemes done on the studied matrices, experiments with exactly a dozen different precursors and TD DFT vertical excitation energies calculated for the stable isomers of Figure A.12—to the *cis* pair (**C+**) of a planar *trans*- $C_6H_4^+$  species (**B+**) reported earlier at 603 nm (Figure A.13). [98] It is worthwhile to note that the three observed isomers **B+**, **C+** and **D+** exhibit entirely different band profiles, thereby representing a case study of observable features of UV/Vis matrix spectra.

Furthermore, photo-induced transformation of the **B+** and **C+** isomer pair was feasible in both the  $c \leftrightarrow t$  channels upon irradiating relevant absorption bands. This is similar to that observed for protonated naphthalenes, where flips between the two stereoisomers could be brought forth in the  $\alpha \leftrightarrow \beta$  directions (Section A.1). The detection of isomerization reactions in low-temperature (neon) matrices by the observation electronic spectra is an especially interesting topic, and it is hoped that gas-phase studies and the confirmation of these results will duly follow. However, the growing variety of different possible structures with an increasing number of atoms complicates an unambiguous assignment of spectral features and underlines the necessity for high-level, quantum chemical calculations. TD DFT might not succeed in describing the electronic transitions adequately, especially if they are to higher states.



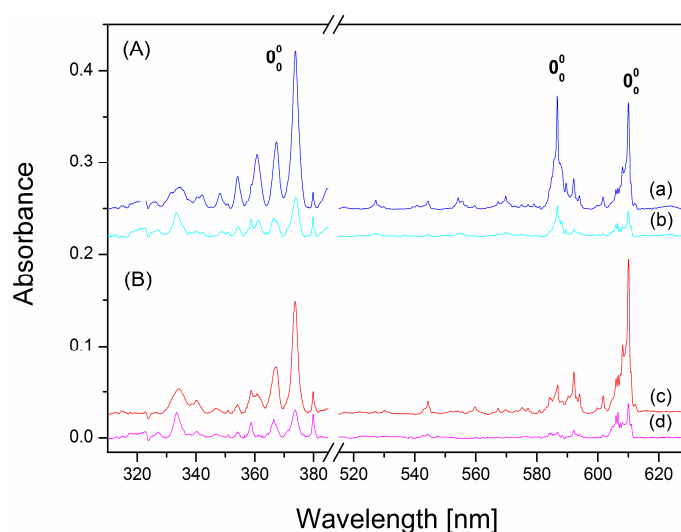


**Figure A.11:** Overview electronic absorption spectra of  $C_6H_4^+$  ( $m/z = 76$ ) cations made from (A) phenylacetylene and (B) 2,4-hexadiyne. Traces a and c were measured after deposition, while traces b and d after UV bleaching.

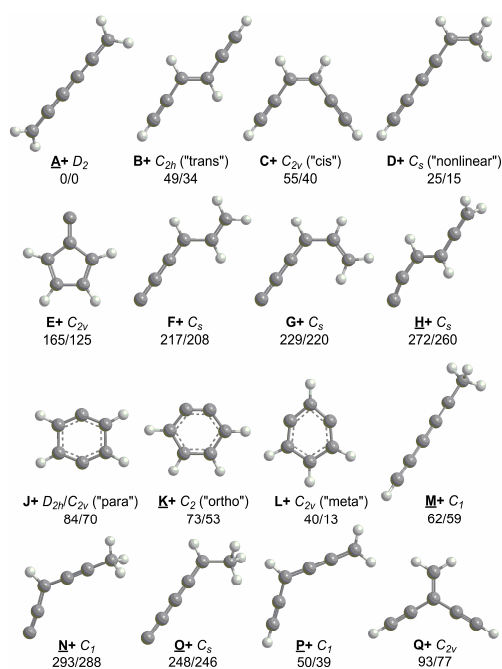


**Figure A.12:** Scheme of considered  $C_6H_4^+$  isomers with their ground-state symmetry and their relative energies ( $\text{kJ mol}^{-1}$ , without zero-point corrections) calculated with DFT using the BLYP or B3LYP functionals and the cc-pVTZ basis set. Isomer **J**+ converges at slightly different symmetries as indicated. Those underlined are non-planar structures.

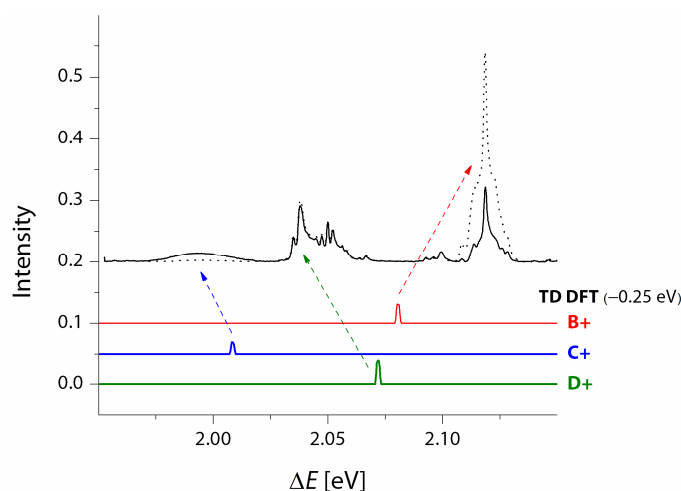


**Figure A.13:** Electronic spectra of  $C_6H_4^+$  in the 600 nm region illustrating the (light-induced) *cis/trans* isomerization processes (black curves). The assignment is based on TD DFT vertical excitation energy calculations (colored) on the stable isomers of Figure A.12.

CASPT2 and EOM-CCSD(T) usually under-/overestimates excitation energies, respectively; therefore, a combination of these methods shall provide reasonable assignment to the UV systems of  $C_6H_4^+$  (Figure A.11) and is in progress. [101] It is also to be explained why the rigid neon matrix allows upon electronic excitation such large a structural change as the *cis/trans* rearrangement of  $C_6H_4^+$  isomers imply.

A few other hydrocarbon series including  $C_5H_y^+$  and  $C_7H_y^+$  (with  $y$  in the range 3–6 but not fully covering it) have been also investigated. Their spectra are not shown here but can be found for future reference in the file database and relevant notebooks of the Matrix Isolation Laboratory, or can be obtained upon request.

### A.3.2 Metal-containing clusters

A number of metallic cluster anions and their neutrals were studied using the cesium sputtering source (Chapter 2) and sample rods or pellets, including compounds that contain Ti, Fe, Mg or Al. The magnetron approach should be a better alternative to investigate such species (Chapter 7); nevertheless, two systems in need of confirmation are given in Figures A.14 and A.15.

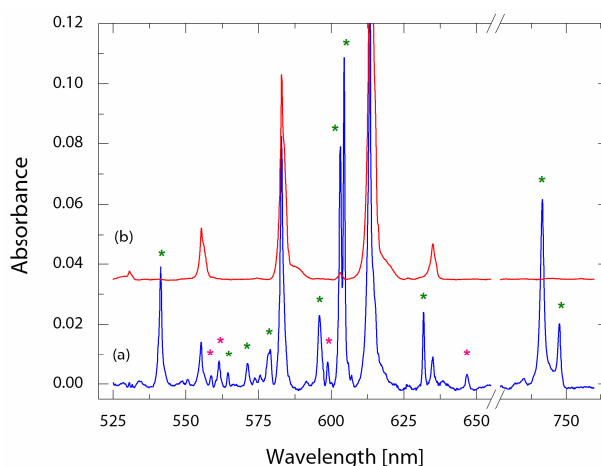


**Figure A.14:**  $\text{TiO}_3^-/\text{TiC}_4^-$  (of the same  $m/z$ ) anions were produced in a cesium sputter negative ion source from  $\text{TiO}_2/\text{graphite}$ ,  $\text{TiO}_2/\text{silver}$  and (a)  $\text{PbTiO}_3/\text{Ag}$  composite rods, embedded in 6 K neon matrices, and their electronic spectra recorded before and (b) after irradiation. The spectra are complex and overlap with transitions arising from  $\text{TiO}$  and  $\text{TiO}_2$  upon partial fragmentation. Nonetheless, several strong absorptions could be assigned to  $\text{TiO}_3$  and  $\text{TiC}_4$  (asterisks/not shown) on the basis of quantum chemical calculations. A (mass- and) precursor-selective REMPI or magnetron confirmation is desirable.

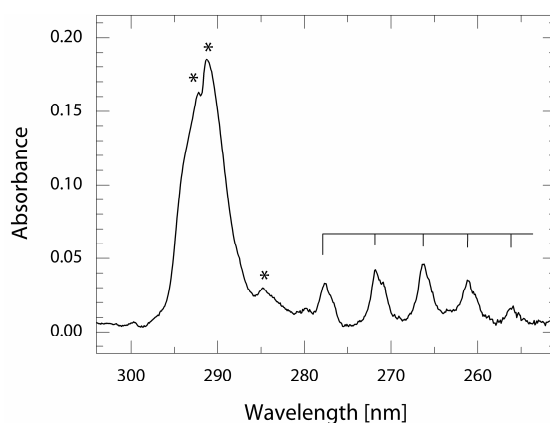


**Figure A.15:** Electronic absorption spectrum recorded after deposition of  $\text{Al}^-$  produced in a cesium sputtering source. The broad band on the left (asterisks, maximum at 291.3 nm) may correspond to the  $3s^23d\ ^2D - 3s^23p\ ^2P$  triplet of  $\text{Al}(\text{I})$  ( $\lambda_{\text{vac}} = 309.36\text{ nm}$  for the  $5/2-3/2$  transition), whereas the vibrational progression  $\Delta\tilde{\nu} = (770 \pm 10)\text{ cm}^{-1}$  on the right is likely to be due to  $\text{C}\ ^3\Pi \leftarrow \text{X}\ ^3\Pi$  of  $\text{AlN}$  (obtained spectroscopic terms:  $T_e = 17\,495\text{ cm}^{-1}$ ;  $\omega_e = 658\text{ cm}^{-1}$ ), resulting from a recombination with atoms from residual  $\text{N}_2$  in the deposition chamber.



## Bibliography

- [1] S. Chakrabarty, V. Rudnev, J. Fulara, R. Dietsche, A. Nagy, I. Garkusha, F.J. Mazzotti, C.A. Rice, J.P. Maier. *Electronic spectra of C<sub>4</sub>H<sub>3</sub>Cl<sup>+</sup> isomers*. *Mol. Phys.* **2012**, 110(24): 3077–3084.
- [2] J.P. Maier, G.A.H. Walker, D.A. Bohlender, F.J. Mazzotti, R. Raghunandan, J. Fulara, I. Garkusha, A. Nagy. *Identification of H<sub>2</sub>CCC as a diffuse interstellar band carrier*. *Astrophys. J.* **2011**, 726(1): 41/1–9.
- [3] I. Garkusha. *Electronic spectroscopy of mass-selected protonated polycyclic aromatic hydrocarbons in neon matrices*. Ph.D. thesis, University of Basel, Faculty of Science, **2012**.
- [4] I.G. Shnitko. *Absorption spectroscopy of carbon and sulfur chains in 6 K neon matrices*. Ph.D. thesis, University of Basel, Faculty of Science, **2008**.
- [5] I. Garkusha, J. Fulara, A. Nagy, J.P. Maier. . *Electronic transitions of protonated benzene and fulvene, and of C<sub>6</sub>H<sub>7</sub> isomers in neon matrices*. *J. Am. Chem. Soc.* **2010**, 132(42): 14979–14985.
- [6] I. Garkusha, A. Nagy, J. Fulara, M.F. Rode, A.L. Sobolewski, J.P. Maier. *Electronic spectra and reversible photoisomerization of protonated naphthalenes in solid neon*. *J. Phys. Chem. A* **2012**, published online; doi: 10.1021/jp310612j.
- [7] I. Garkusha, J. Fulara, A. Nagy, J.P. Maier. *Electronic absorption spectra of protonated anthracenes and phenanthrenes, and their neutrals in neon matrices*. *Astrophys. J.* **2011**, 728(2): 131/1–7.
- [8] I. Shnitko, J. Fulara, I. Garkusha, A. Nagy, J.P. Maier. *Electronic transitions of S<sub>2</sub><sup>-</sup> and S<sub>3</sub><sup>-</sup> in neon matrixes*. *Chem. Phys.* **2008**, 346(1–3): 8–12.
- [9] I. Garkusha, A. Nagy, Z. Guennoun, J.P. Maier. *Electronic absorption spectrum of titanium dioxide in neon matrices*. *Chem. Phys.* **2008**, 353(1–3): 115–118.
- [10] V. Le Page, Y. Keheyan, V.M. Bierbaum, T.P. Snow. *Chemical constraints on organic cations in the interstellar medium*. *J. Am. Chem. Soc.* **1997**, 119(35): 8373–8374.
- [11] T.P. Snow, V. Le Page, Y. Keheyan, V.M. Bierbaum. *The interstellar chemistry of PAH cations*. *Nature* **1998**, 391: 259–260.
- [12] E. Herbst, V. Le Page. *Do H atoms stick to PAH cations in the interstellar medium?* *Astron. Astrophys.* **1999**, 344(1): 310–316.
- [13] D.M. Hudgins, C.W. Bauschlicher, L.J. Allamandola. *Closed-shell polycyclic aromatic hydrocarbon cations: a new category of interstellar polycyclic aromatic hydrocarbons*. *Spectrochim. Acta A: Mol. Biomol. Spectr.* **2001**, 57(4): 907–930.
- [14] P. Weilmuenster, A. Keller, K.H. Homann. *Large molecules, radicals, ions, and small soot particles in fuel-rich hydrocarbon flames. Part I: Positive ions of polycyclic aromatic hydrocarbons (PAH) in low-pressure premixed flames of acetylene and oxygen*. *Combust. Flame* **1999**, 116(1–2): 62–83.

- [15] A.B. Fialkov, J. Dennebaum, K.H. Homann. *Large molecules, ions, radicals, and small soot particles in fuel-rich hydrocarbon flames. Part V. Positive ions of polycyclic aromatic hydrocarbons (PAH) in low-pressure premixed flames of benzene and oxygen.* **Combust. Flame** **2001**, 125(1–2): 763–777.
- [16] A. Kiendler, F. Arnold. *First composition measurements of positive chemiions in aircraft jet engine exhaust: Detection of numerous ion species containing organic compounds.* **Atmosph. Env.** **2002**, 36(18): 2979–2984.
- [17] G.A. Olah. *Aromatic substitution. XXVIII. Mechanism of electrophilic aromatic substitutions.* **Acc. Chem. Res.** **1971**, 4(7): 240–248.
- [18] G.A. Olah, J.S. Staral, G. Asencio, G. Liang, D.A. Forsyth, G.D. Mateescu. **J. Am. Chem. Soc.** **1978**, 100(20): 6299–6308.
- [19] G.A. Olah, G.D. Mateescu, Y.K. Mo. *Stable carbocations. 215. Carbon-13 nuclear magnetic resonance spectroscopic study of the benzenium, naphthalenium, and anthracenium ions.* **J. Am. Chem. Soc.** **1973**, 95(6): 1865–1874.
- [20] A. Pathak, P.J. Sarre. *Protonated PAHs as carriers of diffuse interstellar bands.* **Mon. Not. Roy. Astron. Soc.** **2008**, 391(1): L10–L14.
- [21] M. Hammonds, A. Pathak, A. Candian, P.J. Sarre. *Spectroscopy of protonated and deprotonated PAHs.* In *PAHs and the Universe*; Eds.: C. Joblin, A.G.G.M. Tielens; **EAS Publications Series** **2011**, 46: 373–379.
- [22] W. Jones, P. Boissel, B. Chiavarino, M.E. Crestoni, S. Fornarini, J. Lemaire, P. Maitre. *Infrared fingerprint of protonated benzene in the gas phase.* **Angew. Chem. Int. Ed.** **2003**, 42(18): 2057–2059.
- [23] U.J. Lorenz, N. Solca, J. Lemaire, P. Maitre, O. Dopfer. *Infrared spectra of isolated protonated polycyclic aromatic hydrocarbons: Protonated naphthalene.* **Angew. Chem. Int. Ed.** **2007**, 46(35): 6714–6716.
- [24] N. Solca, O. Dopfer. *Protonated benzene: IR spectrum and structure of C<sub>6</sub>H<sup>+</sup>.* **Angew. Chem. Int. Ed.** **2002**, 41(19): 3628–3631.
- [25] G.E. Douberly, A.M. Ricks, P.V.R. Schleyer, M.A. Duncan. *Infrared spectroscopy of gas phase benzenium ions: Protonated benzene and protonated toluene, from 750 to 3400 cm<sup>-1</sup>.* **J. Phys. Chem. A** **2008**, 112(22): 4869–4874.
- [26] A.M. Ricks, G.E. Douberly, M.A. Duncan. *The infrared spectrum of protonated naphthalene and its relevance for the unidentified infrared bands.* **Astrophys. J.** **2009**, 702(1): 301–306.
- [27] D. Zhao, J. Langer, J. Oomens, O. Dopfer. *Infrared spectra of protonated polycyclic aromatic hydrocarbon molecules: Azulene.* **J. Chem. Phys.** **2009**, 131(18): 184307–184312.
- [28] H. Knorke, J. Langer, J. Oomens, O. Dopfer. *Infrared spectra of isolated protonated polycyclic aromatic hydrocarbon molecules.* **Astrophys. J.** **2009**, 706(1): L66–L70.
- [29] A.A.V. Stuart, E.L. Mackor. *Electronic spectra of carbonium ions.* **J. Chem. Phys.** **1957**, 27(3): 826–827.

- [30] C. Reid. *The aromatic carbonium ions*. *J. Am. Chem. Soc.* **1954**, 76(12): 3264–3268.
- [31] G. Dallinga, E.L. Mackor, A.A.V. Stuart. *Mol. Phys.* **1958**, 1(2): 123–140.
- [32] H. Perkampus, E. Baumgarten. *Proton-addition complexes of aromatic hydrocarbons*. *Angew. Chem. Int. Ed.* **1964**, 3(12): 776–783.
- [33] J.H. Waite, D.T. Young, T.E. Cravens, A.J. Coates, F.J. Crary, B. Magee, J. Westlake. *The process of tholin formation in Titan's upper atmosphere*. *Science* **2007**, 316: 870–875.
- [34] B.S. Freiser, J.L. Beauchamp. *Photochemistry of organic ions in the gas phase. Comparison of the gas phase photodissociation and solution absorption spectra of benzoyl cation, protonated benzene, and protonated mesitylene*. *J. Am. Chem. Soc.* **1976**, 98(11): 3136–3139.
- [35] M.F. Rode, A.L. Sobolewski, C. Dedonder, C. Jouvét, O. Dopfer. *Computational study on the photophysics of protonated benzene*. *J. Phys. Chem. A* **2009**, 113(20): 5865–5873.
- [36] J.L. Franklin, S.R. Carroll. *Effect of molecular structure on ionic decomposition. II. An electron-impact study of 1,3- and 1,4-cyclohexadiene and 1,3,5-hexatriene*. *J. Am. Chem. Soc.* **1969**, 91(24): 6564–6569.
- [37] S.G. Lias, P. Ausloos. *Structures of  $C_6H_7^+$  ions formed in unimolecular and bimolecular reactions*. *J. Chem. Phys.* **1985**, 82(8): 3613–3624.
- [38] M.T. Bowers, D.D. Elleman, R.M. Omalley, K.R. Jennings. *Analysis of ion–molecule reactions in allene and propyne by ion cyclotron resonance*. *J. Phys. Chem.* **1970**, 74(13): 2583–2589.
- [39] G. Bouchoux, M.T. Nguyen, J.Y. Salpin. *Condensation reactions between 1,3-butadiene radical cation and acetylene in the gas phase*. *J. Phys. Chem. A* **2000**, 104(24): 5778–5786.
- [40] Z.Q. Zhu, T. Gaumann. *Structures of product ions  $C_6H_7^+$  and  $C_6H_9^+$  of ion–molecule reactions with allyl bromide*. *Org. Mass Spectrom.* **1993**, 28(10): 1111–1118.
- [41] J.A. Herman, K. Herman, T.B. McMahon. *Formation of  $C_6H_7^+$  ions in ion–molecule reactions in vinyl chloride*. *Can. J. Chem.* **1991**, 69(12): 2038–2043.
- [42] L.M. Feaga, M.A. McGrath, P.D. Feldman. *The abundance of atomic sulfur in the atmosphere of Io*. *Astrophys. J.* **2002**, 570(1): 439–446.
- [43] J.R. Spencer, K.L. Jessup, M.A. McGrath, G.E. Ballester, R. Yelle. *Discovery of gaseous  $S_2$  in Io's Pele plume*. *Science* **2000**, 288(5469): 1208–1210.
- [44] J.I. Moses, M.Y. Zolotov, B.J. Fegley. *Photochemistry of a volcanically driven atmosphere on Io: Sulfur and oxygen species from a Pele-type eruption*. *Icarus* **2002**, 156(1): 76–106.
- [45] J.S. Lewis, F.A. Kreimendahl. *Oxidation state of the atmosphere and crust of Venus from Pioneer Venus results*. *Icarus* **1980**, 42(3): 330–337.
- [46] M.Y. Zolotov. *Lunar Planet. Sci.* **1985**, 16: 942.
- [47] A.E. Glassgold. *Circumstellar photochemistry*. *Annu. Rev. Astron. Astrophys.* **1996**, 34: 241–277.
- [48] M.S. Boumedién, J. Corset, E. Picquenard. *Vibrational study and molecular structure of two  $S_4$  isomers in sulphur vapour*. *J. Raman Spectrosc.* **1999**, 30(6): 463–472.

- [49] P. Lenain, E. Picquenard, J. Corset, D. Jensen, R. Steudel. *Ber. Bunsen Ges. Phys. Chem.* **1988**, 92(8): 859–870.
- [50] P. Lenain, E. Picquenard, J.L. Lesne, J. Corset. *Raman spectra of overheated sulfur vapor.* *J. Mol. Struct.* **1988**, 142: 355–358.
- [51] M. Schmidt. *Elemental sulfur – A challenge to theory and practice.* *Angew. Chem. Int. Ed.* **1973**, 12(6): 445–455.
- [52] D.G. Brabson, Z. Mielke, L. Andrews. *Infrared spectra and structures of isotopically enriched sulfur ( $S_3$  and  $S_4$ ) in solid argon.* *J. Phys. Chem.* **1991**, 95(1): 79–86.
- [53] M.C. McCarthy, S. Thorwirth, C.A. Gottlieb, P. Thaddeus. *The rotational spectrum and geometrical structure of thiozone,  $S_3$ .* *J. Am. Chem. Soc.* **2004**, 126(13): 4096–4097.
- [54] S. Thorwirth, M.C. McCarthy, C.A. Gottlieb, P. Thaddeus, H. Gupta, J.F. Stanton. *Rotational spectroscopy and equilibrium structures of  $S_3$  and  $S_4$ .* *J. Chem. Phys.* **2005**, 123(5): 054326/1–10.
- [55] R.I. Billmers, A.L. Smith. *Ultraviolet-visible absorption spectra of equilibrium sulfur vapor: Molar absorptivity spectra of  $S_3$  and  $S_4$ .* *J. Phys. Chem.* **1991**, 95(11): 4242–4245.
- [56] V.E. Bondybey, J.H. English.  *$B^3\Sigma_u^-$  predissociation and relaxation processes in matrix isolated  $S_2$ .* *J. Chem. Phys.* **1980**, 72(5): 3113–3122.
- [57] P. Hassanzadeh, L. Andrews. *Vibronic absorption spectra of sulfur ( $S_3$  and  $S_4$ ) in solid argon.* *J. Phys. Chem.* **1992**, 96(16): 6579–6585.
- [58] B. Meyer, T.V. Oommen, D. Jensen. *Color of liquid sulfur.* *J. Phys. Chem.* **1971**, 75(7): 912–917.
- [59] B. Meyer, T. Stroyer-Hansen. *Infrared spectra of  $S_4$ .* *J. Phys. Chem.* **1972**, 76(26): 3968–3969.
- [60] B. Meyer, T. Stroyer-Hansen, T.V. Oommen. *The visible spectrum of  $S_3$  and  $S_4$ .* *J. Mol. Spectrosc.* **1972**, 42(2): 335–343.
- [61] J. Schneider, B. Dischler, A. Rauber. *Phys. Status Solid.* **1966**, 13(1): 141–157.
- [62] J.H. Lunsford, D.P. Johnson. *Electron paramagnetic resonance study of  $S_3^-$  formed on magnesium oxide.* *J. Chem. Phys.* **1973**, 58(5): 2079–2083.
- [63] S. Kowalak, A. Jankowska, S. Zeidler, A.B. Wieckowski. *Sulfur radicals embedded in various cages of ultramarine analogs prepared from zeolites.* *J. Solid State Chem.* **2007**, 180(3): 1119–1124.
- [64] W. Holzer, W.F. Murphy, H.J. Bernstein. *Raman spectra of negative molecular ions doped in alkali halide crystals.* *J. Mol. Spectr.* **1969**, 32(1): 13–23.
- [65] W. Holzer, W.F. Murphy, H.J. Bernstein. *Resonance raman effect of  $S_3^-$  doped in a NaCl single crystal.* *Chem. Phys. Lett.* **1970**, 4(10): 641–642.
- [66] M. Ikezawa, J. Rolfe. *Zero-phonon transitions in  $O_2^-$ ,  $S_2^-$ ,  $Se_2^-$ , and  $SeS^-$  molecules dissolved in alkali halide crystals.* *J. Chem. Phys.* **1973**, 58(5): 2024–2038.
- [67] C.A. Sawicki, D.B. Fitchen. *Laser-excited spectra and reorientation of the  $S_2^-$  ion in alkali halides.* *J. Chem. Phys.* **1976**, 65(11): 4497–4507.



- [68] R.J.H. Clark, D.G. Cobbold. *Characterization of sulfur radical anions in solutions of alkali polysulfides in dimethylformamide and hexamethylphosphoramide and in the solid state in ultramarine blue, green, and red.* **Inorg. Chem.** **1978**, 17(11): 3169–3174.
- [69] J. Rolfe. **J. Chem. Phys.** **1968**, 49(9): 4193–4197.
- [70] G.J. Vella, J. Rolfe. *Emission spectra of  $S_2^-$ ,  $Se_2^-$ , and  $SeS^-$  ions in KI crystals.* **J. Chem. Phys.** **1974**, 61(1): 41–47.
- [71] T. Chivers. *Ubiquitous trisulphur radical ion  $S_2^{\cdot-}$ .* **Nature** **1974**, 252: 32–33.
- [72] S. Moran, G.B. Ellison. *Photoelectron spectroscopy of sulfur ions.* **J. Phys. Chem.** **1988**, 92(7): 1794–1803.
- [73] N.R. Nimlos, G.B. Ellison. *Photoelectron spectroscopy of sulfur-containing anions ( $SO_2^-$ ,  $S_3^-$ , and  $S_2O^-$ ).* **J. Phys. Chem.** **1986**, 90(12): 2574–2580.
- [74] G. Ganteför, S. Hunsicker, R.O. Jones. *Prediction and observation of ring and chain isomers in  $S_n^-$  ions.* **Chem. Phys. Lett.** **1995**, 236(1–2): 43–49.
- [75] S. Hunsicker, R.O. Jones, G. Ganteför. *Rings and chains in sulfur cluster anions  $S^-$  to  $S_9^-$ : Theory (simulated annealing) and experiment (photoelectron detachment).* **J. Chem. Phys.** **1995**, 102(15): 5917–5936.
- [76] F.A. Cotton, J.B. Harmon, R.M. Hedges. *Calculation of the ground state electronic structures and electronic spectra of di- and trisulfide radical anions by the scattered wave-SCF- $X\alpha$  method.* **J. Am. Chem. Soc.** **1976**, 98(6): 1417–1424.
- [77] C. Heinemann, W. Koch, G.-G. Lindner, D. Reinen. *Electronic spectrum of  $S_2^-$ , the electron affinity of  $S_2$ , and the binding energies of neutral and anionic  $S_3$  clusters.* **Phys. Rev. A** **1995**, 52(2): 1024–1038.
- [78] M.D. Chen, M.L. Liu, L.S. Zheng, Q.E. Zhang, C.T. Au. *A density functional study for the isomers of anionic sulfur clusters  $S_n^-$  ( $n = 3-20$ ).* **Chem. Phys. Lett.** **2001**, 350(1–2): 119–127.
- [79] W. Koch, J. Natterer, C. Heinemann. *Quantum chemical study on the equilibrium geometries of  $S_3$  and  $S_3^-$ . The electron affinity of  $S_3$  and the low lying electronic states of  $S_3^-$ .* **J. Chem. Phys.** **1995**, 102(15): 6159–6167.
- [80] T. Chivers, I. Drummond. *Characterization of the trisulfur radical anion  $S_3^-$  in blue solutions of alkali polysulfides in hexamethylphosphoramide.* **Inorg. Chem.** **1972**, 11(10): 2525–2527.
- [81] E. Anders, N. Grevesse. *Abundances of the elements: Meteoritic and solar.* **Geochim. Cosmochim. Acta** **1989**, 53(1): 197–214.
- [82] R.E.S. Clegg, D.L. Lambert, R.A. Bell. *Isotopes of titanium in cool stars.* **Astrophys. J.** **1979**, 234: 188–199.
- [83] A.J. Merer. *Spectroscopy of the diatomic 3d transition metal oxides.* **Ann. Rev. Phys. Chem.** **1989**, 40: 407–438; and references therein.
- [84] M. Barnes, A.J. Merer, G.F. Metha. **J. Mol. Spectrosc.** **1997**, 181(1): 180–193.

- [85] L.A. Kaledin, J.E. McCord, M.C. Heaven. *Optical–optical double resonance spectroscopy of jet-cooled TiO: New  $^3\Phi$  and  $^3\Pi$  states near 4 eV.* **J. Mol. Spectrosc.** **1995**, 173(2): 499–509.
- [86] A.D. Sappey, G. Eiden, J.E. Harrington, J.C. Weisshaar. *Vibronic structure of TiO<sup>+</sup> from multiphoton ionization photoelectron spectroscopy.* **J. Chem. Phys.** **1989**, 90(3): 1415–1428.
- [87] G.M. Daly, M.S. El-Shall. *Gas phase clustering of N<sub>2</sub> molecules on to TiO<sup>+</sup>: Comparison with Ti<sup>+</sup> and evidence for the octahedral structure of TiO<sup>+</sup>(N<sub>2</sub>)<sub>5</sub>.* **J. Chem. Phys.** **1994**, 100(2): 1771–1772.
- [88] C.M. Sharp, W.F. Huebner. **Astrophys. J. Suppl. Ser.** **1990**, 72(2): 417–431.
- [89] K.S. Jeong, J.M. Winters, T. Le Bertre, E. Sedlmayr. *Self-consistent modeling of the outflow from the O-rich Mira IRC –20197.* **Astron. Astrophys.** **2003**, 407(1): 191–206.
- [90] H. Wu, L.-S. Wang. *Electronic structure of titanium oxide clusters: TiO<sub>y</sub> (y = 1–3) and (TiO<sub>2</sub>)<sub>n</sub> (n = 1–4).* **J. Chem. Phys.** **1997**, 107(20): 8221–8228.
- [91] F. Grein. *Density functional theory and multireference configuration interaction studies on low-lying excited states of TiO<sub>2</sub>.* **J. Chem. Phys.** **2007**, 126(3): 034313/1–8.
- [92] G. Wallerstein, G. Gonzales. **Publ. Astron. Soc. Pac.** **2001**, 113(786): 954–956.
- [93] H. Wang, T.C. Steimle, C. Apetrei, J.P. Maier. *Characterization of the  $\tilde{X}^1A_1$  and  $\tilde{A}^1B_2$  electronic states of titanium dioxide, TiO<sub>2</sub>.* **Phys. Chem. Chem. Phys.** **2009**, 11(15): 2649–2656.
- [94] X. Zhuang, A. Le, T.C. Steimle, R. Nagarajan, V. Gupta, J.P. Maier. *Visible spectrum of titanium dioxide.* **Phys. Chem. Chem. Phys.** **2010**, 12(45): 15018–15028.
- [95] H. Xu, P.M. Johnson, T.J. Sears. *Photoinduced Rydberg ionization spectroscopy of phenylacetylene: Vibrational assignments of the  $\tilde{C}$  state of the cation.* **J. Phys. Chem. A** **2006**, 110(25): 7822–7825.
- [96] J. Fulara, M. Grutter, J.P. Maier. *Higher excited electronic transitions of polyacetylene cations HC<sub>2n</sub>H<sup>+</sup> n = 2–7 in neon matrixes.* **J. Phys. Chem. A** **2007**, 111(46): 11831–11836.
- [97] M. Araki, P. Cias, A. Denisov, J. Fulara, J.P. Maier. *Electronic spectroscopy of the nonlinear carbon chains C<sub>4</sub>H<sub>4</sub><sup>+</sup> and C<sub>8</sub>H<sub>4</sub><sup>+</sup>.* **Can. J. Chem.** **2004**, 82(6): 848–853.
- [98] M. Araki, H. Linnartz, P. Cias, A. Denisov, J. Fulara, A. Batalov, I. Shnitko, J.P. Maier. *High-resolution electronic spectroscopy of a nonlinear carbon chain radical C<sub>6</sub>H<sub>4</sub><sup>+</sup>.* **J. Chem. Phys.** **2003**, 118(23): 10561–10565.
- [99] D. Khoroshev, M. Araki, P. Kolek, P. Birza, A. Chirokolava, J.P. Maier. *Rotationally resolved electronic spectroscopy of a nonlinear carbon chain radical C<sub>6</sub>H<sub>4</sub><sup>+</sup>.* **J. Mol. Spectrosc.** **2004**, 227(1): 81–89.
- [100] M. Araki, T. Motylewski, P. Kolek, J.P. Maier. *Electronic absorption spectrum of a nonlinear carbon chain: trans-C<sub>6</sub>H<sub>4</sub><sup>+</sup>.* **Phys. Chem. Chem. Phys.** **2005**, 7(10): 2138–2141.
- [101] J.F. Stanton, J. Fulara. Private communications, **2012**.

## ELECTRONIC ABSORPTION SPECTRA OF PROTONATED ANTHRACENES AND PHENANTHRENES, AND THEIR NEUTRALS IN NEON MATRICES

IRYNA GARKUSHA<sup>1</sup>, JAN FULARA<sup>1,2</sup>, ADAM NAGY<sup>1</sup>, AND JOHN P. MAIER<sup>1</sup>

<sup>1</sup> Department of Chemistry, University of Basel, Klingelbergstrasse 80, CH-4056 Basel, Switzerland; [j.p.maier@unibas.ch](mailto:j.p.maier@unibas.ch)

Received 2010 November 4; accepted 2010 December 14; published 2011 January 31

### ABSTRACT

Electronic spectra of three isomers of protonated anthracene and five isomers of protonated phenanthrene have been detected in 6 K neon matrices following deposition of mass-selected  $m/z = 179$  cations produced from dihydro-anthracene or -phenanthrene. The cations exhibit moderately intense band systems in the 400–550 nm range. Corresponding neutrals have been observed in the UV. The absorptions are assigned to specific isomers of the protonated species on the basis of time-dependent density functional theory calculations. The astrophysical relevance of protonated anthracenes and phenanthrenes as candidates for carriers of diffuse interstellar bands is discussed.

*Key words:* ISM: molecules – molecular data – techniques: spectroscopic

*Online-only material:* color figures

### 1. INTRODUCTION

It has been suggested that protonated polycyclic aromatic hydrocarbons (H-PAH<sup>+</sup>s) are important constituents of the interstellar medium (ISM). They may play a catalytic role for the synthesis of H<sub>2</sub> (Bauschlicher 1998; Hirama et al. 2004), which likely proceeds in the following steps. The first is formation of H-PAH<sup>+</sup> in a reaction of PAH<sup>+</sup> with H, followed by attachment of a second H atom to produce H<sub>2</sub>-PAH<sup>+</sup>. The latter dissociates leading to H<sub>2</sub>, and PAH<sup>+</sup> is recovered. Protonated PAHs can also be formed in the reaction of atomic hydrogen with PAH<sup>+</sup> cations, hydrogen-deficient aromatic cations with molecular hydrogen, and that of neutral PAHs with H<sub>3</sub><sup>+</sup> (Le Page et al. 1997; Snow et al. 1998; Herbst & Le Page 1999). They might be involved in the unidentified infrared (UIR) emission bands (Hudgins et al. 2001) at 6.2  $\mu\text{m}$ , C–H modes of a CH<sub>2</sub> group and observed as a shoulder near the strong 3.3  $\mu\text{m}$  IR emission band. This has recently stimulated a few gas-phase IR studies on H-PAH<sup>+</sup>s using mass-selected photodissociation (PD) spectroscopy and the messenger atom method (Ricks et al. 2009), or IR laser multiphoton PD spectroscopy (Knorke et al. 2009). IR spectra of a number of H-PAH<sup>+</sup>s have been obtained; the spectrum of protonated coronene (Knorke et al. 2009) resembles to some extent UIRs.

Experimental data on the electronic spectroscopy of this class of molecules are scarce. H-PAH<sup>+</sup>s are known intermediates in organic chemistry and were subject to spectroscopic studies several decades ago. The arenium ions were generated by dissolving PAHs in strong acidic solutions and their properties were investigated by NMR, IR (Olah et al. 1978), and optical methods (Olah et al. 1966; Perkampus & Baumgarten 1964; Reid 1954). The structure elucidated from these studies is the  $\sigma$ -complex of the proton attached to the aromatic hydrocarbon moiety. Recent gas-phase studies have reported the electronic spectra of protonated naphthalene (Alata et al. 2010b) and some larger protonated linear acenes (Alata et al. 2010a). They consist of a sharp origin band followed by a complex, unclear pattern.

The suggestion that protonated PAHs could be responsible for certain diffuse interstellar bands (DIBs) has been put forward (Pathak & Sarre 2008), because time-dependent (TD) density functional theory (DFT) calculations reveal that some such cations could have strong transitions in the visible domain, where DIBs are detected. To test this, laboratory gas-phase spectroscopic measurements on protonated PAHs are necessary. As a step toward this and to decide which protonated PAHs should be focused on, we have succeeded in measuring the electronic absorption spectra of protonated anthracene and phenanthrene isomers isolated in 6 K neon matrices using mass-selected ions. These data are more useful than just the theoretical DFT values as they show unambiguously the wavelength region of the electronic transition and give an indication of their oscillator strength.

### 2. EXPERIMENTAL

The apparatus used in this study was described by Fulara et al. (2010). Protonated phenanthrene and anthracene cations were produced in a hot cathode discharge source from 9,10-dihydro-phenanthrene (9,10DHPH) and 9,10-dihydro-anthracene (9,10DHA) vapors seeded in helium. The cations were extracted from the source by electrostatic lenses and guided to a quadrupole bender, where they were separated from neutral molecules. The ion beam was then directed into a quadrupole mass filter which was set to transmit only  $m/z = 179 \pm 0.5$  cations. These were codeposited with neon onto a rhodium-coated sapphire substrate held at 6 K. The current of the cations arriving at the surface was measured during matrix growth (4–5 hr): total charge was 50–65  $\mu\text{C}$  in the case of protonated phenanthrene and 80–85  $\mu\text{C}$  for protonated anthracene.

The detection system is a single-beam spectrometer. It consists of a light source (xenon or halogen lamp) and a spectrograph equipped with an open-electrode CCD detector. Broad-band light is focused onto the entrance slit of the matrix and propagates  $\sim 20$  mm parallel to the substrate surface through the  $\sim 150$   $\mu\text{m}$  neon layer. The beam coming out of the exit slit is focused onto a bundle of 50 quartz fibers, illuminates the diffraction grating of the 0.3 m spectrograph and is detected by a CCD. The absorption spectra are recorded in several sections covering the 220–1100 nm range.

<sup>2</sup> Permanent address: Institute of Physics, Polish Academy of Sciences, Al. Lotników 32/46, PL-02668 Warsaw, Poland.

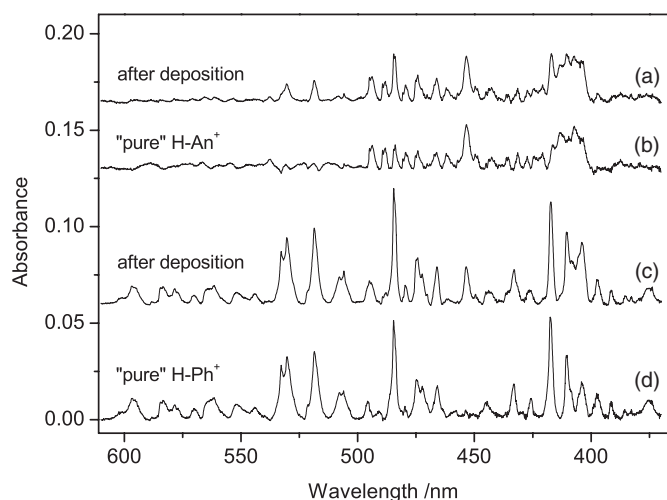


**Figure 1.** Absorption spectra recorded in a 6 K neon matrix after deposition of  $m/z = 179$  cations produced from (a) 9,10-dihydro-anthracene and (c) 9,10-dihydro-phenanthrene; (b) spectrum of protonated anthracenes obtained after scaling trace (c) to the same intensity of the distinct absorption at 532 nm and subtracting it from trace (a); (d) spectrum of protonated phenanthrenes obtained after scaling trace (a) to the same intensity of the absorption at 453 nm and subtracting it from trace (c).

Due to the high intensity of the broadband light source, care was taken to minimize photoconversion of the species during the recordings. Measurements were always started at the longest wavelength and continued into the UV. Appropriate long-pass filters were also used. In order to check whether photoconversion of the isolated species had taken place during the scans, the spectra were recorded anew.

Ions can be trapped in the matrix efficiently if their electrical charge is balanced with counterions. For this purpose chloromethane was added to the neon in the ratio 1:40,000. Some cations hit metal surfaces of the vacuum chamber and release free electrons. These are attracted by the positively charged matrix and captured by  $\text{CH}_3\text{Cl}$ , which dissociatively forms  $\text{Cl}^-$  and  $\text{CH}_3$ . The former compensates the charge of the deposited cations. Due to a very low concentration of  $\text{CH}_3\text{Cl}$  (and even lower of  $\text{CH}_3$  and  $\text{Cl}^-$ ) these species do not perturb the electronic spectra of the trapped cations.

### 3. RESULTS AND DISCUSSION

#### 3.1. Protonated Anthracene ( $\text{H-An}^+$ )

Deposition of  $m/z = 179$  cations produced from 9,10DHAN into a neon matrix resulted in a number of moderately strong absorption systems in the visible range (Figure 1, trace (a)). Known absorptions of the anthracene cation ( $\text{An}^+$ ) in the near infrared and UV (Szczepanski et al. 1993), and weak ones of the phenanthrene cation ( $\text{Ph}^+$ ) in the near IR (Brechignac & Pino 1999; Salama et al. 1994) are also present in the spectrum. The reason why bands of  $\text{An}^+$  appear when  $\text{H-An}^+$  cations are deposited could be the contamination of the precursor sample (9,10DHAN) with  $\text{An}$  or decomposition of the precursor in the ion source. Of 100 anthracene molecules about 15 contain one  $^{13}\text{C}$  atom. Parent ions of the latter isotopologues have the same  $m/z$  as  $\text{H-An}^+$  ions. Fragmentation of  $\text{H-An}^+$  during growth of the matrix could be another reason for the presence of  $\text{An}^+$ . Weak bands of  $\text{Ph}^+$  in the near IR are likely caused by the contamination of 9,10DHAN with 9,10DHPH, though isomerization of  $\text{H-An}^+$  in the ion source resulting in  $\text{H-Ph}^+$  cannot be ruled out.

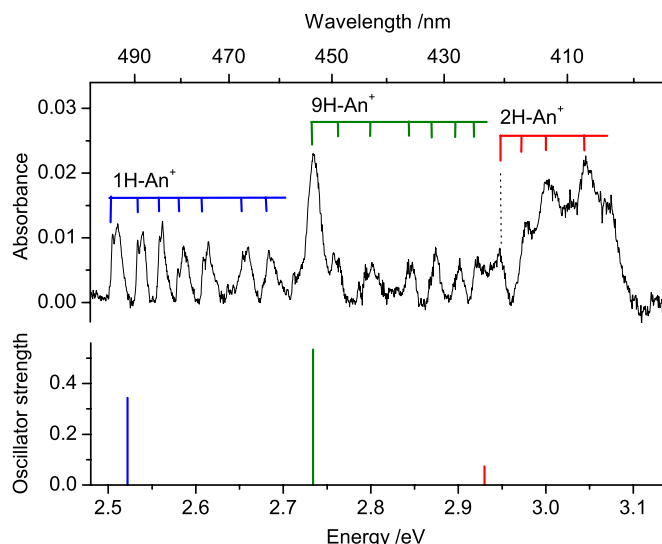


**Figure 2.** Electronic absorption spectrum of protonated anthracenes compared to the strongest computed excitation energies of the three isomers (stick diagram). Transition energies, calculated with TD DFT at the B3LYP/6-311G( $d,p$ ) level of theory, are shifted by  $-0.65$  eV.

(A color version of this figure is available in the online journal.)

In order to test whether the new absorptions seen in Figure 1 (trace (a)) are unique for  $\text{H-An}^+$ , mass-selected  $\text{H-Ph}^+$  generated from 9,10DHPH were deposited; the obtained spectrum is shown in trace (c). Comparison of the two spectra reveals some similarity. The strongest bands of  $\text{H-Ph}^+$  are also seen, although weakly, in the spectrum of  $\text{H-An}^+$ , indicating that in the  $\text{H-An}^+$  experiment  $\text{H-Ph}^+$  cations were also formed.

To separate absorptions of  $\text{H-Ph}^+$  from those of  $\text{H-An}^+$ , the spectrum of the former was subtracted from that of the latter after scaling by an appropriate factor so that the distinct, intense bands of  $\text{H-Ph}^+$  would have the same intensity in both spectra. The result is trace (b). Comparison of traces (a)–(c) indicates that the electronic spectrum of  $\text{H-Ph}^+$  also contains the absorptions of  $\text{H-An}^+$ . They can again be removed by subtraction, after scaling the  $\text{H-An}^+$  trace by a factor such that the distinct band at 453 nm has the same intensity in both spectra. The absorption of  $\text{H-Ph}^+$  is the bottom trace of Figure 1.

The “pure” spectrum of  $\text{H-An}^+$  is redrawn in Figure 2. The intensities of the bands decrease after UV irradiation of the matrix, confirming its ionic origin. Three band systems are distinguished. The first one with onset at 493.8 nm shows a long progression built on the  $\sim 200$   $\text{cm}^{-1}$  mode. Each band of this system has a sharp long-wavelength shoulder, which is spaced from the maximum of the band by  $\sim 50$   $\text{cm}^{-1}$ . It is the zero phonon line, often observed in spectra of matrix-isolated species. The strongest band at 453.5 nm forms the second system; the third system is a group of broad absorptions around 410 nm. The base line was not corrected in this region and may contain a broad bump underneath the absorptions, which could be artificial, due to light interference upon probing the matrix. Wavelengths of the band maxima are collected in Table 1.

Several decades ago  $\text{H-An}^+$  was studied in strong acidic solutions (Aalbersberg et al. 1959; Dallinga et al. 1958; Gold & Tye 1952; Reid 1954) and melted salts (Brigodiot & Lebas 1976; Zingg et al. 1984), and its electronic spectrum was reported. The anthracenium ion  $\text{H-An}^+$  exhibits a strong, broad absorption with maximum around 410–430 nm in these environments. Because these spectra were measured in strongly perturbing

**Table 1**  
Observed Band Maxima and Their Assignments of Protonated Anthracenes and Phenanthrenes, and Their Neutrals in a Neon Matrix

$\lambda$ (nm)	$\bar{\nu}$ (cm <sup>-1</sup> )	$\Delta\bar{\nu}$ (cm <sup>-1</sup> )	Assignment
<b>Protonated anthracenes</b>			
493.8	20 251	0	$0_0^0(2)^1A' \leftarrow \tilde{X}^1A' 1H-An^+$
488.2	20 483	232	$\nu_{46}$
484.0	20 661	410	$2\nu_{46}$
479.4	20 859	608	$3\nu_{46}$
474.2	21 088	837	$\nu_{38}$
466.1	21 455	1204	$\nu_{28-31}$
462.0	21 645	1394	$\nu_{20-23}$
449.8	22 232	1981	$\nu_{38} + \nu_{28-31}$
442.7	22 589	2338	$2\nu_{28-31}$
453.5	22 051	0	$0_0^0(2)^1B_2 \leftarrow \tilde{X}^1A_1 9H-An^+$
442.7	22 589	538	$\nu_{20}$
435.4	22 967	917	$\nu_{17}$
431.4	23 180	1130	$\nu_{15}$
427.4	23 397	1347	$\nu_{11}$
424.5	23 557	1506	$\nu_{20} + \nu_{17}$
420.8	23 764	0	$0_0^0(2)^1A' \leftarrow \tilde{X}^1A' 2H-An^+$
416.5	24 010	246	$\nu_{43}$
413.3	24 195	431	$\nu_{41}$ or $\nu_{42}$
407.2	24 558	794	$\nu_{35}$
<b>Hydro-anthracenyl radical</b>			
326.4	30 637	0	$0_0^0 H-An$
320.7	31 182	545	
313.2	31 928	1291	
305.7	32 712	2075	
<b>Protonated phenanthrenes</b>			
596.6	16 762	0	$0_0^0(1)^1A' \leftarrow \tilde{X}^1A' 9H-Ph^+$
578.2	17 295	533	$\nu_{42}$
561.4	17 813	1051	$2\nu_{42}$
543.7	18 392	1631	$\nu_{12}$
530.3	18 857	0	$0_0^0(2)^1A' \leftarrow \tilde{X}^1A' 9H-Ph^+$
518.6	19 283	425	$\nu_{44}$
506.1	19 759	902	$\nu_{36}$ or $\nu_{37}$
495.5	20 182	1324	$\nu_{22-24}$
465.9	21 464	2607	$2\nu_{22-24}$
583.3	17 144	0	$0_0^0(1)^1A' \leftarrow \tilde{X}^1A' 2H-Ph^+$
570.1	17 541	397	$\nu_{45}$
564.7	17 709	565	$\nu_{41}$
417.4	23 958	0	$0_0^0(2)^1A' \leftarrow \tilde{X}^1A' 2H-Ph^+$
410.5	24 361	403	$\nu_{44}$
404.0	24 752	795	$2\nu_{44}$
397.4	25 164	1206	$3\nu_{44}$
391.3	25 556	1598	$4\nu_{44}$
385.5	25 940	1983	$5\nu_{44}$
532.8	18 769	0	$0_0^0(1)^1A' \leftarrow \tilde{X}^1A' 1H-Ph^+$
518.6	19 283	514	$\nu_{42}$
507.9	19 689	920	$\nu_{36}$
484.5	20 640	0	$0_0^0(2)^1A' \leftarrow \tilde{X}^1A' 3H-Ph^+$
474.6	21 070	431	$\nu_{44}$
472.3	21 173	533	$\nu_{42}$
465.9	21 464	824	$2\nu_{44}$
433.1	23 089	0	$0_0^0(2)^1A' \leftarrow \tilde{X}^1A' 4H-Ph^+$
425.8	23 485	396	$\nu_{45}$
551.8	18 123	Not assigned	
444.7	22 487	Not assigned	
<b>Hydro-phenanthrenyl radical</b>			
375.1	26 660	0	$0_0^0 9H-Ph$

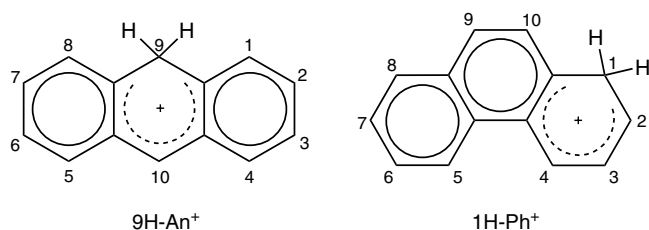


**Figure 3.** Lowest energy isomers of protonated anthracene and phenanthrene.

media, it is meaningless to compare them with the present neon matrix data.

In order to assign the observed band systems of  $\text{H-An}^+$ , DFT calculations using the B3LYP functional and the 6–311G(*d,p*) basis set were carried out for three isomers of  $\text{H-An}^+$  differing in the proton position on the anthracene skeleton. All computations were done using the GAUSSIAN 03 program suite (Frisch et al. 2004). The lowest energy was found for the isomer which has the proton attached at position 9 of anthracene (9H- $\text{An}^+$ ) (Figure 3). Two other isomers, 1H- $\text{An}^+$  and 2H- $\text{An}^+$ , lie 36.4 and 49.3 kJ mol<sup>-1</sup> higher. The values are corrected for zero-point vibrational energies. Excitation energies of these three isomers of  $\text{H-An}^+$  were calculated using the TD DFT method at the B3LYP/6–311G(*d,p*) level of theory and are collected in Table 2. The strongest transition for all considered isomers of  $\text{H-An}^+$  was predicted in the UV and its excitation energy lies within the 3.2–3.6 eV range. Usually, TD DFT overestimates the excitation energy; this can be by as much as 0.5 eV. Taking this into account, the excitation energies of the three isomers are close enough to the onsets of three band systems of  $\text{H-An}^+$ . The match is even better if a shift of 0.65 eV is used. Corrected electronic transition energies of the three isomers of  $\text{H-An}^+$  and the corresponding oscillator strengths are displayed in Figure 2.

The onset of the first band system at 493.8 nm lies close to the calculated transition energy of 1H- $\text{An}^+$ . It agrees also well with recent gas-phase photofragmentation data, where the  $S_1 \leftarrow S_0$  transition of protonated anthracene was observed at 491.43 nm (Alata et al. 2010a). The origin of the second system at 453.5 nm coincides with the calculated excitation energy of 9H- $\text{An}^+$ . The broadband system located around 410 nm has energy close to the predicted transition of isomer 2H- $\text{An}^+$ . Therefore, we tentatively assign each band system of  $\text{H-An}^+$  to its nearest-in-energy transition of different isomers. The assignment of individual vibrational bands that form these systems is given in Table 1. It is based on calculated ground-state frequencies of the species considered. In some cases the assignment is not unambiguous, because several modes have frequencies falling within  $\pm 30$  cm<sup>-1</sup> of the observed ones.

Besides the visible absorptions of  $\text{H-An}^+$  discussed above, the UV range is also relevant for these species. The 295–385 nm section of the spectrum measured after deposition of  $\text{H-An}^+$  into a neon matrix is depicted in Figure 4 (trace (b)). The strongest bands are the absorptions of anthracene cation (trace (a)) and neutral anthracene (trace (e)). The reason why  $\text{An}^+$  is present in the matrix when  $\text{H-An}^+$  was deposited was discussed in the first paragraph of this section. Neutral anthracene appears in the matrix as a result of the neutralization of  $\text{An}^+$ . After stepwise UV irradiation of the matrix new absorptions in the 300–340 nm range appeared and grew in intensity (traces (c) and (d)). They are better seen in the inset of Figure 4 where the bands of  $\text{An}^+$ , which remained after UV irradiation, were removed. The system, which has appeared after UV photobleaching of  $\text{H-An}^+$  cations, is of hydro-anthracenyl radical (H-An).

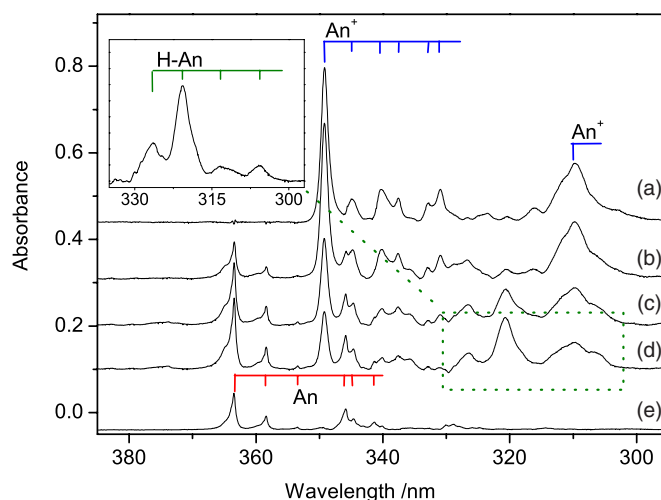


**Figure 4.** UV part of the absorption spectra recorded after (b) deposition of  $\text{C}_{14}\text{H}_{11}^+$  cations in a 6 K neon matrix produced from 9,10-dihydro-anthracene, (c) 20 minute and (d) subsequent 25 minute irradiation with a medium-pressure Hg lamp; (a) and (e) are spectra of anthracene cation ( $\text{An}^+$ ) and neutral anthracene (An), respectively. The inset shows absorption of hydro-anthracenyl radical (H-An), appearing as a result of photobleaching of the  $\text{H-An}^+$  cations. (A color version of this figure is available in the online journal.)

According to TD DFT calculations, two isomers of neutral H-An, 9H-An and 1H-An, have strong transition in the UV range around 342 and 337 nm respectively (J. Fulara et al. 2010, electronic excitation energies calculated with TD DFT at the B3LYP/6–311G(*d,p*) level of theory, unpublished). These are close to the observed band system with onset at 326.4 nm. It is difficult to find out from the present experimental data which H-An isomer is responsible for the absorptions in this region. It is also possible that both 9H-An and 1H-An contribute to the spectrum in Figure 4, as the bands have a peculiar intensity distribution and may belong to two overlapping systems.

### 3.2. Protonated Phenanthrene ( $\text{H-Ph}^+$ )

The electronic absorption spectrum obtained after mass-selective deposition of  $m/z = 179$  cations produced from 9,10DHPH is presented in Figure 1 (trace (c)), and after removing the absorptions of  $\text{H-An}^+$  in trace (d). The spectrum is rich in absorption bands, which probably belong to several electronic systems. Thus, a number of UV irradiation experiments were carried out on a matrix containing  $\text{H-Ph}^+$  ions. These differed in exposure time and wavelength domain of the UV radiation. Spectra recorded after deposition and some irradiation steps are compared in Figure 5. The absorption measured after deposition of the cations is trace (a) and those detected after subsequent UV irradiation are traces (b)–(e). To indicate the changes in intensity of the bands, two spectra measured after different irradiation schemes were subtracted from each other after normalizing them to the same intensity of the specific band (traces (f) and (g)).

The spectra in Figure 5 reveal several electronic band systems, which behave differently under irradiation conditions; this indicates their different origin. Eight band systems of  $\text{H-Ph}^+$  could be distinguished after deposition in a neon matrix. The spectrum is redrawn in Figure 6 and the absorptions belonging to the same isomer of  $\text{H-Ph}^+$  are marked with a specific color.

Seven of the eight systems decrease in intensity after prolonged irradiation with a medium-pressure Hg lamp (Figure 5, trace (e)). Only the absorption at 375 nm behaves in an opposite

**Table 2**  
Excited State Symmetries, Calculated Excitation Energies and Oscillator Strengths for Protonated Anthracenes and Phenanthrenes<sup>a,b</sup>

Protonated Anthracenes			Protonated Phenanthrenes		
Exc. St. Symm.	$\Delta E$ (eV)	$f$	Exc. St. Symm.	$\Delta E$ (eV)	$f$
9H-An <sup>+</sup> , $\tilde{X}^1A_1, C_{2v}$ (0)			1H-Ph <sup>+</sup> , $\tilde{X}^1A', C_s$ (0)		
$^1A_1$	2.78	0.02	$^1A'$	2.39	0.15
$^1B_2$	3.13	0.0002	$^1A'$	2.64	0.02
$^1B_2$	3.39	0.5	$^1A'$	3.95	0.2
$^1B_1$	4.78	0.0003	$^1A'$	4.33	0.005
$^1A_2$	4.83	0	$^1A''$	4.66	0
1H-An <sup>+</sup> , $\tilde{X}^1A', C_s$ (36.4)			9H-Ph <sup>+</sup> , $\tilde{X}^1A', C_s$ (0.6)		
$^1A'$	1.92	0.05	$^1A'$	2.36	0.06
$^1A'$	3.17	0.3	$^1A'$	2.60	0.09
$^1A'$	3.69	0.006	$^1A'$	3.89	0.002
$^1A'$	4.35	0.04	$^1A'$	4.37	0.06
$^1A''$	4.56	0.0003	$^1A''$	4.56	0.0001
2H-An <sup>+</sup> , $\tilde{X}^1A', C_s$ (49.3)			3H-Ph <sup>+</sup> , $\tilde{X}^1A', C_s$ (2.4)		
$^1A'$	1.91	0.07	$^1A'$	2.63	0.04
$^1A'$	3.42	0.006	$^1A'$	2.70	0.2
$^1A'$	3.58	0.07	$^1A'$	4.13	0.03
$^1A'$	4.57	0.04	$^1A'$	4.56	0.009
$^1A''$	4.60	0	$^1A'$	4.64	0.06
			4H-Ph <sup>+</sup> , $\tilde{X}^1A', C_s$ (4.4)		
			$^1A'$	2.01	0.03
			$^1A'$	2.96	0.2
			$^1A'$	3.74	0.03
			$^1A'$	4.43	0.2
			$^1A''$	4.49	0.0002
			2H-Ph <sup>+</sup> , $\tilde{X}^1A', C_s$ (9.0)		
			$^1A'$	2.24	0.04
			$^1A'$	3.26	0.2
			$^1A'$	3.80	0.03
			$^1A''$	4.58	0
			$^1A'$	4.63	0.5

**Notes.**<sup>a</sup> Excitation energies were calculated with TD DFT at the B3LYP/6-311G(*d,p*) level of theory.<sup>b</sup> Relative ground-state energies (kJ mol<sup>-1</sup>) with respect to the most stable isomer are given in parentheses.

way. Therefore, it belongs to neutral species. Most likely it is the hydro-phenanthrenyl radical (H-Ph) which should appear in the matrix as a result of the neutralization of H-Ph<sup>+</sup> cations. The most stable neutral fragment (phenanthrene molecule), which could be formed from the H-Ph<sup>+</sup> ions, can be excluded as a carrier of this band, because it absorbs at shorter wavelengths (Salama et al. 1994) and its systems were also detected in this experiment.

In the past, 9-hydro-phenanthrenyl radical (9H-Ph) was studied in organic solutions. It was produced by hydrogen subtraction from 9,10DHPH (Koizumi et al. 1997) or by hydrogen addition to phenanthrene (Grodzowski et al. 2003; Kawakubo 1980) following pulse radiolysis. The spectrum consists of a broad band with maximum at 395 nm. This is not too far from the observed absorption at 375 nm for the neutral product in the present experiment. Therefore, the absorption is assigned to the 9H-Ph radical.

The other seven systems have ionic origin, because they decrease upon UV irradiation. They belong to different isomers of H-Ph<sup>+</sup>. Protonated phenanthrene has been studied in strong acidic solutions and the spectrum exhibits two broad absorptions with maxima at 410 and 520 nm (Dallinga et al. 1958; Reid

1954). These electronic systems were tentatively assigned to two isomers: 1H-Ph<sup>+</sup> and 9H-Ph<sup>+</sup>. The spectrum of H-Ph<sup>+</sup> in solution covers the same spectral range as in Figure 6. Interaction of solvent molecules with dissolved ionic species is much stronger than with neutrals. Therefore, detailed comparison of these two spectra is of no relevance, in contrast to the neutral hydro-phenanthrenyl radical.

In order to deduce which isomers of H-Ph<sup>+</sup> are responsible for the spectrum in Figure 6 the ground-state energy of the isomers 1H-, 2H-, 3H-, 4H- and 9H-Ph<sup>+</sup> have been calculated using the DFT method with the B3LYP functional and the 6-311G(*d,p*) basis set. All considered isomers have similar energies spanning only 9 kJ mol<sup>-1</sup> (Table 2). The calculations predict 1H-Ph<sup>+</sup> to be the most stable isomer, but 9H-Ph<sup>+</sup> lies only 0.6 kJ mol<sup>-1</sup> higher. The highest in energy was found to be 2H-Ph<sup>+</sup>, located 9 kJ mol<sup>-1</sup> above 1H-Ph<sup>+</sup>. Because the energy difference of the five isomers is so small, their relative order may change with higher-level calculations.

To assign the spectrum in Figure 6 to a specific isomer of H-Ph<sup>+</sup>, excitation energies are needed. TD DFT calculations were carried out for the five isomers considered above. Computed excitation energies and their oscillator strengths are

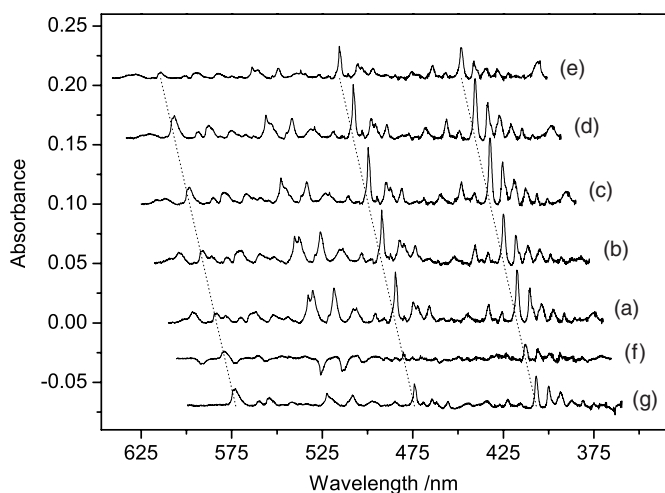


**Figure 5.** Absorption spectra recorded after deposition of  $C_{14}H_{11}^+$  cations in a 6 K neon matrix produced from 9,10-dihydro-phenanthrene after (a) deposition, (b) exposure to the UV radiation of a high-pressure Xe lamp during measurement, (c) 30 minute and (d) additional 30 minute photobleaching with  $390 \text{ nm} > \lambda > 250 \text{ nm}$ , (e) subsequent 20 minute irradiation with a full medium-pressure Hg lamp; (f) = (c)–(a) and (g) = (d)–(e) show changes in the intensities of bands following the irradiation steps.

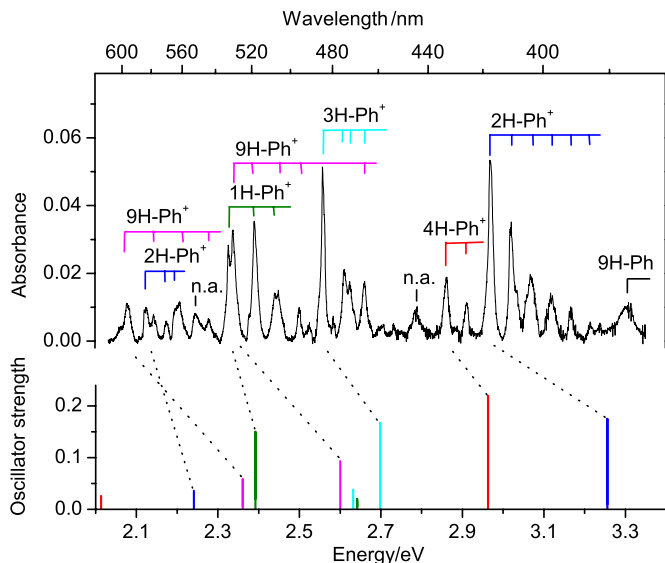


**Figure 6.** Electronic absorption spectrum of protonated phenanthrenes compared to the excitation energies of the five considered isomers (stick spectrum), calculated with TD DFT at the B3LYP/6–311G(*d,p*) level of theory; n.a.—not assigned bands.

(A color version of this figure is available in the online journal.)

collected in Table 2 and displayed in Figure 6. All H-Ph<sup>+</sup> isomers have two allowed electronic transitions in the visible, where the absorptions of protonated phenanthrenes have been detected. We tentatively assign the observed band systems to specific isomers of H-Ph<sup>+</sup> by comparing the excitation energy of its strongest transition with the onset of the nearest system. Dotted lines indicate which isomer is responsible for a certain band system. Individual bands of a given system are assigned using calculated vibrational frequencies of the H-Ph<sup>+</sup> isomers in their ground state (Table 1).

#### 4. RELEVANCE OF H-An<sup>+</sup> AND H-Ph<sup>+</sup> TO DIBs

It has been considered that H-PAH<sup>+</sup>s could be carriers of some DIBs (Pathak & Sarre 2008). H-PAH<sup>+</sup>s can be formed in the ISM in ion–molecule reactions of hydrogen-deficient PAH<sup>+</sup>

cations with H<sub>2</sub>, of atomic hydrogen with PAH<sup>+</sup> or neutral PAHs with highly abundant H<sub>3</sub><sup>+</sup>. All the above mechanisms assume the presence of PAH<sup>+</sup> ions in the ISM; therefore, their astrophysical relevance should also be discussed.

The present spectroscopic studies on protonated anthracene and phenanthrene allow a direct comparison of their transition intensities with the anthracene An<sup>+</sup> and phenanthrene Ph<sup>+</sup> cations. The electronic transitions of An<sup>+</sup> and Ph<sup>+</sup> in the near IR are an order of magnitude stronger than the visible absorptions of the protonated species.

The electronic transition of Ph<sup>+</sup> in a neon matrix (Salama et al. 1994) and in the gas phase, as the Ph<sup>+</sup>–Ar complex (Brechignac & Pino 1999), have been reported. The position of all bands reported in neon agrees well with our studies; however, their relative intensities in the near IR system are different. In the present mass-selective experiment, besides Ph<sup>+</sup> the absorption of neutral phenanthrene has also been detected in the UV. The oscillator strength of the near IR band system of Ph<sup>+</sup> is evaluated to be 0.25 by measuring the change of the intensity of cationic and neutral phenanthrene absorptions induced by UV irradiation of the matrix, and using the experimental oscillator strength of the latter (Clar 1964). This value is about four orders of magnitude higher than that reported by Salama et al. (1994), but is close to the gas-phase value ( $0.15 \pm 0.05$ ; Brechignac & Pino 1999). High oscillator strength of the near-IR transition of Ph<sup>+</sup> is confined mainly to the origin band at 892 nm and makes it favorable for the search in the ISM. An<sup>+</sup>, similarly to Ph<sup>+</sup>, has a strong electronic transition in the near-IR region with the onset around 709 nm, as well as about a five times stronger system around 349 nm (in a neon matrix). The latter could be used for a sensitive detection of An<sup>+</sup>.

The results of the present spectroscopic study on protonated anthracene and phenanthrene isolated in neon matrices reveal that their electronic transitions fall in the 400–550 nm range, where a number of broad DIBs are found (Jenniskens & Désert 1994; Hobbs et al. 2008). Several isomers of these species are detected in the neon matrix; they have moderately intense absorption systems. In the case of protonated phenanthrene, all five isomers have energies within 9 kJ mol<sup>−1</sup> of each other. If H-Ph<sup>+</sup> is formed in the reaction of neutral phenanthrene with H<sub>3</sub><sup>+</sup> in the ISM, then these five isomers should be about equally populated, and hence their column density in a specific line of sight would be lower than for Ph<sup>+</sup>. This and the lower oscillator strength of the visible transition of protonated phenanthrenes in comparison with the near IR one of Ph<sup>+</sup> could hamper their optical detection in the ISM. Similar arguments apply to the detection of H-An<sup>+</sup>. More promising are the protonated PAHs which form fewer isomers (e.g., coronene) and if they have a larger oscillator strength.

This work has been supported by the Swiss National Science Foundation (project no. 200020–124349/1).

#### REFERENCES

- Aalbersberg, W. I., Hoijtink, G. J., Mackor, E. L., & Weijland, W. P. 1959, *J. Chem. Soc.*, 3049  
 Alata, I., Dedonder, C., Broquier, M., Marceca, E., & Jouvet, C. 2010a, <http://hal.inria.fr/inria-00505242/en/>  
 Alata, I., Omidyan, R., Broquier, M., Dedonder, C., Dopfer, O., & Jouvet, C. 2010b, *Phys. Chem. Chem. Phys.*, 12, 14456  
 Bauschlicher, C. W. 1998, *ApJ*, 509, L125  
 Brechignac, P., & Pino, T. 1999, *A&A*, 343, L49  
 Brigodiot, M., & Lebas, J. M. 1976, *J. Mol. Struct.*, 32, 311  
 Clar, E. 1964, *Polycyclic Hydrocarbons Vol. 1* (New York: Academic)



- Dallinga, G., Mackor, E. L., & Stuart, A. A. V. 1958, *Mol. Phys.*, **1**, 123
- Frisch, M. J., et al. 2004, Gaussian 03, Revision C.01 (Wallingford, CT: Gaussian, Inc.)
- Fulara, J., Nagy, A., Garkusha, I., & Maier, J. P. 2010, *J. Chem. Phys.*, **133**, 024304
- Gold, V., & Tye, F. L. 1952, *J. Chem. Soc.*, 2172
- Grodzowski, J., Neta, P., & Wishart, J. F. 2003, *J. Phys. Chem. A*, **107**, 9794
- Herbst, E., & Le Page, V. 1999, *A&A*, **344**, 310
- Hirama, M., Tokosumi, T., Ishida, T., & Aihara, J. 2004, *Chem. Phys.*, **305**, 307
- Hobbs, L. M., et al. 2008, *ApJ*, **680**, 1256
- Hudgins, D. M., Bauschlicher, C. W., & Allamandola, L. J. 2001, *Spectrochim. Acta A*, **57**, 907
- Jenniskens, P., & Désert, F.-X. 1994, *A&AS*, **106**, 39
- Kawakubo, T. 1980, *Mol. Cryst. Liq. Cryst.*, **62**, 41
- Knorke, H., Langer, J., Oomens, J., & Dopfer, O. 2009, *ApJ*, **706**, L66
- Koizumi, H., Fukamura, S., Ichikawa, T., Yoshida, H., & Kubo, J. 1997, *Radiat. Phys. Chem.*, **50**, 567
- Le Page, V., Keheyan, Y., Bierbaum, V. M., & Snow, T. P. 1997, *J. Am. Chem. Soc.*, **119**, 8373
- Olah, G. A., Pittman, C. U., Waack, R., & Doran, M. 1966, *J. Am. Chem. Soc.*, **88**, 1488
- Olah, G. A., Staral, J. S., Asencio, G., Liang, G., Forsyth, D. A., & Mateescu, G. D. 1978, *J. Am. Chem. Soc.*, **100**, 6299
- Pathak, A., & Sarre, P. J. 2008, *MNRAS*, **391**, L10
- Perkampus, H.-H., & Baumgarten, E. 1964, *Angew. Chem., Int. Ed. Engl.*, **3**, 776
- Reid, C. 1954, *J. Am. Chem. Soc.*, **76**, 3264
- Ricks, A. M., Douberly, G. E., & Duncan, M. A. 2009, *ApJ*, **702**, 301
- Salama, F., Joblin, C., & Allamandola, L. J. 1994, *J. Chem. Phys.*, **101**, 10252
- Snow, T. P., Le Page, V., Keheyan, Y., & Bierbaum, V. M. 1998, *Nature*, **391**, 259
- Szczepanski, J., Vala, M., Talbi, D., Parisel, O., & Ellinger, Y. 1993, *J. Chem. Phys.*, **98**, 4494
- Zingg, S. P., Dworkin, A. S., Sorlie, M., Chapman, D. M., Buchanan, A. C., & Smith, G. P. 1984, *J. Electrochem. Soc.*, **131**, 1602



# CURRICULUM VITAE

---

## PERSONAL DETAILS

Name                      ÁDÁM NAGY  
Date of birth             December 5, 1979  
Nationality              Hungarian



## EDUCATION

*University of Basel, Faculty of Science*

Basel, Switzerland

- **Ph.D. in Chemistry**, 2012  
'Summa cum laude'; Thesis title: *Electronic spectroscopy of open-chain and aromatic hydrocarbon cations in neon matrices*

12/2005–03/2012

*Eötvös Loránd University, Faculty of Science*

Budapest, Hungary

- **M.Sc. in Chemistry**, 2005  
'Good'; Cumulative GPA: 'Very good'
- Specializations in molecular structure determination and chemical informatics

09/1998–06/2005

*Földes Ferenc High School*

Miskolc, Hungary

- Experimental six-years training  
**School-leaving examination** (Matura), 1998  
5× 'Excellent' (Hons in mathematics, chemistry and history)

09/1992–06/1998

*Nº 7 Szabó Lőrinc Elementary*

Miskolc, Hungary

- German-specialized class

09/1986–06/1992

## ACTIVITIES

- Teaching assistance (Physical chemistry II/III:  
Quantum mechanics, spectroscopy and group theory) 10/2006–06/2011
- Research group site webmaster 07/2006–03/2012
- Chess champion of the *University of Basel* 10/2007

## POSTER PRESENTATIONS

- [1] A. Nagy, J. Fulara, I. Garkusha, J.P. Maier. *Electronic absorption spectra of mass-selected hydrocarbon cations in solid neon:  $C_nH_4^+$  ( $n=5-8,10,12$ )*. IAU Symposium 280: The Molecular Universe **2011**, Toledo, Spain.
- [2] A. Nagy, I. Garkusha, J. Fulara, J.P. Maier. *Electronic absorption spectra of aromatic hydrocarbon cations in neon matrices*. Faraday Discussion 150: Frontiers in Spectroscopy **2011**, Basel, Switzerland.
- [3] A. Nagy, J. Fulara, I. Garkusha, J.P. Maier. *Aromatic structure(s) from a linear precursor mixture:  $C_{11}H_9^+$  in a neon matrix*. 8<sup>th</sup> International Conference on Low-Temperature Chemistry **2010**, Yerevan, Armenia.
- [4] Á. Nagy, I. Garkusha, J. Fulara, J.P. Maier. *Electronic spectroscopy of fragment cations derived from small PAHs*. GRC: Physics & Chemistry of Matrix-Isolated Species **2009**, Oxford, United Kingdom.
- [5] I. Garkusha, A. Nagy, Z. Guennoun, J.P. Maier. *Electronic absorption spectrum of titanium dioxide isolated in 6 K neon matrices*. The 20<sup>th</sup> International Conference on High Resolution Molecular Spectroscopy **2008**, Prague, Czech Republic.

## PEER-REVIEWED PUBLICATIONS

- [1] A. Nagy, I. Garkusha, J. Fulara, J.P. Maier. [Perspective] *Electronic spectroscopy of transient species in solid neon: the indene polycyclic hydrocarbon cation family  $C_9H_n^+$  ( $n = 7-9$ ) and their neutrals.* (Phys. Chem. Chem. Phys.) **2012**, in preparation.
- [2] I. Garkusha, A. Nagy, J. Fulara, M.F. Rode, A.L. Sobolewski, J.P. Maier. *Electronic spectra and reversible photoisomerization of protonated naphthalenes in solid neon.* **J. Phys. Chem. A** **2012**, published online; doi: 10.1021/jp310612j.
- [3] S. Chakrabarty, V. Rudnev, J. Fulara, R. Dietsche, A. Nagy, I. Garkusha, F.J. Mazzotti, C.A. Rice, J.P. Maier. *Electronic spectra of  $C_4H_3Cl^+$  isomers.* **Mol. Phys.** **2012**, 110(24): 3077–3084.
- [4] A. Nagy, J. Fulara, J.P. Maier. *Formation of aromatic structures from chain hydrocarbons in electrical discharges: Absorption and fluorescence study of  $C_{11}H_9^+$  and  $C_{11}H_9^{\bullet}$  isomers in neon matrices.* **J. Am. Chem. Soc.** **2011**, 133(49): 19796–19806.
- [5] A. Nagy, J. Fulara, I. Garkusha, J.P. Maier. [VIP] *On the benzylium/tropylium ion dichotomy: Electronic absorption spectra in neon matrices.* **Angew. Chem. Int. Ed.** **2011**, 50(13): 3022–3025; **Angew. Chem.** **2011**, 123(13): 3078–3081.
- [6] I. Garkusha, J. Fulara, A. Nagy, J.P. Maier. *Electronic absorption spectra of protonated anthracenes and phenanthrenes, and their neutrals in neon matrices.* **Astrophys. J.** **2011**, 728(2): 131/1–7.
- [7] J.P. Maier, G.A.H. Walker, D.A. Bohlender, F.J. Mazzotti, R. Raghunandan, J. Fulara, I. Garkusha, A. Nagy. *Identification of  $H_2CCC$  as a diffuse interstellar band carrier.* **Astrophys. J.** **2011**, 726(1): 41/1–9.
- [8] I. Garkusha, J. Fulara, A. Nagy, J.P. Maier. *Electronic transitions of protonated benzene and fulvene, and of  $C_6H_7$  isomers in neon matrices.* **J. Am. Chem. Soc.** **2010**, 132(42): 14979–14985.
- [9] J. Fulara, A. Nagy, I. Garkusha, J.P. Maier. *Higher energy electronic transitions of  $HC_{2n+1}H^+$  ( $n=2-7$ ) and  $HC_{2n+1}H$  ( $n=4-7$ ) in neon matrices.* **J. Chem. Phys.** **2010**, 133(2): 024304/1–9.
- [10] I. Garkusha, A. Nagy, Z. Guennoun, J.P. Maier. *Electronic absorption spectrum of titanium dioxide in neon matrices.* **Chem. Phys.** **2008**, 353(1–3): 115–118.
- [11] I. Shnitko, J. Fulara, I. Garkusha, A. Nagy, J.P. Maier. *Electronic transitions of  $S_2^-$  and  $S_3^-$  in neon matrixes.* **Chem. Phys.** **2008**, 346(1–3): 8–12.
- [12] M. Ripszám, Á. Nagy, A. Volford, F. Izsák, I. Lagzi. *The Liesegang eyes phenomenon.* **Chem. Phys. Lett.** **2005**, 414(4–6): 384–388.
- [13] V. Szalay, G. Czakó, Á. Nagy, T. Furtenbacher, A.G. Császár. *On one-dimensional discrete variable representations with general basis functions.* **J. Chem. Phys.** **2003**, 119(20): 10512–10518.



## COLOPHON

---



This thesis was written and edited by *Ádám Nagy* with the help indicated, and submitted only to the *Faculty of Science* of the *University of Basel* and to no other faculty or university.

The original document is stored on the institutional repository of the *University of Basel*, <http://edoc.unibas.ch>.



It is licensed under a **Creative Commons Attribution-NonCommercial-ShareAlike 3.0 Unported License**.

It was typeset with MS Office Word 2003 using the *Palatino Linotype* text face of H. Zapf. The captions are in R. Slimbach's *Myriad Pro*.

The design was inspired by the guide *How to Write a Successful Science Thesis* from W.E. Russey, H.F. Ebel and C. Bliefert, A. Miede's L<sup>A</sup>T<sub>E</sub>X template *A Classic Thesis Style*, R. Bringhurst's book *The Elements of Typographic Style*, and a number of dissertations from this and other research groups freely available on the Web.

The bound version is printed on 100 g/m<sup>2</sup> A4 ultra-white application paper.

